INCORPORATION OF TETRAVALENT ACTINIDES IN MONAZITE-TYPE CERAMICS : SYNTHESIS, SINTERING AND LONG-TERM BEHAVIOR

Danwen Qin

THESE POUR OBTENIR LE GRADE DE DOCTEUR DE L'ECOLE NATIONALE SUPERIEURE DE CHIMIE DE MONTPELLIER

En Chimie Séparative Matériaux et Procédés

École doctorale Sciences Chimiques Balard

Unité de recherche UMR 5257 - ICSM

INCORPORATION D'ACTINIDES TÉTRAVALENTS DANS DES STRUCTURES DE TYPE MONAZITE : SYNTHÈSE, FRITTAGE ET COMPORTEMENT À LONG TERME

Présentée par **Danwen QIN**
le 25 août 2020

Sous la direction de **Nicolas DACHEUX**
et **Nicolas CLAVIER**

Devant le jury composé de

Mme. Fabienne AUDUBERT, Directrice de recherches, CEA Cadarache	Rapporteure
M. Michel VILASI, Professeur, Université de Lorraine	Rapporteur
Mme. Nathalie MONCOFFRE, Directrice de Recherches CNRS, IPN Lyon	Examinatrice
M. Oliver CAMBON, Professeur, Université de Montpellier	Examinateur
M. Nicolas DACHEUX, Professeur, Université de Montpellier	Directeur de thèse
M. Nicolas CLAVIER, Chargé de Recherche CNRS, ICSM	Co-directeur de thèse
Mme. Stéphanie SZENKNECT, Ingénieure, CEA Marcoule - ICSM	Co-encadrante, membre invitée
M. Adel MESBAH, Chargé de Recherche CNRS, ICSM	Co-encadrant, membre invité

En premier lieu, je remercie Stéphane Pellet-Rostaing pour m'avoir accueilli au sein de l'Institut de Chimie Séparative de Marcoule, dont il assure la direction. Je souhaite remercier Nicolas Dacheux et Nicolas Clavier pour m'avoir accueilli au sein du Laboratoire des Interfaces en Evolution et pour m'avoir dirigé mes travaux de thèse. Je les admire pour leurs grandes connaissances scientifiques, leur rigueur dans le travail, leur passion pour la recherche, leur gentillesse et leur patience. Je les remercie pour leurs conseils scientifiques, qui m'aident beaucoup à approfondir mes connaissances et à rendre mes pensées plus claires et plus logiques.

J'adresse de sincères remerciements à mon co-encadrant Adel Mesbah pour m'avoir permis de mener à bien la synthèse des rhabdophanes et m'avoir initié à l'art de la diffraction des rayons X. De plus, ses affirmations m'ont donné beaucoup de confiance et de motivation.

Ma profonde gratitude va aussi à ma co-encadrante Stéphanie Szenknect pour son expertise dans le domaine de la dissolution. Merci pour son soutien, sa gentillesse et sa patience. C'est vraiment un plaisir de travailler avec elle.

Il m'est très difficile de décrire le sentiment de gratitude que j'exprime à l'égard de mes co-directeurs et co-encadrant(e)s pour avoir corrigé maintes fois les diverses versions de mon manuscrit.

J'adresse mes sincères remerciements au Professeur Michel Vilasi et à la Docteure Fabienne Audubert pour avoir accepté de juger ce travail en tant que rapporteurs. Je remercie également la Docteure Nathalie Moncoffre et le Professeur Olivier Cambon pour avoir accepté de participer à ce jury de thèse.

Je voudrais remercier Bertrand Mercier et Philippe Moisy pour leur appui à ma candidature sur cette bourse de thèse du China Scholarship Council et Mingliang Kang pour avoir accepté de devenir mon garant pour cette bourse CSC.

J'exprime aussi ma profonde gratitude à toutes les personnes qui ont contribué activement à ce travail de thèse ; en premier lieu Joseph Lautru et Renaud Podor pour leur aide précieuse lors des nombreuses journées passées devant le MEBE. Je pense également à Bruno Corso, Béatrice Baus-Lagarde, Laurent Claparède, Cyrielle Rey, Henri Pierre Brau et Xavier Le Goff pour leur aide précieuse lors du déroulement de mes expérimentations.

J'adresse un grand merci à toutes les personnes de l'administration, Dominique Alpe-Conchy, Mathilde Dias, Vainina Russello, Hélène Martin, Aurélie Menasria, Alice Vidal, etc. Sans elles, cette thèse n'aurait pas pu se dérouler cette manière.

Il est important pour moi de remercier tous les doctorant(e)s et les postdoctrant(e)s qui m'ont accompagné pendant mon séjour à l'ICSM : Ran Ji, Maximilian Pleines, Ricardo Navarro Amador, Mario Špadina, Régis Mastretta, Alexandre Artese, Markus Baum, Tamir Sukhbaatar, Simon Gourdin, Rémi Boubon, Jun Lin, Zijie Lu, Julie Durain, Sayed Ali Moussaoui, Élisa Rey, Jingxian Wang, Laura Bonato, Sarah El Hakim, Max Hohenschutz, Tania Merhi, Justine Ben Ghozi Bouvrande, Nicolas Félines, Zijun Lu…

J'adresse moult remerciements à l'équipe de LIME : Florent Tocino, Clémence Gausse, Galy Ingrid Nkou Bouala, Paul Estevenon, Théo Cordara, Yanis Cherkaski, Thomas Dalger, Victor Trillaud, Delhia Alby, Alvaro Saravia, Ruwaid Mohamed Rafiuddin, Solène Bertolotto, Jérémie Manaud, Malvina Massonnet, Thibault Kaczmarek, Théo Montaigne, Pierre Asplanato…

La vie dans un pays étranger n'est pas toujours facile, surtout pour une personne comme moi qui ne voyageait pas beaucoup. Grâce à l'aide de Nicolas Dacheux et Nicolas Clavier, même des « accidents » deviennent des anecdotes. En particulier, j'exprime ma gratitude à Nicolas Dacheux pour avoir facilité les préparations des dossiers administratifs. Je remercie également Nicolas Clavier pour son aide dans ma vie quotidienne, surtout lorsque j'ai perdu ma valise à mon arrivée. La dernière chose que je voudrais dire c'est qu'ils ont su me montrer le charme de la vie française : un équilibre délicat entre travail et vie. J'ai donc découvert les marathons, les vins et la cuisine, l'humour français, etc.

En particulier, je voudrais remercier Vainina Russello de son aide indispensable pour préparer les documents, chercher un logement, et me prêter des recettes de cuisine…

Je tiens à remercier les coureur(se)s de l'ICSM pour m'avoir encouragé dans mon entraînement : Nicolas Clavier, Théo Cordara, Jérémie Manaud, Alexandre Artese, Laura Bonato, Matthieu Virot, Stéphanie Szenknect, Jérémy Causse, Damien Bourgeois, Solène Bertolotto, Justine Ben Ghozi Bouvrande, Malvina Massonnet…

Un grand merci aussi à mes amis pour les soirées magnifiques auxquelles j'ai été convié : Jérémie Manaud, Malvina Massonnet, Victor Trillaud, Max Hohenschutz, Tamir Sukhbaatar, Maximilian Pleines, Vainina Russello, Rémi Boubon, Élisa Rey…

Merci à mes amis qui m'ont accompagné dans ma vie Avigonnaise : Ran Ji, Max Hohenschutz, Jun Lin, Zijie Lu, Zijun Lu, Qingru Xu… Je garderai plein de très bons souvenirs.

Enfin, merci à mes parents pour m'avoir soutenu tout au long de me parcours scientifique.

Table of Contents

List of Figures

List of Tables

Introduction

According to the International Atomic Energy Agency (IAEA) [1], nuclear power is affordable, reliable, and clean energy for a sustainable development. There are over 440 reactors in operation worldwide, providing 11 % of the global electricity (> 30% of the world's low-carbon electricity). In terms of environment protection, 1.5 to 2 billion tons of greenhouse gases have been saved per year since 1990 due to the use of the nuclear power [1]. Compared to other clean energies, such as hydropower, wind power, solar power, etc., the levelized costs of nuclear power are the lowest (< 100 US $\$_{2013}$ per MW.h) [2]. Moreover, nuclear reactors operate at a high capacity factor (about 90%), providing continuous, reliable power. France is the leading country in the nuclear industry. In 2018, there were 58 reactors in operation, producing 71.7% of its electricity (*i.e.*, 395.9 TW.h). [3] In terms of nuclear technologies, France designed the European Pressurised Reactors (EPR), which is the first type of the third generation reactor applied in industry [4]. France is also the leader in the spent fuel reprocessing (reprocessing capacity of 1700 tons per year in the La Hague facility [5] and 110 tons of MOX produced in 2017 in the Melox facility [6]). These advanced techniques have contributed to help other countries (such as Japan, UK, China) to treat their spent fuel [7]. Facing the challenge of pollution and climate change, China has decided to expand its nuclear energy in recent years. According to the released white paper in 2019 titled "Nuclear Safety in China" [8], at the end of 2020, the total installed capacity of the nuclear reactors will reach 58 GW while that of under-construction reactors will be over 30 GW. In 2015, the total installed capacity reached 27.17 GW [9]. The close Franco-Chinese cooperation in nuclear energy has lasted for over 30 years. In 1994, Chinese first commercialized reactor began to operate in Daya Bay, which was based on the design of Framatome ANP French 900 MWe [10]. In 2018, the first EPR entering commercial operation was Taishan 1[4]. In 2010, Sino-French Institute of Nuclear Engineering and Technology (IFCEN) [11] has welcomed the first students in the campus of Sun Yat-sen University (SYSU, Zhuhai China). This institute provide a French-style training to about 100 Chinese students per year in nuclear engineering. Moreover, there is a close cooperation between IFCEN and École Nationale Supérieure de Chimie de Montpellier (ENSCM). As one of the first graduate of IFCEN, this PhD work is also under the cooperation between Institute of Separative Chemistry of Marcoule (ICSM – UMR5257) and IFCEN.

One of the main challenges faced by the nuclear industry, either in terms of technical solutions and public acceptance, is the management and disposal of radioactive waste (radwaste). In France, the deep geological repository was chosen for the final disposal of high-level radioactive waste (HLW) under the legislative framework of the Bataille's law (enacted in 1991) [12], the "loi de programmation relative à la gestion durable des matières et déchets

radioactifs" (in 2006) [13], and the "loi sur la création d'une installation de stockage réversible en couche géologique profonde" (in 2016) [14]. Similarly, China has also decided to adopt the option of a deep geological repository for HLW disposal on the level of legislation [15–17].

According to the IAEA standards [18] (No. GSG-1), HLW are defined by an activity concentration over 10^4-10^6 TBq.m^{-3} or by a specific activity over 0.1-1 TBq.kg^{-1}. As such, they are mainly produced from the reprocessing of spent fuels. Indeed, containing a large amount of radionuclides, the specific activity of the spent fuel is about 92.5 TBq.kg^{-1} when it comes out of the reactor, 14.8 TBq.kg^{-1} after 10 years or interim storage and remains equal to 1.85 TBq.kg^{-1} even after 100 years [19]. The main contributors to the radiotoxicity of spent fuel are actinides, especially plutonium and minor actinides (neptunium, americium, and curium) [20]. The radiotoxicity of actinides and associated daughter products take 10^6 years to drop down to the level of natural uranium mine [20]. Consequently, there is a strong interest in the specific conditioning of actinides.

In order to avoid the exposure to radiation, the key to the management of radwaste is to limit its accessibility. In this case, the deep geological disposal is by far the most practical method, which stores the HLW in a repository deep underground (several hundred meters in depth) within a stable geological environment [21,22]. The multi-barrier approach was considered to avoid the HLW contamination [14,17]. For instance, in France, the radwaste matrix, such as vitrified HLW (*i.e.* R7T7 glass), is considered as the first protection barrier against radioactive contamination and radionuclides migration [23]. The radwaste matrix is placed in a stainless-steel canister, which is also protected from underground water by another container. Finally, the HLW packages are placed in the disposal gallery, which is planned to be located in a Callovo-Oxfordian argillite layer (about 490 m in depth) in Bure [24], in the frame of the CIGEO project [25]. This geological environment is stable as Callovo-Oxfordian rock presents a low permeability (mean permeability K of 5×10^{-14} m.s^{-1}), low apparent diffusion coefficient (10^{-10} m².s^{-1}) and low water content (7-8 wt.%) which could efficiently delay the contact between HLW and the underground water [24]. Nevertheless, in the worst-case scenario, the underground water could penetrate the geological barrier then reach the canister and finally the HLW wasteform, leading to its progressive dissolution and then to the release of the radionuclides. Consequently, the HLW matrix has to present a high chemical durability.

To fulfilled the requests of the HLW disposal, French Research Groups (gathering support from CNRS/CEA/ORANO/EDF/French universities) have been dedicated to ceramic wasteforms for the specific conditioning for actinides [26,27]. Four ceramic materials were

proposed, which were britholites $Ca_9An^{III}_{1-x}An^{IV}_x(PO_4)_{5-x}(SiO_4)_{1+x}F_2$ [28–30], monazite cheralite solid solutions $Ln_{1-x-2y}An^{III}_xCa_yAn^{IV}_yPO_4$, [31–40], thorium phosphate diphosphate (β-TPD) with associated β-$Th_{4-x}An^{IV}_x(PO_4)_4P_2O_7$ solid solutions [30,41–43] and zirconolite $(Ca_{1-x}An^{III}_x)(Zr_{1-y}An^{IV}_y)Ti_{2-x}Al_xO_7$ [26,44]. In this PhD work, the study will focus on monazite-type matrix. Indeed, Dacheux *et al.* [45] underlined the two main arguments for its application: the high structural flexibility of monazite, which allowed the incorporation of large amount of actinides and of other elements, and its high chemical durability.

Monazite was first reported by Johann August Friedrich Breithaupt in 1829 [46]. The etymological origins of "monazite" come from the Greek μονάζειν (meaning "to be alone") as its crystals stand alone in the zircon- and iron-ore [46,47]. Monazite ($LnPO_4$, Ln = La-Tb) is the most abundant lanthanide phosphate observed in natural samples [48,49]. Boatner *et al.* [50] reported that the microcrystals of monazite widely exist as an accessory mineral in granites, rhyolites, gneisses, and pegmatites. It was also found in carbonatites, chamockites, migmatites, and quartz veins as well as in alluvial deposits, including beach sands [51]. These alluvial deposits are produced by the weathering of granites, granitic pegmatites, and other host rock types. Besides lanthanides, natural monazite samples contain large amounts of thorium and uranium [49,52,53]. Overstreet reported that the thorium contents in monazite (expressed as ThO_2 contents) could reach 31.5 wt.%, with an average value of 6 wt.% [53]. As instance, Gramaccioli and Segalstad [54] reported the thorium and uranium contents (calculated as ThO_2 and UO_2) in monazite ores at Piona, Italy: 11.34 wt.% and 15.64 wt.%, respectively [50,54]. Lumpkin analyzed the Rutherford # 2 pegmatite in Virginia and found a content of 29 wt.% ThO_2 in the monazite crystals [55]. Some specific monazite samples were also found to incorporate up to 50 wt.% of ThO_2 [48,56,57].

Apart from these large thorium and uranium contents, monazite type minerals were used in geochronology for radiometric dating because they constituted closed systems for the U-Th-Pb decay chains at the geological scale [57,58]. In fact, natural monazite samples were found to resist from multiple sedimentations and metamorphic cycles, which could extend over several hundred million years [50]. Despite this long period, the contained actinides and their daughter nuclides remained confined within the monazite crystals. Moreover, it was stated by Montel *et al.* [57,58] that the weathering erosion and transport processes only led to mechanical abrasion of monazite, but not to chemical alteration during such geological periods. These geological observations suggested that the monazite exhibits high chemical durability and good resistance to self-irradiation.

Oelkers and Poitrasson [59] studied the leaching of Manangotry monazite, with the chemical formula $(Ca_{0.04}La_{0.21}Ce_{0.43}Pr_{0.05}Nd_{0.15}Sm_{0.02}Gd_{0.01}Th_{0.13})P_{0.90}Si_{0.09}O_4$. The normalized dissolution rates R_L (Ce) at 70°C ranged from 2 to 3.2 × 10^{-5} g.m^{-2}.d^{-1} at pH = 2 down to 8 × 10^{-7} g.m^{-2}.d^{-1} at pH = 6. This normalized dissolution rate was much lower than those of other HLW wasteforms (1 g.m^{-2}.d^{-1} [60], about 10^{-2} g.m^{-2}.d^{-1} [44] and about 10^{-2} g.m^{-2}.d^{-1} [44] for R7T7 glass, zirconolite and Nd-britholite, respectively) and almost similar to that mentioned for the highly durable Thorium Phosphate (2.4 × 10^{-7} to 3.6 × 10^{-7} g.m^{-2}.d^{-1} in neutral medium at room temperature and 5.0 × 10^{-6} to 7.5 × 10^{-6} g.m^{-2}.d^{-1} at 90°C) [61]. Additionally, such high chemical durability of natural monazites could bring difficulties during their dissolution in order to recover rare-earth elements. Indeed, the application of extreme chemical conditions (concentrated H_2SO_4 at 210°C or concentrated NaOH at 140°C) is always required to reach quantitative dissolution rate in the field of industrial applications [62]

Monazites also exhibit good resistance to self-irradiation [63–68]. U-Pb geochronological zircon [69] (U content ≈ 100 ppm) is easily amorphized at α-decay doses of 10^{18}–10^{19} α.g^{-1}. However, monazite crystals are not amorphous, even for very old samples (up to 2 Ga) containing higher actinides contents (up to 10 wt.% ThO_2 and ~1 wt.% UO_2) and sustain irradiation doses up to 1.7 × 10^{20} α.g^{-1} [70,71]. One of the reasons is that the critical amorphization temperature, above which the amorphization would not happen (*i.e.,* 180°C for monazite [72]) is lower than that reported for other minerals (830°C and 440°C for zircon and zirconolite, respectively [69]). Moreover, the temperature and activation energy associated to its recrystallization from the amorphous state (~300°C, 2.7 eV for monazite [66,73,74]) are also lower than those obtained for other host matrices (as instance 1200°C and 5.3-6.6 eV for zircon [75]). Recently, Seydoux-Guillaume *et al.* [70] reported a new defect recovery mechanism, called α-healing. The electronic energy loss of α particles is able to anneal the structure defect, which could explain the absence of amorphization in natural monazite samples.

Monazite was therefore considered as a promising uranium or thorium host matrix, based on the observations above. Several studies were dedicated to the preparation of monazite type ceramics, with a focus on three aspects: synthesis, sintering, and long-term behavior.

The solid state reactions have been well developed for preparing the monazite $LnPO_4$, $AnPO_4$ (An = Pu, Am), $Ln_{1-x}An_xPO_4$ [76–82], $Ca_{0.5}An^{IV}_{0.5}PO_4$ cheralite (An = Th, U, Np, and Pu)[31,35,36] and monazite-cheralite solid solutions [83,84]. Besides, most of the monazite-type ceramics were prepared from powdered precursors through solid state reactions [77,78,83–86]. However, the precursors prepared via dry chemistry routes might lead to a too small specific

surface area to obtain dense ceramic [77,83,84]. Furthermore, in order to guarantee the final distribution of cations in the samples, repetitive calcination/milling cycles are required, which can increase the risk of contaminations [76]. On the contrary, wet chemistry synthesis could be used as an advantage to prepare homogeneous precursors showing large specific surface area. They have been reported for preparing $LnPO_4$ monazite end-member and $Ln'_{1-x}Ln''_xPO_4$ monazite-type solid solutions [87–94]. However, the incorporation of tetravalent elements could be associated with the formation of secondary phases [76,95]. In this way, Podor *et al.* [32,39] successfully synthesized monazite-cheralite solid solutions $La_{1-2x}Ca_xAn_xPO_4$ (x = 0 -0.5) trough hydrothermal process under extreme conditions (T = 780°C, P = 200 MPa). Consequently, there is a great interest in preparing An(IV)-bearing monazites via wet chemistry routes in less "extreme" conditions (*e.g.*, T ≤ 250°C).

The monazite-type ceramics prepared by dry route chemistry exhibited good chemical durability during the leaching tests. Veilly *et al.* [96] reported that the normalized dissolution rate of $Ca_{0.5}Th_{0.5}PO_4$ cheralite equaled (2.2 ± 0.2) × 10^{-5} $g.m^{-2}.d^{-1}$. Similarly, Du Fou de Kerdaniel [86] showed that the initial normalized dissolution rate of uranium was (2.5 ± 0.2) × 10^{-4} $g.m^{-2}.d^{-1}$ for $Ca_{0.5}Th_{0.4}U_{0.1}PO_4$ in 0.1 $mol.L^{-1}$ HNO_3 at 90°C. Moreover, the precipitation of uranium was observed after 10 days, leading to the significant decrease of the normalized dissolution rate $R_{L,t}$ (U) down to (2.5 ± 0.3) × 10^{-5} $g.m^{-2}.d^{-1}$. Nevertheless, to our best knowledge, the dissolution of monazite-cheralite solid solutions prepared via wet chemistry has not studied yet.

During his PhD, Du Fou de Kerdaniel [86] developed a wet chemistry route to prepare Th-bearing rhabdophane precursors, $Ln_{0.8}Ca_{0.1}Th_{0.1}PO_4.nH_2O$ (Ln = La, Pr, Nd, Eu). The rhabdophane precursors were easily converted into monazite-cheralite solid-solutions by heating at high temperature (T ≥ 1100 °C) [77,97–99]. Even though, a slight amount of $Th_2(PO_4)_2(HPO_4).H_2O$ (TPHPH) was presented in some obtained rhabdophane samples prepared, the synthesis conditions (T ≤ 150 °C and P = 1 bar) were "accessible".

Later, during her PhD, Gausse [100] studied the synthesis and the dissolution of monazite end-members $LnPO_4$ (Ln = La - Gd). She proposed the preparation of monazite by thermal treatment of rhabdophane type precursors $LnPO_4.0.667H_2O$ synthesized by wet chemistry methods. Furthermore, multiparametric dissolution tests were performed in order to evaluate the chemical durability of the synthesized monazite samples. The determined normalized dissolution rates, at room temperature and pH =1, of the as-prepared monazite were found to be low: from 4 × 10^{-5} to 3.7 × 10^{-4} $g.m^{-2}.day^{-1}$, which confirmed the excellent chemical

durability of the materials. The solubility constants of the potential solubility-controlling phase, *i.e.*, rhabdophanes was also very low (log $K_{s,0}°$ = -24.1 ± 0.3 to -25.8 ± 0.3 with T =25°C).

Based on the results reported by Du Fou de Kerdaniel [86] and by Gausse [100–102], this PhD has been dedicated to the incorporation of tetravalent actinides (Th and U) in the monazite type ceramics by wet chemistry route using a methodology similar to that reported by Gausse [100]. Therefore, the manuscript will be divided in five parts:

In the first chapter, rhabdophane type precursors $Ln_{1-2x}Ca_xTh_xPO_4.nH_2O$ will be prepared through wet chemistry route. A multiparametric study will be performed to optimize the conditions of synthesis (in terms of stoichiometry between the reactants, synthesis temperature and duration). The domain of stability of the as-synthesized rhabdophanes will be determined as well. Finally, the associated monazite-cheralite solid solutions will be prepared by thermal treatment of the prepared precursors. The successive steps leading from rhabdophanes to monazite-cheralite solid solutions (*i.e.* dehydration, phase conversion, densification, etc.) will be evidenced by combining *in-situ* High Temperature Powder X-Ray Diffraction (*in-situ* HT-PXRD), thermogravimetry (TGA) and dilatometry analyses. The results are gathered in chapter II.

The direct reactive sintering of Th-rhabdophane into monazite-cheralite pellets will be investigated in Chapter III. The conditions of densification will be first evaluated by dilatometry. Activation energy associated with the densification process will be determined. In order to get a better microstructural control for the final ceramics (*i.e.* density, porosity, grain size, etc.), sintering maps will be built to unveil the effects of sintering parameters (chemical composition, temperature and sintering time). Finally, the microhardness of the prepared ceramics will be measured by performing the Vickers tests.

The chemical durability of the powdered monazite-cheralite solid solution $Nd_{0.8}Ca_{0.1}Th_{0.1}PO_4$ will be presented in Chapter IV. During the kinetic stage of the multiparametric dissolution, the normalized dissolution rates will be determined. Moreover, the solubility constants associated with the neoformed solubility-controlling phases obtained when saturation conditions were reached in solution, will be calculated. The associated thermodynamic data of formation, such as the Gibbs free energy $\Delta_f G°$, the enthalpy $\Delta_f H°$, and the entropy $\Delta_f S°$ will be determined as well. These results will be compared with those obtained by Gausse for the monazite end-members [100]. Finally, the impact of the thorium incorporation on the chemical durability of the monazite type ceramic will be discussed.

In Chapter V, the synthesis of U-rhabdophanes $Nd_{1-2x}Ca_xU_xPO_4.nH_2O$ will be explored by adapting the protocol determined for Th-based samples. The thermal conversion of these rhabdophane precursors to prepare U-monazite-cheralite solid solution, will be studied with the help of TGA and dilatometry analyses.

Selon l'Agence Internationale de l'Energie Atomique (AIEA) [1], l'énergie nucléaire constitue une énergie abordable, fiable et propre dans un objectif de développement durable. 440 réacteurs sont en service dans le monde, fournissant 11% de l'électricité mondiale (et plus de 30% de l'électricité « bas carbone ») [1]. En terme de protection de l'environnement, l'émission de 1,5 à 2 milliards de tonnes de gaz à effet de serre a été évitée chaque année depuis 1990 grâce à l'énergie nucléaire [1]. Par rapport à d'autres énergies propres, telles que l'énergie hydraulique, l'énergie éolienne, l'énergie solaire, etc., les coûts actualisés de l'énergie nucléaire sont les plus bas (< 100 US $_{2013}$ par MW.h) [2]. De plus, les réacteurs nucléaires fonctionnent à un facteur de charge élevé (environ 90%) et fournissent donc une puissance fiable et continue. La France est le leader de l'industrie nucléaire. En 2018, 58 réacteurs ont produit 71,7% de son électricité totale (soit 395,9 TW.h) [3]. En terme de technologies nucléaires, la France a conçu le réacteur EPR, qui correspond au premier type de réacteurs de troisième génération. [4]. La France est également le leader dans le domaine du retraitement des combustibles usés (avec une capacité de traitement de 1700 tonnes.an^{-1} à l'usine de La Hague [5] et de fabrication de 110 tonnes de MOX en 2017 à l'usine Melox de Marcoule [6]). Ces techniques avancées ont également contribué à aider d'autres pays comme le Japon, le Royaume-Uni ou la Chine, pour le retraitement de leur combustibles usés [7].

Face à des défis majeurs en terme de pollution et de changement climatique, la Chine s'est engagée ces dernières années à développer l'énergie nucléaire. Selon le livre blanc publié en 2019 et intitulé « *Nuclear Safety in China* » [8], la puissance totale des réacteurs installée atteindra, à la fin de l'année 2020, 58 GW (contre 27,17 GW à la fin 2015 [9]). Celle des réacteurs en construction dépassera 30 GW. L'étroite coopération franco-chinoise dans l'énergie nucléaire perdure depuis plus de 30 ans. En 1994, le premier réacteur commercialisé en Chine a commencé à produire de l'électricité dans la Baie de Daya. Ce réacteur était basé sur le design de Framatome ANP 900 MWe [10]. En 2018, Taishan 1 a été le premier réacteur EPR à produire de l'électricité [4]. En 2010, l'Institut Franco-Chinois de l'Énergie Nucléaire (IFCEN) a accueilli sa première promotion sur le campus de l'Université Sun Yat-Sen (SYSU, Zhuhai, Chine) [11]. Chaque année, cet institut dispense une formation en ingénierie nucléaire sur le modèle français à une centaine d'étudiants chinois. Par ailleurs, il existe une étroite coopération entre l'IFCEN et l'École Nationale Supérieure de Chimie de Montpellier (ENSCM). En tant que l'un des premiers diplômés de l'IFCEN, cette thèse s'inscrit également dans le cadre d'une coopération entre l'Institut de Chimie Séparative de Marcoule (ICSM - UMR5257) et l'IFCEN.

L'un des enjeux majeurs de l'énergie nucléaire réside dans la gestion et le stockage des déchets radioactifs. En France, le cadre législatif, encadré par la loi « *Bataille* » du 30 Décembre 1991 [12] puis par la « *loi de programmation relative à la gestion durable des matières et déchets radioactifs* » du 28 Juin 2006 [13] et la « *loi sur la création d'une installation de stockage réversible en couche géologique profonde* » du 26 Juillet 2016 [14], a inscrit l'option d'un stockage en couche géologique profonde comme exutoire de référence des déchets de Haut Activité (HA). La Chine a également adopté une telle option [15–17].

Selon les critères de l'AIEA (No° GSG-1), les déchets de Haute Activité et de Vie Longue (HA-VL) sont définis par une activité volumique supérieure à 10^4-10^6 TBq.m^{-3} ou par activité massique dépassant 0.1-1 TBq.kg^{-1}. Ces déchets proviennent principalement du retraitement des combustibles nucléaires [103]. Du fait de la grande quantité et de la grande variété de radionucléides incorporés, l'activité massique du combustible usé est d'environ 92,5 TBq.kg^{-1} à la sortie du réacteur et de 14,8 TBq.kg^{-1} après un refroidissement de 10 ans. Cette valeur atteint encore 1,85 TBq. kg^{-1} à l'issue d'un refroidissement de 100 ans [19]. Les principaux contributeurs à la radiotoxicité du combustible usé sont les actinides, en particulier le plutonium et les actinides mineurs (c'est-à-dire le neptunium, l'américium et le curium) [20]. Il faut environ un million d'années pour que la radiotoxicité des actinides et de leurs descendants diminue à un niveau proche de celui des minéraux uranifères naturels [20]. Par conséquent, le conditionnement spécifique des actinides constitue un très grand intérêt.

Pour éviter une exposition future aux rayonnements ionisants qu'ils renferment, un principe important de la gestion des déchets radioactifs consiste à en limiter l'accessibilité. Dans cette optique, le stockage géologique en formation géologique profonde constitue la méthode la plus sûre et la plus pragmatique. Il suppose de stocker les déchets HA-VL dans des alvéoles dédiées et creusées à environ 500 m de profondeur, au sein d'un environnement géologiquement stable [21,22]. Le concept multi-barrières est alors très important pour éviter la dispersion des radionucléides dans la biosphère [14,17]. En France, la matrice de confinement (*e.g.* verre R7T7) constitue la première barrière de protection contre la contamination et la migration des radionucléides [23]. Cette matrice est alors placée dans un containeur en acier inoxydable, lui-même protégé par un sur-containeur. Enfin, les colis de déchets sont placés dans une alvéole de stockage, creusée dans une couche d'argilite du Callovo-Oxfordien (490 m de profondeur) dans le cas du projet CIGEO (Bure, Meuse / Haute-Marne) [24]. La couche d'argilite du Callovo-Oxfordien est considérée comme géologiquement stable. Ces roches sont en effet peu perméables (perméabilité moyenne K de 5×10^{-14} m.s^{-1}) et présentent un faible coefficient de

diffusion apparent (10^{-10} $m^2.s^{-1}$) et une faible teneur en eau (7-8 en masse %). Par conséquent, ce type de roches devrait retarder efficacement le contact entre les déchets HA-VL et l'eau souterraine. Néanmoins, dans le pire des scénarii possibles, l'eau souterraine pourrait pénétrer au sein de la barrière géologique puis dans les containeurs avant d'atteindre la matrice de conditionnement des déchets HA-VL. Il en résulterait la dissolution de la matrice puis le relâchement de radionucléides au sein de l'environnement. Par conséquent, les matrices de confinement des déchets HA-VL doivent en premier lieu présenter une excellente durabilité chimique.

Pour répondre aux questionnements scientifiques et techniques liés à la gestion des déchets radioactifs, les Groupes de Recherche Français du programme PACEN (regroupant CNRS / CEA / ORANO / EDF et plusieurs Universités françaises) se sont consacrés au design de matériaux céramiques pouvant assurer un conditionnement spécifique et efficace des actinides [26,27]. Quatre matrices céramiques ont ainsi été retenues : les britholites $Ca_9An^{III}_{1-x}An^{IV}_x(PO_4)_{5-x}(SiO_4)_{1+x}F_2$ [28–30], les solutions solides monazite-chéralite $Ln_{1-x-2y}An^{III}_xCa_yAn^{IV}_yPO_4$ [31–40], le phosphate-diphosphate de thorium (β-PDT) et les solutions solides associées $\beta\text{-}Th_{4-x}An^{IV}_x(PO_4)_4P_2O_7$ [30,41–43,104] ainsi que les zirconolites $(Ca_{1-x}An^{III}_x)(Zr_{1-y}An^{IV}_y)Ti_{2-x}Al_xO_7$ [26,44]. Au cours de ce travail, l'étude sera focalisée sur les matrices de type monazite-cheralite. En effet, Dacheux *et al.* [45] ont proposé plusieurs arguments venant en appui de l'application des monazites en tant que matrice de confinement : il s'agit d'une très grande flexibilité structurale permettant l'incorporation d'actinides et d'autres éléments en quantité importante ainsi que d'une durabilité chimique exceptionnelle.

Les monazites ont été reportées pour la première fois par Johann August Friedrich Breithaupt en 1829 [46]. Les origines étymologiques de la «monazite» viennent du grec « μονάζειν » (signifiant « être seul ») car ses cristaux existent indépendamment dans les minerais de zircon et de fer [46,47]. Les monazites ($LnPO_4$, Ln = La-Tb) sont des phosphates d'éléments lanthanide, parmi les phases les plus abondantes observées naturellement [48,49]. Boatner *et al.* [50] ont rapporté que des microcristaux de monazites existaient largement en tant que minéral accessoire au sein des granites, des rhyolites, des gneiss et des pegmatites. Elles ont également été rencontrées dans les carbonatites, les chamockites, les migmatites et les veines de quartz ainsi que dans les dépôts alluviaux, y compris aux sein de sables monazitiques sur de nombreuses plages [51]. Ces dépôts alluviaux proviennent de l'altération de granites, de pegmatites granitiques et d'autres types de roches. Outre les éléments lanthanide, les échantillons de monazite naturelle contiennent de grandes quantités de thorium et d'uranium

[49,52,53]. Overstreet a déterminé que la teneur en thorium au sein de la monazite pouvait atteindre 31,5% en masse de ThO_2, avec une moyenne de 6% en masse. Gramaccioli et Segalstad [54] ont reporté des teneurs en thorium et en uranium de respectivement de 11,34% en masse de ThO_2 et 15,64% en masse de UO_2 au sein de certaines monazites à Piona (Italie) [50,54]. Lumpkin a analysé les Rutherford # 2 pegmatites, en Virginie [55]. Il a observé une teneur de 29% en masse de ThO_2. Finalement, certains échantillons spécifiques de monazite se sont également avérés contenir jusqu'à 50% en masse de ThO_2 [48,56,57].

Outre ces fortes teneurs en thorium et en uranium, des minéraux de type monazite ont été utilisés en géochronologie pour la datation radiométrique car ils constituent des systèmes fermés pour les chaînes de désintégration U-Th-Pb [57,58]. En fait, des échantillons naturels de monazite ont été préservés de multiples sédimentations et cycles métamorphiques, qui se sont étendus sur plusieurs centaines de millions d'années [50]. Pendant ces longues périodes, les actinides et leurs descendants radioactifs sont restés confinés à l'intérieur des échantillons monazitiques. De plus, Montel *et al.* [57,58] ont marqué que les processus d'érosion et de transport ne conduisent qu'à l'abrasion mécanique des monazites, sans modification de leurs composition chimique, y compris sur des périodes de temps géologiques. Ces observations géologiques suggèrent que les monazites présentent une durabilité chimique excellente et une très bonne résistance à l'auto-irradiation.

Oelkers and Poitrasson [59] ont étudié la lixiviation d'échantillons de monazite de Manangotry de formule chimique $(Ca_{0,04}La_{0,21}Ce_{0,43}Pr_{0,05}Nd_{0,15}Sm_{0,02}Gd_{0,01}Th_{0,13})P_{0,90}Si_{0,09}O_4$. Les vitesses de dissolution normalisées R_L (Ce) à 70°C s'étendent de 2 – 3,2 × 10^{-5} $g.m^{-2}.j^{-1}$ pour pH =2 à 8 × 10^{-7} $g.m^{-2}.j^{-1}$ pour pH = 6. Ces vitesses de dissolution normalisées sont nettement inférieures à celles relevées pour d'autres matrices de confinement (1 $g.m^{-2}.j^{-1}$ [60], environ 10^{-2} $g.m^{-2}.j^{-1}$ [44] et environ 10^{-2} $g.m^{-2}.j^{-1}$ [44] respectivement pour les verres R7T7, la zirconolite and la britholite-Nd,). Elles apparaissent similaires à celles relevées pour le Phosphate-Diphosphate de Thorium (entre 2,4 × 10^{-7} et 3,6 × 10^{-7} $g.m^{-2}.j^{-1}$ en milieu neutre et à température ambiante et entre 5,0 × 10^{-6} et 7,5 × 10^{-6} $g.m^{-2}.j^{-1}$ à 90°C)[61]. De plus, dans les applications industrielles, la dissolution quantitative des monazites n'a lieu que sous des conditions chimiques extrêmes (H_2SO_4 concentré à 210°C ou NaOH concentré à 140°C) [62].

Une telle durabilité chimique des monazites naturelles induite de grandes difficultés lors de leur dissolution à des fins de récupération des ions terre-rares. En effet, l'application de conditions extrêmes (H_2SO_4 concentré à 210°C ou NaOH concentré à 140°C) est souvent

nécessaire pour atteindre une dissolution quantitative dans le cadre d'applications industrielles [62]

Les monazites présentent également une très bonne résistance à l'auto-irradiation [63–68]. Les zircons [69], utilisés pour la U-Pb géochronologique, renferment des teneurs d'uranium d'environ 100 ppm et sont aisément amorphisés pour des doses de α de 10^{18}–10^{19} $\alpha.g^{-1}$. En revanche, une telle amorphisation n'est pas observée dans le cas de cristaux de monazites, y compris dans le cas de vieux échantillons (jusqu'à 2 milliards d'années) [70,71]. En fait, ces monazites présentent des teneurs en actinides plus importantes que les zircons (jusqu'à 10 % en masse de ThO_2 et ~1 % en masse de UO_2) et ont donc subi de plus fortes doses (jusqu'à 1,7 × 10^{20} $\alpha.g^{-1}$) [70,71]. L'une des raisons est que la température critique d'amorphisation , au-dessus de laquelle l'amorphisation ne se produirait pas, est inférieure pour la monazite (180°C [72]) à celles relevées pour d'autres minéraux (830°C pour zircon et 440°C pour zirconolite [69]). De plus, la température et l'énergie d'activation associées à la recristallisation du réseau à partir de l'état amorphe sont également inférieure à celles obtenues pour les autres matrices (~300°C et 2,7 eV pour monazite [66,73,74] *vs.* 1200°C et 5,3-6,6 eV pour le zircon [75]). Récemment, Seydoux-Guillaume *et al.* [70] ont signalé un nouveau mécanisme de recuit de la structure cristalline, appelé recuit-alpha. La perte d'énergie électronique des particules α pourrait contribuer au recuit des défauts structuraux, ce qui explique l'absence d'amorphisation au sein des échantillons naturels de monazite.

Sur la base de ces observations, les monazites sont donc considérées comme des matrices de confinement prometteuses pour l'uranium ou le thorium (et donc pour les autres éléments actinide). À ce titre, plusieurs études ont été consacrées aux céramiques de type monazite en incluant trois aspects : la synthèse, le frittage et l'étude de la dissolution.

Les réactions de l'état solide ont déjà été développées pour préparer les monazites de formulation $LnPO_4$, $AnPO_4$ (An = Pu, Am) et $Ln_{1-x}An_xPO_4$ [76–82], les chéralites $Ca_{0,5}An^{IV}_{0,5}PO_4$ (An = Th, U, Np, et Pu)[31,35,36] et les solutions solides associées de type monazite-chéralite [83,84]. En outre, la plupart des céramiques de type monazite ont été fabriquées à partir de précurseurs préparés par voie sèches (*i.e.*, par réaction en phase solide) [77,78,83–86]. Cependant, les précurseurs préparés par de telles méthodes peuvent conduire à des surfaces spécifiques trop faibles pour préparer des matériaux céramiques denses [77,83,84]. De plus, plusieurs cycles de calcination / broyage sont nécessaires afin de garantir l'homogénéité des solides, ce qui pourrait augmenter le risque de contamination [76]. Au contraire, les synthèses par voies humides pourrait permettre d'obtenir des précurseurs homogènes présentant de grandes surfaces spécifiques. Ces méthodes

ont été reportées dans le cas des pôles purs $LnPO_4$ et des solutions solides $Ln'_{1-x}Ln''_xPO_4$ [87–94]. Cependant, dans le cas des éléments tétravalents, les voies humides peuvent conduire à la formation de phases secondaires [5,94]. De rares publications ont traité de ce sujet. Ainsi, Podor *et al.* [32,39] ont réussi à préparer des solutions solides de type monazite-chéralite de formule $La_{1-2x}Ca_xAn_xPO_4$ (x = 0 - 0,5) par voie hydrothermale dans des conditions extrêmes (T = 780°C, P = 200 MPa). Par conséquent, il existe un grand intérêt pour développer des méthodes de synthèse par voie humide de solutions solides de monazite-chéralite contenant des actinides tétravalents dans des conditions plus «accessibles», par exemple pour des températures inférieures à 250 °C.

Les céramiques de type monazite préparées via voie sèche présentent généralement une bonne durabilité chimique au cours des tests de lixiviation. À ce titre, Veilly *et al.* [96] ont reporté une vitesse de dissolution normalisée de la chéralite $Ca_{0,5}Th_{0,5}PO_4$ égale à $(2,2 \pm 0,2) \times 10^{-5}$ $g.m^{-2}.j^{-1}$. De même, Du fou de Kerdaniel [86] a déterminé que la vitesse de dissolution initiale $R_{L,0}(U)$ était voisine de $(2,5 \pm 0,2) \times 10^{-4}$ $g.m^{-2}.j^{-1}$ pour $Ca_{0,5}Th_{0,4}U_{0,1}PO_4$ dans 0,1 $mol.L^{-1}$ HNO_3 à 90 °C. De plus, la précipitation de l'uranium a été observée après 10 jours de dissolution, conduisant à une diminution significative de la vitesse de dissolution normalisée $R_{L,t}(U)$ pour atteindre $(2,5 \pm 0,3) \times 10^{-5}$ $g.m^{-2}.j^{-1}$.

Dans le cadre de son travail de thèse, Du Fou de Kerdaniel [86] a reporté une voie humide pour préparer des précurseurs de rhabdophane-Th, $Ln_{0,8}Ca_{0,1}Th_{0,1}PO_4,nH_2O$ (Ln = La, Pr, Nd, Eu). De tels précurseurs de type rhabdophane sont facilement convertis en monazite après calcination à haute température (T ≥ 1100 ° C) [77,97–99]. Même si une faible quantité de $Th_2(PO_4)_2(HPO_4),H_2O$ (PHPTH) a parfois été relevé dans certaines rhabdophanes obtenues, les conditions de synthèse de cette méthode se sont avérées «accessibles» (T ≤ 150 °C).

Dans sa thèse, Gausse [100] a étudié la synthèse de pôles purs de monazite $LnPO_4$ (Ln = La - Gd) ainsi que leur dissolution. Ainsi, des 'précurseurs de type rhabdophane $LnPO_4,0,667H_2O$ ont été préparés par voie humide puis ont été convertis en monazite par traitement thermique. De plus, une étude multiparamétrique de dissolution a été menée afin d'évaluer la durabilité chimique de tels échantillons. Les vitesses de dissolution normalisées de telles monazites se sont avérées faibles (de 4×10^{-5} à $3,7 \times 10^{-4}$ $g.m^{-2}.j^{-1}$ à température ambiante et pH = 1). La solubilité des rhabdophanes, qui contrôlent les équilibres thermodynamiques à l'issue de la dissolution des monazites, demeurent également très faibles (log $K_{s,0}°$ = -24,1 ± 0,3 à -25,8 ± 0,3 à température). Par conséquent, les monazites préparées présentent une excellente durabilité chimique.

En s'inspirant des travaux menés par Du Fou de Kerdaniel [86] puis par Gausse [100–102], ce travail de thèse est dédié à l'incorporation d'actinides tétravalents (Th et U) au sein de céramiques de type monazite-chéralite. Une méthodologie d'étude transversale, similaire à celle développée par Gausse [100], a été mise en œuvre de manière à relier les aspects relevant de la synthèse, du frittage et du comportement à long-terme des matériaux céramiques. Ainsi, ce manuscrit est divisé en cinq chapitres.

Dans le Chapitre I, des précurseurs de type rhabdophane $Ln_{1-2x}Ca_xTh_xPO_4.nH_2O$ seront préparés par voie humide. L'étude multiparamétrique réalisée pour optimiser le protocole de synthèse (effet de la stœchiométrie initiale des réactifs, de la température et de la durée de synthèse) sera exposée. Le domaine de stabilité des rhabdophanes synthétisées sera également évalué. Enfin, la synthèse de solutions solides de type monazite-chéralite par conversion thermique des précurseurs sera exposée. Le Chapitre II s'attachera à décrire le comportement thermique (déshydratation, transition de phase, densification, etc.) des précurseurs de rhabdophanes-Th obtenus en combinant la Diffraction des Rayons X à Haute Température (DRX-HT), des analyses thermogravimétriques (ATG) et dilatométriques.

Le Chapitre III sera dédié au frittage réactif des rhabdophanes-Th. La préparation de pastilles denses de monazite-chéralite sera suivie au moyen d'études dilatométriques. L'énergie d'activation associée au processus de densification sera déterminée grâce à la méthode de Dorn. En outre, pour assurer un meilleur contrôle de la microstructure des céramiques finales, des cartes de frittage seront établies. Enfin, la microdureté des céramiques obtenues sera mesurée à partir de tests Vickers.

La durabilité chimique des solutions solides $Nd_{0,8}Ca_{0,1}Th_{0,1}PO_4$ sera étudiée dans le chapitre IV de ce manuscrit à travers une étude multiparamétrique de la dissolution. En régime cinétique, la vitesse de dissolution normalisée sera déterminée dans plusieurs conditions de température et de pH. Lorsque les conditions de saturation seront atteintes en solution, les constantes de solubilité des phases contrôlant les concentrations élémentaires dans les lixiviats seront calculées à partir des concentrations des espèces à l'équilibre. Par ailleurs, les données thermodynamiques de formation, telles que l'énergie libre de Gibbs $\Delta_f G°$, l'enthalpie $\Delta_f H°$, et l'entropie $\Delta_f S°$ seront évaluées. Ces résultats seront notamment comparés à ceux reportés par Gausse dans le cas des pôles purs de monazite [100]. Ainsi, l'impact lié à l'incorporation du thorium sur la durabilité chimique de la céramique sera discuté.

Enfin, le Chapitre V présentera la synthèse de rhabdophanes-U, de formule $Nd_{1-2x}Ca_xU_xPO_4.nH_2O$, en adaptant le protocole mis au point pour les échantillons à base de thorium.

Le comportement thermique de ces précurseurs, conduisant en particulier à la formation de monazites-chéralites sera suivi à l'aide d'analyses thermogravimétriques et dilatométriques.

References

(1) International Atomic Energy Agency (IAEA). *Nuclear Power for Sustainable Development*; Vienna, Austria, 2017.
(2) *Projected Costs of Generating Electricity 2015*; IEA: IEA, Paris, 2015.
(3) Pozwer Reactor Information System (PRIS). Nuclear Power Status 2018, 2018.
(4) World Nuclear News. First EPR Enters Commercial Operation. *World Nuclear News*. December 14, 2018.
(5) ORANO. *Rapport d'information Du Site Orano La Hague. Edition 2017*; 2017.
(6) ORANO. *Rapport d'information Du Site Orano Melox. Edition 2017*; 2017.
(7) ORANO. The world leader in recycling used nuclear fuels https://www.orano.group/en/expertise/from-exploration-to-recycling/world-leader-in-recycling-used-nuclear-fuelsthe.
(8) *Nuclear Safety in China*; White Paper; The State Council Information Office of the People's Republic of China, 2019.
(9) *China 13th Five-Year Plan for Energy Development*; National Development Plan; Entity: National Development and Reform Commission (NDRC), National Energy Administration Organisation: National Development and Reform Commission (NDRC), National Energy Administration: China, 2016.
(10) AREVA. *AREVA in China*; Press kit; France, 2007.
(11) IFCEN. Sino-French Institute of Nuclear Engineering and Technology. IFCEN 2014.
(12) Bataille, C. *Loi N° 91-1381 Du 30 Décembre 1991 Relative Aux Recherches Sur La Gestion Des Déchets Radioactifs*; 1991; Vol. 91–1381.
(13) *Loi N° 2006-739 Du 28 Juin 2006 de Programme Relative à La Gestion Durable Des Matières et Déchets Radioactifs.*; 2006.
(14) *Loi N° 2016-1015 Du 25 Juillet 2016 Précisant Les Modalités de Création d'une Installation de Stockage Réversible En Couche Géologique Profonde Des Déchets Radioactifs de Haute et Moyenne Activité à Vie Longue.*; 2016.
(15) *Law of the People's Republic of China on Prevention and Control of Radioactive Pollution*; 2003; Vol. CHN-2003-L-76093.
(16) *Regulation on the Safety Management of Radioactive Waste*; 2012; Vol. 612.
(17) *Nuclear Safety Guidelines Radioactive Waste Geological Disposal Facility*; 2020; Vol. HAD 401/10-2020.
(18) *Classification of Radioactive Waste*; General Safety Guides; INTERNATIONAL ATOMIC ENERGY AGENCY: Vienna, 2009.
(19) High-level waste (HLW) https://www.radioactivity.eu.com/site/pages/HLW_Waste.htm.
(20) Hedin, A. *Spent Nuclear Fuel - How Dangerous Is It? A Report from the Project "Description of Risk";* Sweden, 1997; p 72.
(21) OECD; Agency, N. E. *Geological Disposal of Radioactive Waste*; 1999. https://doi.org/10.1787/9789246180547-en.
(22) Kim, J.-S.; Kwon, S.-K.; Sanchez, M.; Cho, G.-C. Geological Storage of High Level Nuclear Waste. *KSCE Journal of Civil Engineering* **2011**, *15* (4), 721–737. https://doi.org/10.1007/s12205-011-0012-8.
(23) *Inventaire National Des Matières et Déchets Radioactifs*; Les Essentiels 2018; ANDRA, 2018.
(24) *Dossier 2005 Argile*; Evaluation de sûreté du stockage géologique; ANDRA: France, 2005.
(25) *Proposition de Plan Directeur Pour l'exploitation d Cigéo*; CG-TE-D-NTE-AMOA-SDR-0000-15-0063/A; 2016.

(26) Dacheux, N.; Clavier, N.; Robisson, A.-C.; Terra, O.; Audubert, F.; Lartigue, J.-É.; Guy, C. Immobilisation of Actinides in Phosphate Matrices. *Comptes Rendus Chimie* **2004**, *7* (12), 1141–1152. https://doi.org/10.1016/j.crci.2004.02.019.
(27) Terra, O.; Dacheux, N.; Audubert, F.; Podor, R. Immobilization of Tetravalent Actinides in Phosphate Ceramics. *Journal of Nuclear Materials* **2006**, *352* (1), 224–232. https://doi.org/10.1016/j.jnucmat.2006.02.058.
(28) Montel, J.-M. Minerals and Design of New Waste Forms for Conditioning Nuclear Waste. *Comptes Rendus Géoscience* **2010**, *1856* (2), 83–259. http://dx.doi.org/10.1016/j.crte.2010.11.006.
(29) Boyer, L.; Piriou, B.; Carpena, J.; Lacout, J. L. Study of Sites Occupation and Chemical Environment of Eu^{3+} in Phosphate-Silicates Oxyapatites by Luminescence. *Journal of Alloys and Compounds* **2000**, *311* (2), 143–152. https://doi.org/10.1016/S0925-8388(00)01085-9.
(30) Terra, O. Incorporation d'actinides Tétravalents Dans Trois Matrices Phosphatées : Britholite, Monazite/Brabantite et Phosphate-Diphosphate de Thorium (β-PDT). PhD Thesis, Université de Paris XI Orsay, 2005.
(31) Bregiroux, D.; Terra, O.; Audubert, F.; Dacheux, N.; Serin, V.; Podor, R.; Bernache-Assollant, D. Solid-State Synthesis of Monazite-Type Compounds Containing Tetravalent Elements. *Inorg. Chem.* **2007**, *46* (24), 10372–10382. https://doi.org/10.1021/ic7012123.
(32) Podor, R. Synthèse et Caractérisation Des Monazites Uranifères et Thorifères. PhD Thesis, Université de Lorraine, 1994.
(33) Rose, D. Brabantite, $CaTh(PO_4)_2$, a New Mineral of the Monazite Group. *Neues Jahresbuch Mineralogische Monatshefte* **1980**, *6*, 247–257.
(34) Davis, D. D.; Vance, E. R.; McCarthy, G. J. *Crystal Chemistry and Phase Relations in the Synthetic Minerals of Ceramic Waste Forms II Studies of Uranium-Containing Monazites*; Plenum Press: United States, 1981.
(35) Tabuteau, A.; Pagès, M.; Livet, J.; Musikas, C. Monazite-like Phases Containing Transuranium Elements (Neptunium and Plutonium). *Journal of Materials Science Letters* **1988**, *7* (12), 1315–1317. https://doi.org/10.1007/BF00719969.
(36) Raison, P. E.; Jardin, R.; Bouëxière, D.; Konings, R. J. M.; Geisler, T.; Pavel, C. C.; Rebizant, J.; Popa, K. Structural Investigation of the Synthetic $CaAn(PO_4)_2$ (An = Th and Np) Cheralite-like Phosphates. *Physics and Chemistry of Minerals* **2008**, *35* (10), 603–609. https://doi.org/10.1007/s00269-008-0252-4.
(37) Pepin, J. G.; Vance, E. R.; McCarthy, G. J. The Crystal Chemistry of Cerium in the Monazite Structure-Type Phase of Tailored-Ceramic Nuclear Waste Forms. *Materials Research Bulletin* **1981**, *16* (6), 627–633. https://doi.org/10.1016/0025-5408(81)90261-0.
(38) Kitaev, D. B.; Volkov, Yu. F.; Orlova, A. I. Orthophosphates of Tetravalent Ce, Th, U, Np, and Pu with the Monazite Structure. *Radiochemistry* **2004**, *46* (3), 211–217. https://doi.org/10.1023/B:RACH.0000031674.74780.a8.
(39) Podor, R.; Cuney, M.; Nguyen, T. C. Experimental Study of the Solid Solution between Monazite-(La) and $(Ca_{0.5}U_{0.5})PO_4$ at 780 °C and 200 MPa. *American Mineralogist* **1995**, *80* (11–12), 1261–1268. https://doi.org/10.2138/am-1995-11-1215.
(40) Terra, O.; Dacheux, N.; Clavier, N.; Podor, R.; Audubert, F. Preparation of Optimized Uranium and Thorium Bearing Brabantite or Monazite/Brabantite Solid Solutions. *Journal of the American Ceramic Society* **2008**, *91* (11), 3673–3682. https://doi.org/10.1111/j.1551-2916.2008.02678.x.
(41) Dacheux, N.; Clavier, N.; Wallez, G.; Brandel, V.; Emery, J.; Quarton, M.; Genet, M. Characterization of the Thorium Phosphate-Hydrogenphosphate Hydrate (TPHPH) and Study of Its Transformation into the Thorium Phosphate-Diphosphate (β-TPD). *Materials*

Research Bulletin **2005**, *40* (12), 2225–2242. https://doi.org/10.1016/j.materresbull.2005.06.011.
(42) Clavier, N. Elaboration de Phosphate-Diphosphate de Thorium et d'uranium (β-PDTU) et de Matériaux Composites β-PDTU/Monazite à Partir de Précurseurs Cristallisés : Études Du Frittage et de La Durabilité Chimique. PhD Thesis, Université de Paris-Sud, 2004.
(43) Dacheux, N.; Chassigneux, B.; Brandel, V.; Le Coustumer, P.; Genet, M.; Cizeron, G. Reactive Sintering of the Thorium Phosphate-Diphosphate. Study of Physical, Thermal, and Thermomechanical Properties and Chemical Durability during Leaching Tests. *Chem. Mater.* **2002**, *14* (7), 2953–2961. https://doi.org/10.1021/cm011277g.
(44) Guy, C.; Audubert, F.; Lartigue, J.-E.; Latrille, C.; Advocat, T.; Fillet, C. New Conditionings for Separated Long-Lived Radionuclides. *Comptes Rendus Physique* **2002**, *3* (7), 827–837. https://doi.org/10.1016/S1631-0705(02)01377-4.
(45) Dacheux, N.; Clavier, N.; Podor, R. Versatile Monazite: Resolving Geological Records and Solving Challenges in Materials Science: Monazite as a Promising Long-Term Radioactive Waste Matrix: Benefits of High-Structural Flexibility and Chemical Durability†. *American Mineralogist* **2013**, *98* (5–6), 833–847. https://doi.org/10.2138/am.2013.4307.
(46) Breithaupt, J. A. F. Neue Krystallographische Bestimmung Und Mineralogische Charakteristik Verschiedener Mineralspecien. *Journal für Chemie und Physik* **1829**, *55*, 296–306.
(47) Babelot, C. Monazite-Type Ceramics for Conditioning of Minor Actinides: Structural Characterization and Properties. PhD Thesis, RWTH Aachen University, Jülich, 2012.
(48) Förster, H.-J. The Chemical Composition of REE-Y-Th-U-Rich Accessory Minerals in Peraluminous Granites of the Erzgebirge-Fichtelgebirge Region, Germany; Part I, The Monazite-(Ce)-Brabantite Solid Solution Series. *American Mineralogist* **1998**, *83* (3–4), 259–272. https://doi.org/10.2138/am-1998-3-409.
(49) Cuney, M.; Mathieu, R. Extreme Light Rare Earth Element Mobilization by Diagenetic Fluids in the Geological Environment of the Oklo Natural Reactor Zones, Franceville Basin, Gabon. *Geology* **2000**, *28* (8), 743–746. https://doi.org/10.1130/0091-7613(2000)28<743:ELREEM>2.0.CO;2.
(50) Boatner, L. A. Synthesis, Structure, and Properties of Monazite, Pretulite, and Xenotime. *Reviews in Mineralogy and Geochemistry* **2002**, *48* (1), 87–121. https://doi.org/10.2138/rmg.2002.48.4.
(51) Rapp, R. P.; Watson, E. B. Monazite Solubility and Dissolution Kinetics: Implications for the Thorium and Light Rare Earth Chemistry of Felsic Magmas. *Contributions to Mineralogy and Petrology* **1986**, *94* (3), 304–316. https://doi.org/10.1007/BF00371439.
(52) Slodowska-Curie, M. Rayons Émis Par Les Composés de l'uranium et Du Thorium. *Comptes-rendus de l'Académie des Sciences* **1898**, *126*, 1101–1103.
(53) Overstreet, W. C. *The Geologic Occurrence of Monazite*; Geological Survey professional paper; U.S. Government Printing Office, 1967.
(54) Gramaccioli, C. M.; Segalstad, T. V. A Uranium- and Thorium-Rich Monazite from a South-Alpine Pegmatite at Piona, Italy. *American Mineralogist* **1978**, *63* (7–8), 757–761.
(55) Lumpkin, G. R. Rare-Element Mineralogy and Internal Evolution of the Rutherford #2 Pegmatite, Amelia County, Virginia; a Classic Locality Revisited. *The Canadian Mineralogist* **1998**, *36* (2), 339–353.
(56) Förster, H.-J.; Harlov, D. E. Monazite-(Ce)-Huttonite Solid Solutions in Granulite-Facies Metabasites from the Ivrea-Verbano Zone, Italy. *Mineralogical Magazine* **1999**, *63* (4), 587–594. https://doi.org/10.1180/minmag.1999.063.4.11.
(57) Montel; Kornprobst; Vielzeuf. Preservation of Old U–Th–Pb Ages in Shielded Monazite: Example from the Beni Bousera Hercynian Kinzigites (Morocco). *Journal of*

Metamorphic Geology **2000**, *18* (3), 335-342. https://doi.org/10.1046/j.1525-1314.2000.00261.x.

(58) Montel, J.-M.; Razafimahatratra, D.; Ralison, B.; De Parseval, P.; Thibault, M.; Randranja, R. Monazite from Mountain to Ocean: A Case Study from Trolognaro (Fort-Dauphin), Madagascar. *European Journal of Mineralogy* **2011**, *23* (5), 745–757. https://doi.org/10.1127/0935-1221/2011/0023-2149.

(59) Oelkers, E. H.; Poitrasson, F. An Experimental Study of the Dissolution Stoichiometry and Rates of a Natural Monazite as a Function of Temperature from 50 to 230 °C and PH from 1.5 to 10. *Chemical Geology* **2002**, *191* (1), 73–87. https://doi.org/10.1016/S0009-2541(02)00149-3.

(60) Delage, F.; Dussossoy, J. L. R7T7 Glass Initial Dissolution Rate Measurements Using a High-Temperature Soxhlet Device. *MRS Proceedings* **1990**, *212*, 41. https://doi.org/10.1557/PROC-212-41.

(61) Robisson, A. C.; Dacheux, N.; Aupiais, J. Influence of the PH on the Dissolution of TPD and Associated Solid Solutions. *Journal of Nuclear Materials* **2002**, *306* (2), 134–146. https://doi.org/10.1016/S0022-3115(02)01246-1.

(62) El-Nadi, Y. A.; Daoud, J. A.; Aly, H. F. Modified Leaching and Extraction of Uranium from Hydrous Oxide Cake of Egyptian Monazite. *International Journal of Mineral Processing* **2005**, *76* (1), 101–110. https://doi.org/10.1016/j.minpro.2004.12.005.

(63) Boatner, L. A.; Sales, B. C. Monazite. In *Radioactive waste forms for the future*; Lutze, W., Ewing, R. C., Eds.; Elsevier: Amsterdam, 1988; pp 495–564.

(64) Lumpkin, G. R.; Geisler-Wierwille, T. 5.22 - Minerals and Natural Analogues. In *Comprehensive Nuclear Materials*; Konings, R. J. M., Ed.; Elsevier: Oxford, 2012; pp 563–600. https://doi.org/10.1016/B978-0-08-056033-5.00111-7.

(65) Ewing, R. C.; Haaker, R. F. The Metamict State: Implications for Radiation Damage in Crystalline Waste Forms. *Nuclear and Chemical Waste Management* **1980**, *1* (1), 51–57. https://doi.org/10.1016/0191-815X(80)90028-5.

(66) Karioris, F. G.; Gowda, K. A.; Cartz, L. Heavy Ion Bombardment of Monoclinic $ThSiO_4$, ThO_2 and Monazite. *Radiation Effects* **1981**, *58* (1–2), 1–3. https://doi.org/10.1080/01422448108226520.

(67) Meldrum, A.; Boatner, L. A.; Weber, W. J.; Ewing, R. C. Radiation Damage in Zircon and Monazite. *Geochimica et Cosmochimica Acta* **1998**, *62* (14), 2509–2520. https://doi.org/10.1016/S0016-7037(98)00174-4.

(68) Burakov, B. E.; Yagovkina, M. A.; Garbuzov, V. M.; Kitsay, A. A.; Zirlin, V. A. Self-Irradiation of Monazite Ceramics: Contrasting Behavior of $PuPO_4$ and $(La,Pu)PO_4$ Doped with Pu-238. *MRS Proceedings* **2004**, *824*, CC4.1. https://doi.org/10.1557/PROC-824-CC4.1.

(69) Ewing, R. C.; Meldrum, A.; Wang, L.; Wang, S. Radiation-Induced Amorphization. *Reviews in Mineralogy and Geochemistry* **2000**, *39* (1), 319–361. https://doi.org/10.2138/rmg.2000.39.12.

(70) Seydoux-Guillaume, A.-M.; Deschanels, X.; Baumier, C.; Neumeier, S.; Weber, W. J.; Peuget, S. Why Natural Monazite Never Becomes Amorphous: Experimental Evidence for Alpha Self-Healing. *American Mineralogist* **2018**, *103* (5), 824–827. https://doi.org/10.2138/am-2018-6447.

(71) Seydoux-Guillaume, A.-M.; Wirth, R.; Deutsch, A.; Schärer, U. Microstructure of 24-1928 Ma Concordant Monazites; Implications for Geochronology and Nuclear Waste Deposits. *Geochimica et Cosmochimica Acta* **2004**, *68* (11), 2517–2527. https://doi.org/10.1016/j.gca.2003.10.042.

(72) Meldrum, A.; Boatner, L. A.; Ewing, R. C. Displacive Radiation Effects in the Monazite- and Zircon-Structure Orthophosphates. *Phys. Rev. B* **1997**, *56* (21), 13805–13814. https://doi.org/10.1103/PhysRevB.56.13805.
(73) Ehlert, T. C.; Gowda, K. A.; Karioris, F. G.; Cartz, L. Differential Scanning Calorimetry of Heavy Ion Bombarded Synthetic Monazite. *Radiation Effects* **1983**, *70* (1–4), 173–181. https://doi.org/10.1080/00337578308219214.
(74) Deschanels, X.; Seydoux-Guillaume, A. M.; Magnin, V.; Mesbah, A.; Tribet, M.; Moloney, M. P.; Serruys, Y.; Peuget, S. Swelling Induced by Alpha Decay in Monazite and Zirconolite Ceramics: A XRD and TEM Comparative Study. *Journal of Nuclear Materials* **2014**, *448* (1), 184–194. https://doi.org/10.1016/j.jnucmat.2014.02.003.
(75) Weber, W. J. Radiation-Induced Defects and Amorphization in Zircon. *Journal of Materials Research* **1990**, *5* (11), 2687–2697. https://doi.org/10.1557/JMR.1990.2687.
(76) Bregiroux, D. Synthèse Par Voie Solide et Frittage de Céramiques à Structure Monazite : Application Au Conditionnement Des Actinides Mineurs. PhD Thesis, Université de Limoges, 2005.
(77) Bregiroux, D.; Lucas, S.; Champion, E.; Audubert, F.; Bernache-Assollant, D. Sintering and Microstructure of Rare Earth Phosphate Ceramics $REPO_4$ with RE=La, Ce or Y. *Journal of the European Ceramic Society* **2006**, *26* (3), 279–287. https://doi.org/10.1016/j.jeurceramsoc.2004.11.004.
(78) Perrière, L.; Bregiroux, D.; Naitali, B.; Audubert, F.; Champion, E.; Smith, D. S.; Bernache-Assollant, D. Microstructural Dependence of the Thermal and Mechanical Properties of Monazite $LnPO_4$ (Ln=La to Gd). *Journal of the European Ceramic Society* **2007**, *27* (10), 3207–3213. https://doi.org/10.1016/j.jeurceramsoc.2006.12.005.
(79) Bregiroux, D.; Belin, R.; Valenza, P.; Audubert, F.; Bernache-Assollant, D. Plutonium and Americium Monazite Materials: Solid State Synthesis and X-Ray Diffraction Study. *Journal of Nuclear Materials* **2007**, *366* (1), 52–57. https://doi.org/10.1016/j.jnucmat.2006.12.042.
(80) Jardin, R.; Pavel, C. C.; Raison, P. E.; Bouëxière, D.; Santa-Cruz, H.; Konings, R. J. M.; Popa, K. The High-Temperature Behaviour of $PuPO_4$ Monazite and Some Other Related Compounds. *Journal of Nuclear Materials* **2008**, *378* (2), 167–171. https://doi.org/10.1016/j.jnucmat.2008.05.011.
(81) Popa, K.; Colineau, E.; Wastin, F.; Konings, R. J. M. The Low-Temperature Heat Capacity of $(Pu_{0.1}La_{0.9})PO_4$. *Solid State Communications* **2007**, *144* (1), 74–77. https://doi.org/10.1016/j.ssc.2007.07.011.
(82) Popa, K.; Vigier, J.-F.; Martel, L.; Manara, D.; Colle, J.-Y.; Blanco, O. D.; Wiss, T.; Freis, D.; Konings, R. J. M. Synthesis, Characterization, and Stability of Americium Phosphate, $AmPO_4$. *Inorg. Chem.* **2020**. https://doi.org/10.1021/acs.inorgchem.0c00697.
(83) Montel, J.-M.; Glorieux, B.; Seydoux-Guillaume, A.-M.; Wirth, R. Synthesis and Sintering of a Monazite–Brabantite Solid Solution Ceramic for Nuclear Waste Storage. *Journal of Physics and Chemistry of Solids* **2006**, *67* (12), 2489–2500. https://doi.org/10.1016/j.jpcs.2006.07.004.
(84) Glorieux, B.; Montel, J. M.; Matecki, M. Synthesis and Sintering of a Monazite–Brabantite Solid Solution Ceramics Using Metaphosphate. *Journal of the European Ceramic Society* **2009**, *29* (9), 1679–1686. https://doi.org/10.1016/j.jeurceramsoc.2008.10.004.
(85) Popa, K.; Cologna, M.; Martel, L.; Staicu, D.; Cambriani, A.; Ernstberger, M.; Raison, P. E.; Somers, J. $CaTh(PO_4)_2$ Cheralite as a Candidate Ceramic Nuclear Waste Form: Spark Plasma Sintering and Physicochemical Characterisation. *Journal of the European Ceramic Society* **2016**, *36* (16), 4115–4121. https://doi.org/10.1016/j.jeurceramsoc.2016.07.016.

(86) Du Fou de Kerdaniel, E. Etude de La Dissolution de Britholites et de Solutions Solides Monazite / Brabantite Dopées Avec Des Actinides. PhD Thesis, Université de Paris XI Orsay, 2007.
(87) Hikichi, Y.; Hukuo, K.; Shiokawa, J. Solid Solutions in the Systems Monazite($CePO_4$)-Huttonite($ThSiO_4$), and Monazite-$Ca_{0.5}Th_{0.5}PO_4$. *NIPPON KAGAKU KAISHI* **1978**, *1978* (12), 1635–1640. https://doi.org/10.1246/nikkashi.1978.1635.
(88) Hikichi, Y.; Nomura, T.; Tanimura, Y.; Suzuki, S.; Miyamoto, M. Sintering and Properties of Monazite-Type $CePO_4$. *Journal of the American Ceramic Society* **1990**, *73* (12), 3594–3596. https://doi.org/10.1111/j.1151-2916.1990.tb04263.x.
(89) Arinicheva, Y.; Bukaemskiy, A.; Neumeier, S.; Modolo, G.; Bosbach, D. Studies on Thermal and Mechanical Properties of Monazite-Type Ceramics for the Conditioning of Minor Actinides. *Progress in Nuclear Energy* **2014**, *72*, 144–148. https://doi.org/10.1016/j.pnucene.2013.09.004.
(90) Babelot, C.; Bukaemskiy, A.; Neumeier, S.; Modolo, G.; Bosbach, D. Crystallization Processes, Compressibility, Sinterability and Mechanical Properties of La-Monazite-Type Ceramics. *Journal of the European Ceramic Society* **2017**, *37* (4), 1681–1688. https://doi.org/10.1016/j.jeurceramsoc.2016.11.047.
(91) Neumeier, S.; Arinicheva, Y.; Clavier, N.; Podor, R.; Bukaemskiy, A.; Modolo, G.; Dacheux, N.; Bosbach, D. The Effect of the Synthesis Route of Monazite Precursors on the Microstructure of Sintered Pellets. *Progress in Nuclear Energy* **2016**, *92*, 298–305. https://doi.org/10.1016/j.pnucene.2016.07.011.
(92) Arinicheva, Y.; Clavier, N.; Neumeier, S.; Podor, R.; Bukaemskiy, A.; Klinkenberg, M.; Roth, G.; Dacheux, N.; Bosbach, D. Effect of Powder Morphology on Sintering Kinetics, Microstructure and Mechanical Properties of Monazite Ceramics. *Journal of the European Ceramic Society* **2018**, *38* (1), 227–234. https://doi.org/10.1016/j.jeurceramsoc.2017.08.008.
(93) Mesbah, A.; Clavier, N.; Elkaim, E.; Gausse, C.; Kacem, I. B.; Szenknect, S.; Dacheux, N. Monoclinic Form of the Rhabdophane Compounds: $REEPO_4{\cdot}0.667H_2O$. *Crystal Growth & Design* **2014**, *14* (10), 5090–5098. https://doi.org/10.1021/cg500707b.
(94) Mesbah, A.; Clavier, N.; Elkaim, E.; Szenknect, S.; Dacheux, N. In Pursuit of the Rhabdophane Crystal Structure: From the Hydrated Monoclinic $LnPO_4.0.667H_2O$ to the Hexagonal $LnPO_4$ (Ln = Nd, Sm, Gd, Eu and Dy). *Journal of Solid State Chemistry* **2017**, *249*, 221–227. https://doi.org/10.1016/j.jssc.2017.03.004.
(95) McCarthy, G. J.; White, W. B.; Pfoertsch, D. E. Synthesis of Nuclear Waste Monazites, Ideal Actinide Hosts for Geologic Disposal. *Materials Research Bulletin* **1978**, *13* (11), 1239–1245. https://doi.org/10.1016/0025-5408(78)90215-5.
(96) Veilly, E.; du Fou de Kerdaniel, E.; Roques, J.; Dacheux, N.; Clavier, N. Comparative Behavior of Britholites and Monazite/Brabantite Solid Solutions during Leaching Tests: A Combined Experimental and DFT Approach. *Inorg. Chem.* **2008**, *47* (23), 10971–10979. https://doi.org/10.1021/ic801169d.
(97) Qin, D.; Mesbah, A.; Clavier, N.; Szenknect, S.; Dacheux, N. From Th-Rhabdophane to Monazite-Cheralite Solid Solutions: Thermal Behavior of $Nd_{1-2x}Th_xCa_xPO_4{\cdot}nH_2O$ (x = 0–0.15). *Crystal Growth & Design* **2019**, *19* (5), 2794–2801. https://doi.org/10.1021/acs.cgd.9b00028.
(98) Jonasson, R. G.; Vance, E. R. DTA Study of the Rhabdophane to Monazite Transformation in Rare Earth (La-Dy) Phosphates. *Thermochimica Acta* **1986**, *108*, 65–72. https://doi.org/10.1016/0040-6031(86)85078-X.
(99) Kijkowska, R. Thermal Decomposition of Lanthanide Orthophosphates Synthesized through Crystallisation from Phosphoric Acid Solution. *Thermochimica Acta* **2003**, *404* (1), 81–88. https://doi.org/10.1016/S0040-6031(03)00085-6.

(100) Gausse, C. Synthèse et Dissolution de Matrices Phosphatées de Structure Monazitique. PhD Thesis, Université de Montpellier, 2016.
(101) Gausse, C.; Szenknect, S.; Qin, D. W.; Mesbah, A.; Clavier, N.; Neumeier, S.; Bosbach, D.; Dacheux, N. Determination of the Solubility of Rhabdophanes $LnPO_4 \cdot 0.667H_2O$ (Ln = La to Dy). *European Journal of Inorganic Chemistry* **2016**, *2016* (28), 4615–4630. https://doi.org/10.1002/ejic.201600517.
(102) Gausse, C.; Szenknect, S.; Mesbah, A.; Clavier, N.; Neumeier, S.; Dacheux, N. Dissolution Kinetics of Monazite $LnPO_4$ (Ln = La to Gd): A Multiparametric Study. *Applied Geochemistry* **2018**, *93*, 81–93. https://doi.org/10.1016/j.apgeochem.2018.04.005.
(103) 放射性固体废物分类办法（征求意见稿）; 2017.
(104) Clavier, N.; Dacheux, N.; Podor, R. Synthesis, Characterization, Sintering, and Leaching of β-TUPD/Monazite Radwaste Matrices. *Inorg. Chem.* **2006**, *45* (1), 220–229. https://doi.org/10.1021/ic051607p.

Chapter I. Incorporation of Thorium into the Rhabdophane Structure Type $Ln_{1-2x}Ca_xTh_xPO_4.nH_2O$ and the Associated Monazite-Cheralite Solid Solution $Ln_{1-2x}Ca_xTh_xPO_4$ (Ln = Pr, Nd)

Results published in

Qin, D.; Mesbah, A.; Gausse, C.; Szenknect, S.; Dacheux, N.; Clavier, N. Incorporation of Thorium in the Rhabdophane Structure: Synthesis and Characterization of $Pr_{1-2x}Ca_xTh_xPO_4.nH_2O$ Solid Solutions. *J. Nucl. Mater.* **2017**, *492*, 88–96.

I-1. Introduction

I-1.1. Monazite type ceramics as a promising matrix for actinides conditioning

The conditioning and long-term disposal of nuclear waste (radwaste) represents a major challenge for the nuclear industry. In France, a framework for long-term management of the French nuclear waste was established according to the Bataille's law in 1991, including Pu and minor actinides produced in the back-end of the fuel cycle [1]. Even though, the borosilicate glasses "R7T7" appear as the reference matrix for all radionuclides derived from nuclear waste solution, several studies have been dedicated to ceramic waste forms for specific actinides immobilization [2,3]. This is mainly due to the radiotoxicity of plutonium and minor actinides which could remain for 10^4-10^6 years [4]. To meet the needs of this specific conditioning, the ceramics matrix should fulfill several properties, *e.g.*, capability to incorporate high contents of actinides [2], interesting sintering capability [5–7], high chemical durability in weathering conditions [8–16], and resistance to radiation damage [17–21]. In this frame, four materials were highlighted as potential candidates:

1) Britholites $Ca_9An^{III}_{1-x}An^{IV}_x(PO_4)_{5-x}(SiO_4)_{1+x}F_2$, where An refers to actinides [22–24];
2) Monazite/cheralite solid solutions $Ln_{1-x-2y}An^{III}_xCa_yAn^{IV}_yPO_4$, where Ln refers to lanthanides [25–34];
3) Thorium phosphate diphosphate (β-TPD) with associated β-$Th_{4-x}An^{IV}_x(PO_4)_4P_2O_7$ solid solutions [5,6,24,35] and associations with monazites [11];
4) Zirconolite $(Ca_{1-x}An^{III}_x)(Zr_{1-y}An^{IV}_y)Ti_{2-x}Al_xO_7$ [2,36]

In this PhD work, our study focused on monazite/cheralite type ceramics matrix. Monazite ($LnPO_4$, Ln = La-Tb) is the most abundant lanthanide phosphate observed in natural samples [37,38]. Boatner *et al.* [39] reported that the monazite usually appears as an accessory mineral in granites, gneisses, and pegmatites; or exists as alluvial deposits and beach sands resulting from the weathering of these host rocks. Besides lanthanides, natural monazite samples contain large amounts of thorium and uranium [38,40,41]. The thorium and uranium contents in monazite ores (calculated as ThO_2 and UO_2) can reach 29 wt.% and 16 wt.%, respectively [39,42,43]. Specific samples of monazite were also found to incorporate up to 50 wt.% of ThO_2 [37,44,45]. Despite these large thorium and uranium contents, it has been found that natural monazite samples were preserved from multiple sedimentation and metamorphic cycles occurring over several hundred million years [39]. During this long period, all the radionuclides and its associated descendants

remained confined inside the monazites. For this reason, monazite type minerals were used in geochronology for radiometric dating since they constitute closed systems for U-Th-Pb decay chains [45,46]. The study published by Montel *et al.* [45,46] suggested that the weathering erosion and transport processes only mechanically abraded monazite, but did not chemically alter the mineral during the long geological periods. These geological observations argued for their use as a uranium or thorium host matrix. Indeed, Dacheux *et al.* [47] have thoroughly reviewed the researches on monazites and proposed the application of monazite as a promising matrix for actinides conditioning. The two main arguments given in their study were the high structural flexibility of monazite, which allowed the incorporation of large amount actinides and other elements, and its exceptional high chemical durability. In this chapter, the discussion will concern the incorporation of actinides in the structure whereas the chemical durability of the monazite samples will be described in the following chapter.

I-1.2. Incorporation of actinides into monazite thanks to its structural flexibility

The monazite-type structure, AXO_4, is monoclinic with a space group $P2_1/n$. According to the review published by Clavier *et al.*, this structure allows the incorporation of a wide range of elements, providing various combinations of cations in different oxidation states [48] This structural flexibility is correlated to the low symmetry of the LnO_9 coordination polyhedron so that no severe charge or size constraints were induced [49]. Since the actinide elements have rich redox chemistry with stabilized oxidation states varying from +III to +VI [50], the flexibility of the monazite-type structure is favourable for large actinide incorporation rates. Additionally, the incorporation mechanism depends on the oxidation state. For trivalent actinides, the incorporation could be simply achieved through direct substitution $Ln^{3+} \leftrightarrow An^{3+}$. Several studies already reported stable $An^{III}PO_4$ samples for An = Pu, Am, Cm, Bk, Cf, and even for Es [51–53]. Moreover, monazite type solid solutions, such as $La_{1-x}Pu_xPO_4$ and $La_{1-x}Am_xPO_4$, have been successfully synthesized by different research teams [20,54–58].

Contrary to the plutonium and minor actinides, for which the more stable oxidation state is III, thorium and uranium are incorporated in their tetravalent oxidation state. The associated direct substitution mechanism consists in the replacement of 4 Ln^{3+} by 3 An^{4+} with the simultaneous formation of a cation vacancy:

$$4Ln^{3+} \leftrightarrow 3An^{4+} + \square \qquad \text{(I-1)}$$

However, with such a substitution mechanism, the incorporation of thorium or uranium appears to be limited to few weight percents only, according to the PhD work of R. Podor [26].

In fact, the incorporation of tetravalent actinides was mainly achieved thorough coupled substitution, which avoids the formation of cation vacancies. Two mechanisms have been reported. For the first one, when trivalent lanthanide ion is replaced by tetravalent actinide (Th or U), phosphate group is simultaneously substituted by silicate group.

$$(1\text{-}x)\ Ln^{3+} + x\ An^{4+} + (1\text{-}x)\ PO_4^{3-} + x\ SiO_4^{4-} \leftrightarrow Ln^{III}_{1-x}An^{IV}_x(PO_4)_{1-x}(SiO_4)_x \quad \text{(I-2)}$$

This mechanism leads to the formation of monazite-huttonite solid-solutions. It was reported by Hikichi *et al.* [59] and Montel *et al.* [46]. The huttonite, first discovered by Hutton, is a stable form of the thorium silicate, which crystallizes with the same structure than monazite [60].

The second mechanism involves incorporation by purely cations substitution. It consists in replacing two lanthanide (+III) cations by one tetravalent actinide and a divalent cation, such as alkaline earth metal [48].

$$(1\text{-}2x)\ Ln^{3+} + x\ An^{4+} + x\ M^{2+} + PO_4^{3-} \leftrightarrow Ln^{III}_{1-2x}M^{II}_xAn^{IV}_xPO_4 \quad \text{(I-3)}$$

The solids formed by this way are monazite-cheralite solid solutions. The end-member cheralite [61], $Ca_{0.5}Th_{0.5}PO_4$, previously known as brabantite [62], is isomorphous with monazite and huttonite [48]. This mechanism is the best-documented in the literature [25–34]. Moreover, Rodor *et al.* and Bregiroux *et al.* [25,26,33] has given two criteria for the stability of monazite-cheralite solid solution.

$$1.107\text{Å} \leq \overline{{}^{IX}r\left(M^{II+III+IV}\right)} \leq 1.216\text{Å} \quad \text{(I-4)}$$

$$1 \leq \overline{{}^{IX}r\left(M^{II+III}\right)} \,/\, \overline{{}^{IX}r\left(M^{III+IV}\right)} \leq 1.238 \quad \text{(I-5)}$$

where $\overline{{}^{IX}r\left(M^{II+III+IV}\right)}$, $\overline{{}^{IX}r\left(M^{II+III}\right)}$ and ${}^{IX}r\left(M^{III+IV}\right)$ correspond to the average cation radius in nine-fold coordination calculated according to:

$$\overline{{}^{IX}r\left(M^{II+III+IV}\right)} = (1\text{-}2x)\times{}^{IX}r\left(Ln^{III}\right) + x \times {}^{IX}r\left(M^{II}\right) + x \times {}^{IX}r\left(An^{IV}\right) \quad \text{(I-6)}$$

$$\overline{{}^{IX}r\left(M^{II+III}\right)} = (1\text{-}2x) \times {}^{IX}r\left(Ln^{III}\right) + x \times {}^{IX}r\left(M^{II}\right) \quad \text{(I-7)}$$

$$\overline{{}^{IX}r\left(M^{III+IV}\right)} = (1\text{-}2x) \times {}^{IX}r\left(Ln^{III}\right) + x \times {}^{IX}r\left(An^{IV}\right) \quad \text{(I-8)}$$

For $Ln_{1-2x}Ca_xTh_xPO_4$ (Ln = Pr, Nd) solid solutions, the value of $\overline{{}^{IX}r\left(M^{II+III+IV}\right)}$ varies between 1.135 Å and 1.179 Å and that of $\overline{{}^{IX}r\left(M^{II+III}\right)} \,/\, \overline{{}^{IX}r\left(M^{III+IV}\right)}$ is between 1 and 1.083 (**Table I-1**). As both values are in accordance with the criteria reported above, the Ln_{1-}

$_{2x}Ca_xTh_xPO_4$ solid solution is theoretically achievable from a structural point of view. The incorporation of thorium in the monazite structure will follow this mechanism during this PhD.

Table I-1. Ionic radius (Å) in the 9-fold coordination for Ca^{II}, Th^{IV}, Pr^{III}, and Nd^{III} extracted from the Shannon tables [63].

Ca^{II}	Th^{IV}	Pr^{III}	Nd^{III}	$\overline{^{IX}r(M^{II+III+IV})}$	$\overline{^{IX}r(M^{II+III})}/\overline{^{IX}r(M^{III+IV})}$
1.18	1.09	1.179	1.163	[1.135 - 1.179]	[1 - 1.083]

I-1.3. Interest of rhabdophane as precursor of monazite-cheralite solid solutions via hydrothermal syntheses

Several studies have reported the syntheses of monazite-cheralite solid solutions via solid-state reactions [7,25,32,34,64]. These methods were based on mixtures of oxides (*i.e.* Ln_2O_3, ThO_2, and CaO) and of phosphate salts (*e.g.* $NH_4H_2PO_4$, $La(PO_3)_3$, etc.) that further went through several milling-calcination cycles to obtain homogenous monazite-cheralite. As example, Montel [7] and Glorieux [64] reported the synthesis of monazite-cheralite $La_{0.73}Ce_{0.09}Th_{0.09}Ca_{0.09}PO_4$, which required a thermal treatment at 1250°C for one night. The dust, produced during the multiple milling/grinding cycles, might be another drawback due to potential risks of contamination. Moreover, the specific surface area of the final product was about 6-7 $m^2.g^{-1}$ [7,64], which was relatively low and hence not in favor of sintering. Similarly, Bregiroux *et al.* [25] has reported the synthesis of $Ca_{0.5}An^{IV}_{0.5}PO_4$, with An = Th, U, and Ce. The syntheses were performed thanks to DTA/TGA experiments up to 1400 °C. They pointed out that the synthesis temperatures for single-phase $Ca_{0.5}Th^{IV}_{0.5}PO_4$ and $Ca_{0.5}U^{IV}_{0.5}PO_4$ in inert atmosphere (Ar) were 1100°C and 1200°C, respectively. Below these temperatures, secondary phases, α-AnP_2O_7 would exist in the samples. However, the decomposition temperature of these two materials were closed to their temperatures of synthesis, *i.e.*, higher than 1400°C and 1300°C for $Ca_{0.5}Th^{IV}_{0.5}PO_4$, and $Ca_{0.5}U^{IV}_{0.5}PO_4$, respectively. Otherwise, single-phase $Ca_{0.5}Ce^{IV}_{0.5}PO_4$ was not obtained, as Ce^{IV} was always partially reduced in Ce^{III} even in air, which resulted in mixtures of $Ce^{III}_{1-2x}Ca_xCe^{IV}_xPO_4$ and α–$Ca_2P_2O_7$. Bregiroux *et al.* [65] also reported the preparation of monazite-type solid solutions $Pu^{III}_{1-2x}Ca_xPu^{IV}_xPO_4$ (x = 0, 0.3 and 0.5) and $AmPO_4$ by similar methods. Finally, $Ca_{0.5}Np^{IV}_{0.5}PO_4$ was synthesized by Raison *et al.* after a heat treatment at 1250 °C for 100 hours in N_2 atmosphere.

Contrary to dry chemistry routes, wet chemical processes usually performed at low temperature (*i.e.* ≤ 250 °C) [15,66–69] can bring better control of the morphology coupled with higher specific surface area [70,71]. Furthermore, the samples produced are generally closer to the

expected stoichiometry (especially regarding the M/P ratio), but also present higher homogeneity in the cationic distribution [15,72].

Wet chemical syntheses could be achieved through multiple methods, such as for instance, co-precipitation [67,72,73], hydrothermal syntheses [15,66,70,72], sol-gel reactions [74,75], reverse micro-emulsion [76,77], etc.

For monazite-cheralite solid solutions, R Podor [26] successfully synthesized single-phase $La_{1-2x}Ca_xTh_xPO_4$ under extreme hydrothermal conditions, *i.e.*, 780 °C and 200 MPa [26]. However, these conditions were difficult to apply for large quantity of material. Therefore, it has been of interest to use "low-temperature" precursor (≤ 250 °C) for the preparation of monazite-cheralite solid solutions.

Rhabdophanes, hydrated compounds with general formula of $LnPO_4.0.667\ H_2O$ (Ln = La to Dy), are easily synthesized through wet chemistry route with T ≤ 170 °C [78–81]. The hydrated rhabdophanes were previously considered in hexagonal structure ($P6_222$ or $P3_121$) [82,83]. However, Mesbah *et al.* [78] have recently re-examined the structure of the hydrated rhabdophanes $SmPO_4.0.667H_2O$ with the application of synchrotron radiation. They suggested the compound crystalize in monoclinic C2 space group with a = 28.0903(1) Å, b = 6.9466(1) Å, c = 12.0304(1) Å, β = 115.23 (1)°, and V = 2123.4(1) $Å^3$ with 24 formula units per unit cell. Later, Mesbah *et al.* [84] have investigated the dehydration process of hydrated rhabdophane and pointed out the complete dehydration, taking place between 200 and 300°C, resulted in the hexagonal anhydrous rhabdophane.

At higher temperature (*i.e.* above 800 °C), several studies have reported the conversion of pure lanthanide rhabdophane into monazite by heat treatment [85–88]. These coversion temperatrues were much lower than the synthesis temperatures applied for solid-state reactions mentioned above (> 1250°C)[7,25,30,64,65], which might avoid the potential decomposition. It is, therefore, worth to investigate this synthesis protocol to prepare actinides bearing monazite *via* hydrothermal synthesized rhabdophane type precursors. Indeed, for trivalent actinides, wet chemistry were applied to prepare $An^{III}PO_4.0.5\ H_2O$ (An = Pu, Am) rhabdophane. Monazite-type ceramics were thus obtained by heating these precursors between 800 and 1500 °C [51,52,89]. For instance, $PuPO_4.0.5\ H_2O$ rhabdophane were precipitated from a mixture of plutonium trichloride and $NH_4H_2PO_4$ between 75 and 90°C. The associated $PuPO_4$ monazite was converted from $PuPO_4.0.5\ H_2O$ by heating above 950°C [51].

However, there are only few studies dedicated to hydrothermal precipitation adapted for the synthesis of thorium-doped rhabdophane $Ln_{1-2x}Ca_xTh_xPO_4.nH_2O$. To our knowledge, only

Du Fou de Kerdaniel and Gausse reported several experiments in this sense during their PhD [79,80]. Nevertheless, according to the works reported by Du Fou de Kerdaniel *et al.* [15], Mesbah *et al.* [78], and Gausse [80], a very robust synthesis protocol, which led to well-crystallized rhabdophane end-members $LnPO_4.nH_2O$ (Ln = La – Dy), was established. Consequently, this protocol was applied for the syntheses of thorium-doped rhabdophanes in this work. The main challenges of this application were to fix the suitable synthesis conditions, especially in terms of molar ratio between the starting reactants, the temperature and the reaction time associated to the hydrothermal treatment. A multi-parametric study was thus undertaken below to determine the optimal conditions of synthesis.

Later, the samples prepared were converted into monazite-cheralite solid solutions by applying a thermal treatment at 1100°C for 6 hours. The choice of this temperature was made according to the synthesis protocol reported by Montel [7], in which formation of single-phase monazite-cheralite occurred at 1100°C by using dry chemistry route. Both initial rhabdophane precursor and converted monazite-cheralite were thoroughly characterized using different techniques, such as Powder X-Ray Diffraction (PXRD), X-ray spectroscopy analysis (X-EDS), Scanning Electron Microscopy (SEM) observation, etc., so that their crystal structures, chemical compositions and morphologies could be determined.

I-2. Preparation and Characterization of the samples

I-2.1. Preparation of $Ln_{1-2x}Ca_xTh_xPO_4.nH_2O$ rhabdophanes and associated monazite-cheralite $Ln_{1-2x}Ca_xTh_xPO_4$

The metal salts used as staring materials were analytical grade and provided by Sigma-Aldrich: $PrCl_3.6H_2O$ (99.9%), $NdCl_3.6H_2O$ (99.9%), $CaCl_2.nH_2O$, $Th(NO_3)_4.4\text{-}5H_2O$. Considering the hygroscopic character of these salts, each powder was first dissolved in acidic solution, in order to weigh the exact amounts of cations. As a result, $PrCl_3$, $NdCl_3$ and $CaCl_2$ were dissolved in 0.1 $mol.L^{-1}$ HCl and $Th(NO_3)_4.4\text{-}5H_2O$ in 4 $mol.L^{-1}$ HNO_3. The acids above were prepared from concentrated HCl (37%, Carlo Erba) and HNO_3 (69.5%, Carlo Erba). The final concentration of each cation was determined in solution by ICP-OES (the selected wavelengths are listed in **Table A. 1**). They were found to reach about 0.5 $mol.L^{-1}$ for praseodymium, neodymium, and thorium and about 1.5 $mol.L^{-1}$ for calcium.

In order to synthesize the $Ln_{1-2x}Ca_xTh_xPO_4.nH_2O$ compounds (x = 0 – 0.30 for Pr and x = 0 – 0.15 for Nd), the calculated amount of each cation (Ca+Th+Ln) was weighed then introduced into Teflon® jars. With the help of a magnetic stirrer, the introduced reactants were thoroughly mixed and 5 $mol.L^{-1}$ H_3PO_4 (with 3% mole excess compared to the calculated Th and Ln amounts) was added dropwise. The mixture was stirred at room temperature for another 15 minutes then the PTFE containers were sealed. They were further simply heated on a sand bath or placed in Parr autoclaves to reach hydrothermal conditions. The typical range of temperatures investigated was between 90 and 250°C, while the heat duration varied from 2 to 11 days. Afterwards, the precipitate was separated from the solution by centrifugation at 14000 rpm for 5 minutes then washed twice with water then once with ethanol. After drying overnight in an oven at 90°C in air, the obtained solid was ground manually using an agate mortar. Finally, the rhabdophane was calcined at 1100°C for 6 hours in order to achieve its conversion into the monazite-cheralite solid solution.

I-2.2. PXRD characterization

PXRD characterization was performed on a Bruker D8 advance diffractometer equipped with copper radiation (Cu $K\alpha_{1,2}$, λ=1.54184 Å) and using the reflection geometry. The powders were placed in a special sample holder (dome-shaped container) to avoid any radioactive contamination; however, it could increase the background of the collected data. Each PXRD pattern was collected from 5 to 100° (2θ) with a Δθ step of 0.019°. For each step, the collection

time was 3.68 s resulting in a total counting time of about 3 hours. In addition, the powder standard pattern, applied to extract the instrumental function, was collected from pure silicon under similar conditions. The measured data were refined by the Rietveld method with the use of the Fullprof_Suite package [90]. During the refinement, different profile and structure parameters were allowed to vary for each phase such as the zero shift, scale factors, preferred orientation, asymmetry parameters, lattice parameters and a global thermal displacement. Moreover, an anisotropic size model was added for each phase to simulate the microstructural effect so that the strain effect was not considered. The Th-rhabdophane samples were refined in the same structure than the lanthanides end-members. The hydrated form of the rhabdophane at room temperature was reported recently and contains 41 atomic positions with a general formula of $LnPO_4.0.667H_2O$ [78]. In the case of the $Ln_{1-2x}Ca_xTh_xPO_4.nH_2O$ compounds, the Th/Ca atoms were equally distributed in the six different cationic positions. However, due to the important number of atoms and the quality of the data, the atomic parameters were fixed to those of the $PrPO_4.0.667H_2O$ and $NdPO_4.0.667H_2O$ end-members.

I-2.3. Total dissolution tests

The chemical composition of the synthesized Th-rhabdophane $Pr_{1-2x}Ca_xTh_xPO_4.nH_2O$ powders was determined through ICP-OES measurements after their complete dissolution. With this aim, about 20 mg of the obtained powder were dissolved in 2.5 mL fresh aqua regia. Once the dissolution was completed, these solutions were diluted with 0.16 $mol.L^{-1}$ HNO_3 solution so that the elementary concentration of lanthanide was about 15 $mg.L^{-1}$. The elemental concentrations of Th, P, Ca and Ln were determined by ICP-OES (Spectro Arcos EOP) after initial calibration with SPEX standard solutions. For each element, its elemental concentration was the mean value calculated from recommended emission wavelengths and these data were finally used to deduce the atomic ratios in the solids.

I-2.4. SEM observation and X-EDS analyses

The morphology and the chemical composition of synthesized compound were investigated with the use of a FEI Quanta 200 electron microscope. For morphological characterizations, powdered sample was deposited on a carbon tape and analyzed directly without any further preparation step such as metallization. The acceleration voltage of the electron beam was fixed to 8-10 kV while the pressure in the chamber was under 100 Pa. X-EDS analyzer (BRUKER XFlash ® 5010 SDD) was used for quantitative chemical analyses,

with an acceleration voltage of 15 kV and a chamber pressure below 2×10^{-4} Pa. The sample powders were first embedded in an epoxy resin then polished and metalized. For each sample, 30 spots were analyzed and the averages were considered as the measured chemical compositions.

I-3. Preparation of $Ln_{1-2x}Ca_xTh_xPO_4.nH_2O$

I-3.1. Synthesis of $Pr_{1-2x}Ca_xTh_xPO_4.nH_2O$ compounds

I-3.1.1. Starting conditions

Being inspired from the previous works reported by Du Fou de Kerdaniel *et al.* [15] and by Gausse [80], a first batch of experiments aimed to prepare $Pr_{1-2x}Ca_xTh_xPO_4.nH_2O$ with x = 0 – 0.20. The hydrothermal synthesis conditions were set to 110°C for 2 days using a sand bath, and considering a stoichiometric Ca:Th molar ratio (1:1). In order to investigate the nature of the precipitates, combined PXRD, SEM and total dissolution tests analyses were conducted to determine their crystal structure, chemical composition and morphology.

PXRD data (**Figure I-1**) confirmed that rhabdophane was the only observed crystalline phase for x = 0 – 0.1 [78]. It's worth noting that a standard PXRD diffractor might not be able to distinguish the differences between the monoclinic C2 structure, proposed by Mesbah *et al.* [78], and the hexagonal structure, proposed by Mooney *et al.* [82,83]. Nevertheless, the as-prepared hydrated Th-rhabdophanes were supposed to crystallize in monoclinic C2 structure, as the end-member $SmPO_4.0.667H_2O$ was previously proven to be this structure by high resolution synchrotron diffraction [78]. For higher thorium contents (*i.e.*, $x \geq 0.15$), secondary phases characterized by broad peaks were detected in very low amount, *i.e.*, 16.6°, 21.3°, 27.2°, 32.6°, and 34.5°. It might correspond to amorphous and/or nanometric thorium phosphate-hydrogenphosphate hydrate (TPHPH, $Th_2(HPO_4)(PO_4)_2.H_2O$) [91,6,35] or thorium hydroxide phosphate $Th(OH)PO_4$ [92].

SEM observations (**Figure I-2**) revealed the formation of hexagonal shaped rods, which is the typical morphology of rhabdophane-type compounds [93]. A slight increase of the grain size was also observed with the thorium incorporation rate, from about 1 µm (x = 0.05) to 3 µm (x = 0.15 and 0.20). However, it appeared that the crystallization process was not complete for x = 0.05, as a remaining translucent gel could be observed on the SEM picture. The chemical compositions of the synthesized Th-rhabdophanes are listed on **Table I-2**. Whatever the substitution rate considered, the results indicated deviation from the target composition. Despite the presence of both calcium and thorium, a clear lack of calcium was systematically observed, particularly for $x \geq 0.1$, while thorium seemed to be always in excess for all the prepared samples. The praseodymium content, however, was closed to the target value. As such, the P/(Pr+Th+Ca) mole ratio increased significantly with the Ca and Th contents. Therefore, it was

very likely that a secondary phase, which was thorium and phosphate enriched, appeared during the hydrothermal syntheses. This observation supported the results from PXRD analysis which indicated the presence of TPHPH and/or $TH(OH)PO_4$ in the precipitate solid for $x \geq 0.15$ [6,35,91,92]. Moreover, as a lack of incorporation in calcium was also detected for low thorium contents ($x \leq 0.10$), it could suggest the stabilization of Th-rhabdophane compounds through the formation of small amounts of cationic vacancies. Such charge-balance mechanism was already observed in natural analogues (See Equation I-1) [26]:

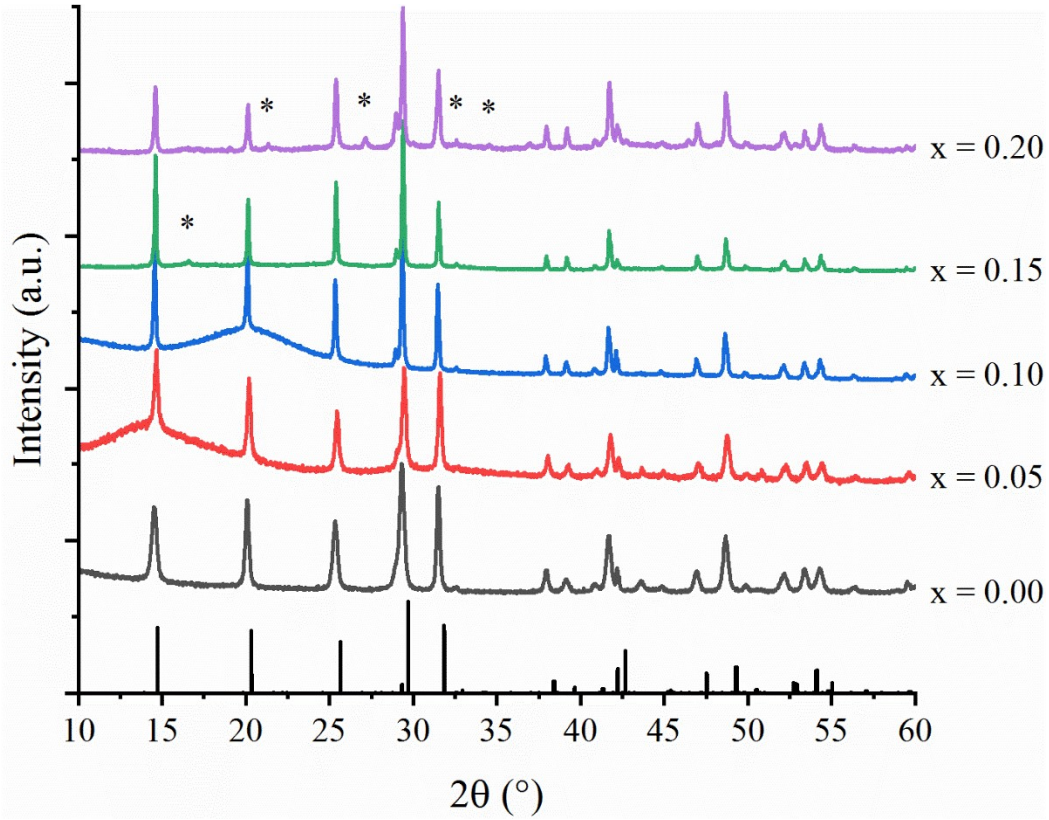

Figure I-1. PXRD patterns of the $Pr_{1-2x}Ca_xTh_xPO_4.nH_2O$ samples ($x \leq 0.20$) prepared at 110°C for 2 days with initial Ca:Th mole ratio equal to 1:1. The vertical bars represented the structure of hydrated rhabdophane $SmPO_4.0.667H_2O$ [78]. The additional peaks marked by asterisks (*) indicate the presence of secondary phases.

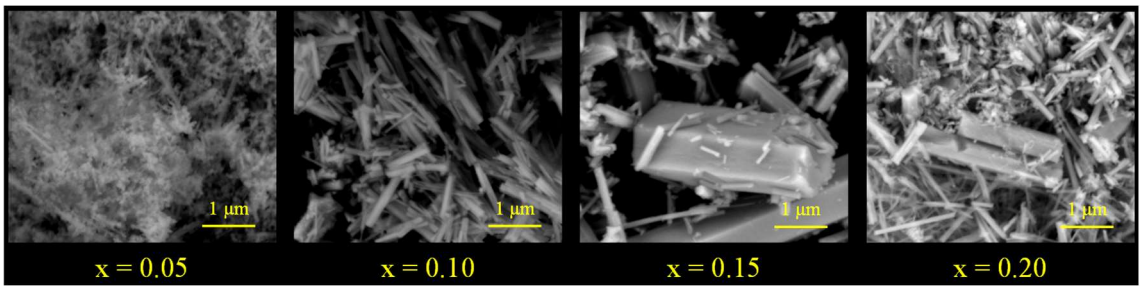

Figure I-2. SEM images of $Pr_{1-2x}Ca_xTh_xPO_4.nH_2O$ samples ($0.05 \leq x \leq 0.20$) prepared at 110°C for 2 days with initial Ca:Th mole ratio equal to 1:1.

Consequently, according to the analyses above, it seems clear that the experimental conditions reported previously by Du Fou de Kerdaniel *et al* [15] are not the most favorable for the preparation of pure and single phase Th-rhabdophane samples with the desired stoichiometric values for thorium and calcium. Therefore, with the purpose to establish a reliable protocol allowing the synthesis of homogeneous Th-rhabdophane samples, the role of different parameters was investigated, including starting Ca:Th ratio, synthesis temperature and holding time at this temperature.

Table I-2. Chemical composition of the $Pr_{1-2x}Ca_xTh_xPO_4.nH_2O$ compounds synthesized at 110°C for 2 days with initial Ca:Th ratio = 1:1.

x (target value)	$\frac{Ca}{Ca+Th+Pr}$	$\frac{Th}{Ca+Th+Pr}$	$\frac{Pr}{Ca+Th+Pr}$	$\frac{P}{Ca+Th+Pr}$
0.05	0.03 ± 0.01	0.05 ± 0.01	0.92 ± 0.06	1.06 ± 0.07
0.10	0.03 ± 0.01	0.12 ± 0.01	0.85 ± 0.04	1.10 ± 0.06
0.15	0.04 ± 0.01	0.27 ± 0.02	0.69 ± 0.04	1.26 ± 0.07
0.20	0.06 ± 0.01	0.26 ± 0.01	0.69 ± 0.02	1.22 ± 0.06

I-3.1.2. Effect of calcium excess in the starting mixture

The first improvement of the synthesis protocol focused on resolving the systematical lack of calcium, which might be due to the higher solubility of Ca compared to Th. Indeed, according to the ThermoChimie database [94], one of the least soluble calcium phosphate solid compound is $Ca(HPO_4)$ (s), which solubility product, as defined below, is equal to 0.03 [95]:

$$Ca(HPO_4) + H^+ \rightleftarrows Ca^{2+} + H_2PO_4^- \quad \text{(I-9)}$$

The pH condition during our hydrothermal synthesis was very acid (pH < 1). Supposing that $Ca(HPO_4)$ was the phase controlling the calcium solubility, the calcium concentration at pH = 0 could reach 12 $mol.L^{-1}$. On the contrary, in the reported saturation tests of TPHPH [96], the concentration of Th at equilibrium in 1 $mol.L^{-1}$ HNO_3, was only 1.9 $mmol.L^{-1}$. From the thermodynamic point of view, Ca is then far more mobilized than Th. However, in the first batch of syntheses, the starting Ca:Th ratio was only 1:1 which might cause the Ca-depletion. Hence, an excess of calcium in the starting reactants was naturally considered as a way to improve the calcium incorporation within the rhabdophane structure. Different experiments were then carried out for the synthesis of $Pr_{0.8}Ca_{0.1}Th_{0.1}PO_4.nH_2O$ by varying the starting Ca:Th ratio from 1 to 10. Meanwhile, heating time was extended to 4 days at 110°C in order to reach larger grain size.

The PXRD patterns (**Figure I-3**) collected for the different $Pr_{0.8}Ca_{0.1}Th_{0.1}PO_4.nH_2O$ samples synthesized indicate that single-phase rhabdophane was systematically obtained whatever the initial Ca:Th ratio. For x = 0.1, the initial Ca:Th ratio then seemed to have low impact on the final structure of the precursor.

However, the chemical composition of the samples (Listed in **Table I-3**), determined by total dissolution tests and X-EDS analyses, confirmed the better incorporation rate of calcium for higher initial Ca:Th ratio. It is worth noting that, in the same time, SEM pictures (**Figure I-4**) showed the increase of the average length of the needle-like crystals with the Ca:Th mole ratio. As a result, the ratio 10:1 was kept unchanged for all the synthesis performed afterwards in order to guarantee the stoichiometry of the prepared materials and to obtain larger grains with less amount of gelatinous compound.

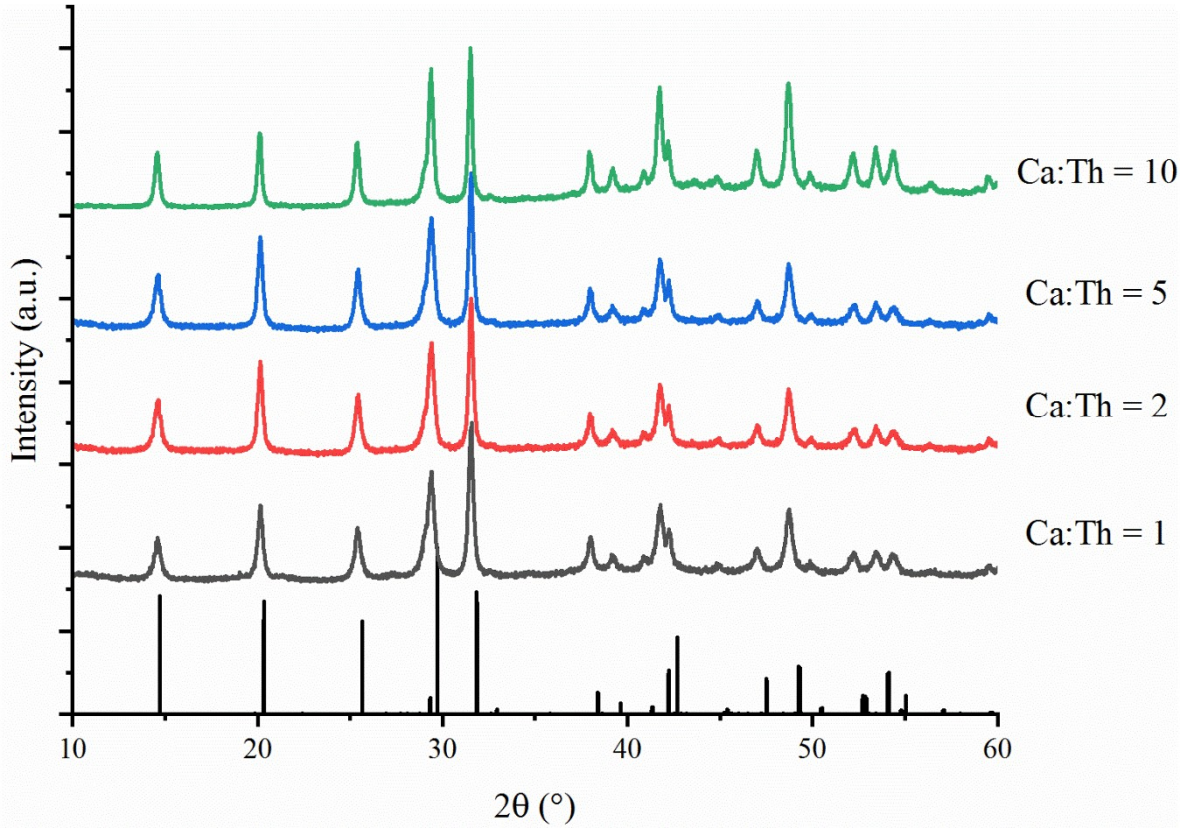

Figure I-3. PXRD patterns of $Pr_{0.8}Ca_{0.1}Th_{0.1}PO_4.nH_2O$ with initial Ca:Th from 1 to 10. The vertical bars represented the structure of hydrated rhabdophane $SmPO_4.0.667H_2O$ [78]

Table I-3. Chemical composition of the $Pr_{0.8}Ca_{0.1}Th_{0.1}PO_4.nH_2O$ compounds synthesis at 110°C for 4 days with initial Ca:Th from 1 to 10.

Ca:Th	Method	$\frac{Ca}{Ca+Th+Pr}$	$\frac{Th}{Ca+Th+Pr}$	$\frac{Pr}{Ca+Th+Pr}$	$\frac{P}{Ca+Th+Pr}$
1:1	ICP-OES	0.07 ± 0.01	0.11 ± 0.01	0.82 ± 0.03	1.04 ± 0.04
	X-EDS	0.08 ± 0.08	0.10 ± 0.05	0.8 ± 0.1	1.0 ± 0.5

Ca:Th	Method	$\frac{Ca}{Ca+Th+Pr}$	$\frac{Th}{Ca+Th+Pr}$	$\frac{Pr}{Ca+Th+Pr}$	$\frac{P}{Ca+Th+Pr}$
2:1	ICP-OES	0.10 ± 0.01	0.10 ± 0.01	0.81 ± 0.03	0.98 ± 0.07
	X-EDS	0.11 ± 0.05	0.09 ± 0.03	0.8 ± 0.1	1.0 ± 0.2
5:1	ICP-OES	0.08 ± 0.01	0.11 ± 0.01	0.81 ± 0.03	1.04 ± 0.04
	X-EDS	0.10 ± 0.04	0.10 ± 0.02	0.8 ± 0.1	1.0 ± 0.2
10:1	ICP-OES	0.11 ± 0.01	0.11 ± 0.01	0.79 ± 0.02	1.03 ± 0.04
	X-EDS	0.14 ± 0.06	0.10 ± 0.03	0.8 ± 0.1	1.0 ± 0.2

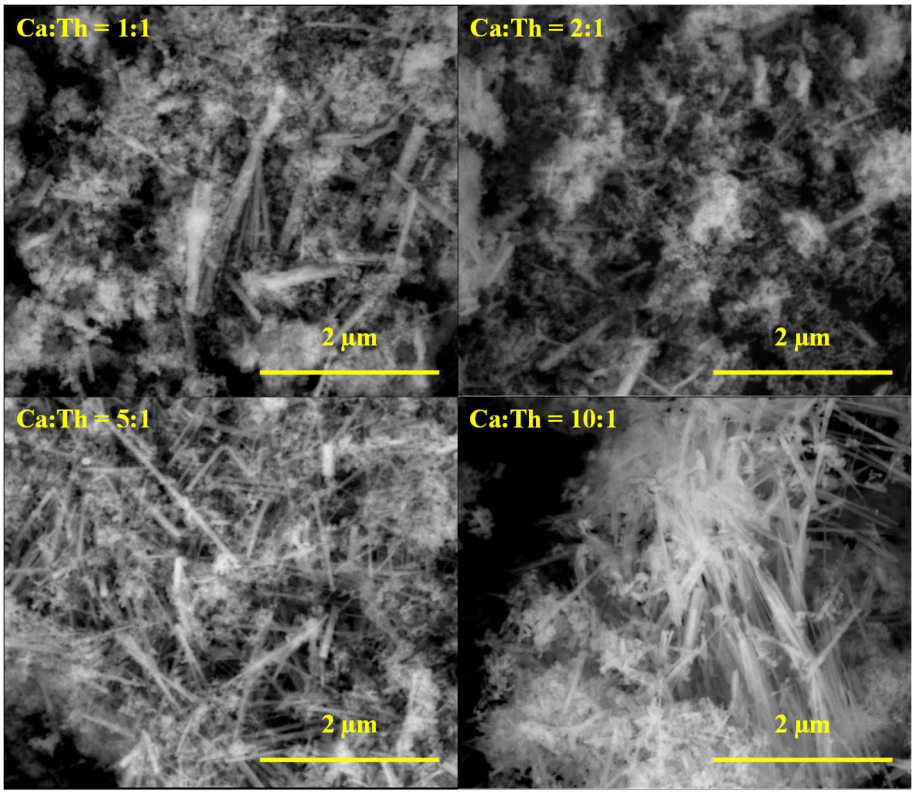

Figure I-4. SEM images of $Pr_{0.8}Ca_{0.1}Th_{0.1}PO_4.nH_2O$ samples prepared at 110°C for 4 days with various starting Ca:Th mole ratios (ranging from 1:1 to 10:1)

I-3.1.3. Determination of the optimal temperature of the hydrothermal treatment

Since rhabdophane is reported to be stable at low temperature, *i.e.* for T ≤ 170°C [79], the conditions of the hydrothermal treatment must be studied carefully in order to avoid the direct formation of monazite from ions in solution. For the $PrPO_4.0.667H_2O$ end-member, the "critical" temperature was reported to be 150 °C; above that, monazite $PrPO_4$ would form in the precipitate [15]. Therefore, monazite-cheralite $Pr_{0.8}Ca_{0.1}Th_{0.1}PO_4$ might also appear by thermal conversion of rhabdophane when the synthesis temperature was above 150°C. Moreover, N. Clavier already reported the synthesis of TPHPH under hydrothermal conditions (T = 120-

170°C) [6,96]. The range of the temperature associated to the formation of TPHPH is closed to that of monazite, which means that the formation of Th-rhabdophane might be in competition with that of TPHPH. Clavier also pointed out that TPHPH precipitated more rapidly at higher temperature, *i.e.* after1 hour at 170°C *vs* 7.5 hours at 120 °C, which suggest that the used of higher synthesis temperature might be in favor of the formation of TPHPH [6]. In order to study the effect of temperature on the preparation of single-phase Th-rhabdophane compounds, experiments were performed at 90, 100, 110, 120, 130, 150, 200 and 250°C for 4 days. Corresponding PXRD data are reported in **Figure I-5** while SEM micrographs are viewed in **Figure I-6**.

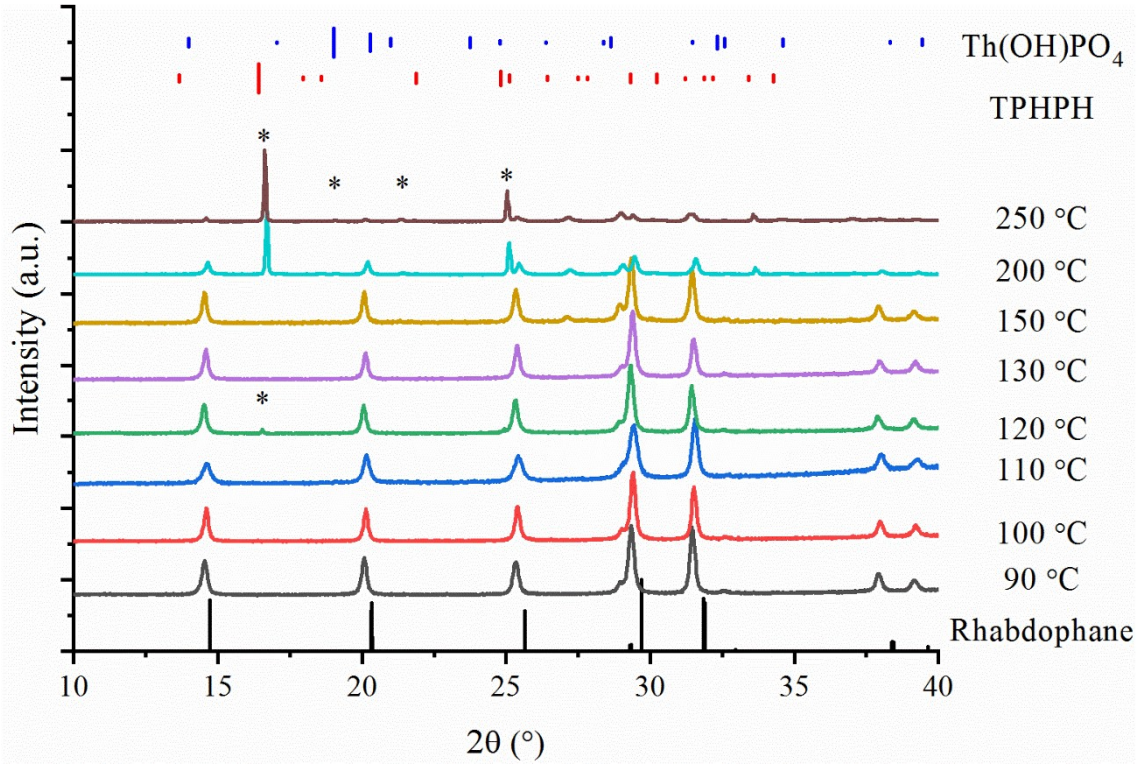

Figure I-5. PXRD pattern of $Pr_{0.8}Ca_{0.1}Th_{0.1}PO_4.nH_2O$ samples prepared after heating for 4 days at various temperatures (90°C ≤ T ≤ 250°C) using an initial Ca:Th mole ratio equal to 10. The standard pattern of $SmPO_4.0.677H_2O$ is presenting as black vertical bars [78]. Additional peaks of TPHPH and $Th(OH)PO_4$ formed as a secondary phase are pointed by an asterisk * [6,35]

According to the PXRD patterns viewed in **Figure I-5**, the intense peak observed at 2θ = 16° for the samples synthesized at 200 and 250 °C suggested the formation of TPHPH (orthorhombic system, Cmcm space group), while the peaks correlated to the rhabdophane structure remained weak [6,35,91]. This result suggested that the precipitation of TPHPH was predominant at 200 and 250 °C. Consequently, these temperature conditions were not in favor of the formation of Th-rhabdophane. For the samples prepared at 90-150 °C, PXRD patterns

evidenced the stabilization of the rhabdophane structure. However, weak additional peaks located at 15.9° and 26.5° when heating at 120 °C and 150 °C, respectively, once again suggested the formation of very small amounts of TPHPH as a secondary phase, which could result from local heterogeneities during the precipitation process. For lower temperatures (*i.e.* T ≤ 110 °C), the prepared samples were assigned to a single-phase rhabdophane structure.

For each sample obtained between 90 °C and 150 °C, the chemical composition determined by total dissolution tests and X-EDS analyses (**Table I-4**) agreed well with the expected stoichiometry. As TPHPH is a thorium-enriched phase, the results of analysis indicated that the quantity of the TPHPH remained low between 120°C and 150°C samples, which is consistent with the analysis of the PXRD patterns.

Table I-4. Effect of temperature on the chemical composition of the $Pr_{0.8}Ca_{0.1}Th_{0.1}PO_4.nH_2O$ compounds synthesis with initial Ca:Th =10.

Temperature (°C)	Method	$\frac{Ca}{Ca+Th+Pr}$	$\frac{Th}{Ca+Th+Pr}$	$\frac{Pr}{Ca+Th+Pr}$	$\frac{P}{Ca+Th+Pr}$
90	ICP-OES	0.10 ± 0.01	0.12 ± 0.01	0.79 ± 0.03	0.97 ± 0.06
	X-EDS	0.08 ± 0.08	0.10 ± 0.05	0.8 ± 0.1	1.0 ± 0.5
100	ICP-OES	0.10 ± 0.01	0.11 ± 0.01	0.79 ± 0.03	1.01 ± 0.07
	X-EDS	0.11 ± 0.05	0.09 ± 0.03	0.8 ± 0.1	1.0 ± 0.2
110	ICP-OES	0.11 ± 0.01	0.11 ± 0.01	0.79 ± 0.02	1.03 ± 0.04
	X-EDS	0.14 ± 0.07	0.10 ± 0.03	0.8 ± 0.1	1.0 ± 0.2
120	ICP-OES	0.09 ± 0.01	0.11 ± 0.01	0.80 ± 0.04	1.01 ± 0.08
	X-EDS	0.10 ± 0.04	0.10 ± 0.02	0.8 ± 0.1	1.0 ± 0.2
130	ICP-OES	0.09 ± 0.01	0.11 ± 0.01	0.80 ± 0.03	1.01 ± 0.08
	X-EDS	–	–	–	–
150	ICP-OES	0.10 ± 0.01	0.12 ± 0.01	0.78 ± 0.04	1.05 ± 0.05
	X-EDS	–	–	–	–

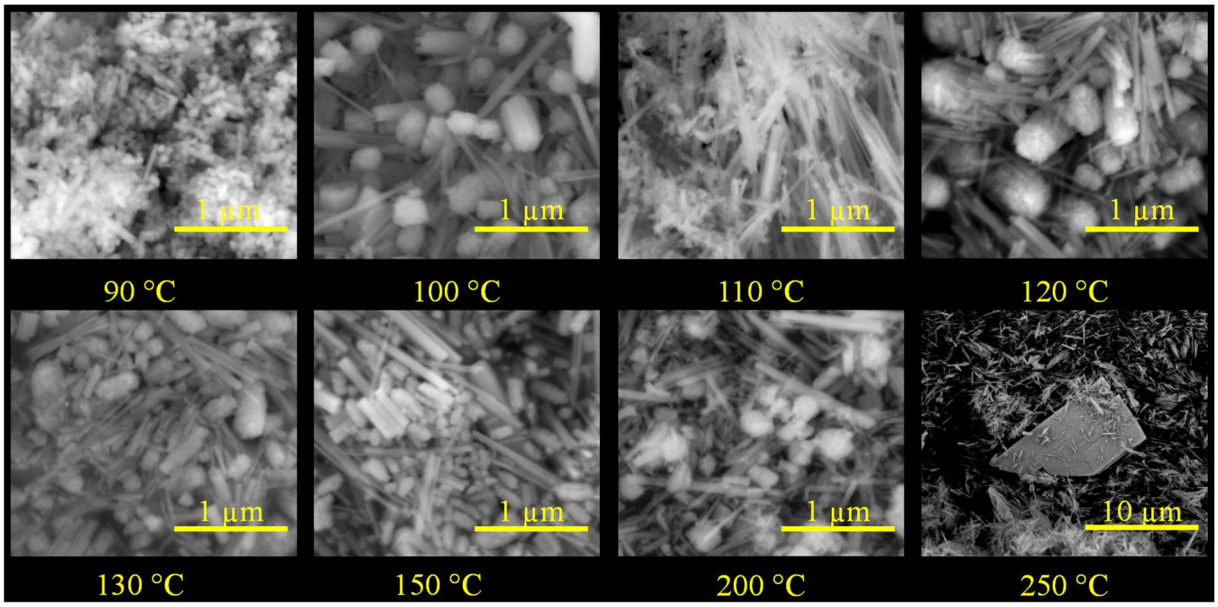

Figure I-6. SEM images of $Pr_{0.8}Ca_{0.1}Th_{0.1}PO_4.nH_2O$ samples prepared after heating for 4 days at various temperatures (90°C ≤ T ≤ 250°C) using an initial Ca:Th mole ratio equal to 10.

Simultaneously, SEM observations revealed that the predominant morphology of the sample was tiny rod-like or needle-like aggregates for the samples prepared between 90°C and 150 °C, which was the characteristic morphology of rhabdophane [78–80]. Finally, the plate-like morphology, shown in the image of the sample prepared at 250 °C, indicated that the predominant phase was no longer rhabdophane. This plate-like morphology is usually characteristic of TPHPH crystals [6,35,91,96], which agrees well with the results obtained from PXRD.

I-3.1.4. Determination of the reaction time

The results reported above fixed the initial Ca:Th stoichiometry and the optimal temperature range required to prepare pure Th-rhabdophanes with the expected composition. However, heating time could also affect the thorium and calcium incorporation in the rhabdophane structure. In order to underline this effect, experiments were undertaken at 110°C during 2, 4 and 11 days. PXRD patterns were collected for the three synthesized powders (**Figure I-7**). All the PXRD patterns showed that rhabdophane was the only crystalline phase formed. Meanwhile, total dissolution tests and X-EDS analyses (**Table I-5**) suggested that all the samples obtained presented the expected stoichiometry. Thus, it seemed that the synthesis time had only a weak influence on the formation of $Pr_{1-2x}Ca_xTh_xPO_4.nH_2O$. However, the comparison of the unit cell parameters obtained from Rietveld refinements (**Figure I-7**) underlined higher unit cell volume after 2 days. Moreover, both samples synthesized for 4 and 11 day exhibited the same value, which suggested that the crystal structure was stable after 4-

days. Consequently, the incorporation of calcium and thorium in the rhabdophane structure required at least 4 days to reach the targeted composition. Regarding to these results, a holding time of 4 days was then fixed for the synthesis of $Ln_{1-2x}Ca_xTh_xPO_4.nH_2O$ (Ln = Pr, Nd) samples during the rest of this study.

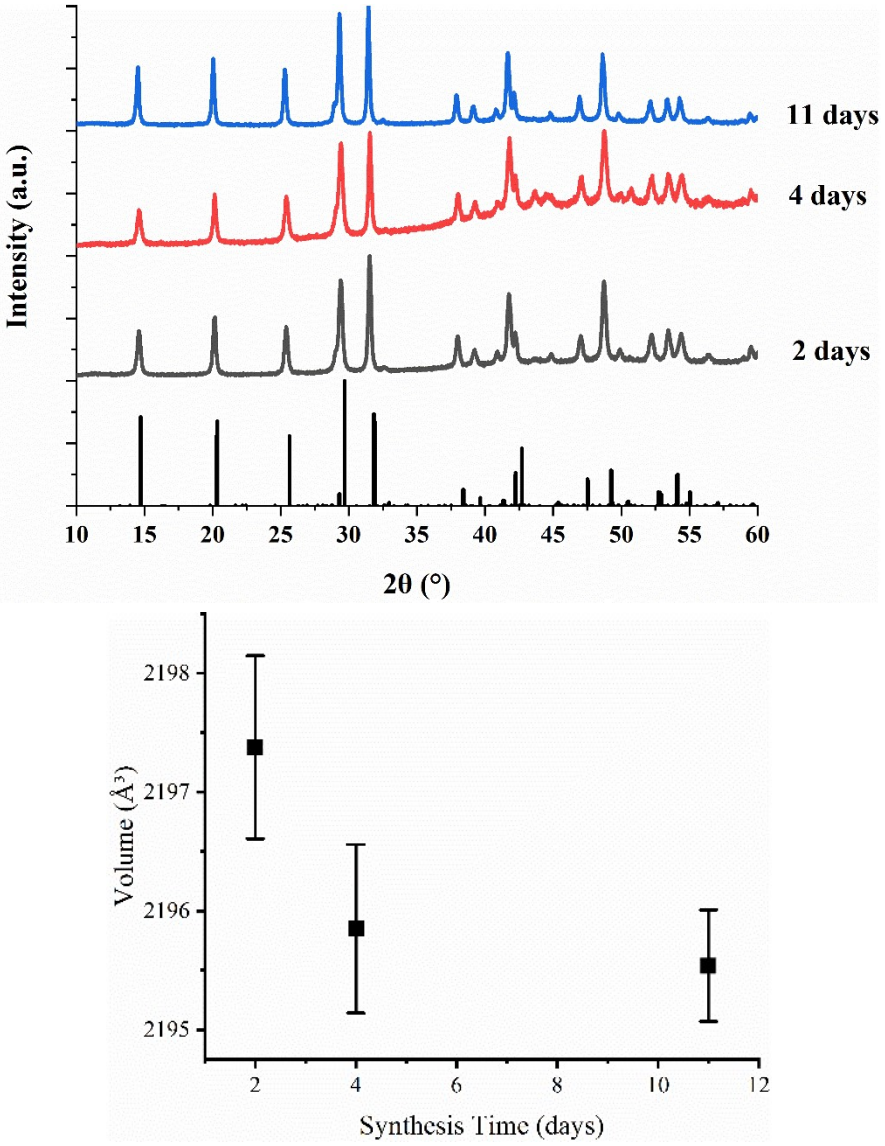

Figure I-7. PXRD patterns of the $Pr_{0.8}Ca_{0.1}Th_{0.1}PO_4.nH_2O$ samples prepared at 110°C for various holding times (2 to 11 days) and starting molar ratio Ca:Th = 10:1. The standard pattern of $SmPO_4.0.677H_2O$ is presenting as black vertical bars [78] (Top). Variation of the unit cell volume of $Pr_{0.8}Ca_{0.10}Th_{0.10}PO_4.nH_2O$ rhabdophane as a function of the holding time. (Bottom)

Table I-5. The effect of reaction time on chemical composition of the $Pr_{0.8}Ca_{0.1}Th_{0.1}PO_4.nH_2O$ compounds synthesis at 110°C initial Ca:Th =10.

Time (Days)	Method	Ca / Ca+Th+Pr	Th / Ca+Th+Pr	Pr / Ca+Th+Pr	P / Ca+Th+Pr
2	ICP-OES	0.10 ± 0.01	0.12 ± 0.01	0.78 ± 0.03	1.01 ± 0.07
	X-EDS	0.11 ± 0.02	0.12 ± 0.01	0.8 ± 0.1	1.1 ± 0.1
4	ICP-OES	0.11 ± 0.01	0.11 ± 0.01	0.79 ± 0.02	1.03 ± 0.04
	X-EDS	0.14 ± 0.06	0.10 ± 0.03	0.8 ± 0.1	1.0 ± 0.2
11	ICP-OES	0.10 ± 0.01	0.11 ± 0.01	0.79 ± 0.04	1.04 ± 0.05
	X-EDS	0.10 ± 0.02	0.10 ± 0.03	0.8 ± 0.1	1.0 ± 0.1

I-3.2. Stability domain of $Pr_{1-2x}Ca_xTh_xPO_4.nH_2O$

Thanks to the multiparametric study described above, the operating conditions required to prepare homogenous and single-phase $Pr_{1-2x}Ca_xTh_x.nH_2O$ rhabdophanes were fixed to T = 110°C and t = 4 days with an initial mole ratio Ca:Th equal to 10:1. The domain of chemical stability of such solid solutions was examined using these initial conditions, by varying the thorium incorporation rate x from 0 to 0.30. The recorded PXRD patterns (**Figure I-8**) suggested the formation of pure rhabdophane for $x \leq 0.15$. Indeed, TPHPH was formed as a secondary phase from $x = 0.20$ to 0.30.

It is worth noting that the intensity of the pic located at $2\theta = 16°$, associated with the presence of TPHPH, became lower with the incorporation of thorium. In fact, the increase of the Th content in the starting materials resulted in a more gelatinous mixture before the hydrothermal syntheses. As the syntheses took place at 110°C for 4 days, this gel was stable according to Clavier [6] and the precipitation of TPHPH was slowing down.

Besides, the chemical compositions of the synthesized rhabdophane were obtained after total dissolution using ICP-OES measurements and X-EDS analyses. From **Table I-6**, it appeared that the insertion of calcium and thorium stopped being quantitative for $x > 0.15$. Consequently, the chemical range of stability of the $Pr_{1-2x}Ca_xTh_xPO_4.nH_2O$ solid solution seemed to be limited to $x \leq 0.15$. In this composition range, the refinement of the PXRD patterns using the Rietveld method led to the data reported in **Table I-7** and in **Figure I-9**.

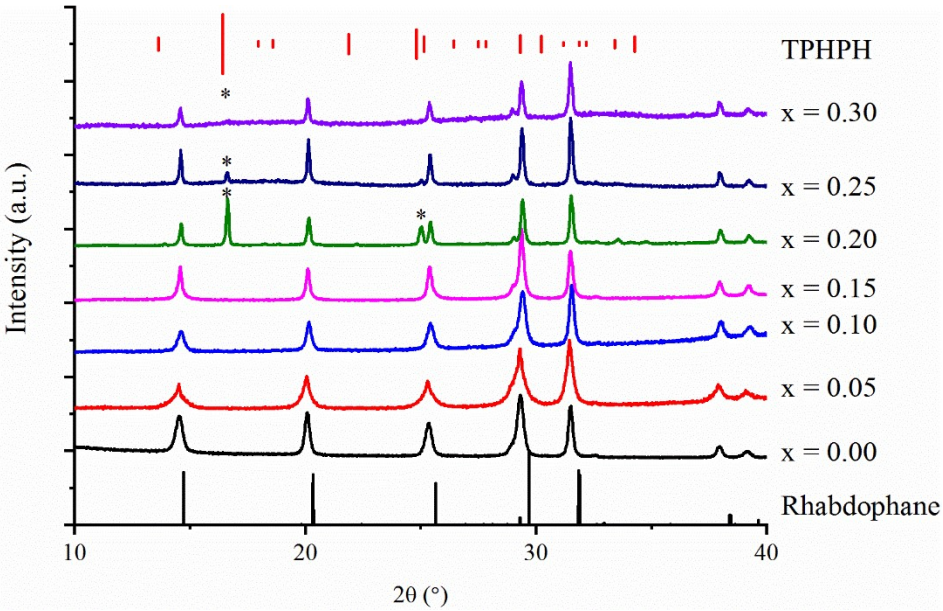

Figure I-8. PXRD patterns of $Pr_{1-2x}Ca_xTh_xPO_4.nH_2O$ samples ($x \leq 0.30$) prepared for 4 days at 110°C for initial molar ratio Ca:Th equal to 10:1. The standard pattern of $SmPO_4.0.677H_2O$ is presenting as black vertical bars [78]. Additional peaks of formed secondary phases TPHPH are pointed by * [91].

Table I-6. Chemical composition of the $Pr_{1-2x}Ca_xTh_xPO_4.nH_2O$ samples ($0.05 \leq x \leq 0.30$) prepared at 110°C for 4 days with initial Ca:Th ratio 10:1.

x	Total dissolution tests				X-EDS analyses			
	$\frac{Ca}{Ca+Th+Pr}$	$\frac{Th}{Ca+Th+Pr}$	$\frac{Pr}{Ca+Th+Pr}$	$\frac{P}{Ca+Th+Pr}$	$\frac{Ca}{Ca+Th+Pr}$	$\frac{Th}{Ca+Th+Pr}$	$\frac{Pr}{Ca+Th+Pr}$	$\frac{P}{Ca+Th+Pr}$
0.05	0.05 ± 0.01	0.06 ± 0.01	0.89 ± 0.05	1.01 ± 0.06	0.06 ± 0.03	0.06 ± 0.02	0.88 ± 0.04	1.0 ± 0.1
0.10	0.11 ± 0.01	0.11 ± 0.01	0.79 ± 0.02	1.03 ± 0.04	0.14 ± 0.06	0.10 ± 0.03	0.77 ± 0.07	1.0 ± 0.2
0.15	0.14 ± 0.01	0.16 ± 0.01	0.70 ± 0.02	1.05 ± 0.03	0.16 ± 0.04	0.14 ± 0.04	0.70 ± 0.05	1.0 ± 0.1
0.20	0.12 ± 0.01	0.25 ± 0.01	0.62 ± 0.02	1.12 ± 0.04				
0.25	0.14 ± 0.01	0.33 ± 0.01	0.53 ± 0.02	1.17 ± 0.03				
0.30	0.17 ± 0.01	0.37 ± 0.02	0.45 ± 0.02	1.20 ± 0.06				

Table I-7. Refined unit cell parameters of $Pr_{1-2x}Ca_xTh_xPO_4.nH_2O$ samples ($x \leq 0.15$) prepared at 110°C for 4 days with Ca:Th = 10.

x	a (Å)	b (Å)	c (Å)	β (°)	Volume (Å^3)	R_p, R_{wp}
0.00	28.4381(23)	7.0238(7)	12.1712(8)	115.30(1)	2197.9(4)	0.036, 0.048
0.05	28.4131(37)	7.0307(23)	12.1678(28)	115.34(2)	2196.8(9)	0.068, 0.093
0.10	28.4260(22)	7.0201(17)	12.1699(23)	115.28(1)	2195.8(7)	0.051, 0.072
0.15	28.4524(17)	7.0215(8)	12.1612(9)	115.39(1)	2194.8(3)	0.097, 0.133

Table I-8. Ionic radius (Å) for Ca^{2+}, Th^{4+}, Pr^{3+}, and Nd^{3+} extracted from the Shannon tables [63].

Ions	r_{CN8}	r_{CN9}	½ r_{CN8} + ½ r_{CN9}
Ca^{2+}	1.120	1.180	1.150
Th^{4+}	1.050	1.090	1.070
Pr^{3+}	1.126	1.179	1.153
Nd^{3+}	1.109	1.163	1.136

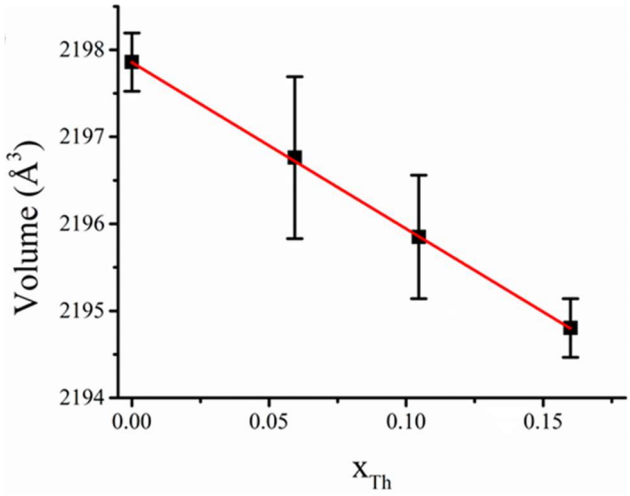

Figure I-9. Variation of the unit cell volume of $Pr_{1-2x}Ca_xTh_xPO_4.nH_2O$ rhabdophane as a function of the thorium incorporation rate.

Consequently, these results confirmed the formation of $Pr_{1-2x}Ca_xTh_xPO_4.nH_2O$ solid solution following the coupled substitution: 2 Pr^{3+} ↔ Th^{4+} + Ca^{2+}. A limit of incorporation of thorium seemed to be reached between 0.15 and 0.20, surely due to a potential ordering between Ca and Th within the structure. It is worth noting that for lanthanum based samples, Rawat. *et al.* mentioned that the anhydrous compound $Ca_{0.125}Th_{0.125}La_{0.75}PO_4$ [88] was the most stable. However, for praseodymium-based compounds, the limit of the thorium incorporation was found up to 14.1 mol. %, which appeared to be sufficient for the specific immobilization of actinide in such materials compared to the usually considered maximum target value, *i.e.* 10 wt.% (x = 0.1) [47].

I-3.3. Monazite-cheralite type solid solution $Pr_{1-2x}Ca_xTh_xPO_4$ (x = 0 – 0.15)

According to literature, monazite-cheralite solid solutions studied in the field of the specific immobilization of tetravalent actinides were more often prepared by dry chemistry routes, based on several successive heating/grinding steps [7,25,64]. Consequently, the use of rhabdophanes as low temperature precursors could become of strong interest, especially when handling tetravalent actinides such as uranium, neptunium and plutonium as it provides an

almost dust-free process. In order to validate the final goal of this study, powdered Th-rhabdophanes were then heated in air at 1100°C for 6 hours. This temperature was selected to ensure the complete conversion of rhabdophane into the final monazite which was known to be irreversible and to avoid the potential decomposition (as the decomposition temperature of $Ca_{0.5}Th_{0.5}PO_4$ is reported to be 1400°C) [25]. The powders issued from this heating step were then analyzed by PXRD (**Figure I-10**). The collected patterns were systematically consistent with that of pure $PrPO_4$ monazite. Moreover, the variation of the refined unit cell volumes was plotted versus the thorium incorporation rate (**Table I-9** and **Figure I-10**). As a comparison, the final data point, which represents the unit cell volume of $Ca_{0.5}Th_{0.5}PO_4$, was selected from the value reported by Raison *et al* [97]. From the data obtained, it is clear that the unit cell volume decreased linearly as a function of the thorium incorporation rate, as the confirmation of the formation of monazite-cheralite solid solution, $Pr_{1-2x}Ca_xTh_xPO_4$. To our knowledge, this corresponds to the first synthesis of monazite-cheralite solid solution by wet chemistry route which paves the way to important improvements, either in the field of homogenization within the samples or for sintering purpose.

Table I-9. Refined unit cell parameters of $Pr_{1-2x}Ca_xTh_xPO_4$ samples ($x \leq 0.15$) obtained after the conversion of rhabdophane analogues at 1100°C under air for 6 hours.

x	a (Å)	b (Å)	c (Å)	B (°)	Volume (Å^3)	R_p, R_{wp}
0.00	6.7494(1)	6.9867(1)	8.1727(1)	126.40(1)	295.89(1)	0.06, 0.09
0.05	6.7619(1)	6.9804(1)	6.4388(1)	103.56(1)	295.45(1)	0.06, 0.09
0.10	6.7542(1)	6.9716(1)	6.4358(1)	103.56(1)	294.59(1)	0.10, 0.13
0.15	6.7494(1)	6.9656(1)	6.4336(1)	103.57(1)	294.02(1)	0.05, 0.08
0.50 [97]	6.7085(8)	6.9160(6)	6.4152(6)	103.71(9)	289.16	

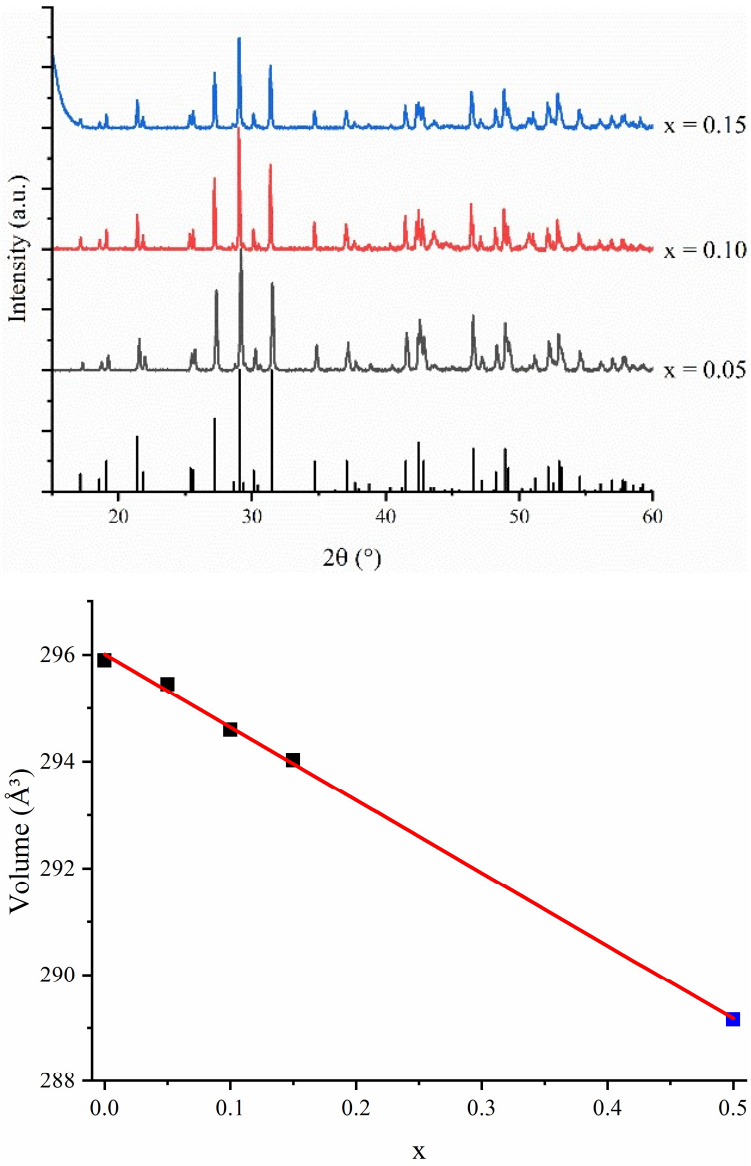

Figure I-10. PXRD pattern of the monazite-cheralite $Pr_{1-2x}Ca_xTh_xPO_4$ solid solutions prepared after firing the corresponding rhabdophane-type precursors at 1100°C for 6 hours (Top). Variation of the unit cell volume of $Pr_{1-2x}Ca_xTh_xPO_4$ monazite-cheralite solid solutions prepared by thermal conversion of the corresponding rhabdophane-type precursors as a function of the thorium incorporation rate: present study (■) and Raison *et al.* (■) [97] (Bottom).

I-3.4. Application of the hydrothermal synthesis protocol on the synthesis of rhabdophane type $Nd_{1-2x}Ca_xTh_xPO_4.nH_2O$

In the previous sections, the synthesis conditions of Th-rhabdophane samples, $Pr_{1-2x}Ca_xTh_xPO_4.nH_2O$ (x = 0 – 0.15), were determined. In order to apply this protocol to other lanthanide elements, several neodymium bearing samples were also prepared: $Nd_{1-2x}Ca_xTh_xPO_4.nH_2O$ with x = 0 – 0.15. Their analysis by PXRD analysis showed that the samples were systematically single-phase and crystallized with the rhabdophane structure (**Figure I-11**).

The chemical composition of the precursor powders was then determined by ICP-OES after total dissolution of the samples in aqua regia (**Table I-10**).

Table I-10. Chemical composition of $Nd_{1-2x}Ca_xTh_xPO_4.nH_2O$ rhabdophane-type samples obtained by ICP-OES analysis after complete dissolution of the powdered samples.

x	$\frac{Nd}{Ca+Th+Nd}$	$\frac{Th}{Ca+Th+Nd}$	$\frac{Ca}{Ca+Th+Nd}$	$\frac{P}{Ca+Th+Nd}$
0.00	1.00 ± 0.01	---	---	1.04 ± 0.01
0.05	0.90 ± 0.01	0.05 ± 0.01	0.05 ± 0.01	1.0 ± 0.1
0.10	0.80 ± 0.03	0.11 ± 0.01	0.10 ± 0.01	1.0 ± 0.1
0.15	0.71 ± 0.03	0.17 ± 0.02	0.11 ± 0.02	1.1 ± 0.2

From these data, the prepared powders exhibited the expected stoichiometry for $x = 0.05$ and 0.1. However, the precipitation of thorium and calcium appeared to be slightly different from the expected values for $x = 0.15$. This problem was already described during the synthesis of $Pr_{1-2x}Ca_xTh_xPO_4.nH_2O$ solid solutions, the precipitation becoming non-stoichiometric for $x \geq 0.20$. Consequently, the coupled substitution might exhibit a slightly lower limit for Nd-based rhabdophane, with the maximum Ca and Th incorporation between $x = 0.10$ and 0.15. Nevertheless, for $x = 0.15$, the charge balance was remained respected. Indeed, the total positive charge, *i.e.* 3 (Nd^{3+}) + 4 (Th^{4+}) + 2 (Ca^{2+}) equaled 3.03 ± 0.21 while the total negative charge, *i.e.* 3 (PO_4^{3-}), reached 3.21 ± 0.51. Both values were thus not significantly different considering the associated uncertainties. One explanation of the slight difference between the Th and Ca contents could result from the formation of vacancies in the structure [26]. Additionally, it is worth noting that during the synthesis of $Pr_{1-2x}Ca_xTh_xPO_4.nH_2O$ samples, XRD analysis revealed the formation of crystallized TPHPH [35,91] as a secondary phase for $x \geq 0.20$. Such an additional thorium-enriched phase was not detected by PXRD for the Nd-based samples, which also argued in favor of a non-stoichiometric substitution [35,91].

Finally, the precursors were converted into the final monazite-cheralite solid solutions by heating for 6 hours at 1100 °C in air. The PXRD patterns of the resulting samples are gathered in **Figure I-11**. For $x \leq 0.1$, the obtained products were single-phase monazite-cheralite whereas the characteristic diffraction lines of α-$Th_2P_2O_7$ [98] were observed for $x = 0.15$. Once again, the formation of such a secondary phase was assigned to a non-stoichiometric substitution in the rhabdophane structure. As reported by R. Podor [26], the monazite structure has little tolerance to cations vacancies. Therefore, the excess of thorium was no longer stable within the monazite-cheralite solid solution and thus led to segregation by forming α-$Th_2P_2O_7$.

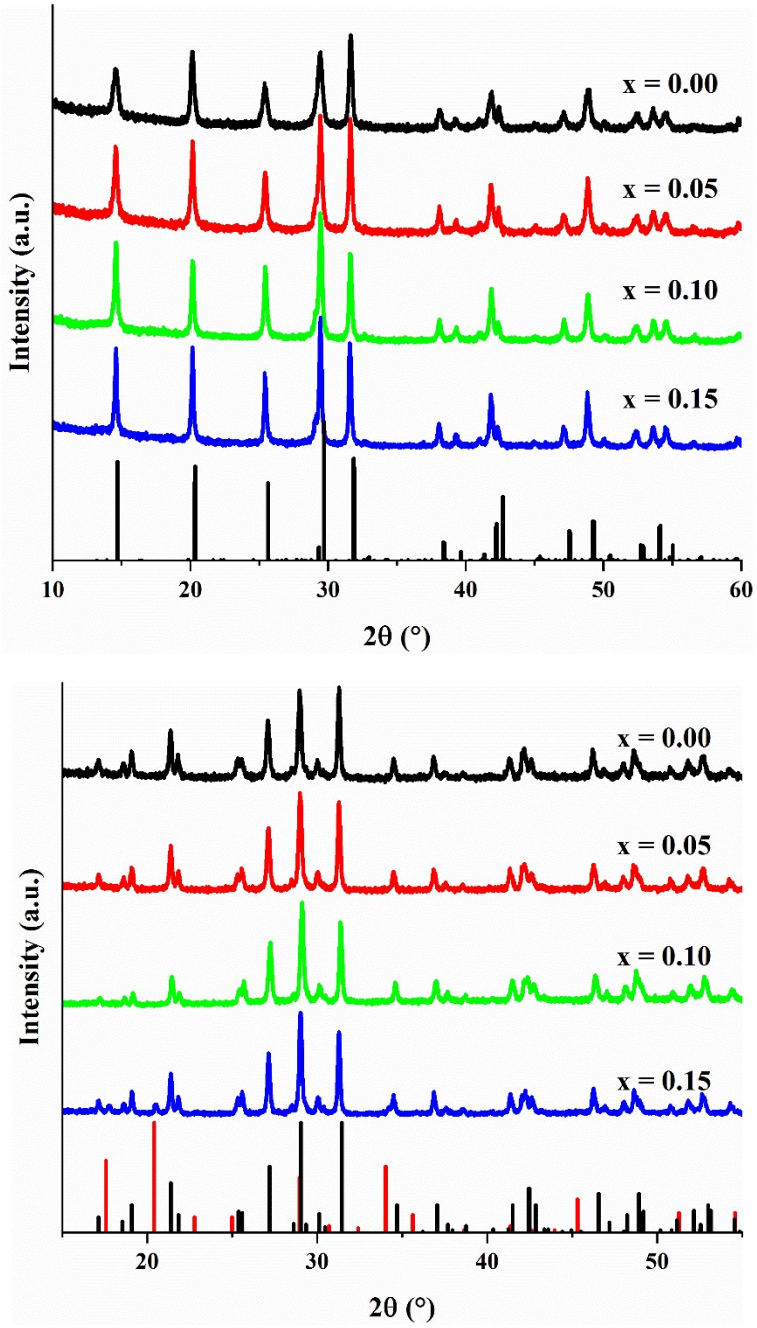

Figure I-11. PXRD patterns obtained for rhabdophane type precursors $Nd_{1-2x}Ca_xTh_xPO_4.nH_2O$ samples (with $0 \leq x \leq 0.15$); the black vertical bars corresponding to the hydrated rhabdophane structure [78] (Top); associated monazite-cheralite type solid solution $Nd_{1-2x}Ca_xTh_xPO_4$; the black and red vertical bars corresponding to the monazite $NdPO_4$ [82] and α-$Th_2P_2O_7$ [98] patterns, respectively (Bottom).

In conclusion, the synthesis protocol optimized for praseodymium was applied with success for the preparation of Nd-rhabdophane $Nd_{1-2x}Ca_xTh_xPO_4.nH_2O$ (x = 0 – 0.1). Their thermal conversion led to the formation of monazite-cheralite solid solution $Nd_{1-2x}Ca_xTh_xPO_4$.

Summary

Thorium incorporation was successfully achieved in the rhabdophane structure as $Ln_{1-2x}Ca_xTh_xPO_4.nH_2O$ (Ln = Pr, Nd) solid solutions. It resulted in the preparation of low-temperature precursors of the monazite-cheralite solid solutions $Ln_{1-2x}Ca_xTh_xPO_4$ (Ln = Pr, Nd). A multiparametric study was thus undertaken to specify the wet chemistry conditions (starting stoichiometry, temperature, heating time) leading to single-phase $Ln_{1-2x}Ca_xTh_xPO_4.nH_2O$ powdered samples. The excess of calcium appeared to be a prevailing factor with a required initial molar ratio Ca:Th of 10:1. Similarly, the recommended heating time should exceed 4 days for an optimal temperature of synthesis of 110 °C. Under these conditions, the stability domains of $Pr_{1-2x}Ca_xTh_xPO_4.nH_2O$ and $Nd_{1-2x}Ca_xTh_xPO_4.nH_2O$ ranged from x = 0 to 0.15 and from x = 0 to 0.10, respectively. Above these x values, the formation of calcium-depleted gel resulted in the formation of TPHPH as an additional secondary phase in the final mixtures. This new wet chemistry route was taken as an advantage for the elaboration of single phase thorium bearing monazite-cheralite solid solutions. It avoided the use of long and repetitive grinding/heating steps and allowed significant improvements, both in the field of cationic homogenization within the sample and for sintering process. Finally, the thermal conversion of such as-synthesized rhabdophane precursors will be investigated in the following chapter.

Résumé

L'incorporation de thorium au sein de la structure de la rhabdophane a été développée avec succès par synthèse hydrothermale à basse température dans le cas des solutions solides $Ln_{1-2x}Ca_xTh_xPO_4,nH_2O$ (Ln = Pr, Nd). Le traitement thermique de ces précurseurs a été mené, conduisant à la formation de solutions solides monazite-chéralite, $Ln_{1-2x}Ca_xTh_xPO_4$ (Ln = Pr, Nd). Une étude multiparamétrique a été menée afin de déterminer les conditions optimales de synthèse des précurseurs. L'excès molaire de calcium apparaît comme l'un des facteurs les plus importants puisqu'il assure la stœchiométrie attendue au sein des précipités. Ainsi, le rapport molaire initial Ca : Th doit atteindre 10 : 1. Simultanément, les conditions optimales associées au traitement hydrothermal ont été fixées à 100°C et 4 jours, respectivement pour la température et la durée du traitement thermique. En appliquant ce protocole, le domaine de stabilité des rhabdophanes $Pr_{1-2x}Ca_xTh_xPO_4,nH_2O$ et $Nd_{1-2x}Ca_xTh_xPO_4,nH_2O$ correspond respectivement à $x \leq 0,15$ et $x \leq 0,10$. Dans le cas d'une incorporation de thorium plus importante, le gel formé pendant la synthèse limite l'incorporation de calcium au sein des précipités et conduit, de ce fait, à la formation de phases secondaires enrichies en thorium, telles que le phosphate hydrogeno-phosphate de thorium hydratée (PHPTH). Par calcination des précurseurs obtenus, cette nouvelle méthode de synthèse par voie humide conduit à la préparation de solutions solides monophasés de monazite-chéralite. Elle évite ainsi la multiplication de cycles de broyage-calcination long et répétitifs. Elle contribue également à une amélioration significative de l'homogénéité cationique au sein des échantillons pulvérulents puis de leur aptitude au frittage. Les différentes étapes conduisant des précurseurs initiaux aux solutions solides ultimes sont étudiées dans le second chapitre de ce manuscrit.

$2\ Ln^{3+} \leftrightarrow Ca^{2+} + Th^{4+}$ | Hydrothermal Synthesis | $Ln_{1-2x}Ca_xTh_xPO_4.nH_2O$

Stoichiometry	Temperature?	Reaction time?
Lack of calcium	**Crystallization vs Secondary phases**	**Crystallization vs Energy & Time**
Calcium Excess **Ca:Th =10:1**	Suggested Temperature **110 °C**	Suggested Time **4 days**

Maximum thorium incorporation rate: **15 mol %** for **Pr**, **10 mol %** for **Nd**

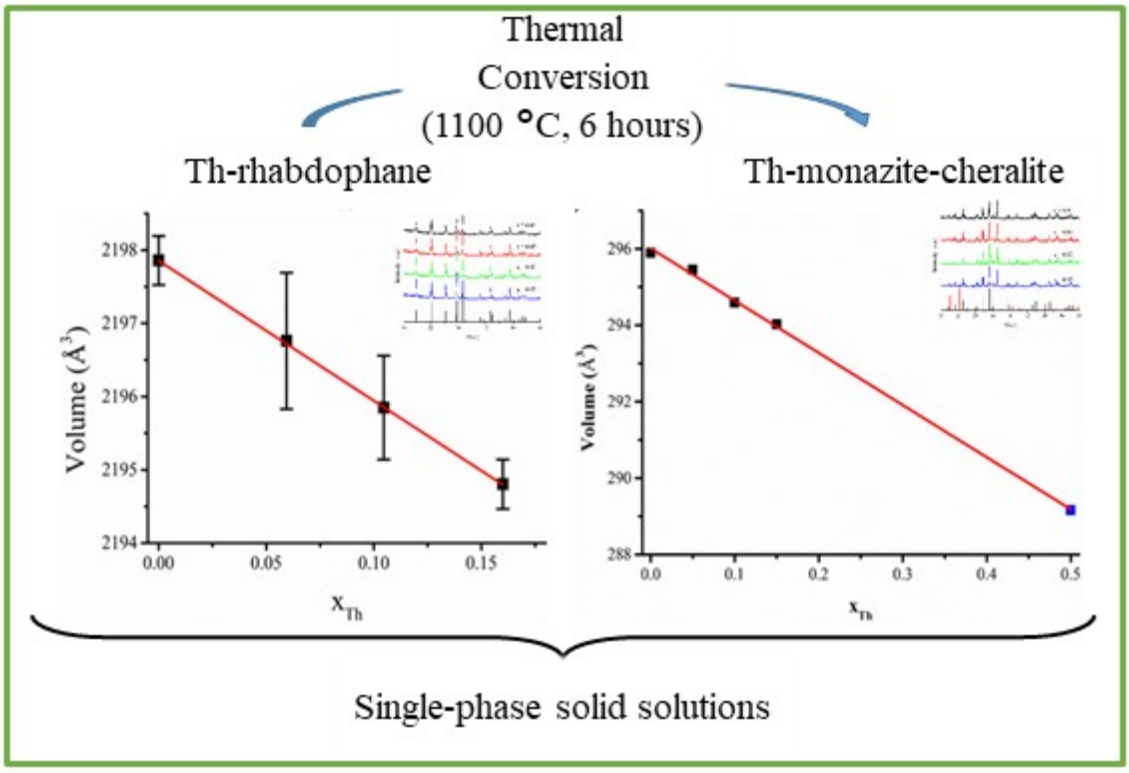

References

(1) Bataille, C. Loi N° 91-1381 Du 30 Décembre 1991 Relative Aux Recherches Sur La Gestion Des Déchets Radioactifs; 1991; Vol. 91–1381.

(2) Dacheux, N.; Clavier, N.; Robisson, A.-C.; Terra, O.; Audubert, F.; Lartigue, J.-É.; Guy, C. Immobilisation of Actinides in Phosphate Matrices. Comptes Rendus Chimie **2004**, 7 (12), 1141–1152. https://doi.org/10.1016/j.crci.2004.02.019.

(3) Terra, O.; Dacheux, N.; Audubert, F.; Podor, R. Immobilization of Tetravalent Actinides in Phosphate Ceramics. Journal of Nuclear Materials **2006**, 352 (1), 224–232. https://doi.org/10.1016/j.jnucmat.2006.02.058.

(4) Billard, I. Déchets Nucléaires : État Des Lieux. In Le cycle électronucléaire : de la fission aux nouvelles filières; École Internationale Joliot Curie de Physique Nucléaire: Maubuisson, France, 2006; pp 223–248.

(5) Dacheux, N.; Chassigneux, B.; Brandel, V.; Le Coustumer, P.; Genet, M.; Cizeron, G. Reactive Sintering of the Thorium Phosphate-Diphosphate. Study of Physical, Thermal, and Thermomechanical Properties and Chemical Durability during Leaching Tests. Chem. Mater. **2002**, 14 (7), 2953–2961. https://doi.org/10.1021/cm011277g.

(6) Clavier, N. Elaboration de Phosphate-Diphosphate de Thorium et d'uranium (β-PDTU) et de Matériaux Composites β-PDTU/Monazite à Partir de Précurseurs Cristallisés : Études Du Frittage et de La Durabilité Chimique. PhD Thesis, Université de Paris-Sud, 2004.

(7) Montel, J.-M.; Glorieux, B.; Seydoux-Guillaume, A.-M.; Wirth, R. Synthesis and Sintering of a Monazite–Brabantite Solid Solution Ceramic for Nuclear Waste Storage. Journal of Physics and Chemistry of Solids **2006**, 67 (12), 2489–2500. https://doi.org/10.1016/j.jpcs.2006.07.004.

(8) Oelkers, E. H.; Poitrasson, F. An Experimental Study of the Dissolution Stoichiometry and Rates of a Natural Monazite as a Function of Temperature from 50 to 230 °C and PH from 1.5 to 10. Chemical Geology **2002**, 191 (1), 73–87. https://doi.org/10.1016/S0009-2541(02)00149-3.

(9) Poitrasson, F.; Oelkers, E.; Schott, J.; Montel, J.-M. Experimental Determination of Synthetic NdPO4 Monazite End-Member Solubility in Water from 21°C to 300°C: Implications for Rare Earth Element Mobility in Crustal Fluids. Geochimica et Cosmochimica Acta **2004**, 68 (10), 2207–2221. https://doi.org/10.1016/j.gca.2003.12.010.

(10) Cetiner, Z. S.; Wood, S. A.; Gammons, C. H. The Aqueous Geochemistry of the Rare Earth Elements. Part XIV. The Solubility of Rare Earth Element Phosphates from 23 to 150 °C. Chemical Geology **2005**, 217 (1), 147–169. https://doi.org/10.1016/j.chemgeo.2005.01.001.

(11) Clavier, N.; Dacheux, N.; Podor, R. Synthesis, Characterization, Sintering, and Leaching of β-TUPD/Monazite Radwaste Matrices. Inorg. Chem. **2006**, 45 (1), 220–229. https://doi.org/10.1021/ic051607p.

(12) Clavier, N.; du Fou de Kerdaniel, E.; Dacheux, N.; Le Coustumer, P.; Drot, R.; Ravaux, J.; Simoni, E. Behavior of Thorium–Uranium (IV) Phosphate–Diphosphate Sintered Samples during Leaching Tests. Part II. Saturation Processes. Journal of Nuclear Materials **2006**, 349 (3), 304–316. https://doi.org/10.1016/j.jnucmat.2005.11.010.

(13) Dacheux, N.; Clavier, N.; Ritt, J. Behavior of Thorium–Uranium (IV) Phosphate–Diphosphate Sintered Samples during Leaching Tests. Part I – Kinetic Study. Journal of Nuclear Materials **2006**, 349 (3), 291–303. https://doi.org/10.1016/j.jnucmat.2005.11.009.

(14) Dacheux, N.; Du Fou de Kerdaniel, E.; Clavier, N.; Podor, R.; Aupiais, J.; Szenknect, S. Kinetics of Dissolution of Thorium and Uranium Doped Britholite Ceramics. Journal of Nuclear Materials **2010**, 404 (1), 33–43. https://doi.org/10.1016/j.jnucmat.2010.06.023.

(15) Du Fou de Kerdaniel, E.; Clavier, N.; Dacheux, N.; Terra, O.; Podor, R. Actinide Solubility-Controlling Phases during the Dissolution of Phosphate Ceramics. Journal of Nuclear Materials **2007**, 362 (2), 451–458. https://doi.org/10.1016/j.jnucmat.2007.01.132.
(16) Veilly, E.; du Fou de Kerdaniel, E.; Roques, J.; Dacheux, N.; Clavier, N. Comparative Behavior of Britholites and Monazite/Brabantite Solid Solutions during Leaching Tests: A Combined Experimental and DFT Approach. Inorg. Chem. **2008**, 47 (23), 10971–10979. https://doi.org/10.1021/ic801169d.
(17) Ewing, R. C.; Haaker, R. F. The Metamict State: Implications for Radiation Damage in Crystalline Waste Forms. Nuclear and Chemical Waste Management **1980**, 1 (1), 51–57. https://doi.org/10.1016/0191-815X(80)90028-5.
(18) Karioris, F. G.; Gowda, K. A.; Cartz, L. Heavy Ion Bombardment of Monoclinic $ThSiO_4$, ThO_2 and Monazite. Radiation Effects **1981**, 58 (1–2), 1–3. https://doi.org/10.1080/01422448108226520.
(19) Meldrum, A.; Boatner, L. A.; Weber, W. J.; Ewing, R. C. Radiation Damage in Zircon and Monazite. Geochimica et Cosmochimica Acta **1998**, 62 (14), 2509–2520. https://doi.org/10.1016/S0016-7037(98)00174-4.
(20) Burakov, B. E.; Yagovkina, M. A.; Garbuzov, V. M.; Kitsay, A. A.; Zirlin, V. A. Self-Irradiation of Monazite Ceramics: Contrasting Behavior of $PuPO_4$ and $(La,Pu)PO_4$ Doped with Pu-238. MRS Proceedings **2004**, 824, CC4.1. https://doi.org/10.1557/PROC-824-CC4.1.
(21) Seydoux-Guillaume, A.-M.; Deschanels, X.; Baumier, C.; Neumeier, S.; Weber, W. J.; Peuget, S. Why Natural Monazite Never Becomes Amorphous: Experimental Evidence for Alpha Self-Healing. American Mineralogist **2018**, 103 (5), 824–827. https://doi.org/10.2138/am-2018-6447.
(22) Montel, J.-M. Minerals and Design of New Waste Forms for Conditioning Nuclear Waste. Comptes Rendus Géoscience **2010**, 1856 (2), 83–259. http://dx.doi.org/10.1016/j.crte.2010.11.006.
(23) Boyer, L.; Piriou, B.; Carpena, J.; Lacout, J. L. Study of Sites Occupation and Chemical Environment of Eu^{3+} in Phosphate-Silicates Oxyapatites by Luminescence. Journal of Alloys and Compounds **2000**, 311 (2), 143–152. https://doi.org/10.1016/S0925-8388(00)01085-9.
(24) Terra, O. Incorporation d'actinides Tétravalents Dans Trois Matrices Phosphatées : Britholite, Monazite/Brabantite et Phosphate-Diphosphate de Thorium (β-PDT). PhD Thesis, Université de Paris XI Orsay, 2005.
(25) Bregiroux, D.; Terra, O.; Audubert, F.; Dacheux, N.; Serin, V.; Podor, R.; Bernache-Assollant, D. Solid-State Synthesis of Monazite-Type Compounds Containing Tetravalent Elements. Inorg. Chem. **2007**, 46 (24), 10372–10382. https://doi.org/10.1021/ic7012123.
(26) Podor, R. Synthèse et Caractérisation Des Monazites Uranifères et Thorifères. PhD Thesis, Université de Lorraine, 1994.
(27) Rose, D. Brabantite, $CaTh(PO_4)_2$, a New Mineral of the Monazite Group. Neues Jahresbuch Mineralogische Monatshefte **1980**, 6, 247–257.
(28) Davis, D. D.; Vance, E. R.; McCarthy, G. J. Crystal Chemistry and Phase Relations in the Synthetic Minerals of Ceramic Waste Forms II Studies of Uranium-Containing Monazites; Plenum Press: United States, 1981.
(29) Tabuteau, A.; Pagès, M.; Livet, J.; Musikas, C. Monazite-like Phases Containing Transuranium Elements (Neptunium and Plutonium). Journal of Materials Science Letters **1988**, 7 (12), 1315–1317. https://doi.org/10.1007/BF00719969.
(30) Raison, P. E.; Jardin, R.; Bouëxière, D.; Konings, R. J. M.; Geisler, T.; Pavel, C. C.; Rebizant, J.; Popa, K. Structural Investigation of the Synthetic $CaAn(PO_4)_2$ (An = Th and

Np) Cheralite-like Phosphates. Physics and Chemistry of Minerals **2008**, 35 (10), 603–609. https://doi.org/10.1007/s00269-008-0252-4.
(31) Pepin, J. G.; Vance, E. R.; McCarthy, G. J. The Crystal Chemistry of Cerium in the Monazite Structure-Type Phase of Tailored-Ceramic Nuclear Waste Forms. Materials Research Bulletin **1981**, 16 (6), 627–633. https://doi.org/10.1016/0025-5408(81)90261-0.
(32) Kitaev, D. B.; Volkov, Yu. F.; Orlova, A. I. Orthophosphates of Tetravalent Ce, Th, U, Np, and Pu with the Monazite Structure. Radiochemistry **2004**, 46 (3), 211–217. https://doi.org/10.1023/B:RACH.0000031674.74780.a8.
(33) Podor, R.; Cuney, M.; Nguyen, T. C. Experimental Study of the Solid Solution between Monazite-(La) and $(Ca_{0.5}U_{0.5})PO_4$ at 780 °C and 200 MPa. American Mineralogist **1995**, 80 (11–12), 1261–1268. https://doi.org/10.2138/am-1995-11-1215.
(34) Terra, O.; Dacheux, N.; Clavier, N.; Podor, R.; Audubert, F. Preparation of Optimized Uranium and Thorium Bearing Brabantite or Monazite/Brabantite Solid Solutions. Journal of the American Ceramic Society **2008**, 91 (11), 3673–3682. https://doi.org/10.1111/j.1551-2916.2008.02678.x.
(35) Dacheux, N.; Clavier, N.; Wallez, G.; Brandel, V.; Emery, J.; Quarton, M.; Genet, M. Characterization of the Thorium Phosphate-Hydrogenphosphate Hydrate (TPHPH) and Study of Its Transformation into the Thorium Phosphate-Diphosphate (β-TPD). Materials Research Bulletin **2005**, 40 (12), 2225–2242. https://doi.org/10.1016/j.materresbull.2005.06.011.
(36) Guy, C.; Audubert, F.; Lartigue, J.-E.; Latrille, C.; Advocat, T.; Fillet, C. New Conditionings for Separated Long-Lived Radionuclides. Comptes Rendus Physique **2002**, 3 (7), 827–837. https://doi.org/10.1016/S1631-0705(02)01377-4.
(37) Förster, H.-J. The Chemical Composition of REE-Y-Th-U-Rich Accessory Minerals in Peraluminous Granites of the Erzgebirge-Fichtelgebirge Region, Germany; Part I, The Monazite-(Ce)-Brabantite Solid Solution Series. American Mineralogist **1998**, 83 (3–4), 259–272. https://doi.org/10.2138/am-1998-3-409.
(38) Cuney, M.; Mathieu, R. Extreme Light Rare Earth Element Mobilization by Diagenetic Fluids in the Geological Environment of the Oklo Natural Reactor Zones, Franceville Basin, Gabon. Geology **2000**, 28 (8), 743–746. https://doi.org/10.1130/0091-7613(2000)28<743:ELREEM>2.0.CO;2.
(39) Boatner, L. A. Synthesis, Structure, and Properties of Monazite, Pretulite, and Xenotime. Reviews in Mineralogy and Geochemistry **2002**, 48 (1), 87–121. https://doi.org/10.2138/rmg.2002.48.4.
(40) Slodowska-Curie, M. Rayons Émis Par Les Composés de l'uranium et Du Thorium. Comptes-rendus de l'Académie des Sciences **1898**, 126, 1101–1103.
(41) Overstreet, W. C. The Geologic Occurrence of Monazite; Geological Survey professional paper; U.S. Government Printing Office, 1967.
(42) Gramaccioli, C. M.; Segalstad, T. V. A Uranium- and Thorium-Rich Monazite from a South-Alpine Pegmatite at Piona, Italy. American Mineralogist **1978**, 63 (7–8), 757–761.
(43) Lumpkin, G. R. Rare-Element Mineralogy and Internal Evolution of the Rutherford #2 Pegmatite, Amelia County, Virginia; a Classic Locality Revisited. The Canadian Mineralogist **1998**, 36 (2), 339–353.
(44) Förster, H.-J.; Harlov, D. E. Monazite-(Ce)-Huttonite Solid Solutions in Granulite-Facies Metabasites from the Ivrea-Verbano Zone, Italy. Mineralogical Magazine **1999**, 63 (4), 587–594. https://doi.org/10.1180/minmag.1999.063.4.11.
(45) Montel; Kornprobst; Vielzeuf. Preservation of Old U–Th–Pb Ages in Shielded Monazite: Example from the Beni Bousera Hercynian Kinzigites (Morocco). Journal of Metamorphic Geology **2000**, 18 (3), 335-342. https://doi.org/10.1046/j.1525-1314.2000.00261.x.

(46) Montel, J.-M.; Razafimahatratra, D.; Ralison, B.; De Parseval, P.; Thibault, M.; Randranja, R. Monazite from Mountain to Ocean: A Case Study from Trolognaro (Fort-Dauphin), Madagascar. European Journal of Mineralogy **2011**, 23 (5), 745–757. https://doi.org/10.1127/0935-1221/2011/0023-2149.
(47) Dacheux, N.; Clavier, N.; Podor, R. Versatile Monazite: Resolving Geological Records and Solving Challenges in Materials Science: Monazite as a Promising Long-Term Radioactive Waste Matrix: Benefits of High-Structural Flexibility and Chemical Durability†. American Mineralogist **2013**, 98 (5–6), 833–847. https://doi.org/10.2138/am.2013.4307.
(48) Clavier, N.; Podor, R.; Dacheux, N. Crystal Chemistry of the Monazite Structure. Journal of the European Ceramic Society **2011**, 31 (6), 941–976. https://doi.org/10.1016/j.jeurceramsoc.2010.12.019.
(49) Boatner, L. A.; Beall, G. W.; Abraham, M. M.; Finch, C. B.; Huray, P. G.; Rappaz, M. Monazite and Other Lanthanide Orthophosphates as Alternate Actinide Waste Forms. In Scientific Basis for Nuclear Waste Management; Northrup, C. J. M., Ed.; Springer US: Boston, MA, 1980; pp 289–296. https://doi.org/10.1007/978-1-4684-3839-0_35.
(50) Runde, W. Geochemical Interactions of Actinides in the Environment. In Geochemistry of Soil Radionuclides; John Wiley & Sons, Ltd, 2015; pp 21–44. https://doi.org/10.2136/sssaspecpub59.c2.
(51) Bjorklund, C. W. The Preparation of PuP_2O_7 and $PuPO_4$. J. Am. Chem. Soc. **1957**, 79 (24), 6347–6350. https://doi.org/10.1021/ja01581a001.
(52) Keller, C.; Walter, K. H. Darstellung, Gitterkonstanten Und Chemische Eigenschaften Einiger Ternärer Oxide Des Plutoniums, Americiums Und Curiums Vom Typ $Me^{III}_XVO_4$. Journal of Inorganic and Nuclear Chemistry **1965**, 27 (6), 1253–1260. https://doi.org/10.1016/0022-1902(65)80087-2.
(53) Popa, K.; Vigier, J.-F.; Martel, L.; Manara, D.; Colle, J.-Y.; Blanco, O. D.; Wiss, T.; Freis, D.; Konings, R. J. M. Synthesis, Characterization, and Stability of Americium Phosphate, $AmPO_4$. Inorg. Chem. **2020**. https://doi.org/10.1021/acs.inorgchem.0c00697.
(54) Popa, K.; Colineau, E.; Wastin, F.; Konings, R. J. M. The Low-Temperature Heat Capacity of $(Pu_{0.1}La_{0.9})PO_4$. Solid State Communications **2007**, 144 (1), 74–77. https://doi.org/10.1016/j.ssc.2007.07.011.
(55) Abraham, M. M.; Boatner, L. A.; Quinby, T. C.; Thomas, D. K.; Rappaz, M. Preparation and Compaction of Synthetic Monazite Powders. Radioactive Waste Management **1980**, No. 1, 181–191.
(56) Anderson, E. B.; Burakov, B. E. Ceramics for the Immobilization of Plutonium and Americium: Current Progress of R&D of the V.G. Khlopin Radium Institute. MRS Proceedings **2003**, 807, 207. https://doi.org/10.1557/PROC-807-207.
(57) Kitsay, A. A.; Garbuzov, V. M.; Burakov, B. E. Synthesis of Actinide-Doped Ceramics: From Laboratory Experiments to Industrial Scale Technology. MRS Proceedings **2003**, 807, 237. https://doi.org/10.1557/PROC-807-237.
(58) Zhang, Y.; Vance, E. R. Plutonium in Monazite and Brabantite: Diffuse Reflectance Spectroscopy Study. Journal of Nuclear Materials **2008**, 375 (3), 311–314. https://doi.org/10.1016/j.jnucmat.2007.11.011.
(59) Hikichi, Y.; Hukuo, K.; Shiokawa, J. Solid Solutions in the Systems Monazite($CePO_4$)-Huttonite($ThSiO_4$), and Monazite-$Ca_{0.5}Th_{0.5}PO_4$. NIPPON KAGAKU KAISHI **1978**, 1978 (12), 1635–1640. https://doi.org/10.1246/nikkashi.1978.1635.
(60) Hutton, C. O. Occurrence, Optical Properties and Chemical Composition of Huttonite. American Mineralogist **1951**, 36 (1–2), 66–69.

(61) Bowie, S. H. U.; Horne, J. E. T. Cheralite, a New Mineral of the Monazite Group. Mineralogical Magazine and Journal of the Mineralogical Society **1953**, 30 (221), 93–99. https://doi.org/10.1180/minmag.1953.030.221.02.
(62) Linthout, K. Tripartite Division of the System $2REEPO_4$ – $CaTh(PO_4)_2$ – $2ThSiO_4$, Discreditation of Brabantite, and Recognition of Cheralite as the Name for Members Dominated by $CaTh(PO_4)_2$. The Canadian Mineralogist **2007**, 45 (3), 503–508. https://doi.org/10.2113/gscanmin.45.3.503.
(63) Shannon, R. D. Revised Effective Ionic Radii and Systematic Studies of Interatomic Distances in Halides and Chalcogenides. Acta Crystallographica Section A **1976**, 32 (5), 751–767. https://doi.org/10.1107/S0567739476001551.
(64) Glorieux, B.; Montel, J. M.; Matecki, M. Synthesis and Sintering of a Monazite–Brabantite Solid Solution Ceramics Using Metaphosphate. Journal of the European Ceramic Society **2009**, 29 (9), 1679–1686. https://doi.org/10.1016/j.jeurceramsoc.2008.10.004.
(65) Bregiroux, D.; Belin, R.; Valenza, P.; Audubert, F.; Bernache-Assollant, D. Plutonium and Americium Monazite Materials: Solid State Synthesis and X-Ray Diffraction Study. Journal of Nuclear Materials **2007**, 366 (1), 52–57. https://doi.org/10.1016/j.jnucmat.2006.12.042.
(66) Muto, T.; Meyrowitz, R.; Pommer, A. M.; Murano, T. Ningyoite, a New Uranous Phosphate Mineral from Japan*. American Mineralogist **1959**, 44 (5–6), 633–650.
(67) Schatzmann, M. T.; Mecartney, M. L.; Morgan, P. E. D. Synthesis of Monoclinic Monazite, $LaPO_4$, by Direct Precipitation. J. Mater. Chem. **2009**, 19 (32), 5720–5722. https://doi.org/10.1039/B906456G.
(68) Zaki, M.; Aamili, A.; Sadel, A.; Zahir, M.; El-Ghozzi, M.; Avignant, D. Synthesis, Crystal Chemistry and Physical Study of a New Series of Rare Earth Phosphates with Specific Open Structure. Annales de Chimie Science des Matériaux **2001**, 26 (6), 35–43.
(69) Lucas, S.; Champion, E.; Bregiroux, D.; Bernache-Assollant, D.; Audubert, F. Rare Earth Phosphate Powders $RePO_4{\cdot}nH_2O$ (Re=La, Ce or Y)—Part I. Synthesis and Characterization. Journal of Solid State Chemistry **2004**, 177 (4), 1302–1311. https://doi.org/10.1016/j.jssc.2003.11.003.
(70) Skogareva, L. S.; Shekunova, T. O.; Baranchikov, A. E.; Yapryntsev, A. D.; Sadovnikov, A. A.; Ryumin, M. A.; Minaeva, N. A.; Ivanov, V. K. Synthesis of Cerium Orthophosphates with Monazite and Rhabdophane Structure from Phosphoric Acid Solutions in the Presence of Hydrogen Peroxide. Russian Journal of Inorganic Chemistry **2016**, 61 (10), 1219–1224. https://doi.org/10.1134/S0036023616100181.
(71) Arinicheva, Y.; Clavier, N.; Neumeier, S.; Podor, R.; Bukaemskiy, A.; Klinkenberg, M.; Roth, G.; Dacheux, N.; Bosbach, D. Effect of Powder Morphology on Sintering Kinetics, Microstructure and Mechanical Properties of Monazite Ceramics. Journal of the European Ceramic Society **2018**, 38 (1), 227–234. https://doi.org/10.1016/j.jeurceramsoc.2017.08.008.
(72) Neumeier, S.; Arinicheva, Y.; Clavier, N.; Podor, R.; Bukaemskiy, A.; Modolo, G.; Dacheux, N.; Bosbach, D. The Effect of the Synthesis Route of Monazite Precursors on the Microstructure of Sintered Pellets. Progress in Nuclear Energy **2016**, 92, 298–305. https://doi.org/10.1016/j.pnucene.2016.07.011.
(73) Colomer, M. T.; Mosa, J. Thermal Evolution, Second Phases, and Sintering Behavior of $LaPO_4{\cdot}nH_2O$ Nanorods Prepared by Two Different Chemical Synthesis Routes. Ceramics International **2015**, 41 (6), 8080–8092. https://doi.org/10.1016/j.ceramint.2015.03.006.
(74) Sankar, S.; Warrier, K. G. Aqueous Sol–Gel Synthesis of Lanthanum Phosphate Nano Rods Starting from Lanthanum Chloride Precursor. Journal of Sol-Gel Science and Technology **2011**, 58 (1), 195–200. https://doi.org/10.1007/s10971-010-2377-4.

(75) Rajesh, K.; Shajesh, P.; Seidel, O.; Mukundan, P.; Warrier, K. G. K. A Facile Sol–Gel Strategy for the Synthesis of Rod-Shaped Nanocrystalline High-Surface-Area Lanthanum Phosphate Powders and Nanocoatings. Advanced Functional Materials **2007**, 17 (10), 1682–1690. https://doi.org/10.1002/adfm.200600794.
(76) Lima, J. F.; de Sousa Filho, P. C.; Serra, O. A. Single Crystalline Rhabdophane-Type $CePO_4$ Nanoparticles as Efficient UV Filters. Ceramics International **2016**, 42 (6), 7422–7431. https://doi.org/10.1016/j.ceramint.2016.01.146.
(77) de Sousa Filho, P. C.; Serra, O. A. Reverse Microemulsion Synthesis, Structure, and Luminescence of Nanosized $REPO_4$:Ln^{3+} (RE = La, Y, Gd, or Yb, and Ln = Eu, Tm, or Er). J. Phys. Chem. C **2011**, 115 (3), 636–646. https://doi.org/10.1021/jp109988a.
(78) Mesbah, A.; Clavier, N.; Elkaim, E.; Gausse, C.; Kacem, I. B.; Szenknect, S.; Dacheux, N. Monoclinic Form of the Rhabdophane Compounds: $REEPO_4 \cdot 0.667H_2O$. Crystal Growth & Design **2014**, 14 (10), 5090–5098. https://doi.org/10.1021/cg500707b.
(79) Du Fou de Kerdaniel, E. Etude de La Dissolution de Britholites et de Solutions Solides Monazite / Brabantite Dopées Avec Des Actinides. PhD Thesis, Université de Paris XI Orsay, 2007.
(80) Gausse, C. Synthèse et Dissolution de Matrices Phosphatées de Structure Monazitique. PhD Thesis, Université de Montpellier, 2016.
(81) Gausse, C.; Szenknect, S.; Qin, D. W.; Mesbah, A.; Clavier, N.; Neumeier, S.; Bosbach, D.; Dacheux, N. Determination of the Solubility of Rhabdophanes $LnPO_4 \cdot 0.667H_2O$ (Ln = La to Dy). European Journal of Inorganic Chemistry **2016**, 2016 (28), 4615–4630. https://doi.org/10.1002/ejic.201600517.
(82) Mooney, R. C. L. Crystal Structures of a Series of Rare Earth Phosphates. J. Chem. Phys. **1948**, 16 (10), 1003–1003. https://doi.org/10.1063/1.1746668.
(83) Mooney, R. C. L. X-Ray Diffraction Study of Cerous Phosphate and Related Crystals. I. Hexagonal Modification. Acta Crystallographica **1950**, 3 (5), 337–340. https://doi.org/10.1107/S0365110X50000963.
(84) Mesbah, A.; Clavier, N.; Elkaim, E.; Szenknect, S.; Dacheux, N. In Pursuit of the Rhabdophane Crystal Structure: From the Hydrated Monoclinic $LnPO_4.0.667H_2O$ to the Hexagonal $LnPO_4$ (Ln = Nd, Sm, Gd, Eu and Dy). Journal of Solid State Chemistry **2017**, 249, 221–227. https://doi.org/10.1016/j.jssc.2017.03.004.
(85) Jonasson, R. G.; Vance, E. R. DTA Study of the Rhabdophane to Monazite Transformation in Rare Earth (La-Dy) Phosphates. Thermochimica Acta **1986**, 108, 65–72. https://doi.org/10.1016/0040-6031(86)85078-X.
(86) Bregiroux, D. Synthèse Par Voie Solide et Frittage de Céramiques à Structure Monazite : Application Au Conditionnement Des Actinides Mineurs. PhD Thesis, Université de Limoges, 2005.
(87) Qin, D.; Mesbah, A.; Gausse, C.; Szenknect, S.; Dacheux, N.; Clavier, N. Incorporation of Thorium in the Rhabdophane Structure: Synthesis and Characterization of $Pr_{1-2x}Ca_xTh_xPO_4 \cdot nH_2O$ Solid Solutions. Journal of Nuclear Materials **2017**, 492, 88–96. https://doi.org/10.1016/j.jnucmat.2017.05.019.
(88) Rawat, D.; Phapale, S.; Mishra, R.; Dash, S. Thermodynamic Studies on Charge-Coupled Substituted Synthetic Monazite. Journal of Nuclear Materials **2017**, 487, 406–417. https://doi.org/10.1016/j.jnucmat.2017.02.033.
(89) Rai, D.; Felmy, A. R.; Fulton, R. W. Solubility and Ion Activity Product of $AmPO_4 \cdot xH_2O$(Am). Radiochimica Acta **1992**, 56 (1).
(90) Frontera, C.; Rodríguez-Carvajal, J. FullProf as a New Tool for Flipping Ratio Analysis. Physica B: Condensed Matter **2003**, 335 (1), 219–222. https://doi.org/10.1016/S0921-4526(03)00241-2.

(91) Brandel, V.; Dacheux, N.; Genet, M.; Podor, R. Hydrothermal Synthesis and Characterization of the Thorium Phosphate Hydrogenphosphate, Thorium Hydroxide Phosphate, and Dithorium Oxide Phosphate. Journal of Solid State Chemistry **2001**, 159 (1), 139–148. https://doi.org/10.1006/jssc.2001.9143.

(92) Dacheux, N.; Clavier, N.; Wallez, G.; Quarton, M. Crystal Structures of $Th(OH)PO_4$, $U(OH)PO_4$ and $Th_2O(PO_4)_2$. Condensation Mechanism of $M^{IV}(OH)PO_4$ (M=Th, U) into $M_2O(PO_4)_2$. Solid State Sciences **2007**, 9 (7), 619–627. https://doi.org/10.1016/j.solidstatesciences.2007.04.015.

(93) Terra, O.; Clavier, N.; Dacheux, N.; Podor, R. Preparation and Characterization of Lanthanum–Gadolinium Monazites as Ceramics for Radioactive Waste Storage. New J. Chem. **2003**, 27 (6), 957–967. https://doi.org/10.1039/B212805P.

(94) Giffaut, E.; Grivé, M.; Blanc, Ph.; Vieillard, Ph.; Colàs, E.; Gailhanou, H.; Gaboreau, S.; Marty, N.; Madé, B.; Duro, L. Andra Thermodynamic Database for Performance Assessment: ThermoChimie. Applied Geochemistry **2014**, 49, 225–236. https://doi.org/10.1016/j.apgeochem.2014.05.007.

(95) Nancollas, G. H. The Nucleation and Growth of Phosphate Minerals. In Phosphate Minerals; Nriagu, J. O., Moore, P. B., Eds.; Springer Berlin Heidelberg: Berlin, Heidelberg, 1984; pp 137–154. https://doi.org/10.1007/978-3-642-61736-2_2.

(96) Qin, D.; Gausse, C.; Szenknect, S.; Mesbah, A.; Clavier, N.; Dacheux, N. Solubility Product of the Thorium Phosphate Hydrogen-Phosphate Hydrate ($Th_2(PO_4)_2(HPO_4)\cdot H_2O$, TPHPH). The Journal of Chemical Thermodynamics **2017**, 114, 151–164. https://doi.org/10.1016/j.jct.2017.01.003.

(97) Raison, P. E.; Heathman, S.; Wallez, G.; Zvoriste, C. E.; Bykov, D.; Ménard, G.; Suard, E.; Popa, K.; Dacheux, N.; Konings, R. J. M.; Caciuffo, R. Structure and Nuclear Density Distribution in the Cheralite—$CaTh(PO_4)_2$: Studies of Its Behaviour under High Pressure (36 GPa). Physics and Chemistry of Minerals **2012**, 39 (8), 685–692. https://doi.org/10.1007/s00269-012-0522-z.

(98) Burdese, A.; Borlera, M. L. Sul Sistema Tra i Pirofosfati Di Uranio e Ditorio. Annali di Chimica (Rome) **1963**, 53, 333–343.

Chapter II. Thermal Behavior of Th-Rhabdophane $Nd_{1-2x}Th_xCa_xPO_4.nH_2O$ (x = 0 – 0.10) and Conversion into Monazite-Cheralite Solid Solution

Results published in

Qin, D.; Mesbah, A.; Clavier, N.; Szenknect, S.; Dacheux, N. From Th-Rhabdophane to Monazite-Cheralite Solid Solutions: Thermal Behavior of $Nd_{1-2x}Th_xCa_xPO_4 \cdot nH_2O$ (x = 0–0.15). *Crystal Growth & Design* **2019**, *19* (5), 2794–2801.

II-1. Introduction

All the conditions required to prepare $Pr_{1-2x}Th_xCa_xPO_4.nH_2O$ and $Nd_{1-2x}Th_xCa_xPO_4.nH_2O$, as precursors of monazite-cheralite solid solutions were previously fixed. The results obtained showed that their thermal treatment led to the formation of pure and single-phase monazite-cheralite solid solutions. The successive steps associated to their thermal conversion are now discussed in this chapter.

There are only few reports on the thermal behavior of rhabdophane $LnPO_4.nH_2O$ [1,2]. Indeed, Jonasson and Vance have investigated the transformation of rhabdophane into monazite for Ln = La – Dy using thermogravimetric (TGA) and differential thermal analyses (DTA). They reported dehydration temperatures ranging from 100 to 400°C while the temperature mentioned for the irreversible transformation of rhabdophane into monazite was found to occur between 500 and 900°C. Moreover, the conversion temperature increased with decreasing ionic radius [1]. A similar study has been done by Kijkowska [2] who reported a double endothermic effect below 300°C assigned to a two-step dehydration in the TGA study. Furthermore, the temperature of rhabdophane to monazite transformation was found to increase with the atomic number from below 750°C (La, Ce) to above 900°C (Tb, Dy) [2].

Table II-1. Results of DTA/TGA and isochronal heating reported by Jonasson and Vance [1] and Kijkowska [2]: T_w = endothermic peak temperature(s), T_c = exothermic peak temperature, T_x = structure transformation temperature determined from isochronal heating experiments

	Jonasson and Vance [1]			Kijkowska [2]	
Ln	T_w (°C)	T_c (°C)	T_x (°C)	T_w (°C)	T_c (°C)
La	100, 230		500	94, 263	735
Ce	100, 250	715	600	81, 243	717
Pr	120, 250		700	79, 249	761
Nd	100, 230	790	700	79, 244	784
	110, 230	680	700		
Sm	80, 180	800	700	98, 227	840
Gd	210	815	800	93, 225	887

From the structural point of view, Mesbah *et al.* followed the dehydration process and related crystal structure changes from monoclinic $LnPO_4.0.667H_2O$ (hydrated rhabdophane) to hexagonal $LnPO_4$ (anhydrous rhabdophane) with Ln = Nd, Sm, Gd, Eu and Dy [3]. The initial crystal structure (monoclinic C2, Z = 24) has six independent positions for the cations. Two-thirds of them are coordinated to 9 oxygen atoms from the phosphate groups to form an infinite chain (called Ch1). The ninth oxygen atom is from a water molecule. Meanwhile, the other one-

third of cations coordinated by 8 oxygen atoms to form a second different chain (Ch2) leading to a channeled structure oriented along the [101] direction (**Figure II-1**), where the water molecules are present. During the dehydration of the rhabdophane samples, which involves a two-step process, the lanthanide phosphate first turns into the hemihydrate compound ($LnPO_4.0.5H_2O$, monoclinic C2). Within this structure, there is one kind of chains formed by half of the lanthanide atoms in 8-fold coordinated while the others are 9-fold coordinated. This leads to the disappearance of the anhydrous chains and the reconstruction of the water network. However, all the chains are oriented along the [101] direction and water molecules also stay within the structure channels (**Figure II-1**). The full dehydration towards anhydrous rhabdophane (hexagonal, $P3_121$) takes place between 190°C and 240°C. Finally, the irreversible transformation into monazite occurs for temperatures above 500°C.

Even though the dehydration and conversion process from rhabdophane $LnPO_4.nH_2O$ to monazite $LnPO_4$ has been thoroughly reported, the thermal behavior of thorium-doped rhabdophane is still unclear. In this chapter, single-phase rhabdophane samples with initial crystal structure monoclinic C2, $Nd_{1-2x}Th_xCa_xPO_4.nH_2O$ (x = 0 to 0.15) were prepared by wet chemistry route as reported in Chapter I. The thermal conversion into the final monazite-cheralite compounds was first monitored by *in situ* HT-PXRD to determine the conversion temperature range and to investigate the variation of the unit cell volume. Moreover, a coupled TGA/dilatometry study was undertaken to get better understanding of the dehydration and conversion processes.

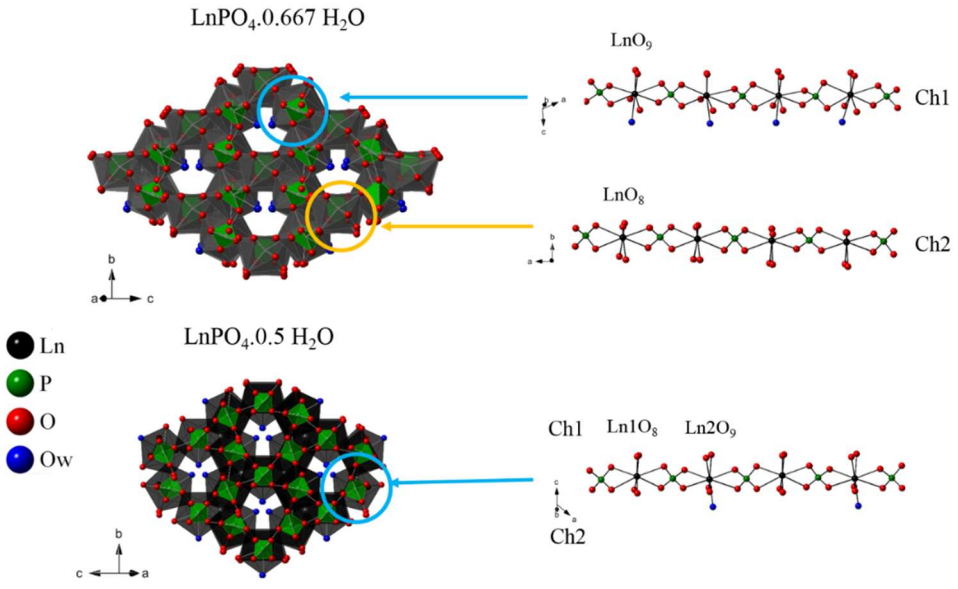

Figure II-1. Representation of the chains and channels present in $LnPO_4.0.667H_2O$ (top) and $LnPO_4.0.5H_2O$ (bottom) [3].

II-2. Experiments and Methods

II-2.1. *in situ* High Temperature-PXRD (HT-PXRD)

The preparation and characterization of the Th-rhabdophane $Nd_{1-2x}Th_xCa_xPO_4.nH_2O$ used in this chapter were reported in detail in chapter I (see Section I-2 and I-3).

In order to identify the successive dehydration steps of rhabdophanes and their phase transformation into monazite-cheralite, *in situ* HT-PXRD experiments were performed using the Bruker D8 advance diffractometer equipped with copper radiation (Cu $K\alpha_{1,2}$, λ=1.54184 Å) for temperatures ranging from room temperature (RT) to 1100°C with a rate of 5°C.min^{-1}. During each experiment, the PXRD patterns were collected on a set of 30 temperatures. For each measurement, the system was held at the target temperature for 15 minutes prior to the beginning of the scan from 5 to 100° (2θ, angular step of 0.014° and time step of 1.10 s). The collected powder patterns were refined by the Rietveld method using of the Fullprof_Suite package [4].

II-2.2. TGA and dilatometric study

TG analyses were undertaken thanks to a Setaram Setsys Evolution apparatus equipped with a type-S thermocouple (Pt / Pt - 10% Rh). After the blank was recorded using an empty alumina crucible (30 µL), about 15 mg of powder was heated in air with a rate of 5°C.min^{-1} from room temperature (RT) to 1000°C in order to follow the dehydration steps then the transition from rhabdophane to monazite.

Accordingly, the dilatometric measurements were conducted with a similar apparatus with a thermo-mechanical analysis (TMA) configuration. Approximately 200 mg of powder was first shaped by uniaxial pressing (500 MPa) in a tungsten carbide die, resulting in a 5 mm diameter cylindrical pellet of about 1 mm in height. The linear shrinkage of the pellet was then followed as a function of temperature from RT to 1000°C with a heating rate of 1 °C.min^{-1}. Thermal dilatation of alumina sample holder was measured under the same conditions and was subtracted from the resulting signal.

II-3. Results and Discussions

II-3.1. Structural evolution followed by *in situ* HT-PXRD.

First investigations regarding the dehydration and conversion processes of $Nd_{1-2x}Th_xCa_xPO_4.nH_2O$ ($x \leq 0.10$) were achieved thanks to *in situ* HT-PXRD experiments. As a matter of example, the powder patterns recorded for $Nd_{0.8}Th_{0.1}Ca_{0.1}PO_4.nH_2O$ are viewed in **Figure II-2**. The rhabdophane structure was identified from the initial sample pattern collected at 30°C. Even though the structural changes linked with rhabdophane dehydration, *i.e.*, $SmPO_4.0.667H_2O \rightarrow SmPO_4.0.5H_2O \rightarrow SmPO_4$ (anhydrous rhabdophane) have been reported by Mesbah *et al.* [3], the PXRD patterns collected in our experiment, using a standard diffractometer, were not accurate enough to distinguish this small variation. However, the patterns collected at 200°C, showed that the peak positions were slightly shifted to the lower angles compared to the patterns collected at 30 °C and 100 °C. This shift indicated a change in the unit cell volume, which was associated with the transformation of the hemihydrate form into the anhydrous rhabdophane.

Conversely, it was easier to identify the conversion into the monazite-cheralite solid solution. Beginning at 700°C and ending at 850°C, the intensity of the peaks associated to the rhabdophane structure decreased, *e.g.*, single peaks at 14.6° (100 plane) and at 20.2° (101) [5]. Meanwhile, the characteristic peaks of the monazite-cheralite structure gradually appeared, *e.g.*, single peak at 17.2° (101 reflection), double peaks at 18.9° (110 and 011) and at 21.7° (-111 and 101) [6]. Besides, once the heat treatment was achieved and the sample returned to 30 °C, the PXRD pattern of the final product remained similar to those collected above 850 °C, which suggested that the conversion from rhabdophane into the monazite-cheralite was irreversible.

Therefore, Th-rhabdophanes appeared to follow the similar two-step transition scheme than the rhabdophane end-member $LnPO_4.0.667\ H_2O$: the first transition observed led to the formation of the anhydrous rhabdophane while the second one was assigned to the irreversible conversion into monazite-cheralite solid solution.

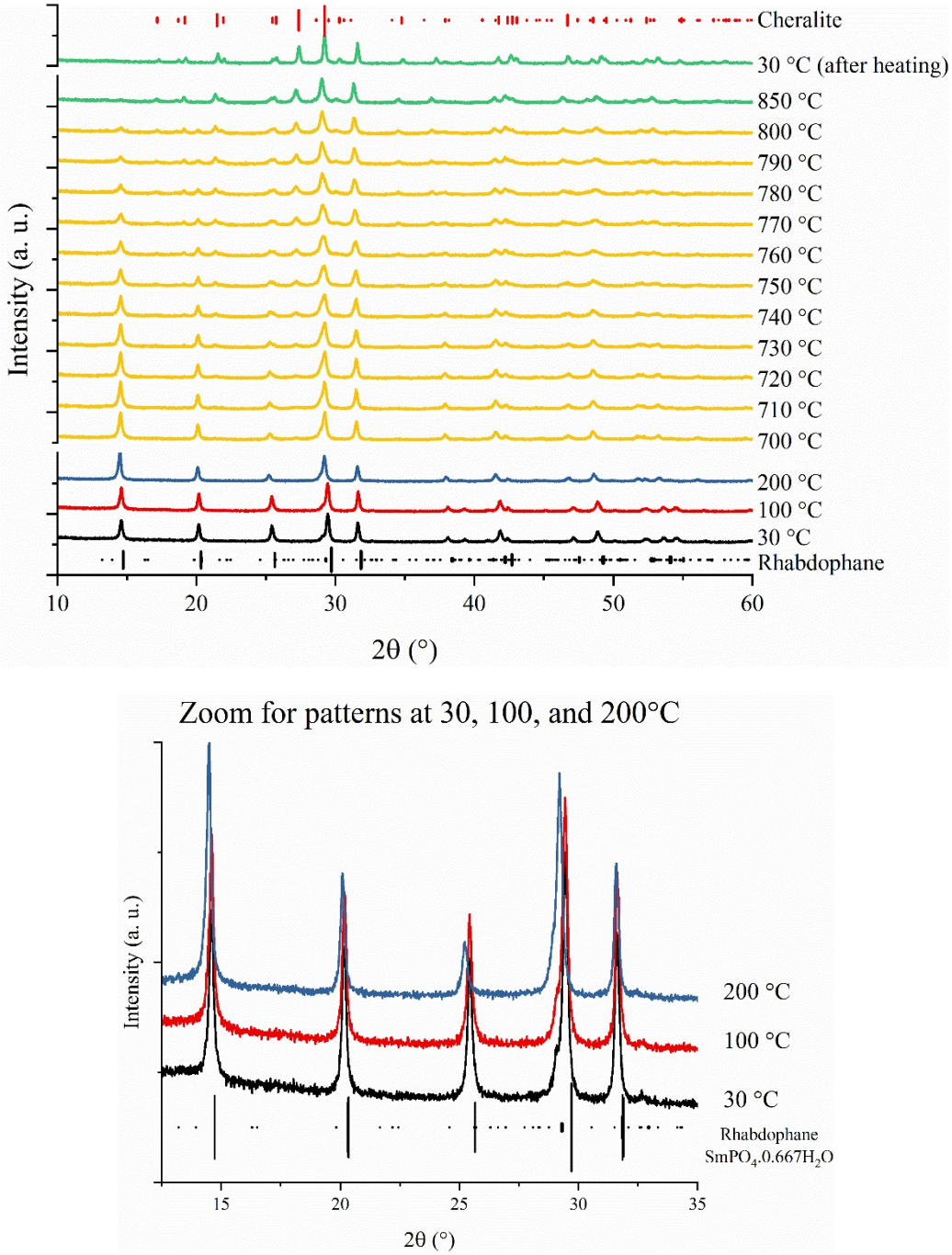

Figure II-2. *In situ* HT-PXRD patterns of $Nd_{0.8}Th_{0.1}Ca_{0.1}PO_4.nH_2O$: standard pattern of $SmPO_4.0.667H_2O$ (black vertical bars) [5] and of cheralite $Ca_{0.5}Th_{0.5}PO_4$ (red vertical bars) [6], XRD patterns recorded for initial rhabdophane (black line), for hemi-hydrated rhabdophane (red line), for anhydrous rhabdophane (blue line), for mixture of rhabdophane and monazite-cheralite (yellow line) and for single-phase monazite-cheralite (green line).

According to this observation, the *in situ* HT-PXRD patterns were refined using the Rietveld method (Appendix **A.2**) by considering the appropriate crystal structure depending on the temperature of the data collection, *i.e.*:

i) at 30°C, the hydrated form $Nd_{1-2x}Th_xCa_xPO_4.0.667\ H_2O$ (monoclinic C2, Z = 24);

ii) between 100 and 200°C, the hemihydrate form $Nd_{1-2x}Th_xCa_xPO_4.0.5\ H_2O$ (monoclinic C2 space group, Z = 12);

iii) above 200°C, the trigonal form associated with anhydrous rhabdophane $Nd_{1-2x}Th_xCa_xPO_4$ ($P3_121$ space group, Z = 3);

iv) above 700°C, the monoclinic form associated with the irreversible formation of monazite $Nd_{1-2x}Th_xCa_xPO_4$ ($P2_1/n$ space group, Z = 4).

The obtained crystal data and refinement parameters are listed in **Table II-2**.

Table II-2. Crystal data and refinement parameters for the $Nd_{1-2x}Th_xCa_xPO_4.nH_2O$ series.

	30°C	100°C	300°C	30°C*
Space group	C2	C2	$P3_121$	$P2_1/n$
x = 0				
a	28.2895(18)	17.5759(12)	7.0871(6)	6.7412(1)
b	6.9812(4)	7.0256(7)		6.9555(1)
c	12.1651(6)	12.1391(8)	6.3808(6)	6.4075(1)
β	115.43(1)	133.50(1)		103.68(1)
V	2169.7(2)	1087.3(2)	277.55(4)	291.91(1)
R_p	0.058	0.058	0.056	0.065
R_{wp}	0.075	0.074	0.071	0.083
χ^2	1.05	1.05	0.92	0.953
x = 0.05				
a	28.2988(18)	17.6422(9)	7.0777(4)	6.7368(1)
b	7.0065(6)	7.0071(5)		6.9519(1)
c	12.1219(8)	12.1435(6)	6.3906(4)	6.4092(1)
β	115.39(1)	133.61(1)		103.70(1)
V	2171.2(3)	1086.8(1)	277.2(1)	291.63(1)
R_p	0.050	0.054	0.053	0.064
R_{wp}	0.064	0.068	0.067	0.081
χ^2	0.89	0.98	0.95	1.16
x = 0.10				
a	28.3127(16)	17.6319(5)	7.0685(1)	6.7352(1)
b	6.9914(3)	7.0111(3)		6.9483(1)
c	12.1418(5)	12.1261(4)	6.3997(1)	6.4113
β	115.37(1)	133.55(2)		103.68(1)
V	2171.58(18)	1086.36(7)	276.91(1)	291.53(1)
R_p	0.058	0.054	0.059	0.064

	30°C	100°C	300°C	30°C*
Space group	C2	C2	$P3_121$	$P2_1/n$
R_{wp}	0.073	0.68	0.073	0.082
χ^2	1.16	1.03	1.21	1.21

* Data collected after heating the sample at 1100°C

In order to achieve a direct comparison of the unit cell volumes between the different structures mentioned above, they were systematically normalized to three formula units per unit cell for each phase. As an example, the variation of unit cell volume for $Nd_{0.8}Th_{0.1}Ca_{0.1}PO_4.nH_2O$ is presented in **Figure II-3**.

All the studied samples showed similar behavior despite the incorporation of thorium. The structure change corresponding to the dehydration led to an increase of unit cell volume of about 1 % around 200°C. After a slight swelling due to the increase of temperature, the irreversible phase transition from anhydrous rhabdophane to monazite-cheralite solid solution occurred above 650°C. It was marked by a strong shrinkage of the unit cell volume (about 18.5%), confirming that the monazite-cheralite solid solutions have a far more compact structure than their rhabdophane end-member. The temperature range of this transition depended on the chemical composition, *i.e.*, 650 – 690 °C for $x = 0$, 670 – 800 °C for $x = 0.05$ and 700 – 850°C for $x = 0.10$, which agreed with the results reported by Jonasson and Vance for $NdPO_4.0.667\ H_2O$ (*i.e.* 680-790°C) [1].

Finally, the dehydration-conversion scheme could be summarized in **Figure II-4** [3]:

(i) The hydrated Th-rhabdophane $Nd_{1-2x}Th_xCa_xPO_4.nH_2O$ with monoclinic structure C2 was converted to hemihydrate $Nd_{1-2x}Th_xCa_xPO_4.0.5\ H_2O$ (monoclinic C2) at about 100°C;

(ii) The complete dehydration took place at 200 – 220°C, leading to anhydrous rhabdophane $Nd_{1-2x}Th_xCa_xPO_4$ (hexagonal $P3_121$);

(iii) Finally, the conversion into monazite-cheralite solid solution $Nd_{1-2x}Th_xCa_xPO_4$ (monazite-cheralite monoclinic $P2_1/n$) occurred between 600-850°C;

(iv) Above 700°C, the monoclinic form associated through the irreversible formation of monazite $Nd_{1-2x}Th_xCa_xPO_4$ ($P2_1/n$ space group).

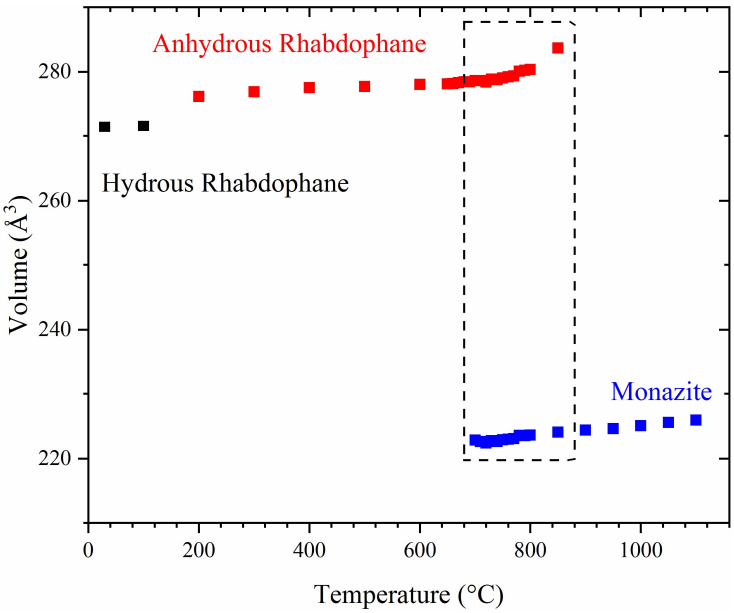

Figure II-3. Variation of refined unit cell volume of $Nd_{0.8}Th_{0.1}Ca_{0.1}PO_4.nH_2O$ versus heating temperature, the volume of each phase was normalized to three formula units per cell for better understanding.

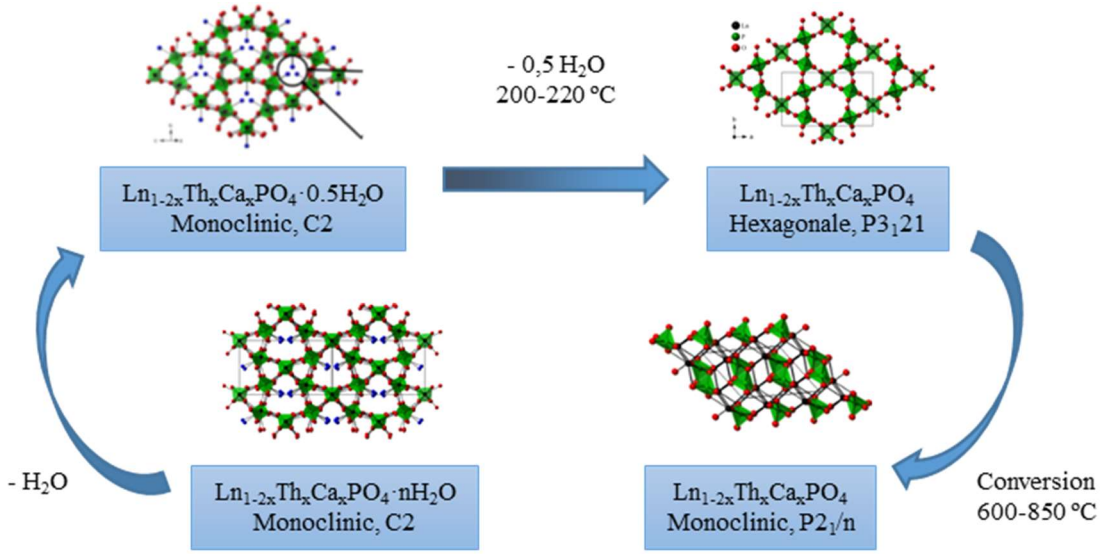

Figure II-4. Full conversion scheme of hydrated Th-rhabdophane to monazite-cheralite solid solution

II-3.2. TGA study.

Even though the *in situ* HT-PXRD experiment argued for a direct dehydration process completed at about 200 °C, it might go through several steps as already observed for lanthanide end-members, *i.e.*, Rhabdophane. nH_2O → Rhabdophane.$0.5H_2O$ → Anhydrous Rhabdophane [3]. Also, the amount of water molecules per unit formula has not been determined yet. TGA experiments were then performed to accurately follow the dehydration process of $Nd_{1-2x}Th_xCa_xPO_4.nH_2O$ ($0 \leq x \leq 0.10$) (**Figure II-5**).

All the prepared samples exhibited similar dehydration process according to the TGA curves. The water content ranged from 0.68 ± 0.01 to 0.88 ± 0.01, which agreed with the hydration ratio proposed by Mesbah *et al.* (*i.e.* 0.667 H_2O per formula unit) [3,5]. The slight excess of water might have two sources. As thorium has a great affinity to water [7], it might introduce extra water molecules within the structure by forming 9-fold coordination. Also, the specific surface area of the hydrated rhabdophane was over 20 $m^2.g^{-1}$, which could lead to extra water absorption on the surface of the powder. The derivative curves (**Figure II-5**) showed that dehydration of $Nd_{1-2x}Th_xCa_xPO_4.nH_2O$ went through two successive steps leading to anhydrous rhabdophane structure type. In all cases, whatever the initial amount of water, the first dehydration step led to the stable hemihydrate form, *i.e.*, $Nd_{1-2x}Th_xCa_xPO_4.0.5\ H_2O$, then to the anhydrous rhabdophane, *i.e.*, $Nd_{1-2x}Th_xCa_xPO_4$. Even though the temperature associated with the first dehydration step was difficult to determine, that corresponding to the full dehydration was deduced from the minimum of the derivative of the relative weight.

Table II-3. Results of TGA obtained on $Nd_{1-2x}Th_xCa_xPO_4.nH_2O$ solid solutions

x	$T_{min\ derivative}$ (°C)	H_2O per unit formula (2^{nd} step)	H_2O per unit formula (total amount)
0.00	210 ± 3	0.46 ± 0.01	0.68 ± 0.01
0.05	213 ± 3	0.47 ± 0.01	0.88 ± 0.01
0.10	214 ± 3	0.46 ± 0.01	0.79 ±0.01

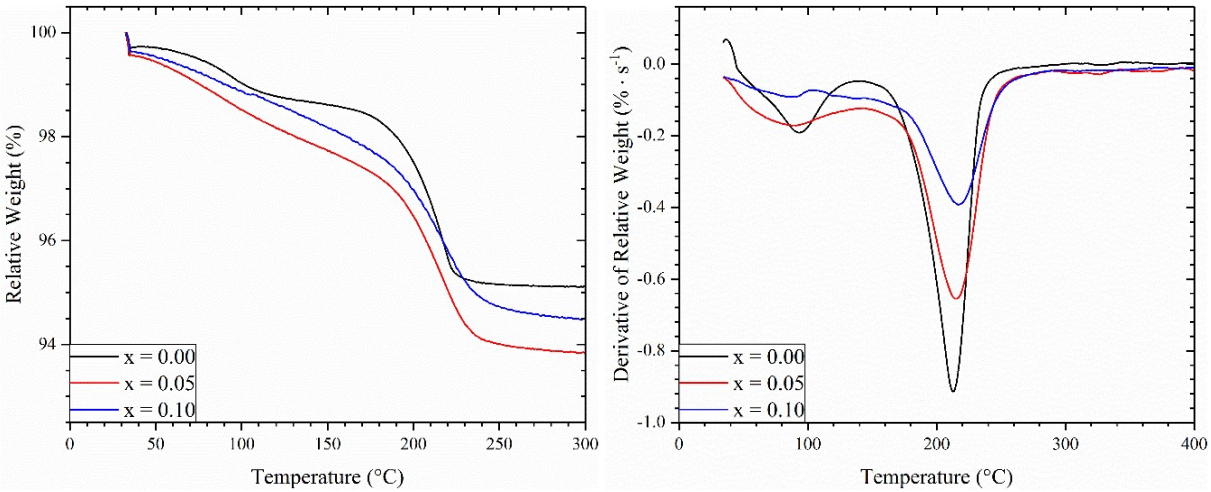

Figure II-5. TGA curves obtained for $Nd_{1-2x}Th_xCa_xPO_4.nH_2O$ samples (Left) and associated derivative curves (Right).

The incorporation of thorium and calcium within the structure has few impacts on the temperature associated with the dehydration of the rhabdophane. Nevertheless, the profile of the derivative curves corresponding to the $NdPO_4.nH_2O$ end-member showed a more evident

two-step transition as the peaks associated with the dehydration processes presented the smaller full width at half maximum (FWHM). Indeed, an enlargement of the FWHM was observed with the increase of the incorporation ratio of calcium and thorium. A possible reason is that thorium has a better affinity to the water molecules because of its higher effective charge, which slows down the dehydration. Nevertheless, the impact of incorporation ratio of calcium and thorium on the temperatures associated to the minimum of derivative curves was not evident (**Table II-3**), which suggested that the dehydration temperature of the solid solution $Nd_{1-2x}Th_xCa_xPO_4.nH_2O$ was in a narrow domain ranging from 210 ± 3 to 214 ± 3 °C.

II-3.3. Dilatometric study

The relative linear shrinkage of $Nd_{1-2x}Th_xCa_xPO_4.nH_2O$ was analyzed by dilatometric measurements (**Figure II-6**) and revealed a three-step variation. The first dehydration step leading to the stabilization of the hemihydrate form was linked to the slight shrinkage observed before 200°C. A small swelling (less than 1 %) then took place around 200°C and was assigned to the complete dehydration of the rhabdophane samples. An important shrinkage was then observed from 600°C to 850°C. It was associated to the irreversible transformation of the rhabdophane into the monazite-cheralite solid solution. These results appeared in good agreement with those obtained by *in situ* HT-PXRD. Finally, the last shrinkage step occurred at higher temperatures (*i.e.* for T > 850°C) and was correlated to the sintering of the monazite-cheralite solid solutions.

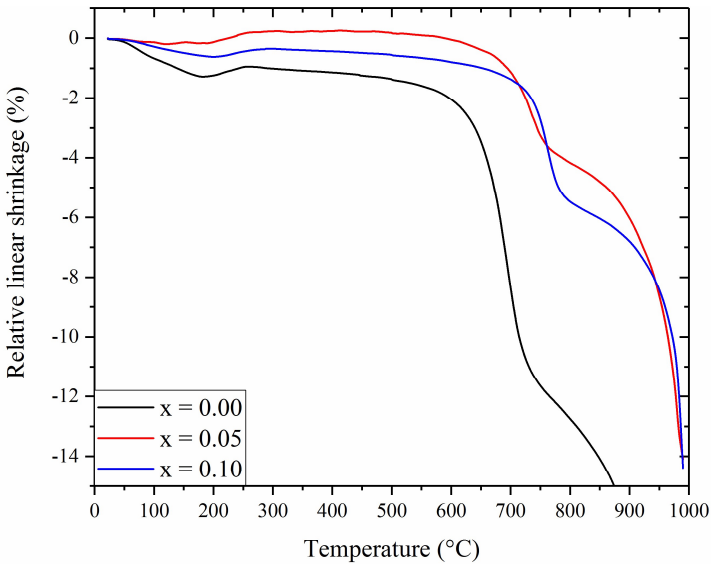

Figure II-6. Dilatometric curves obtained during the sintering of $Nd_{1-2x}Th_xCa_xPO4.nH_2O$ samples.

The temperature of the phase transition, deduced from the maximum shrinkage rate, was found to increase with the Ca-Th coupled substitution rate from 693 ± 1°C (x = 0) to 762 ± 1°C (x = 0.1). It agreed well with the temperatures reported by Jonasson and Vance (500 – 900°C) and by Kijkowska (717 – 910°C) regarding the formation of monazite end-members [1,2]. Moreover, both studies showed an increase of the temperature of transformation with the atomic number. Reviewing the reported data and the results obtained during this work, it might be interesting to investigate the variation of the temperature versus the ionic radius. According to the Shannon's table [8], the average ionic radius of cations could be written as:

$$\bar{r} = x \times \left(r_{Ca(IX)} + r_{Th(IX)}\right) + (1 - 2x) \times r_{Nd(IX)} \qquad \text{(II-1)}$$

where, $\bar{r}$ is the calculated average ionic radius for the incorporation rate of x, $r_{Ca(IX)}$, $r_{Th(IX)}$, and $r_{Nd(IX)}$ are the ion radii of 9-fold coordinated Ca^{2+}, Th^{4+} and Nd^{3+} reported by Shannon [8].

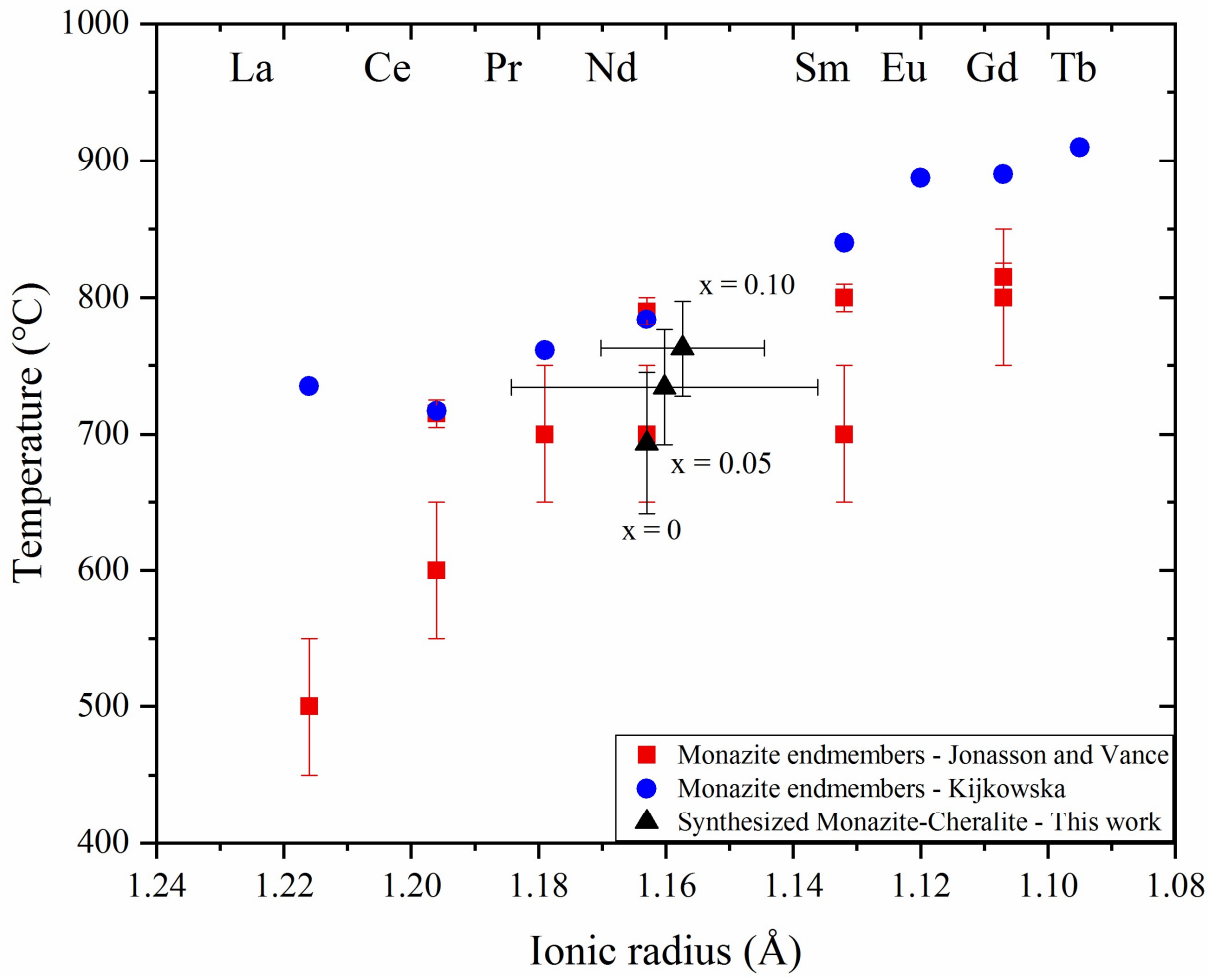

Figure II-7. Variation of the conversion temperature of rhabdophane into the monazite-cheralite solid solution as a function of the ionic radius.

As a result, the temperature of conversion into monazite-cheralite was found to increase with the shrinkage of ionic radius (see **Figure II-7**.) [8]. Moreover, these results agree well with those reported by Jonasson and Vance [1] and by Kijkowska *et al.* [2]. Additionally, the Kijikowska's results seemed to be higher than those published by Jonasson and Vance and our set of data (**Figure II-7**.). This shift of temperature might be due to the rate of temperature applied druing the heating treatments. For our dilatometric experiments, the rate was 1°C.min^{-1} while that used during the DTA experiments by Jonasson and Vance was 10 °C.min^{-1} and 20°C.min^{-1} for the work reported by Kijkowska [1,2].

II-3.4. Influence of coupled substitution on crystal structures

According to the TGA results, the first three temperature set points of the *in situ* HT-PXRD study, *i.e.*, at 30°C, 100°C and 300°C, corresponded to the three distinct phases, *i.e.*, monoclinic C2 $Nd_{1-2x}Th_xCa_xPO_4.nH_2O$, monoclinic C2 $Nd_{1-2x}Th_xCa_xPO_4.0.5H_2O$ and hexagonal $P3_121$ $Nd_{1-2x}Th_xCa_xPO_4$, respectively. Based on such structural models, these collected PXRD patterns were refined by the Rietveld method. The variation of the unit cell volume of $Nd_{1-2x}Th_xCa_xPO_4.nH_2O$ are reported in **Figure II-8**. as a function of the Ca-Th incorporation rate.

Table II-4. Selected ionic radius reported for Ca^{2+}, $Nd^{3+}$and Th^{4+} in the eight and nine fold coordination [8]

Coordination	r_{Ca}^{2+} Å	r_{Th}^{4+} Å	r_{Ca-Th} Å	r_{Nd}^{3+} Å	$\frac{\Delta(r_{Nd(VIII)} - r_{Ca-Th(IX)})}{r_{Nd(VIII)}}$
VIII	1.12	1.05	1.085	1.109	– 2.1%
IX	1.18	1.09	1.135	1.163	

At 30°C, the rhabdophane $LnPO_4.0.667H_2O$ crystallized in the monoclinic system with space group C2. The refined unit cell volume was found to increase when thorium and calcium contents increased within the structure. If we considered the 8-fold ionic radius of Nd^{3+}, Th^{4+} and Ca^{2+} reported in the Shannon' table [8] (see **Table II-4**.), the refined volume of the rhabdophane structure should have decreased when smaller cations were inserted. However, it is not compatible with the results of PXRD refinement. Such abnormal expansion of the unit cell volume might be explained by the preference of thorium and calcium to be coordinated by the water molecules leading to a 9-fold coordination. In this case, on the one hand, the average ionic radius of Ca-Th couple (CN = 9) became greater than that of Nd (CN = 8), as reported in **Table II-4**. On the other hand, this coordination introduced extra water molecules within the channels. The assumption of extra water molecules was also justified by the content of water

measured by TGA, which systematically exceeded 0.667 (**Table II-3**.). Consequently, the Th-Ca incorporation might increase not only the average ionic radius but also the water amount within the structure, leading to a swelling of unit cell volume.

Despite the difficulties to determine the exact temperature associated to the first structural transition leading to the hemihydrate form, we could suggest that this stabilization occurred at temperatures below 100°C, according to the derivative curves (**Figure II-5**). Therefore, the difference of the relative weight measured between 100°C and above 250 °C corresponded to about 0.5 H_2O per formula unit (TGA results, see **Table II-3**.). According to the data viewed in **Figure II-8**., after the first dehydration step, the unit cell volume decreased with the incorporation rate of thorium, in agreement with the ionic radius of Th^{4+}, Ca^{2+} and Nd^{3+} reported in literature [8]. Regarding the structural features of the hemihydrate form (**Figure II-1**.), we could assume that there was no ordering of thorium and calcium on a specific site (*i.e.*, given coordination number) and that the location of water molecules respected the crystal structure properties published previously by Mesbah *et al.* [3]. Moreover, the same observation was made for the structure refined at 300°C when considering the anhydrous form of the rhabdophane structure. It is worth noting that the unit cell volume variations at 100°C and 300°C were consistent with Vegard's law. Therefore, there are more reasons to believe that the increase of the unit cell volume of $Nd_{1-2x}Th_xCa_xPO_4.nH_2O$ samples collected at 30°C should be associated with the increase of water amounts within the channels.

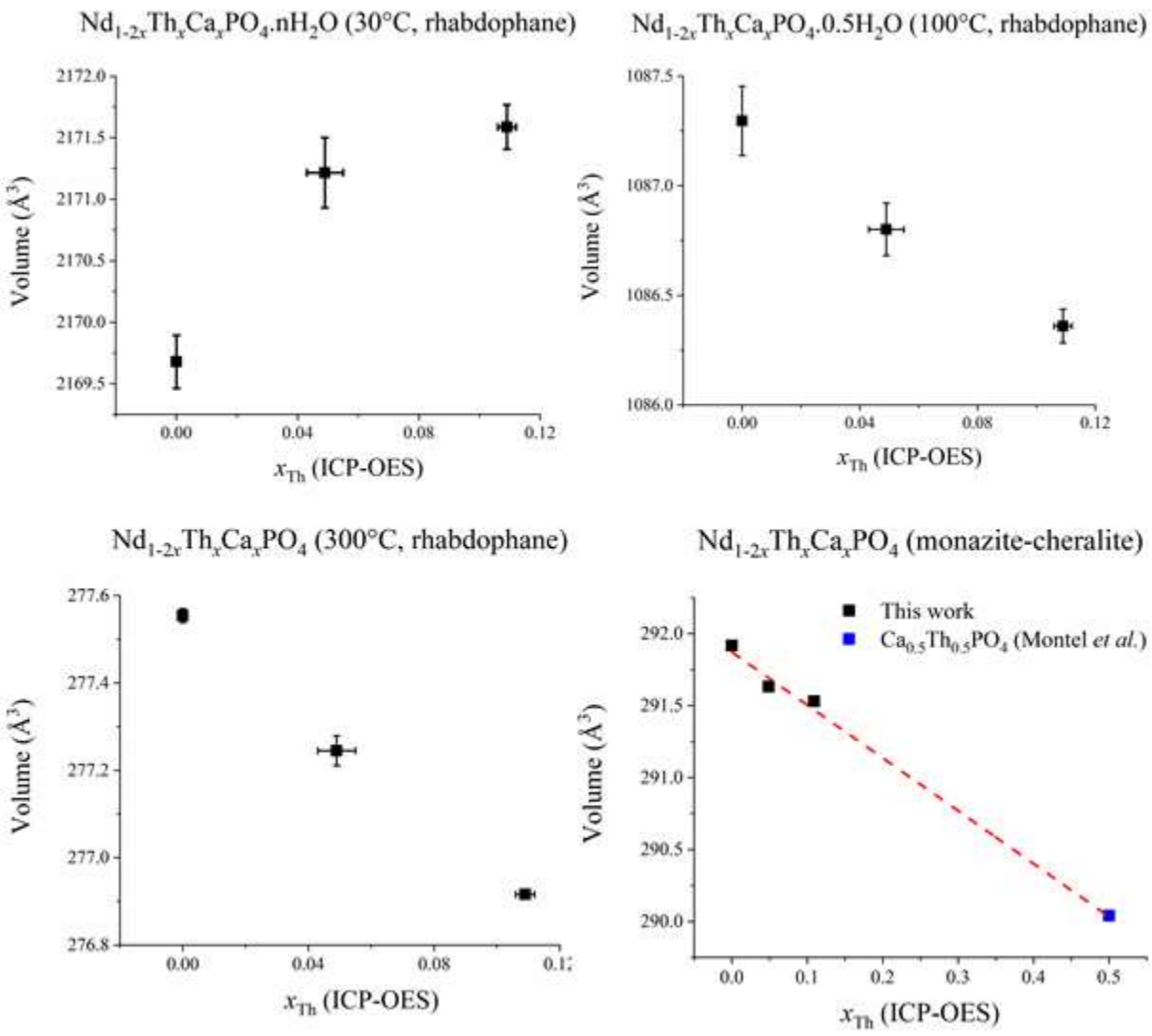

Figure II-8. Refined unit cell volumes obtained for $Nd_{1-2x}Th_xCa_xPO_4.nH_2O$ samples prepared at 30°C, 100°C and 300°C, and for the monazite-cheralite samples collected at 30°C after cooling from 1100°C.[9]

At higher temperatures, anhydrous rhabdophane underwent an irreversible transition into the monazite-cheralite structure crystallizing in the monoclinic system ($P2_1/n$ space group). Hereby, PXRD patterns were recorded back at RT to avoid any bias due to the high-temperature collection. The unit cell volume of $Ca_{0.5}Th_{0.5}PO_4$ end-member [9] was included as reference for comparison with the $Nd_{1-2x}Th_xCa_xPO_4$ series. The unit cell volume decreased linearly with the incorporation rate following the Vegard's law. Such a variation thus suggested the formation of an ideal solid solution $Nd_{1-2x}Th_xCa_xPO_4$ all along the $0 \leq x \leq 0.1$ range (**Figure II-8**.).

Summary

In this chapter, the thermal behavior of $Nd_{1-2x}Th_xCa_xPO_4.nH_2O$ ($x \leq 0.10$) solid solutions crystallizing in the rhabdophane structure type was studied by combining *situ* HT-PXRD, TGA, and dilatometry. The samples were found to follow the same dehydration-conversion scheme than the $NdPO_4.0.667H_2O$ end-member. The dehydration of the rhabdophane type solid solution $Nd_{1-2x}Th_xCa_xPO_4.nH_2O$ ($x \leq 0.10$) occurred in two steps. The hemihydrate $Nd_{1-2x}Th_xCa_xPO_4.0.5H_2O$ formed at 100°C whereas the temperatures associated with the complete dehydration ranged between 200 and 220 °C. The conversion of the rhabdophane to the monazite-cheralite solid solution was observed between 600 and 850 °C. The Ca-Th coupled incorporation rate seemed to affect the conversion temperature by reducing the average cation radius, which modified the structure stability. .Finally, at higher temperatures ($T \geq 100°C$), there was a linear correlation between the unit cell volume and the ionic radius [8]. This trend follows Vegard's law, which indicates the unit cell volumes of the as prepared solid solutions could be expressed as the weighted average of the end members $NdPO_4$ and $Ca_{0.5}Th_{0.5}PO_4$. Consequently, this observation suggested the obtained samples might be ideal solid solutions.

Résumé

Dans ce second chapitre, le comportement thermique des solutions solides $Nd_{1-2x}Th_xCa_xPO_4,nH_2O$ ($x \leq 0,10$) cristallisant dans la structure de type rhabdophane a été étudié en combinant des analyses DRX *in situ* à haute température ainsi que des suivis par ATG et par dilatométrie. Il est apparu que les précurseurs suivaient le même schéma de déshydratation puis de conversion que le pôle pur $NdPO_4,0,667H_2O$. Ainsi, le processus de déshydratation des solutions solides $Nd_{1-2x}Th_xCa_xPO_4,nH_2O$ ($x \leq 0,10$) intervient en deux étapes. La formation de la forme hémi-hydratée $Nd_{1-2x}Th_xCa_xPO_4,0,5H_2O$ ($x \leq 0,10$) est observée vers 100 °C tandis que la déshydratation complète est obtenue entre 200 et 220°C. Les températures associées à la conversion des rhabdophanes en solutions solides de monazite-chéralite s'étendent de 600 à 850°C. Il apparaît que l'incorporation couplée de néodyme par le calcium et le thorium influence la température de conversion, à travers la diminution du rayon cationique moyen ce qui modifie la stabilité de la structure. Enfin, lorsque T ≥ 100°C, la variation du volume de maille demeure en accord avec celle du rayon ionique moyen [8]. Cette variation est en accord avec loi de Vegard, c'est-à-dire, les volumes de maille des solutions solides sont les moyennes pondérées entre les pôles purs $NdPO_4$ et $Ca_{0,5}Th_{0,5}PO_4$. Par conséquent, cette observation indiquent les solides obtenus seraient des solutions solides idéales.

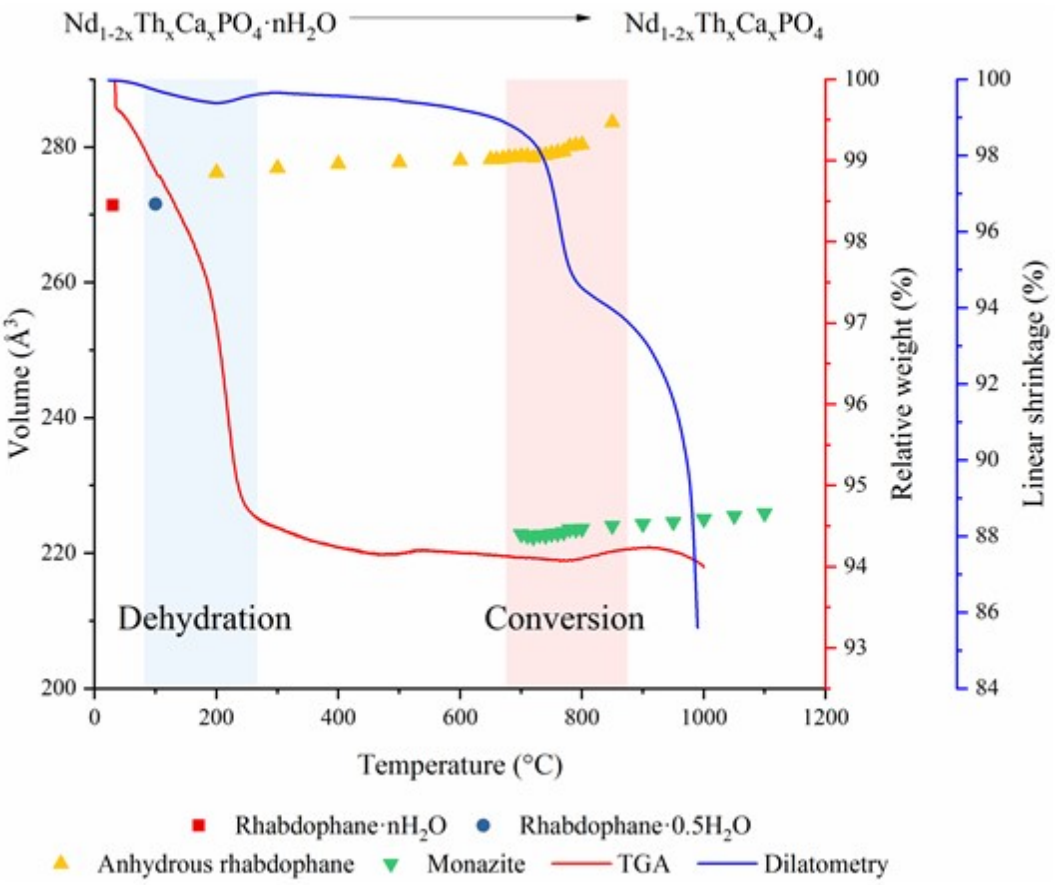

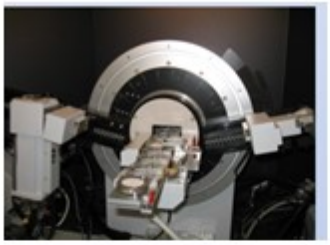

in situ HT-XRD

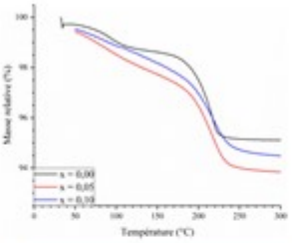

TGA

Dilatometer

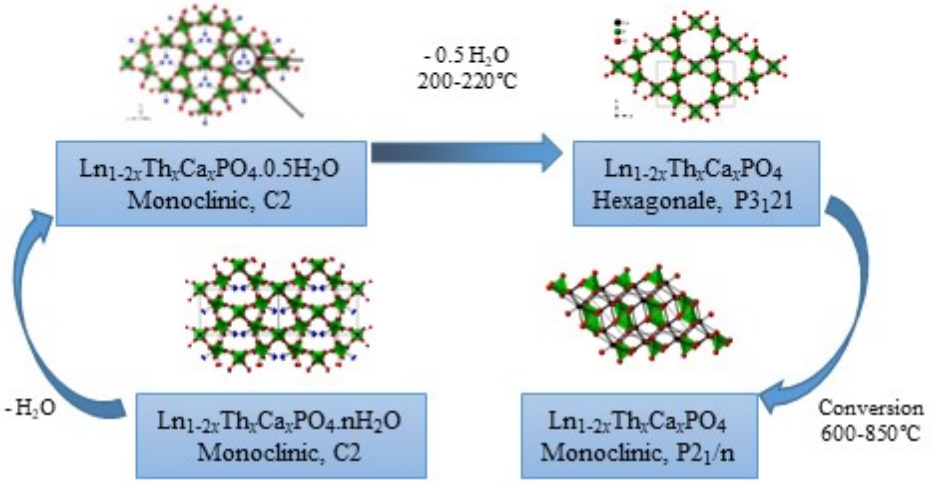

References

(1) Jonasson, R. G.; Vance, E. R. DTA Study of the Rhabdophane to Monazite Transformation in Rare Earth (La-Dy) Phosphates. *Thermochimica Acta* **1986**, *108*, 65–72. https://doi.org/10.1016/0040-6031(86)85078-X.

(2) Kijkowska, R. Thermal Decomposition of Lanthanide Orthophosphates Synthesized through Crystallisation from Phosphoric Acid Solution. *Thermochimica Acta* **2003**, *404* (1), 81–88. https://doi.org/10.1016/S0040-6031(03)00085-6.

(3) Mesbah, A.; Clavier, N.; Elkaim, E.; Szenknect, S.; Dacheux, N. In Pursuit of the Rhabdophane Crystal Structure: From the Hydrated Monoclinic $LnPO_4.0.667H_2O$ to the Hexagonal $LnPO_4$ (Ln = Nd, Sm, Gd, Eu and Dy). *Journal of Solid State Chemistry* **2017**, *249*, 221–227. https://doi.org/10.1016/j.jssc.2017.03.004.

(4) Frontera, C.; Rodríguez-Carvajal, J. FullProf as a New Tool for Flipping Ratio Analysis. *Physica B: Condensed Matter* **2003**, *335* (1), 219–222. https://doi.org/10.1016/S0921-4526(03)00241-2.

(5) Mesbah, A.; Clavier, N.; Elkaim, E.; Gausse, C.; Kacem, I. B.; Szenknect, S.; Dacheux, N. Monoclinic Form of the Rhabdophane Compounds: $REEPO_4{\cdot}0.667H_2O$. *Crystal Growth & Design* **2014**, *14* (10), 5090–5098. https://doi.org/10.1021/cg500707b.

(6) Raison, P. E.; Heathman, S.; Wallez, G.; Zvoriste, C. E.; Bykov, D.; Ménard, G.; Suard, E.; Popa, K.; Dacheux, N.; Konings, R. J. M.; Caciuffo, R. Structure and Nuclear Density Distribution in the Cheralite—$CaTh(PO_4)_2$: Studies of Its Behaviour under High Pressure (36 GPa). *Physics and Chemistry of Minerals* **2012**, *39* (8), 685–692. https://doi.org/10.1007/s00269-012-0522-z.

(7) Zanonato, P. L.; Di Bernardo, P.; Zhang, Z.; Gong, Y.; Tian, G.; Gibson, J. K.; Rao, L. Hydrolysis of Thorium(Iv) at Variable Temperatures. *Dalton Trans.* **2016**, *45* (32), 12763–12771. https://doi.org/10.1039/C6DT01868H.

(8) Shannon, R. D. Revised Effective Ionic Radii and Systematic Studies of Interatomic Distances in Halides and Chalcogenides. *Acta Crystallographica Section A* **1976**, *32* (5), 751–767. https://doi.org/10.1107/S0567739476001551.

(9) Montel, J.-M.; Devidal, J.-L.; Avignant, D. X-Ray Diffraction Study of Brabantite–Monazite Solid Solutions. *Chemical Geology* **2002**, *191* (1), 89–104. https://doi.org/10.1016/S0009-2541(02)00150-X.

Chapter III. Reaction Sintering of Rhabdophane into Monazite-Cheralite $Nd_{1-2x}Th_xCa_xPO_4$ (x = 0 – 0.1) Ceramics

Results published in

Qin, D.; Mesbah, A.; Lautru, J.; Szenknect, S.; Dacheux, N.; Clavier, N. Reaction Sintering of Rhabdophane into Monazite-Cheralite $Nd_{1-2x}Th_xCa_xPO_4$ (x = 0 – 0.1) Ceramics. *Journal of the European Ceramic Society* **2020**, *40* (3), 911–922

III-1. Introduction

The synthesis and their thermal behavior of Th-rhabdophanes $Ln_{1-2x}Th_xCa_xPO_4.nH_2O$ (Ln = Pr, Nd) were investigated in the previous chapters, leading to the formation of powdered single-phase monazite-cheralite solid solutions $Ln_{1-2x}Th_xCa_xPO_4$. However, densified materials have to be synthesized in the field of the long-term immobilization of long-life radionuclides. The possibility to prepare highly densified monazite-cheralite ceramics directly from the associated rhabdophane precursors will be examined in this third chapter with the help of various sintering tests.

III-1.1. General information about sintering

Sintering is usually composed of a heating treatment applied on a powder compact leading to a bulk ceramic without any complete fusion [1]. The sintering aims to produce reproducible sintered ceramics with a designed microstructure. The microstructure of the pellets, including grain size, density, size, and distribution of pores, etc., can be modified by the sintering conditions, leading to a fully dense ceramic with a fine grain structure [2].

The driving force of the sintering is the reduction of total interfacial energy [2]. For a powder compact, its total interfacial energy could be expressed as γA, where γ is the specific interface energy and A its total interface. The reduction of the total interfacial energy could be written as:

$$\Delta(\gamma A) = \Delta\gamma \times A + \gamma \times \Delta A \qquad \text{(III-1)}$$

The decrease of the interfacial energy Δγ is due to densification, which means that the initial solid/air interfaces are replaced by a solid/solid interface. Meanwhile, the reduction of the interfacial area is due to grain coarsening. Consequently, under the driving force of the decline of total interfacial energy, the sintering accompanied by two basic phenomena: densification and grain growth, as presented in **Figure III-1**.

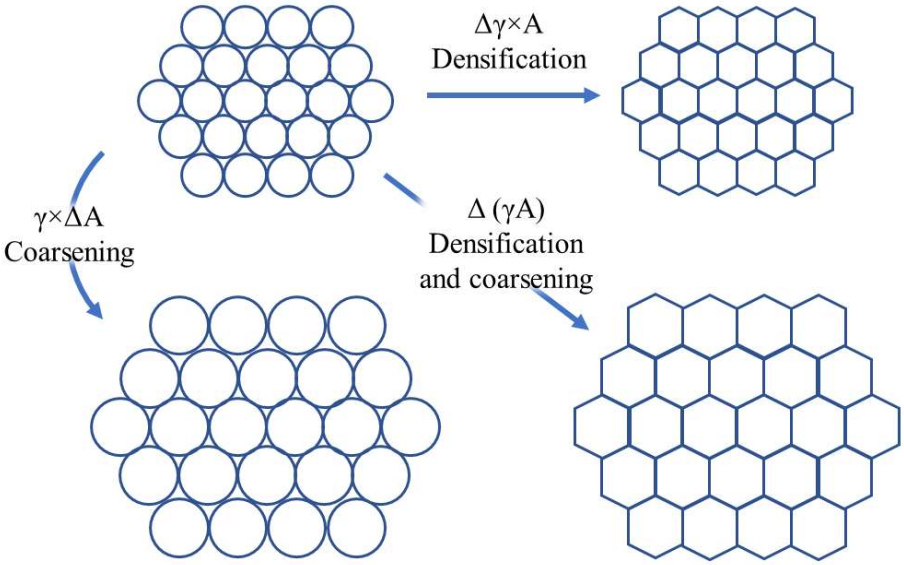

Figure III-1. Basic phenomena of sintering, *i.e.*, densification and grain growth, under the driving force for sintering, the reduction of total interfacial energy Δ(γA).

The sintering process consists of three stages. The relative density noted as, d, is a good indicator of its progress. The relative density is the ratio of the real density to the theoretical density:

$$d_{relative} = \frac{\rho_{real}}{\rho_{theoretical}} \times 100\% \quad \text{(III-2)}$$

Then, the three stages of the sintering can be described as follows (**Figure III-2**) [2]:

1) The **initial stage** ($50\% \leq d \leq 65\%$). In this stage, under the effect of heat treatment, the formation of necks between particles is observed while compact shrinkage is limited to 2 – 3% at most;
2) The **intermediate stage** ($65\% \leq d \leq 92\%$). In this stage, the densification is significant, and the open pores are eliminated. However, grain growth is not evident.
3) The **final stage** ($d \geq 92\%$). In this stage, the densification slows down, and the closed pores are eliminated. Meanwhile, noticeable grain growth can be observed.

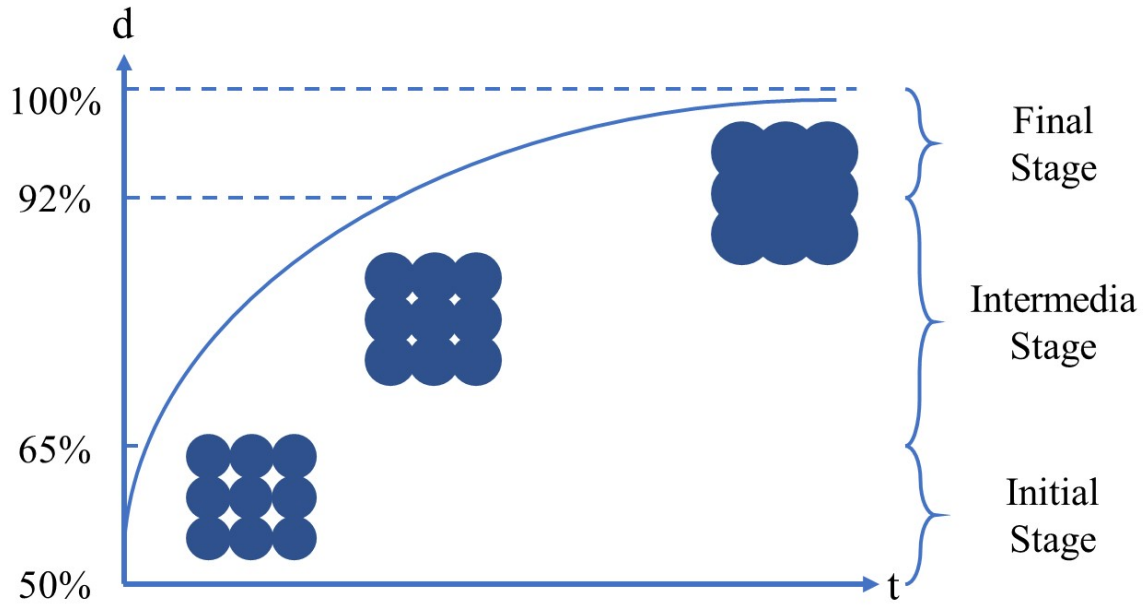

Figure III-2. Representation of the different stages of sintering.

In order to study the different stages of the sintering, two experimental techniques were developed: dilatometry and pycnometry were first used to finally establish the sintering maps. Dilatometric experiments allowed monitoring of the thickness evolution for a compact pellet during the heating treatments. The densification process, therefore, can be presented as the linear shrinkage curves. From these curves, we can identify the initial and final temperatures associated with the densification process. Moreover, by applying the Dorn's method [3–5], the initial stage of densification can be investigated in detail, and the activation energy related to this stage can be determined. Otherwise, to study the intermediate and final stages of the sintering, the establishment of a sintering map is required. This map represents the variation of the average grain size as a function of the relative density under various sintering conditions [6,7]. It appears to be a useful tool to develop an understanding of the effects associated with the densification and the grain growth when modifying sintering parameters such as chemical compositions, sintering temperature, heating treatment duration, etc.

III-1.2. State of art related to the sintering of monazite/monazite-cheralite ceramics

III-1.2.1. The effect of precursor preparation methods on sintering.

Several studies have been dedicated to the sintering of monazite or monazite-cheralite ceramics. The way of preparing the precursors seemed to have a considerable impact on their

sintering capability and on the properties of the final sintered ceramics, especially their final density. Indeed, the precursors obtained through different methods can lead to large variations of specific surface area (S_{SA}). Besides, some synthesis procedures might lead to the presence of impurities or modification of crystal structure. There are several criteria to evaluate the "quality" of a precursor, e.g., S_{SA}, chemical purity, crystal structure, grain size, etc. Among them, the specific surface area seems to be a good indicator. A larger specific surface probably favors the densification process and reduces the temperatures of sintering. Some researches even suggested that it is not possible to prepare fully densified ceramics using a precursor with a too-small specific surface area[8–10]. Meanwhile, the impurities introduced during the preparation procedure might accelerate or slow down the densification process. According to literature, the impact of the starting materials on sintering was reviewed. Several mentioned preparation procedures are listed in **Table III-1** . along with the associated specific surface areas, sintering conditions, and final densities of sintered ceramics:

1) End-members monazite $LnPO_4$ ceramics

Hikichi *et al.* [11,12] reported on the thermal, mechanical, and chemical properties of sintered monazite end-members ($LnPO_4$ with Ln = La, Ce, Nd, and Sm). Rhabdophane type $LnPO_4.nH_2O$ were firstly prepared thorough simple precipitation then converted in monazite-type powders after heating at 600°C for 2 hours. After a ball-milling treatment, the initial specific surface area of these monazite powders ranged between 52.8 and 69.8 $m^2 \cdot g^{-1}$. These S_{SA} values were relatively high among the data listed in **Table III-1**. In this way, Hikichi *et al.* reported that their ceramic reached a relative density close to 99 % of the theoretical density (TD) after sintering at 1200°C for 5 hours. This temperature is relatively low compared to those obtained by other methods.

Perrière *et al.* [13] studied the sintering of monazite end-members with Ln = La, Nd, Eu, and Ce. However, the starting powders were prepared thorough a solid-state route. Even though three cycles of milling were applied, the final S_{SA} reached only 5-10 $m^2.g^{-1}$. The fully densified ceramics (98%TD) was obtained by sintering at 1500°C for 20 hours. The sintering temperature was higher than that reported by Hikichi *et al.* [11,12]. Similarly, Bregiroux *et al.* [14] also reported the sintering of $LaPO_4$ starting from a material prepared through solid-state reaction and involving an attrition milling treatment (S_{SA} = 25 $m^2.g^{-1}$). To reach 98% TD, the pellet needed to be sintered at 1425°C for 1 hour.

In another paper, published by Bregiroux *et al.* [9], the authors investigated the effect of starting materials on the sintering of $LaPO_4$. In this paper, three types of starting materials were

used: the raw $LaPO_4.nH_2O$ rhabdophane and two kinds of monazite powders fired at 700°C or 1400°C. It is worth mentioning that the raw rhabdophane powder contained a phosphate excess, which led to the appearance of $La(PO_3)_3$ in the monazite type starting powders heated at 700°C (noted as M-700). In contrast, the starting powder calcined at 1400 °C was singled-phase monazite because of the decomposition of $La(PO_3)_3$. The S_{SA} value of the rhabdophane reached 78.4 $m^2.g^{-1}$, whereas that obtained for the monazite heated at 700°C equaled 32 $m^2.g^{-1}$. The S_{SA} of the powder heated at 1400°C was lower than 1 $m^2.g^{-1}$. Two kinds of milling treatments were applied to increase the S_{SA} of the powders. The final S_{SA} value was equal to 3.6 $m^2.g^{-1}$ after conventional ball milling (noted as M-1400-B5) and 17.5 $m^2.g^{-1}$ (M-1500-A5) after attrition milling. All three types of starting powder were shaped in pellets and heated at 1400 °C for 1 hour. The direct sintering using rhabdophane resulted in ceramics showing a 95.5% TD, compared to 96% TD when using the starting powder M-700. However, in the presence of 3.1 wt.% of $La(PO_3)_3$, the densification was limited to 78 %. Using powder calcined at 1400°C (M-1400-B5) did not provide enough $S_{SA,}$ leading to a final density of 71.8% TD. Only the attrition milling ensured a sufficient S_{SA} value to prepare a ceramic with 96.7% TD. This observation argued that a large S_{SA} over 15 $m^2.g^{-1}$ was essential to obtain high-densified monazite-type ceramics.

Recently, Babelot *et al.* [15] performed a similar study. The rhabdophane precursor $LaPO_4$ was synthesized by wet chemistry route and exhibited a S_{SA} value of 79 $m^2.g^{-1}$. Meanwhile, this precursor was calcined at 350°C, 500°C, and 950°C for two hours so that three starting materials for sintering were prepared. The powders calcined at 350°C and at 500°C were anhydrous rhabdophane with S_{SA} over 60 $m^2.g^{-1}$. Both these rhabdophanes starting materials allowed to prepare dense ceramics with 97.8-98% TD. The starting powder heated at 950°C was converted into monazite with S_{SA} of 5 $m^2.g^{-1}$ then sintered at 1400°C for 3 hours to finally reach a density of 97.8% TD.

2) Monazite-type solid solution $Ln_{1-x}Ln'_xPO_4$ ceramics

Recently, several articles published by Arinicheva *et al.* [16,17] and Neumeier *et al.* [18] were dedicated to the sintering of monazite-type solid solutions $La_{1-x}Eu_xPO_4$. Arinicheva *et al.* [16] first studied the sintering and mechanical properties of monazite-type $La_{1-x}Eu_xPO_4$. In this study, the rhabdophane precursor was synthesized via the wet chemistry route reported by Meyssamy *et al.* [19]. The starting powder was prepared by heating the rhabdophane precursor at 600 °C for 2 hours. The densification was performed at 1350°C through hot pressing in order to obtain highly densified ceramics (98 %TD) [16]. Later, Neumeier *et al.* investigated the effect of the synthesis

routes on the sintering of $La_{0.5}Eu_{0.5}PO_4$ ceramics [18]. The optimized synthesis route was composed of a hydrothermal precipitation in acid condition (pH ≈ 1). The obtained rhabdophane precursor was calcined at 800°C for 2 hours to produce the monazite type starting powder. After sintering at 1450°C for 5 hours, the final density of the pellet equaled 92.5 %TD [18]. Finally, Arinicheva *et al.* [17] compared their method with that reported by Neumeier *et al.* [16,18,19]. They found that both methods led to large specific surface areas (over 100 $m^2.g^{-1}$) and to well sintered ceramics (> 94% TD) by using either conventional sintering conditions (1340 °C, 7h) or hot pressing conditions (1350°C, 2h) [17].

3) Monazite-cheralite solid solutions ceramics.

Contrary to monazites, all papers concerning the sintering of monazite-cheralite ceramics involved dry chemistry routes based on solid-state reactions. In this way, Montel *et al.* reported the sintering of $La_{0.73}Ce_{0.09}Th_{0.09}Ca_{0.09}PO_4$ [8,10]. The mixture of oxides and $NH_4H_2PO_4$ were calcined at 1250 °C for one night in order to prepare a homogeneous and single-phase monazite-cheralite type powder $La_{0.73}Ce_{0.09}Th_{0.09}Ca_{0.09}PO_4$. The specific surface value was equal to 0.2 $m^2.g^{-1}$ only. Hence, a milling treatment was applied to increase this value up to 6 – 7 $m^2.g^{-1}$. Montel *et al.* [8] reported that the sintering temperature should be higher than 1400°C to ensure a density of 95% TD for the final pellets. The optimized temperature was 1450°C. At this temperature, the densification was complete after 4 hours, with a final density of about 97% TD. Later, Glorieux *et al.* [10] also reported the sintering of $La_{0.73}Ce_{0.09}Th_{0.09}Ca_{0.09}PO_4$. The protocol used for the preparation of the precursor was modified in terms of phosphate source from $NH_4H_2PO_4$ to a mixture of lanthanum phosphates ($LaPO_4$ and $La(PO_3)_3$). The S_{SA} value associated with the starting material was similar to that reported by Montel *et al.* [8]. After sintering at 1450°C for 4 hours, the final density reached 95% TD as well. More recently, Popa *et al.* reported the sintering of cheralite $Ca_{0.5}Th_{0.5}PO_4$ prepared by a solid-state route. As $Ca_{0.5}Th_{0.5}PO_4$ would gradually decompose above 1250°C, the spark plasma sintering was applied. The sintering treatment was rapid, which took only several minutes for temperature ranging from 1255°C to 1310°C. The final density was 96-99% TD.

4) Interest to use rhabdophane as starting material in the sintering of $Nd_{1-2x}Th_xCa_xPO_4$ monazite-cheralite ceramics

According to the literature, there is a big interest in the application of rhabdophanes as starting material for sintering. Indeed, these powders, prepared through hydrothermal conditions, exhibit a large specific surface area that favors the sintering of the powders to prepare high-density ceramic (≥ 95% TD). Moreover, this large S_{SA} value avoids multiple milling cycles, which were necessary when using solid-state reactions. It can also reduce the

risk of dust contamination. Additionally, Bregiroux *et al.*'s dilatometry studies [9] suggested that the densification took place at lower temperatures when using rhabdophane precursors. As pointed out by Popa *et al.* [20], the cheralite has a lower thermal stability than monazite end-member. Thus, making the sintering at lower temperatures could avoid the potential decomposition of monazite-cheralite $Nd_{1-2x}Th_xCa_xPO_4$. Finally, as reported in Chapter I, the rhabdophane precursors prepared in this work exhibited good chemical homogeneity and led to single-phase monazite-cheralite powders by heating. All these results suggest the possibility to prepare homogenous and single-phase monazite-cheralite ceramics via directing sintering, from the as-prepared rhabdophane precursors.

III-1.2.2. Dilatometry study

As mentioned previously, Bregiroux *et al.* [9] reported a dilatometry study of $LaPO_4$ using three types of starting materials, *i.e.*, raw rhabdophane, monazite calcined at 700°C (M-700) and at 1400°C (M-1400-A5). During the analyses, the temperature raised from room temperature to 1400°C, with a rate of 5°C.min^{-1}. After cooling, the linear shrinkage of the pellet reached 20%, 15%, and 13% when starting from rhabdophane, M-700, and M-1400-A5, respectively. The profile of the derivative of the linear shrinkage of raw rhabdophane exhibited three minima, which corresponded to three transitions. The temperatures associated with these minima were noted as $T_{trans.}$ The first stage was observed from room temperature to about 450 °C. It was assigned to the dehydration of the starting rhabdophane. The second stage (observed between 450 and 800°C) corresponded to the phase transition into monazite. The final stage, which was associated with the sintering, began at about 900°C, and the T_{trans} of this stage was at about 1100°C. This result was in good agreement with the results reported in Chapter I for rhabdophane $Nd_{1-2x}Ca_xTh_xPO_4.nH_2O$. In the case of M-700, the sintering began at about 700°C, and the T_{trans} of densification was at about 1160°C. For M-1400-A5, the sintering also began at 900°C. However, the maximum densification rate appeared at about 1450°C (determined in an extra dilatometry test up to 1600°C). The initial S_{SA} of these three materials was 78.4, ~32, and 17.5 m^2.g^{-1} for raw rhabdophane, M-700, and M-1400-A5, respectively. A specific surface area over 30 m^2.g^{-1} reduced significantly the T_{trans} associated with the densification. Moreover, a more detailed study was applied to the monazite type starting from powders heated at 1400°C. Furthermore, Bregiroux *et al.* [9] used various milling processes to modify the initial S_{SA}, *i.e.*, ball milling for 5 hours (M-1400-B5, S_{SA} = 3.6 m^2.g^{-1}), attrition milling for 2 hours (M-1400-A2, S_{SA} = 11 m^2.g^{-1}) and attrition milling for 5 hours (M-1400-A5, S_{SA} = 17.5 m^2.g^{-1}). The linear shrinkage obtained starting from M-1400-B5, M-1400-A2, and

M-1400-A5 after a dilatometry experiment up to 1400°C equaled ~4%, 11%, and 13%, respectively. This experiment suggested a large S_{SA} would accelerate the densification.

For the monazite-cheralite solid solution, Montel *et al.* [8] performed dilatometry to compare the densification behavior of $LaPO_4$ and $La_{0.73}Ce_{0.09}Th_{0.09}Ca_{0.09}PO_4$. The initial S_{SA} was about 6-7 $m^2.g^{-1}$. They reported that the behavior of these two samples during sintering was similar. However, monazite-cheralite was associated with a more rapid densification than the monazite end-member. Later, Glorieux *et al.* [10] reported the dilatometry study of $La_{0.73}Ce_{0.09}Th_{0.09}Ca_{0.09}PO_4$ in detail. The preparation of the starting materials was the same as that reported by Montel *et al.*, but phosphate source was $LaPO_4$ and $La(PO_3)_3$ instead of $NH_4H_2PO_4$. Two sintering atmospheres were applied then compared (*i.e.* air and argon), showing no significant difference. The influence of the heating rate applied during dilatometry was also considered. Heating rates were fixed to 1°C.min^{-1}, 5°C.min^{-1}, 10°C.min^{-1} and 30°C.min^{-1}. These experiments were labeled G-1°C.min^{-1}, G-5°C.min^{-1}, G-10°C.min^{-1}, and G-30°C.min$^{-1,}$ respectively. The shrinkage began at about 1200°C. This starting sintering temperature was higher than that of $LaPO_4$ ($T_{begin} \approx 900$°C) reported by Bregiroux *et al.* [9]. The derivative of the dilatometry curves showed two successive minima and therefore suggested a two-step process, unlike the paper of Bregiroux *et al.* on $LaPO_4$ [9]. The temperatures corresponding to these two minima under different temperature rates are listed in **Table III-2**. Glorieux *et al.* [10] suggested that the first minimum was linked to the densification process, whereas the second minimum was associated with the grain growth. Meanwhile, this study underlined that a lower temperature rate could reduce the temperature of sintering, as these two minima took place at a lower temperature. Finally, the shrinkage of the monazite-cheralite samples prepared by Glorieux *et al.* [10] took place at higher temperatures than when using raw rhabdophane or M-700 but at lower temperatures compared to M-1400-A5 according to the data mentioned by Bregiroux *et al.* [14].

III-1.2.3. Sintering maps

Bregiroux *et al.* [9] built a sintering map for $LaPO_4$ using monazite powder previously calcined at 1400°C and milled by the attrition process. The sintering temperatures considered were equal to 1400°C, 1450°C, and 1500 °C, whereas the heating time ranged from 0.5 to 5.5 hours. For each temperature, the obtained maximum density was over 95% TD. However, to reach this density, the sintering time was 5.5 hours at 1400°C, 1 hour at 1450°C, and only half an hour at 1500°C. Otherwise, the grain growth at 1400°C was not evident; the average grain

size was varying from 0.2 µm to 0.45 µm. Moreover, it reached 0.8 µm and 1.2 µm at 1450°C and 1500°C, respectively.

Perrière *et al.* [13] also established a sintering map for $LnPO_4$, with Ln = La, Pr, Nd, Eu. The sintering conditions were fixed to T = 1500°C and $0.1 \leq t \leq 20$ hours. For all the compositions studied, the final densities were also above 95% TD. The maximum grain size of $LaPO_4$ was about twice that of other compositions (4.8 µm vs. ~ 2 µm). Moreover, the sintering map suggested that the maximum grain size decreased when the atomic number of the lanthanide increased. This result implied that the cationic radius might influence the grain growth in monazite-type ceramics.

These two sintering maps also provided interesting information on the control of the microstructure for monazite ceramics through the adjustment of the sintering temperature or chemical composition. Nevertheless, the authors considered either a single chemical composition or a single sintering temperature. Besides, the influence of actinides incorporation was not taken into account. Indeed, few studies dealt with studies on radioactive materials. To our knowledge, only Clavier *et al.* reported the sintering map of ThO_2 [6], while Cherkaski *et al.* published recently that of $Th_{1-x}Y_xO_{2-x/2}$ [7]. Consequently, the sintering map of $Nd_{1-2x}Th_xCa_xPO_4$ solid solutions ($x = 0 – 0.1$) had to be established during this work. In this way, we will describe the effect of the coupled substitution on the sintering and the impact of the sintering temperature and heating duration on the final monazite-cheralite ceramics prepared. Therefore, they will constitute a useful tool to understand the impact of Th-doping and to monitor the final microstructure of the prepared ceramics

III-1.2.4. Microhardness of monazite or monazite-cheralite type ceramics

In the safety evaluation of a radwaste matrix, several mechanical properties are considered as important indicators for the properties of the ceramics, such as Young's modulus, shear modulus, microhardness, etc. In this study, the microhardness of $Nd_{1-2x}Th_xCa_xPO_4$ will also be determined. Indeed, the microhardness remains of primary importance to anticipate the microstructural evolution of the ceramic wasteform under chemical or radiative stresses and to provide insights on its sustainability. Several studies reported that the microhardness of the monazite type ceramics ranged from 5 to 6 GPa (**Table III-3**) [5,11–13,15]. For instance, Arinicheva *et al.* [16] reported the microhardness of monazite-type solid solutions $La_{1-x}Eu_xPO_4$, which equaled 3-6 GPa. Additionally, Popa *et al.* [20] also gave a value for $Ca_{0.5}Th_{0.5}PO_4$ (6.74 ± 0.15 GPa).

Table III-1. Conditions of preparation and sintering, physicochemical properties of the precursors and density of the resulting pellets according to literature.

	Ln	Synthesis Methods	Precursors*	$T_{calcination}$	Milling	Final starting materials*	S_{SA} ($m^2.g^{-1}$)	Sintering conditions	d_{fin} (%.TD)
Monazite $LnPO_4$									
Hikichi *et al.* [11,12]	La, Ce Nd, Sm	Wet chemistry	R	600°C	Yes	M	52.8–69.8	1200 °C, 3–5h	99
Bregiroux *et al.* [9]	La, Ce	Wet chemistry	R	No	No	R	78.4	1400 °C, 1h	95.5
	La, Ce	Wet chemistry	R	700°C	No	M	~32	1400 °C, 1h	78 – 96
	La, Ce	Wet chemistry	R	1400°C	Ball milling 5h	M	3.6	1400 °C, 1h	71.8
	La, Ce	Wet chemistry	R	1400°C	Attrition milling 2h	M	11	1400 °C, 1h	89
	La, Ce	Wet chemistry	R	1400°C	Attrition milling 5h	M	17.5	1400 °C, 1h	97.2
Perrière *et al.* [13]	La, Nd Eu, Pr	Solid-state reaction	M	No	Ball milling	M	5–10	1500 °C, 20h	98
Bregiroux *et al.* [14]	La	Solid-state reaction	M	No	Attrition milling 5h	M	25	1425 °C, 1h	98
Babelot *et al.* [15]	La	Wet chemistry	R	350°C	No	R	72	1400°C, 3h	97.8
	La	Wet chemistry	R	500°C	No	R	63	1400°C, 3h	98

	Ln	Synthesis Methods	Precursors*	$T_{calcination}$	Milling	Final starting materials*	S_{SA} ($m^2.g^{-1}$)	Sintering conditions	d_{fin} (%.TD)
	La	Wet chemistry	R	950°C	No	M	5	1400°C, 3h	97.8
Monqzite type solid solutions $Ln_xLn'_{1-x}PO_4$									
Arinicheva et al. [16]	$La_{1-x}Eu_x$	Wet chemistry	R	600°C	No	R	No data	1350C°C, 2h Hot press 50 MPa	98
Neumeier et al. [18]	La, Eu (50%)	co-precipitation (pH 1)	R	600°C	No	M	No data	1450°C, 5h	89.8
	La, Eu (50%)	Hydrothermal synthesis (pH 1)	R	800°C	No	M	No data	1450°C, 5h	92.5
	La, Eu (50%)	Hydrothermal synthesis (pH10.5)	R	800°C	No	M	No data	1450°C, 5h	92.4
Arinicheva et al. [17]	La, Eu (50%)	Hydrothermal synthesis (pH 1)	R	800°C	No	M	155	1340°C, 7h	94
	La, Eu (50%)	Hydrothermal synthesis (pH 1)	R	800°C	No	M	155	1350C°C, 2h Hotpress 50 MPa	99
Arinicheva et al. [17]	La, Eu (50%)	Wet synthesis (pH 10)	R	800°C	No	M	110	1340°C, 7h	96
	La, Eu (50%)	Wet synthesis (pH 10)	R	800°C	No	M	110	1350C°C, 2h Hotpress 50 MPa	99
Monazite-Cheralite type solid solutions									

	Ln	Synthesis Methods	Precursors*	$T_{calcination}$	Milling	Final starting materials*	S_{SA} ($m^2.g^{-1}$)	Sintering conditions	d_{fin} (%.TD)
Montel *et al.* [8]	Ca, Th Ce, La (9%, 9% 9%, 73%)	Solid-state reaction	M	No	Ball milling	M	6–7	≥1400°C, ≥2h	≥95
Glorieux *et al.* [10]	Ca, Th Ce, La (9%, 9% 9%, 73%)	Solid-state reaction	M	No	Ball milling	M	≤7	1450°C, 4h	≥95
Popa *et al.* [20]	Ca, Th (50%)	Solid-state reaction	M	No	Ball milling	M	No data	SPS 1255°C 1min dwell	99
	Ca, Th (50%)	Solid-state reaction	M	No	Ball milling	M	No data	SPS 1310°C no dwell	96.5

* R is representing rhabdophane, M is for Monazite.

Table III-2. Temperatures related to the minimum of the derivative of the linear shrinkage (T_{trans}), relative shrinkage and other data reported in the literature.

	Composition	S_{SA}($m^2.g^{-1}$)	Code	T_{trans} (°C)	Relative shrinkage	Final density
Bregiroux *et al.* [9]	$LaPO_4$	78.4	Raw rhabdophane	~1100	20%	95.5%TD
		~ 32	M-700	1160	15%	96%TD
		3.6	M-1400-B5	No data	~4%	71.8%TD
		11.2	M-1400-A2	No data	11%	89.3%TD
		17.5	M-1400-A2	1475	13%	96.7%TD
Glorieux *et al.* [10]	Ca, Th,Ce, La (9%, 9%, 9%, 73%)	≤7	G-1°C.min^{-1}	1226, 1360	12-16%	95.1%TD
		≤7	G-5°C.min^{-1}	1286, 1378	12-16%	93.3%TD
			G-10°C.min^{-1}	1319, 1391	12-16%	91.3%TD
			G-30°C.min^{-1}	1378, 1420	12-16%	93.9%TD

Table III-3. Microhardness of monazite type ceramics reported in the literature.

	Composition of cations	Relative density (% TD)	Grain size (µm)	Microhardness (GPa)
Hikichi *et al.* [11,12]	La, Ce, Nd, Sm	99	No data	5 – 6
Perrière *et al.* [13]	La, Pr, Nd, Eu	≥95	2-5	5 ± 0.5
Bregiroux *et al.* [5]	La	95.8	1.08	5.0 ± 0.8
	Pr	97.2	1.53	5.5 ± 0.5
	Nd	98.2	2.07	5.6 ± 0.6
		98.7	2.59	4.8 ± 0.7
	Eu	91.4	1.25	4.6 ± 0.5
		94.8	1.87	4.4 ± 0.5
Babelot *et al.* [15]	La	98	1.7 ± 0.2	5.7 ± 0.1
Arinicheva *et al.* [16]	$La_{1-x}Eu_x$	98	No data	3 – 6
Popa *et al.* [20]	Ca, Th (50%)	99	No data	6.74 ± 0.15

III-2. Experimental

III-2.1. Preparation of rhabdophane-type $Nd_{1-2x}Th_xCa_xPO_4.nH_2O$ precursors

The synthesis of $Nd_{1-2x}Th_xCa_xPO_4.nH_2O$ rhabdophane precursors followed the procedure reported in the previous chapters (see **Chapter** I-2 **and** I-3). However, the amount of powder prepared from each batch was scaled up four times, *i.e.*, from 500 mg to 2 g. Two batches were made for each targeted composition to provide enough materials for the following experiments. Four chemical compositions were investigated, all of them being within the stability domain of $Nd_{1-2x}Th_xCa_xPO_4.nH_2O$ solid solutions reported in **Chapter** I-3. For each prepared rhabdophane sample, about 100 mg of powder was converted into monazite-cheralite after a heating treatment at 1100 °C for 6 hours. The heated samples and their associated rhabdophane precursors have been examined by PXRD, and the collected patterns confirmed that all the samples were single phase monazite-cheralite solid solutions (**Figure III-3**).Meanwhile, the chemical compositions of the rhabdophanes were also accurately determined after the total dissolution of the solids and ICP-OES measurements. All the samples were found to meet the expected stoichiometry considering the attached uncertainties (**Table III-4**). Consequently, the protocol reported in **Chapter** I-3. could be applied directly in a larger scale synthesis.

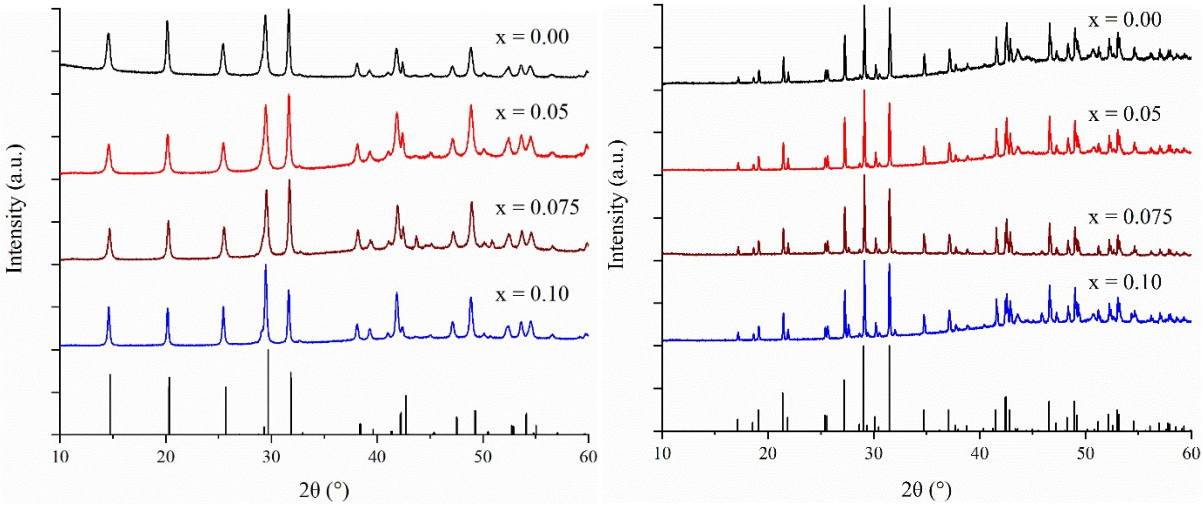

Figure III-3. PXRD patterns obtained for $Nd_{1-2x}Th_xCa_xPO_4.nH_2O$ rhabdophane (left) and associated $Nd_{1-2x}Th_xCa_xPO_4$ monazite-cheralite obtained after conversion at 1100 °C for 6 hours (right)

Table III-4. Chemical composition of the prepared $Nd_{1-2x}Th_xCa_xPO_4.nH_2O$ rhabdophane-type samples obtained by total dissolution analysis of the powdered samples and their specific surface area determined by BET tests.

x (target value)	Ca	Th	Nd	P/(Ca+Th+Nd)	S_{SA} ($m^2.g^{-1}$)
0	---	---	1.00 ± 0.01	1.00 ± 0.01	55 ± 1
0.05	0.07 ± 0.02	0.05 ± 0.01	0.88 ± 0.01	0.99 ± 0.01	51 ± 1
0.075	0.10 ± 0.02	0.08 ± 0.01	0.82 ± 0.01	1.00 ± 0.01	26 ± 1
0.10	0.10 ± 0.02	0.10 ± 0.01	0.80 ± 0.01	1.02 ± 0.01	24 ± 1

Besides, the specific surface areas of the rhabdophane precursors were also determined by using the BET measurement. The S_{SA} values ranged from 24 to 55 $m^2.g^{-1}$ (**Table III-4**.). The Ca-Th coupled substitution then resulted in a decrease of S_{SA}. However, monazite-cheralite type powders prepared through solid-state reactions were usually reported below 20 $m^2.g^{-1}$ [8,10]. Hence, the as-synthesized rhabdophane precursors still presented a relatively large S_{SA} value even for the highest incorporation rate studied (x = 0.10), which should be in favor of efficient densification during sintering.

III-2.2. Pellets preparation

Before sintering, rhabdophane precursors were pelletized using a uniaxial pressing (500 MPa) at room temperature. For dilatometric studies, a typical mass of about 200 mg was introduced in a Ø5 mm tungsten carbide die, resulting in green pellets of about 2 mm in thickness (green density ≈ 60-65 % TD). For the establishment of sintering maps, die of 8mm in diameter was used to produce larger pellets and to make easier further manual polishing step. In this case, about 300 mg of powder was used while applied pressure remained unchanged, resulting in similar green densities.

III-2.3. XRD characterization

XRD characterization was performed on the sintered ceramics pellets, using a Bruker D8 ADVANCE diffractometer with Cu $K\alpha_{1+2}$ radiation (λ = 1.54184 Å). The pellets were previously polished to reach a mirror-grade surface and analyzed without any anti-contamination device. The XRD patterns were collected under the conditions reported in Chapter I (*i.e.* reflection geometry and $5 \leq 2\theta \leq 100°$). A $\Delta 2\theta$ step of 0.019° with a collection time of 3.68 s per step was considered. Besides, a powder pattern of pure silicon was collected in similar conditions and used as an external standard to extract the instrumental function. The collected patterns were refined by the Rietveld method using the Fullprof_Suite package [21].

III-2.4. Density measurements

The masses of the sintered pellets were first measured by Mettler Toledo analytical balance. The bulk volume was then determined by geometric measurements with the help of a precision caliper, leading to bulk density values ρ_{bulk}. In parallel, the pycnometric density ρ_{pycno}, which eliminates the contribution of the open pore volume, was determined by the helium pycnometer, using a Micromeritics Accupyc 1340 apparatus. The theoretical density (TD) was calculated by using the unit cell volumes as follows:

$$\rho_{theoretical} = \frac{M \times Z}{N_A \times V} \quad \text{(III-3)}$$

where M is the molar mass of the compound, Z the number of formula units per cell (Z = 4), N_A the Avogadro number, and V the unit cell volume. As reported in Chapter I, the monazite-cheralite samples could be considered as ideal solid solutions. According to Vegard's law, their unit cell volumes were then be calculated by linear interpolation between $NdPO_4$ and $Ca_{0.5}Th_{0.5}PO_4$ end members [22,23]. The difference between the volume determined by the method Rietveld and the estimated value is less than 1%.

Table III-5. Cell volume of monazite-cheralite $Nd_{1-2x}Ca_xTh_xPO_4$.

x	Unit cell Volume (Å^3)	Reference
0	291.92	Clavier *et al.* [23]
0.05	291.64	
0.075	291.51	
0.10	291.37	
0.50	289.16	Raison *et al.* [22]

Finally, the relative density d_{bulk} and d_{pycno} were determined as follows:

$$d_{bulk} = \frac{\rho_{bulk}}{\rho_{theoretical}} \times 100\% \quad \text{(III-4)}$$

$$d_{pycno} = \frac{\rho_{pycno}}{\rho_{theoretical}} \times 100\% \quad \text{(III-5)}$$

Hence, the respective contributions of open and closed porosities were obtained from:

$$\phi_{open} = d_{pycno} - d_{bulk} \quad \text{(III-6)}$$

$$\phi_{closed} = 1 - d_{pycno} \quad \text{(III-7)}$$

III-2.5. Dilatometric study

Dilatometric measurements were conducted on a Setaram Setsys Evolution apparatus for the establishment of $Nd_{1-2x}Ca_xTh_xPO_4$ sintering maps. Green pellets were initially disposed between two alumina platelets and then heated up to 1400 °C under airflow, with a heating rate of 5 °C.min^{-1}. The same rate was applied for cooling to avoid thermal fracture.

The activation energy associated with the first stage of densification was also determined thanks to Dorn's method [3–5], which is based on several incremental isothermal heat treatments (1000-1500°C). According to Johnson's model [24], the linear shrinkage under isothermal process is a function of time:

$$\frac{\Delta l}{l_0} = k(T)t^n \quad \text{(III-8)}$$

Therefore, the velocity of densification could be expressed by:

$$v = \frac{d\left(\frac{\Delta l}{l_0}\right)}{dt} = nk(T)\left(\frac{\Delta l}{l_0}\right)^{\frac{n-1}{n}} \quad \text{(III-9)}$$

Supposing that the grain growth during densification was negligible, so that:

$$k(T) = \frac{k_0}{T}\exp\left(-\frac{E_A}{RT}\right) \quad \text{(III-10)}$$

In this study, the temperature gap between the two successive isothermal treatments T_1 and T_2 was small enough (50°C) and the heating rate was high (30°C.min^{-1}) which led to:

$$\left(\frac{\Delta l}{l_0}\right)_{end\ step\ T_1} = \left(\frac{\Delta l}{l_0}\right)_{beginning\ step\ T_2} \quad \text{(III-11)}$$

The ratio between the associated velocities of densification could be expressed as:

$$\frac{v_2}{v_1} = \frac{T_1}{T_2}\exp\left(-\frac{E_A}{R}\left(\frac{1}{T_2}-\frac{1}{T_1}\right)\right) \quad \text{(III-12)}$$

Consequently, the activation energy could be deduced, as follows:

$$E_A = \frac{RT_1T_2}{T_1-T_2}\ln\left(\frac{v_1T_1}{v_2T_2}\right) \quad \text{(III-13)}$$

III-2.6. Electronic microscopy and image processing

Before making the SEM observations, sintered pellets were polished to reach a mirror-like surface (with a 1 µm diamond spray). Grain boundaries were further revealed by thermal etching during 8 hours at 1000°C under air atmosphere, which was considered not to modify the microstructure of the samples significantly. Several images (typically 4 to 8) were recorded

on each sample to reach good representativeness. High vacuum conditions, associated with a very low accelerating voltage (2kV), were chosen to obtain high-resolution images.

SEM images were then processed using ImageJ software to assess the grain size distribution [25]. In this aim, grain boundaries were manually drawn to collect 300-1000 grains at the surface of each sample. The data collection depended on the image quality and the sintering conditions applied to the sample. The equivalent diameter of each grain (D) was calculated considering the grain surface (A) measured by ImageJ, as follows:

$$D = 2\left(\frac{A}{\pi}\right)^{1/2} \quad \text{(III-14)}$$

The median diameter D_{50} was applied as the reported diameter for the establishment of the sintering map because it corresponds to 50 % of the cumulative frequency in a log-normal distribution. The mean grain size $\overline{D}$ was also determined as the mean value of the whole collected grain sizes.

III-2.7. Microhardness

Microhardness of the monazite-cheralite samples were measured from Vickers micro-indentation tests (Shimadzu HMV-G21D). The principle of the measurement is based on the application of a constant load for a given time using a pyramidal diamond indenter with a square base and an apex angle equal to 136 ° (**Figure III-4**). The projection of an ideal indentation on the pellet surface is a square with a diagonal of d_c. The surface area A of the indentation is therefore,

$$A = \frac{d_c^2}{2\sin(136°/2)} \approx \frac{d_c^2}{1.85} \quad \text{(III-15)}$$

Microhardness (H_V, expressed in GPa) was, therefore, calculated using the following formula,

$$H_V = \frac{\mathrm{F}}{\mathrm{A}} = 1.85 \times 10^3 \cdot \frac{F}{d_c^2} \quad \text{(III-16)}$$

where F (N) is the applied load, and d_c (µm) is the average length of Vickers indentation's diagonal.

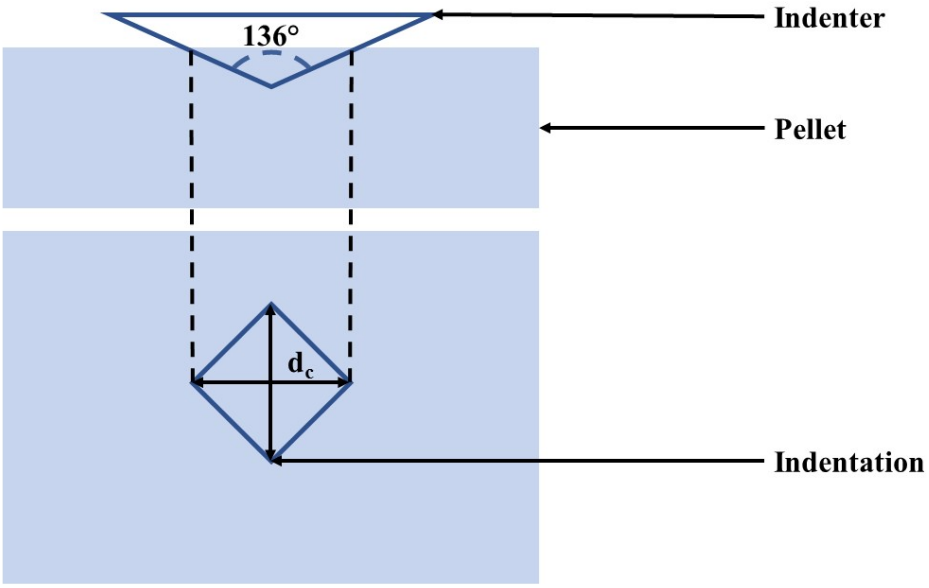

Figure III-4. Scheme of the Vickers test

Before the Vickers test, the pellet surfaces were polished. With the help of the equipped microscope, the indentations were managed to took place in the center of the selected grains (as shown in **Figure III-5**)

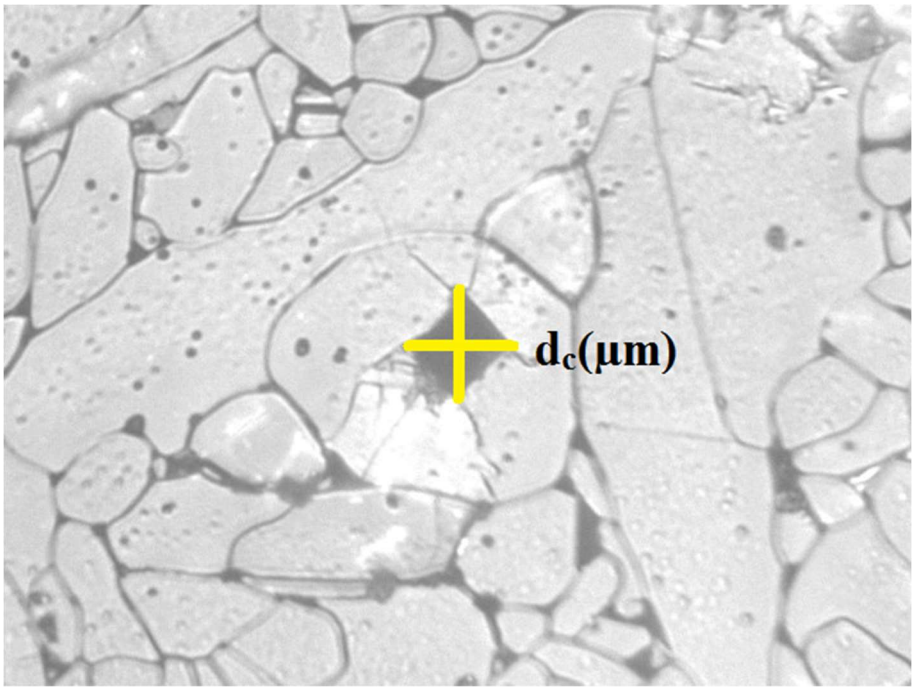

Figure III-5. Example of indentation of the Vickers test

During the first Vickers test, the loading force varied from 0.1 to 2 N to determine the optimal value, which would be applied for all following tests. The full indentation load was

applied for 5s. For each indenting force, ten measurements were performed to obtain the average value.

III-3. Results and Discussions

III-3.1. Dilatometric study

The dilatometric study was undertaken to determine the operating conditions leading to fully densified monazite-cheralite pellets directly from the as-synthesized rhabdophane powders. The variation of the relative linear shrinkage of the pellets versus temperature and the associated derivative is reported in **Figure III-6**. All the samples followed a similar trend, which was described as the succession of three steps. The first one was assigned to the dehydration process leading from the monoclinic $Nd_{1-2x}Th_xCa_xPO_4.nH_2O$ to the hexagonal $Nd_{1-2x}Th_xCa_xPO_4$. It took place between 100 and 300°C, as already mentioned in Chapter II. In this range of temperatures, the vaporization of water was not expected to impact the microstructure of the pellets, neither by modifying the porosity network nor by creating microscopic defects such as cracks. Indeed, as the green density approached 60% of the theoretical value, the water was easily evacuated through a large number of open pores still present in the solid. Also, this dehydration step was only associated with a small swelling of the pellet, which is accommodated without any significant modification of the morphology.

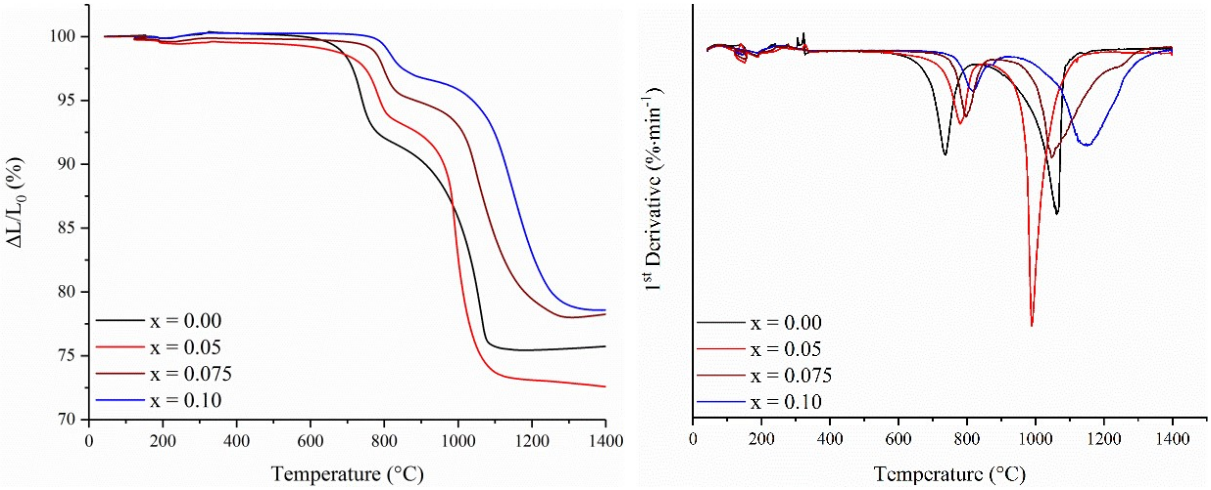

Figure III-6. Dilatometry curves and associated derivative plots obtained from $Nd_{1-2x}Th_xCa_xPO_4.nH_2O$ pellets.

The second step was associated with a 2.5 – 7.5 % relative linear shrinkage, which began at about 600°C and ended at around 900°C. As mentioned in Chapter II, it was correlated to the conversion of the anhydrous rhabdophane precursors to monazite-cheralite solid solutions. Despite the important volume drop observed, no significant crack formation was evidenced at this stage. However, slight deformation of the cylindrical shape was noted in some cases (especially when sintering the pellets at 1200°C). Finally, the last shrinkage step was observed

typically above 850°C. It was correlated to the sintering of the samples. This result was then in agreement with the data reported by Bregiroux *et al.* for the direct sintering of rhabdophane-type $LaPO_4$ ($T \approx 900°C$) [9].

Moreover, it is worth noting that, for all the samples, the densification took place between 850°C and 1350°C since no additional shrinkage was observed above this temperature. This range of temperatures was then significantly lower than that reported by Glorieux *et al.* [10] for the densification of $La_{0.73}Ce_{0.09}Th_{0.09}Ca_{0.09}PO_4$, synthesized by solid-state route (1200°C - 1600°C). Besides, T_{trans}, which was the temperature of the highest densification rate (determined from the minimum of the derivative curve), was systematically found between 990-1151°C in this study (**Table III-6**). In comparison, that of $La_{0.73}Ce_{0.09}Th_{0.09}Ca_{0.09}PO_4$ lied between 1286-1378°C (G-5°C.min^{-1} listed in **Table III-2**) [10]. The direct sintering from Th-bearing rhabdophanes led to a drop of the densification temperature, which was probably due to its high specific surface area and to its good cationic homogeneity

Table III-6. Information on the minimum peaks in the derivative of linear shrinkage, which are relating to the densification during sintering.

x	T_{begin} (°C)	T_{end} (°C)	T_{trans} (°C)
0	849	1129	1062
0.05	856	1162	990
0.075	910	1302	1047
0.10	945	1356	1151

Even though Glorieux *et al.* [10] observed a two-step shrinkage during the sintering of the $La_{0.73}Ce_{0.09}Th_{0.09}Ca_{0.09}PO_4$ monazite-cheralite (peaks positions listed in **Table III-2**), the shrinkage obtained in this study during direct sintering from rhabdophane was more likely a one-step process according to the derivative curves, as reported by Bregiroux *et al.* for $LnPO_4$ end-members [9]. Glorieux *et al.* [10] suggested that the first stage of shrinkage was due to densification while the second, caused by grain growth, would take place at a higher temperature, however with a close gap, *i.e.* 1286°C and 1378°C for G-5°C.min^{-1} (**Table III-2**). In this study, however, the densification took place at a much lower temperature (below 1200°C) and proceeded much faster. The grain growth process might, therefore, has begun at a lower temperature leading to the disappearance of the second minimum peak on the derivative curve.

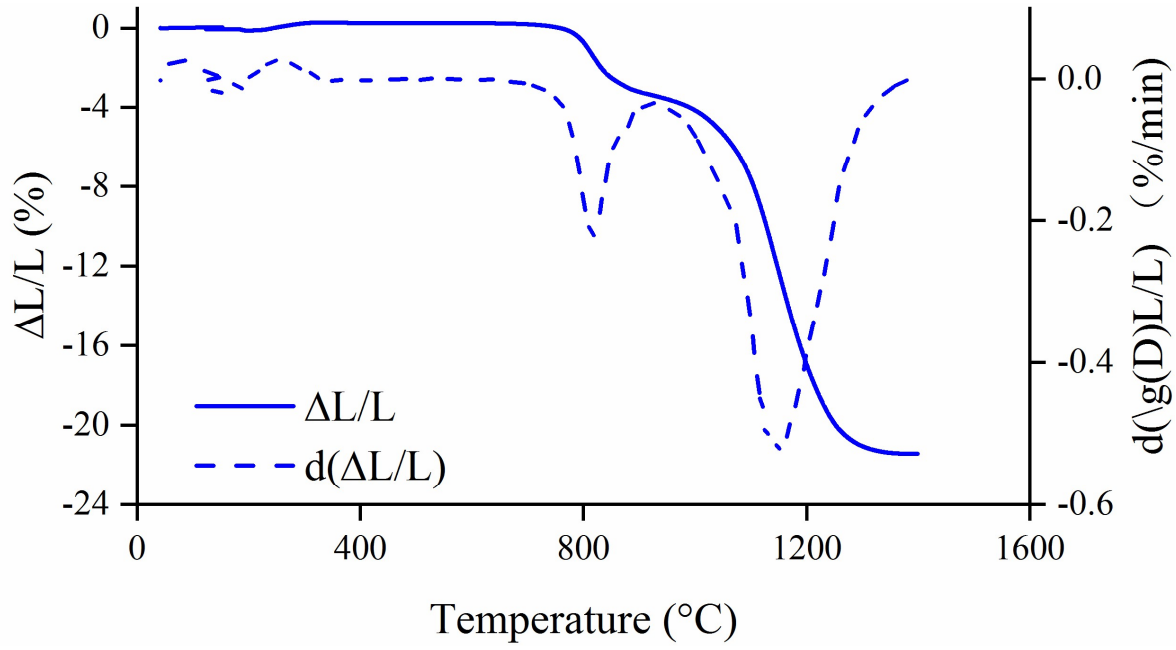

Figure III-7. Dilatometry curse and associated derivative curves reported for $Nd_{0.8}Ca_{0.1}Th_{0.1}PO_4$ in this study

As reported in **Table III-6**, T_{trans}, the temperature associated with the maximum densification rate (*i.e.*, minimum of the derivative curve) globally increased with the Th-Ca doping. However, for the lowest substitution rate investigated, *i.e.*, for x = 0.05, the densification took place at a lower temperature (990°C) than for $NdPO_4$ (1062°C). The T_{trans} was also smaller for x = 0.05, which suggested a more rapid densification. This phenomenon was reported by Colomer *et al.* [26] in their study on the effect of Sr^{2+} on the sintering behavior of $LaPO_4$. According to the derivative curves of linear shrinkage obtained for $LaPO_4$, $La_{0.975}Sr_{0.025}PO_{3.988}$, and $La_{0.950}Sr_{0.050}PO_{3.975}$, they showed that the T_{trans} took place at 1180°C for the undoped material compared to 1000°C for the doped samples. They explained this phenomenon by the creation of oxygen vacancies due to the incorporation of small amounts of a divalent and the formation of sintering aid $La(PO_3)_3$. Even though the formation of $Nd(PO_3)_3$ was not observed in the PXRD diagram of $Nd_{0.9}Ca_{0.05}Th_{0.05}PO_{0.4}$, a slight calcium excess was noted in the determined chemical composition of $Nd_{0.9}Ca_{0.05}Th_{0.05}PO_{0.4}$ (**Table III-4**). The formation of oxygen vacancies was thus possible. They would increase the diffusion of elements, therefore, accelerated the densification rate for $Nd_{0.9}Ca_{0.05}Th_{0.05}PO_{0.4}$. Additionally, the temperatures related to the beginning and the end of the densification process increased with the coupled incorporation, *i.e.*, 849-945°C for the beginning, and 1129-1356°C for the end (**Table III-6**).

From our study, the incorporation of thorium (typically for $x > 0.05$) seemed to slow down the densification and led to higher sintering temperatures. This observation contradicted the results of Montel *et al.* [8], who reported that the shrinkage of $La_{0.73}Ce_{0.08}Ca_{0.09}Th_{0.09}PO_4$ was more efficient than that of pure monazite end-member during a similar dilatometry test. Considering their sample was synthesized through a solid-state route, one could suggest that local heterogeneities might have accelerated the densification step. Conversely, the rhabdophane precursor obtained by hydrothermal treatment during this study presented a better homogeneity in terms of cation distribution. Consequently, solute drag effects might operate due to the segregation of thorium towards grain boundaries, leading the grain growth to slow down. Such a mechanism is well known and was already reported for several kinds of ceramic materials such as oxides [27], titanates [28], or niobiates [29]. Besides, the diffusion of Th in the monazite was reported to be 3 orders of magnitude lower than that of Pb [30], which can be considered to be similar to that of Ca [31] and slower than Nd [32]. Consequently, the incorporation of Th would decrease the diffusion process and hence slow down the densification process.

Dorn's method was later applied to determine the activation energy associated with the densification process of the initial stage (**Table III-7** and **Figure III-8**). To avoid any bias due to the rhabdophane-monazite conversion occurring at about 800°C, the temperature range considered for the isothermal heat treatments was set from 1000 to 1500°C. For $NdPO_4$ and $Nd_{0.9}Th_{0.05}Ca_{0.05}PO_4$ samples, the densification was fast and appeared to be complete at 1100°C, which led to consider only one or two temperature intervals to assess E_A values. On the contrary, for $x = 0.075$ and $x = 0.1$, the densification ended at about 1250°C, thus five values were considered for each composition. The activation energy obtained for pure $NdPO_4$, ($E_A = 530 \pm 90$ kJ.mol^{-1}) [5] appeared in excellent agreement with that reported by Bregiroux *et al.* for $LaPO_4$ (532 ± 80 kJ.mol^{-1}). For $x = 0.05$, the E_A value was significantly lower than for the other compositions, which could explain the faster densification observed. Conversely, for higher Ca-Th coupled substitution, the activation energy increased, even though, for $x = 0.075$ and 0.1, it remained slightly lower than that obtained for $NdPO_4$.

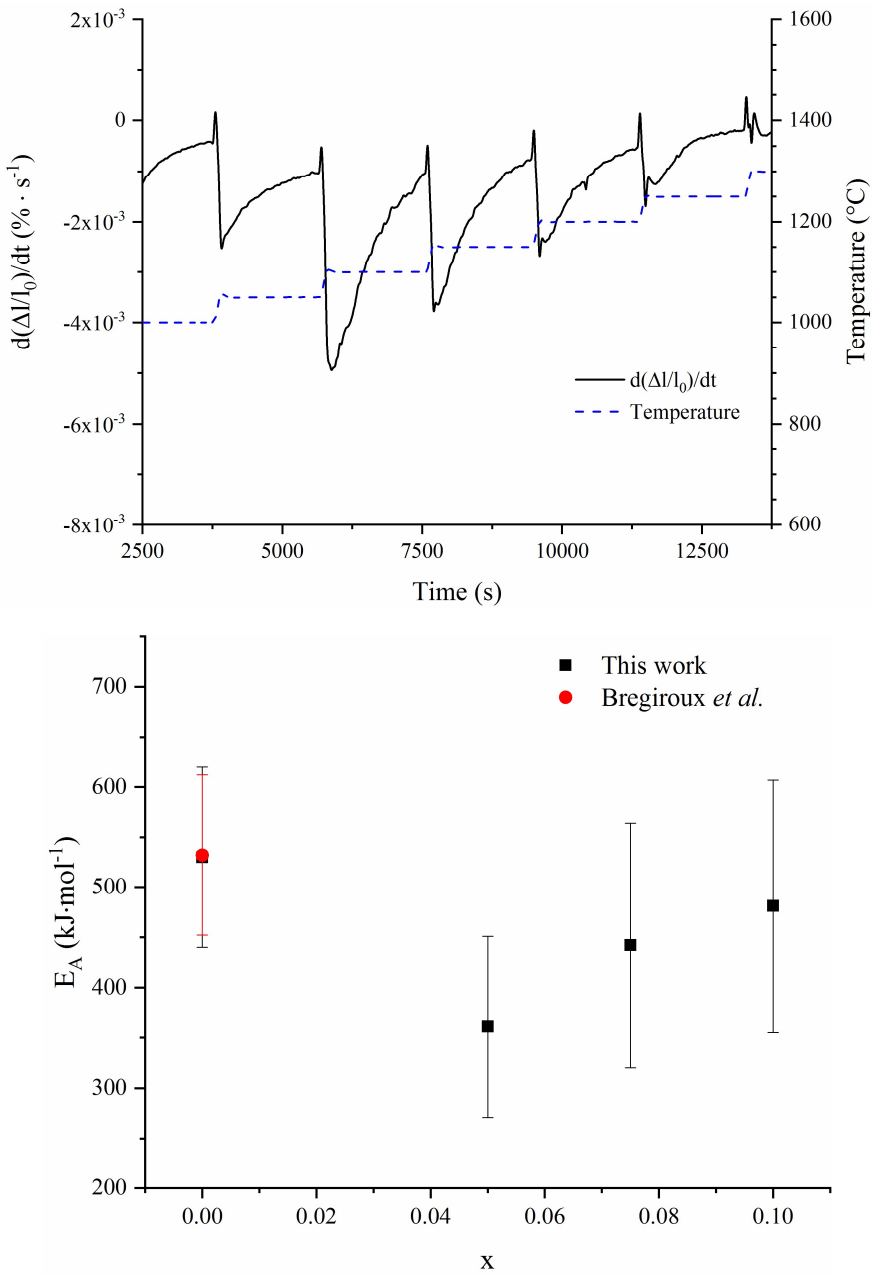

Figure III-8. Determination of $Nd_{1-2x}Th_xCa_xPO_4$ sintering activation energy using the Dorn's method (top) and variation of the activation energy related to the initial stage of sintering as a function of the Ca-Th incorporation rate, *x* (bottom) [5].

Table III-7. Average activation energies determined for $Nd_{1-2x}Th_xCa_xPO_4$ solid solutions using the Dorn's method.

	x	S_{SA} ($m^2.g^{-1}$)	E_A ($kJ.mol^{-1}$)
Bregiroux [5]	$LaPO_4$	17.5 ± 0.2	532 ± 80
This work	0	55 ± 1	530 ± 90
	0.05	51 ± 1	360 ± 90
	0.075	26 ± 1	440 ± 120
	0.10	24 ± 1	480 ± 130

III-3.2. Establishment of sintering map

The sintering map usually represents the variation of the grain size (e.g., mass median diameter D_{50}) versus the relative density under different sintering conditions (*e.g.*, temperature, heating time, chemical composition, etc.). It is thereby of great interest to control the final microstructure of ceramics, including radioactive wasteform ones. According to the dilatometry study already presented, the linear shrinkage of $Nd_{1-2x}Ca_xTh_xPO_4$ was systematically found to be complete above 1200°C. Three temperature set points, *i.e.*, 1200°C, 1300°C, and 1400°C were thus considered while the sintering time window varied from 1 to 8 h.

III-3.2.1. Density measurements

The evolution of the relative measured geometrical density (d_{bulk}) is presented in **Figure III-9**. Despite the variation of the chemical composition, the density of the pellets systematically reached 95 % TD after heating for at least 4 hours at 1400°C, which evidenced that direct sintering from as-synthesized rhabdophane precursors could yield to highly densified monazite-cheralite type ceramics. Nevertheless, the Th-Ca coupled substitution slowed down the densification. Indeed, the densification was complete after only 4 hours at 1200°C for $NdPO_4$, while high-density $Nd_{0.8}Ca_{0.1}Th_{0.1}PO_4$ pellets were only obtained at 1400°C. According to the paper published by Bregiroux *et al.* [9], the direct sintering of $NdPO_4$ allowed to obtain highly densified ceramics at lower temperatures, as their usual sintering conditions was 1400°C for 1 hour. However, for x = 0.10, the sintering temperature was closed to that of $La_{0.73}Ce_{0.09}Th_{0.09}Ca_{0.09}PO_4$ suggested by Montel *et al.* [8] and Glorieux *et al.* [10] (1450°C).

Accordingly, He-pycnometry measurements (**Table III-8** and **Table III-11**) showed that higher temperatures and longer sintering times were required to fully eliminate the open porosity and start removing the closed one when the Th and Ca substitution rate increased.

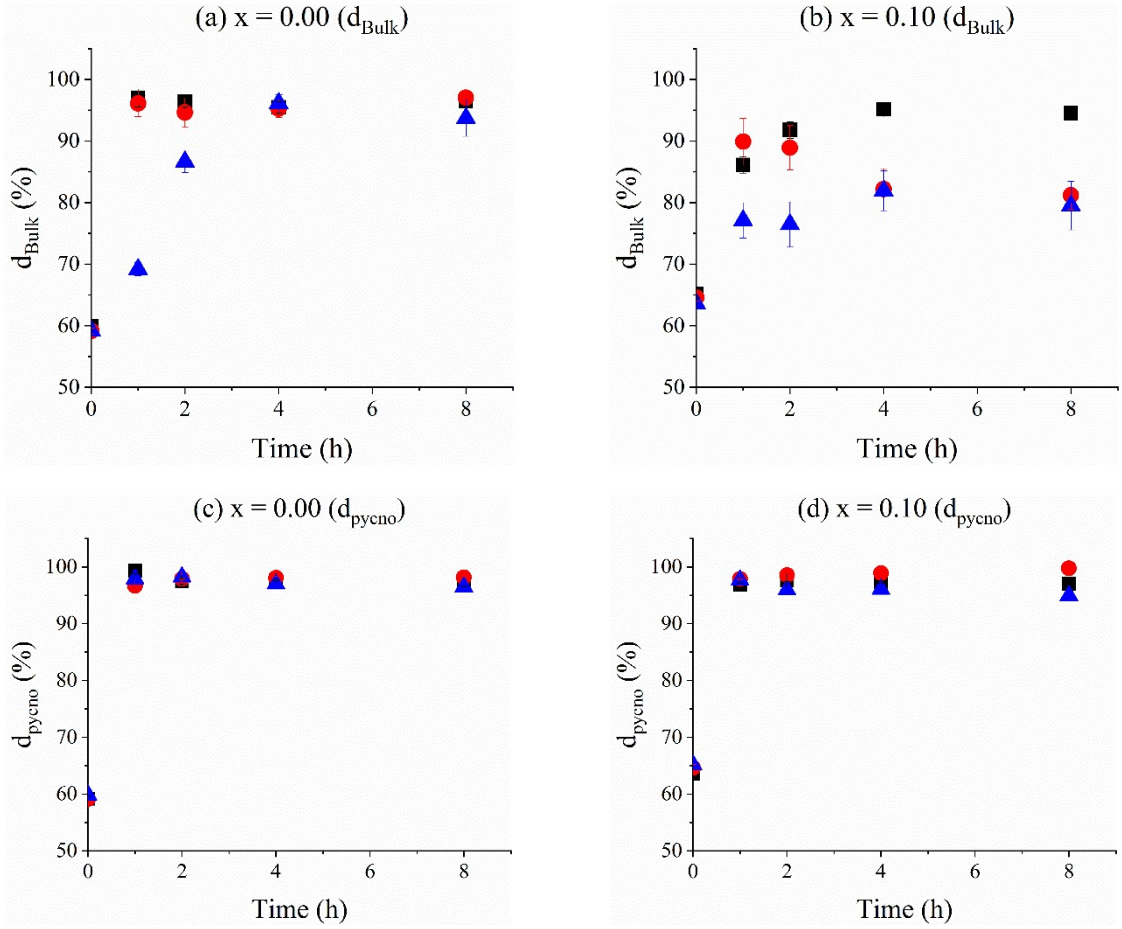

Figure III-9. Evolution of relative density of $Nd_{1-2x}Ca_xTh_xPO_4$ pellets obtained for different temperatures (▲ 1200 °C, ● 1300 °C and ■ 1400 °C). The relative density was determined either by geometric measurement d_{bulk} (a,b) or by He-pycnometry d_{pycno} (c,d).

Table III-8. Densities and D_{50} values determined for the $Nd_{1-2x}Ca_xTh_xPO_4$ pellets ($x = 0$).

Temperature (°C)	Time (h)	d_{bulk} (%)	d_{pycno} (%)	ϕ_{open} (%)	ϕ_{closed} (%)	D_{50} (µm)
1200	1	69 ± 1	99.3 ± 0.5	30 ± 1	0.7 ± 0.5	0.11 ± 0.07
	2	87 ± 2	97.4 ± 0.5	11 ± 2	2.6 ± 0.5	0.18 ± 0.08
	4	96 ± 1	97.6 ± 0.2	1 ± 1	2.4 ± 0.2	0.11 ± 0.07
	8	94 ± 3	96.7 ± 0.2	3 ± 3	3.3 ± 0.2	0.12 ± 0.10
1300	1	96 ± 2	96.7 ± 0.2	1 ± 2	3.3 ± 0.2	0.14 ± 0.13
	2	95 ± 2	97.9 ± 0.2	3 ± 2	2.1 ± 0.2	0.17 ± 0.19
	4	95 ± 1	98.1 ± 0.3	3 ± 1	1.9 ± 0.3	7.22 ± 6.94
	8	97 ± 1	98.2 ± 0.2	1 ± 1	1.8 ± 0.2	8.51 ± 7.68
1400	1	97 ± 1	97.9 ± 0.3	1 ± 1	2.1 ± 0.3	8.01 ± 6.80
	2	96 ± 1	98.2 ± 0.2	2 ± 1	1.8 ± 0.2	9.72 ± 8.32
	4	95 ± 1	97.0 ± 0.4	2 ± 1	3.0 ± 0.4	11.37 ± 9.68
	8	96 ± 1	96.5 ± 0.3	0 ± 1	3.5 ± 0.3	8.12 ± 7.21

Table III-9. Densities and D_{50} values determined for the $Nd_{1-2x}Ca_xTh_xPO_4$ pellets (x = 0.05).

Temperature (°C)	Time (h)	d_{bulk} (%)	d_{pycno} (%)	ϕ_{open} (%)	ϕ_{closed} (%)	D_{50} (µm)
1200	1	68 ± 2	100.3 ± 0.3	32 ± 2	0.0 ± 0.3	0.10 ± 0.05
	2	73 ± 4	99.7 ± 0.3	27 ± 4	0.3 ± 0.3	0.09 ± 0.06
	4	85 ± 3	97.5 ± 0.2	13 ± 3	2.5 ± 0.2	0.12 ± 0.09
	8	75 ± 5	99.2 ± 0.2	24 ± 5	0.8 ± 0.2	0.09 ± 0.08
1300	1	80 ± 4	97.3 ± 0.2	17 ± 4	2.7 ± 0.2	0.11 ± 0.13
	2	88 ± 4	98.8 ± 0.2	11 ± 4	1.2 ± 0.2	0.26 ± 0.27
	4	84 ± 4	97.6 ± 0.3	13 ± 4	2.4 ± 0.3	0.72 ± 0.78
	8	94 ± 1	96.5 ± 0.2	2 ± 1	3.5 ± 0.2	0.54 ± 0.25
1400	1	92 ± 2	96.8 ± 0.3	4 ± 2	3.2 ± 0.3	0.61 ± 0.31
	2	93 ± 1	96.9 ± 0.2	4 ± 1	3.1 ± 0.2	0.78 ± 0.42
	4	92 ± 2	95.9 ± 0.3	4 ± 2	4.1 ± 0.3	0.80 ± 0.67
	8	92 ± 3	96.2 ± 0.3	4 ± 3	3.8 ± 0.3	2.85 ± 2.24

Table III-10. Densities and D_{50} values determined for the $Nd_{1-2x}Ca_xTh_xPO_4$ pellets (x = 0.075).

Temperature (°C)	Time (h)	d_{bulk} (%)	d_{pycno} (%)	ϕ_{open} (%)	ϕ_{closed} (%)	D_{50} (µm)
1200	1	68 ± 2	100.1 ± 0.4	32 ± 2	0.0 ± 0.4	0.10 ± 0.07
	2	69 ± 3	99.5 ± 0.2	31 ± 3	0.5 ± 0.2	0.10 ± 0.08
	4	76 ± 4	97.5 ± 0.2	21 ± 4	2.5 ± 0.2	0.10 ± 0.08
	8	73 ± 4	98.4 ± 0.2	26 ± 4	1.6 ± 0.2	0.09 ± 0.06
1300	1	77 ± 3	94.3 ± 0.2	17 ± 3	5.7 ± 0.2	0.11 ± 0.10
	2	81 ± 6	100.2 ± 0.5	19 ± 6	0.0 ± 0.2	0.11 ± 0.14
	4	88 ± 3	98.8 ± 0.2	11 ± 3	1.2 ± 0.2	0.32 ± 0.21
	8	95 ± 2	98.0 ± 0.2	3 ± 2	2.0 ± 0.2	0.28 ± 0.26
1400	1	88 ± 2	98.7 ± 0.3	11 ± 2	1.3 ± 0.3	0.18 ± 0.11
	2	91 ± 1	98.2 ± 0.3	7 ± 1	1.8 ± 0.3	0.18 ± 0.15
	4	94 ± 1	97.3 ± 0.4	3 ± 1	2.7 ± 0.4	0.97 ± 0.58
	8	94 ± 1	96.7 ± 0.3	3 ± 1	3.3 ± 0.3	1.04 ± 0.65

Table III-11. Densities and D_{50} values determined for the $Nd_{1-2x}Ca_xTh_xPO_4$ pellets (x = 0.1).

Temperature (°C)	Time (h)	d_{bulk} (%)	d_{pycno} (%)	ϕ_{open} (%)	ϕ_{closed} (%)	D_{50} (µm)
1200	1	77 ± 3	96.8 ± 0.3	20 ± 3	3.2 ± 0.3	0.09 ± 0.06
	2	76 ± 4	97.6 ± 0.2	21 ± 4	2.4 ± 0.2	0.09 ± 0.07
	4	82 ± 3	97.3 ± 0.2	16 ± 3	2.7 ± 0.2	0.08 ± 0.06
	8	79 ± 4	97.0 ± 0.2	18 ± 4	3.0 ± 0.2	0.11 ± 0.11
1300	1	90 ± 4	97.9 ± 0.2	8 ± 4	2.1 ± 0.2	0.09 ± 0.09
	2	89 ± 4	98.6 ± 0.2	10 ± 4	1.4 ± 0.2	0.08 ± 0.11
	4	82 ± 3	98.9 ± 0.2	17 ± 3	1.1 ± 0.2	0.11 ± 0.11
	8	81 ± 2	99.7 ± 0.3	19 ± 2	0.3 ± 0.3	0.24 ± 0.11
1400	1	86 ± 1	97.7 ± 0.3	12 ± 1	2.3 ± 0.3	0.28 ± 0.14
	2	92 ± 1	96.0 ± 0.3	4 ± 1	4.0 ± 0.3	0.41 ± 0.20
	4	95 ± 1	96.1 ± 0.4	1 ± 1	3.9 ± 0.4	1.14 ± 0.53
	8	94 ± 1	94.9 ± 0.3	1 ± 1	5.1 ± 0.3	1.32 ± 0.74

III-3.2.2. SEM observations and Grain size determination

The SEM images presented in **Figure III-10** confirmed that highly densified pellets were obtained for all the Ca/Th doping rates studied after heating at 1400°C for 8 hours. Also, the grains exhibited an oblong-polygon morphology, which was in good agreement with the work published by Arinicheva *et al.* [17], who reported that the use of precursors with initial needle-like morphology could result in dense ceramics with elongated grains. For $NdPO_4$, the maximum length of the grains was about 50 µm with a width around 15 µm. On the other hand, the Th-Ca co-substitution was found to inhibit the grain growth, with D_{50} decreasing from 8.1 µm (for $x = 0$) to 1.3 µm (for $x = 0.1$).

Apart from the chemical composition, the temperature appeared as a very important factor in driving the average grain size. For $Nd_{0.8}Ca_{0.1}Th_{0.1}PO_4$, D_{50} reached 0.11 ± 0.11 µm after heating at 1200°C for 8 hours, meaning that no significant grain growth occurred at this temperature (**Figure III-11**). Additionally, several pores were observed, which was consistent with the relative density value determined (79 ± 4 % TD). At 1300°C, the grain size increased slightly as the D_{50} reached 0.24 ± 0.11 µm. However, the pore contribution was not reduced, and the relative density remained comparable (81 ± 2 % TD). Conversely, the grain size increased by about one order of magnitude after heating at 1400°C (1.32 ± 0.74 µm) while open pores were significantly eliminated, leading to a dense ceramic with 94 ± 1 % TD. Consequently, the sintering temperature should be equal to 1400°C to prepare high-density $Nd_{0.8}Ca_{0.1}Th_{0.1}PO_4$ ceramics. For the other compositions, however, the sintering temperature could be lower. For instance, $NdPO_4$ could reach 97 ± 1 % TD with D_{50} = 8.5 µm after only 8 hours at 1300°C.

Finally, the impact of the sintering time was also investigated (**Figure III-13**). At 1400°C, the grain size of $Nd_{0.8}Ca_{0.1}Th_{0.1}PO_4$ grew significantly over time, *i.e.*, from 0.28 µm after 1 hour to 1.32 µm after 8 hours. Simultaneously, the open porosity dropped down, leading the relative density to increase from 86 ± 1 to 94 ± 1 % TD. It is also worth noting that the pellet sintered at 1400°C for 1 hour exhibited slightly larger grain size and higher density than that prepared at 1300°C for 8 hours, which indicated that temperature had a more substantial impact on the sintering process than sintering duration. Moreover, it is important to underline that for all the samples studied, the grain size distribution followed a log-normal distribution (**Figure III-12** and **Figure III-14**), which was in agreement with previous papers [8,10,14].

The normalized grain size, which is the ratio of the equivalent diameter of a grain over the average grain size of the pellet (noted as $D/\bar{D}$), and cumulative normalized grain size distribution is a useful tool to verify whether an abnormal grain growth happened during

sintering. In the case of a normal grain growth, the cumulative normalized grain size distribution is independent of the sintering time under any sintering conditions despite changes in temperature or chemical composition [7,17,33]. This invariance versus time called self-similarity, was observed during the sintering of $Nd_{1-2x}Ca_xTh_xPO_4$ (**Figure III-12**), showing no abnormal grain growth phenomenon for such kinds of monazite-cheralite solid solutions.

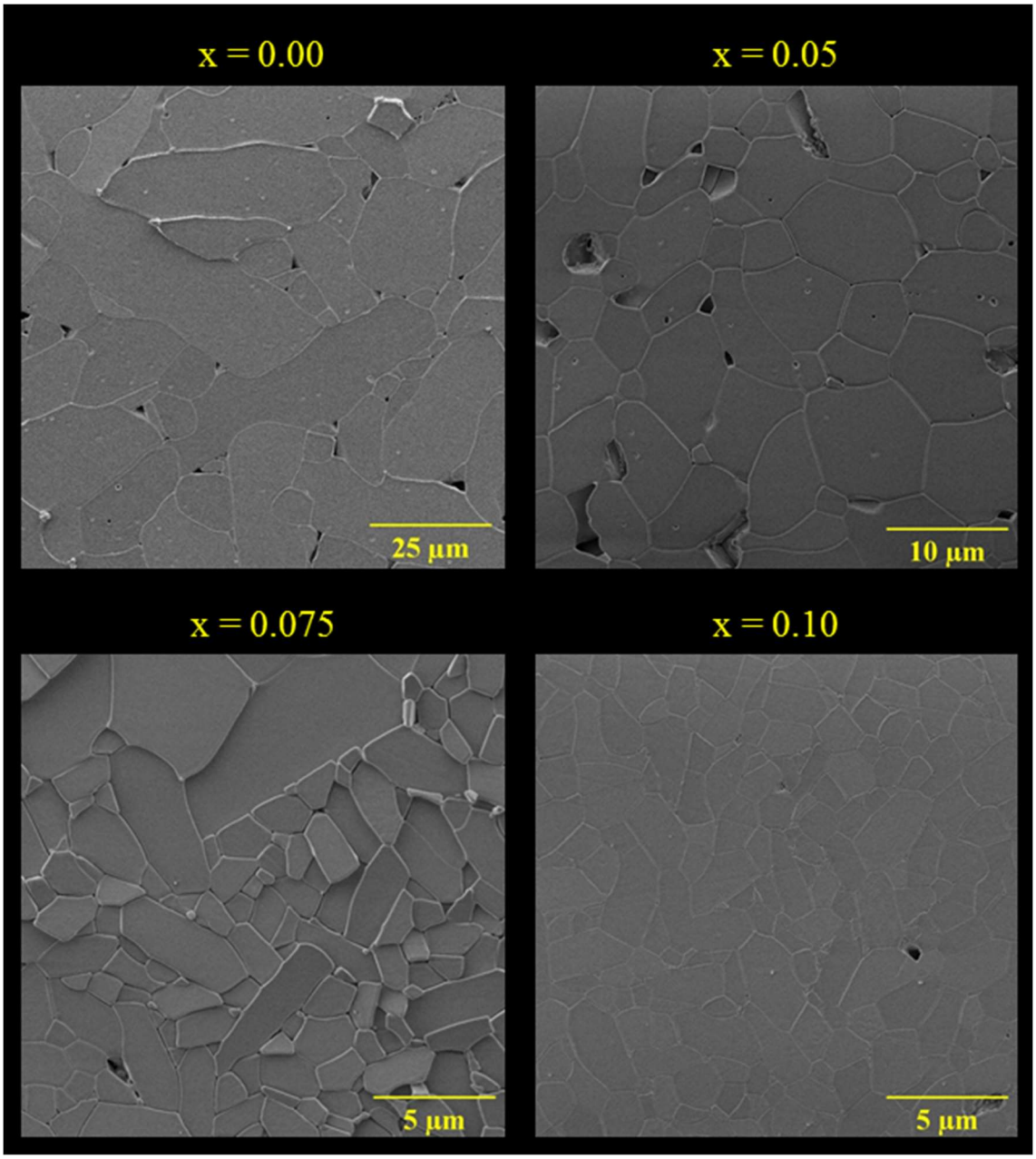

Figure III-10. SEM micrographs obtained for $Nd_{1-2x}Ca_xTh_xPO_4$ pellets obtained after sintering at 1400°C for 8 hours.

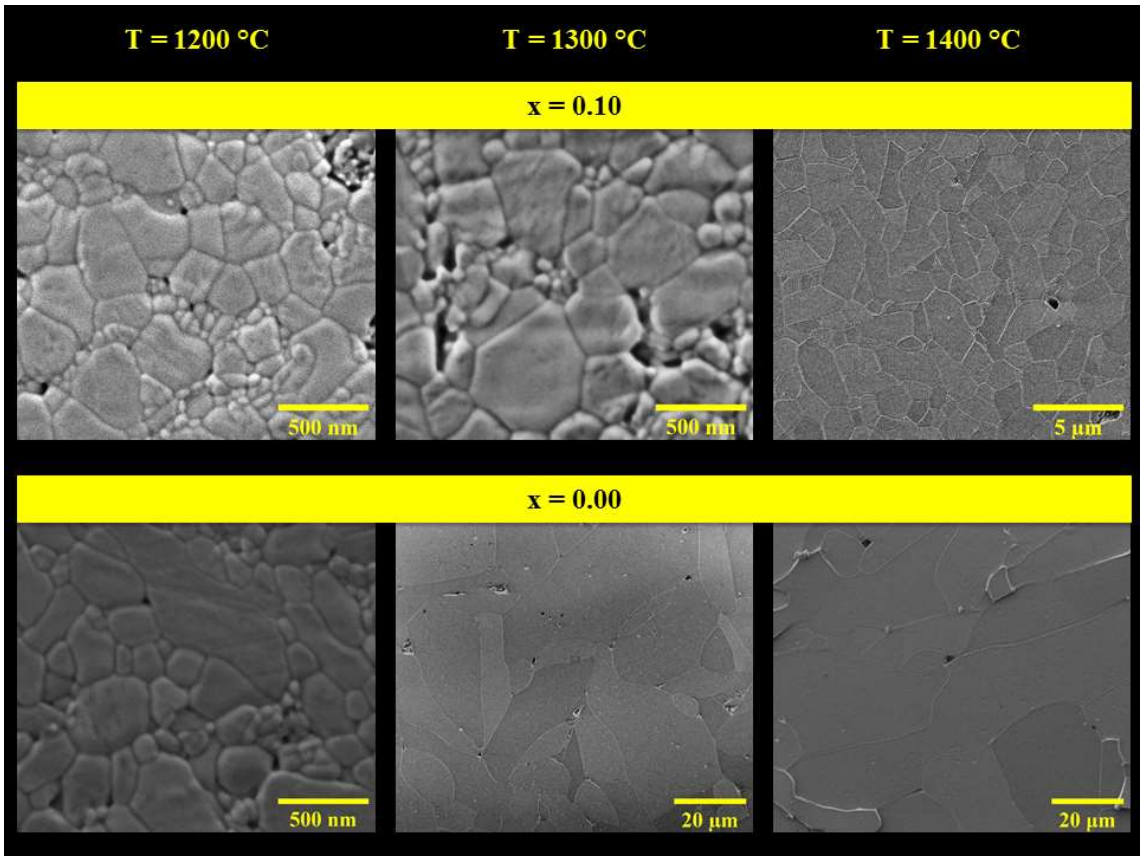

Figure III-11. SEM micrographs obtained for $Nd_{0.8}Ca_{0.1}Th_{0.1}PO_4$ and $NdPO_4$ pellets obtained after sintering at 1200°C, 1300°C and 1400°C for 8 hours.

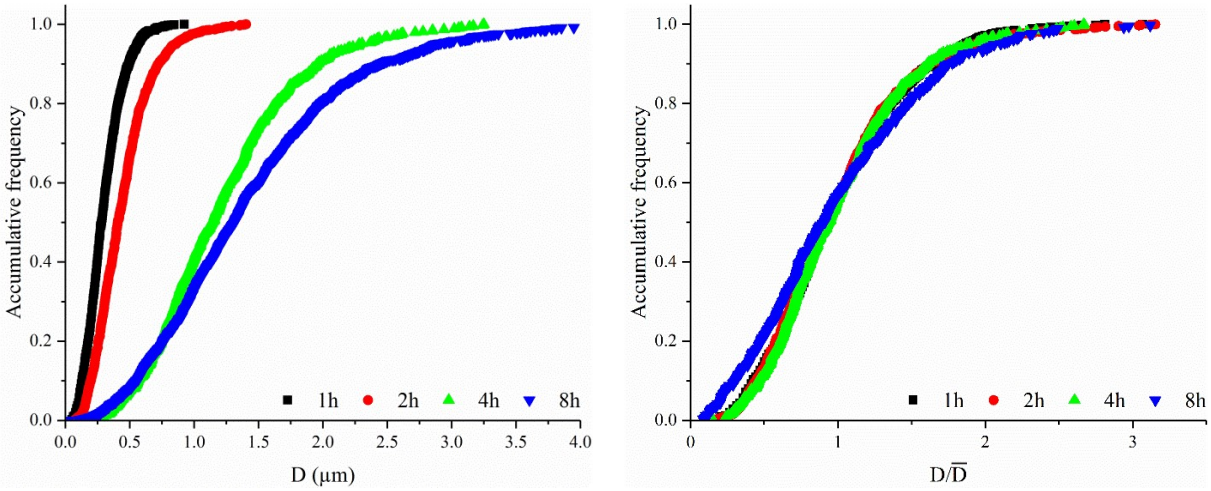

Figure III-12. Cumulative grain size distribution obtained for $Nd_{0.8}Ca_{0.1}Th_{0.1}PO_4$ pellets *vs* sintering time at 1400°C.

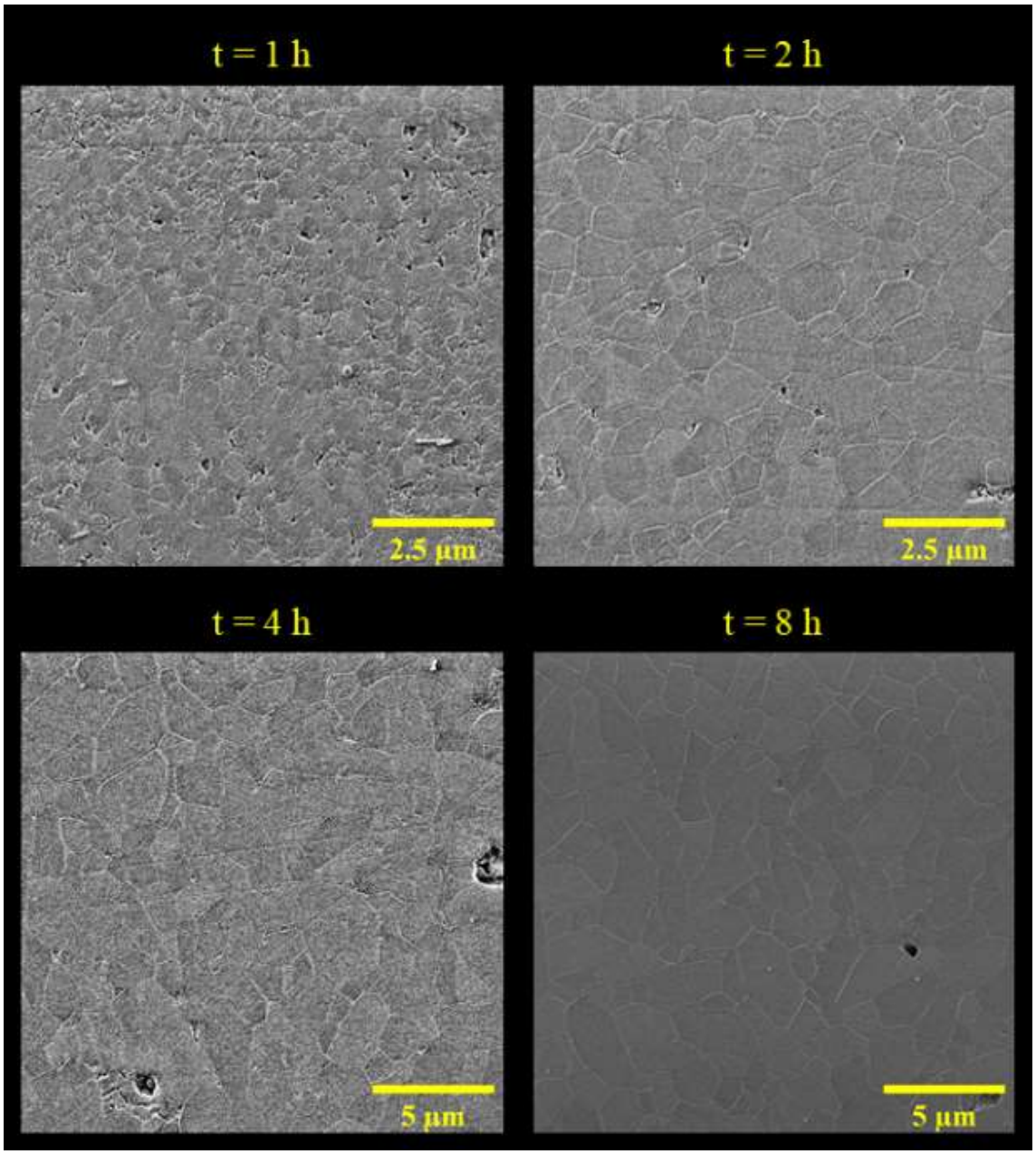

Figure III-13. SEM micrographs obtained for $Nd_{0.8}Ca_{0.1}Th_{0.1}PO_4$ pellets prepared after sintering at 1400°C for various sintering durations.

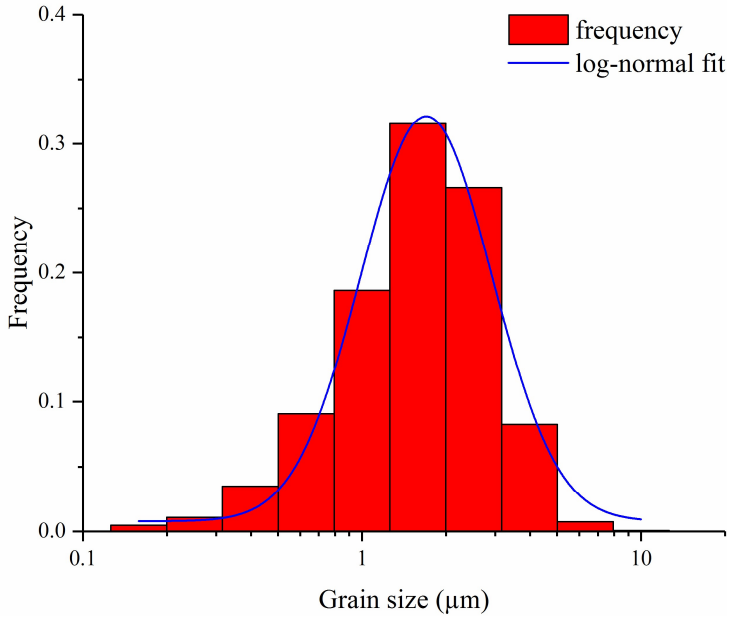

Figure III-14. Grain size distribution obtained for $Nd_{0.8}Ca_{0.1}Th_{0.1}PO_4$ sintered pellets prepared after heating at 1400°C for 8 hours.

III-3.2.3. Sintering map

After the determination of bulk relative densities and grain sizes (D_{50}), the sintering trajectories of $Nd_{1-2x}Ca_xTh_xPO_4$ solid solutions were finally built up. All the 48 tests were first gathered according to the sintering temperature (**Figure III-15a**). At 1200°C, the grain growth appeared to be limited ($D_{50} \leq 0.24$ µm). Conversely, sintering was dominated by densification with relative density rising from 68 % TD to 96 % TD. This result then paved the way to the elaboration of highly densified ceramics showing a submicrometric microstructure. At 1400°C, most of the samples presented a relative density higher than 90 % TD, while D_{50} ranged across two orders of magnitude (from 0.18 to 11.4 µm, depending on the chemical composition considered). This indicated that the densification was complete, and the grain growth became the predominant behavior. On this basis, samples sintered at 1300°C exhibited an intermediate behavior, where both densification and grain growth played essential roles, leading pellet density to rise from 77 % TD to 97 % TD and D_{50} to increase from 0.08 to 8.5 µm.

Besides, all the samples were grouped according to their chemical composition (**Figure III-15b**). As already discussed, the Th and Ca coupled substitution seemed to slow down both the densification and the grain growth. For $NdPO_4$, all the prepared samples usually presented a high relative density (> 90 % TD) and could reach an important grain size ($D_{50} > 8$ µm) when heating at 1300-1400°C. Therefore, they were mostly located on the top right region of the sintering map. With the increase of the substitution rate, the samples gradually occupied the

lower left region. As a matter of example, the maximum D_{50} for $Nd_{0.8}Ca_{0.1}Th_{0.1}PO_4$ samples was 1.3 µm, which was one order of magnitude smaller than for $NdPO_4$ (11.4 µm).

Finally, we established the sintering map of $NdPO_4$, including the data reported by Bregiroux *et al.* for $LaPO_4$ [9]. The application of the rhabdophane ($S_{SA} \approx 55\ m^2.g^{-1}$) as starting material led to a highly densified ceramic with a median grain size of 8.5 µm for a sintering temperature of 1300°C. It has to be compared to that was observed starting from monazite heated at 1400°C (S_{SA} =17.5 $m^2.g^{-1}$) for which the grain growth was limited to only 1 µm despite a higher sintering temperature considered (1500°C) [9]. Once again, these results support the importance of the starting specific surface area for the improvement of the grain growth during sintering.

As radioactive wasteform ceramic, the pellets should be highly densified, with a reduced porosity, which could decrease the specific surface of the matrix and therefore improve the chemical durability. Meanwhile, a larger grain size is associated to lower density of grain boundaries and triple junctions, which act as weakness zones during leaching tests, and consequently, strengthen the chemical durability of the ceramic during corrosion processes. For these reasons, the preparation of monazite-cheralite type pellets using $Nd_{1-2x}Ca_xTh_xPO_4.nH_2O$ rhabdophane as the starting precursor appears as a promising method to produce highly refractory conditioning ceramics in the field of specific actinide immobilization.

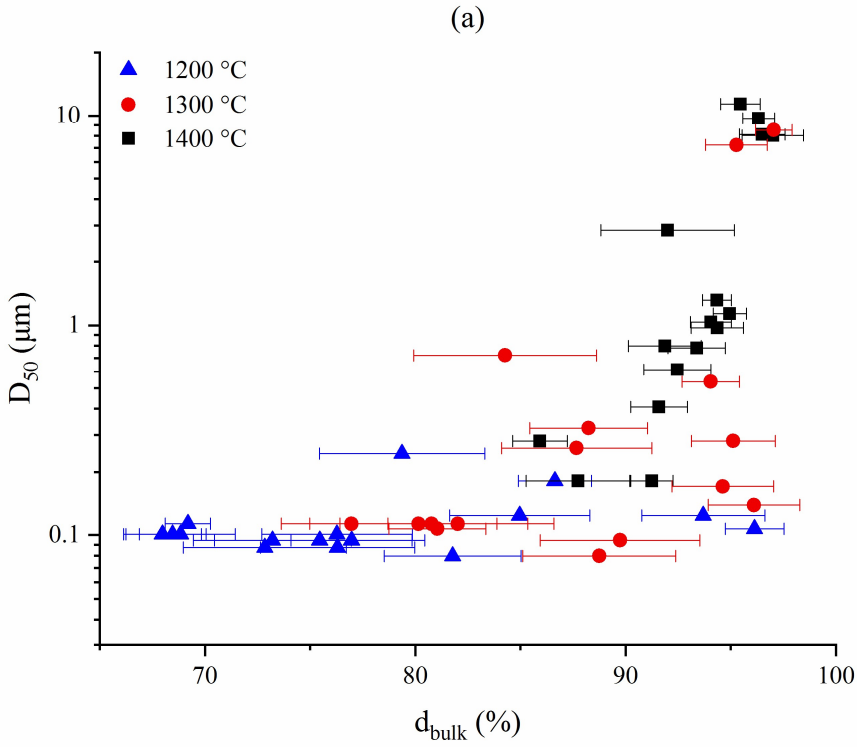

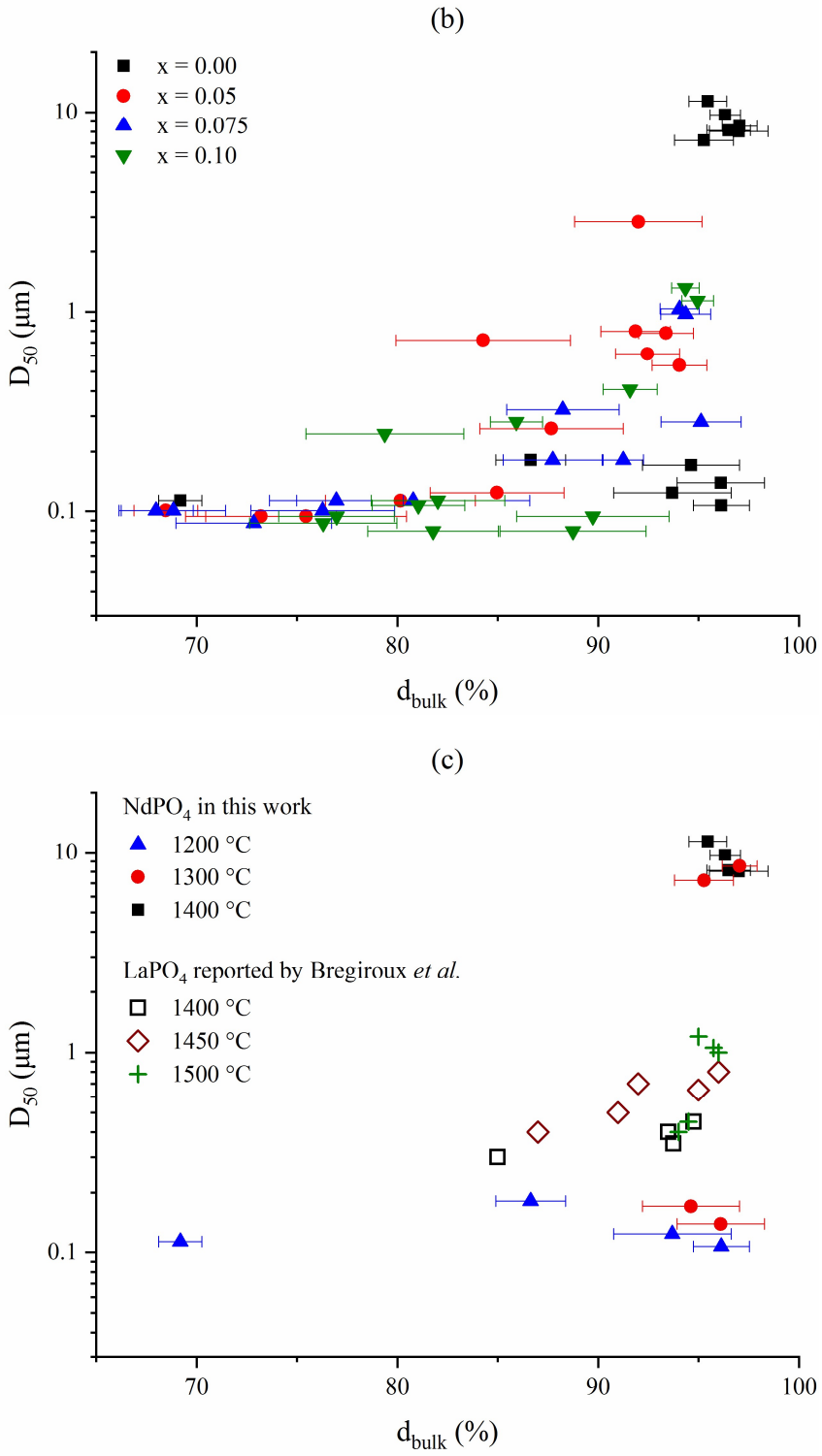

Figure III-15. Sintering map obtained for $Nd_{1-2x}Ca_xTh_xPO_4$ ceramics. All the samples are gathered depending on their sintering temperature (a) or on their chemical composition (b). Comparison between $NdPO_4$ (this work) and $LaPO_4$ (Bregiroux *et al.* [14]) (c).

III-3.3. Microhardness

The microhardness of the $Nd_{1-2x}Ca_xTh_xPO_4$ ceramics was determined by using the Vickers hardness test. With this objective, all the pellets were sintered at 1400°C for 8 hours to

produce dense ceramics and finally polished to reach a mirror-grade surface. According to the previous reports, the microhardness determined by the Vickers test depends on the loading force [5,16]. If the loading force is too high, the material around the indenter broke, leading to an underestimation of the microhardness. As a result, the $NdPO_4$ pellet was firstly indented with different loads ranging from 0.1 to 2 N in order to optimize the loading force. In this test, ten measurements were performed randomly on the polished surface for each loading force to determine the average microhardness. The collected results presented no significant variation when the loading force increased from 0.1 N to 0.5 N (**Figure III-16**). However, for $F \geq 1$ N, the microhardness decreased significantly. Hence, the applied loading force was chosen to 0.25 N in further tests.

During the hardness determination, each pellet underwent 15 measurements randomly located on its polished surface to obtain the average hardness. For $NdPO_4$, the microhardness reached 4.9 ± 0.8 GPa, which was in agreement with the value reported by Bregiroux *et al.* (4.8 ± 0.7 GPa, **Table III-3**) [5]. The influence of the Ca and Th coupled substitution was further found to be negligible (**Table III-12**). Indeed, even if a slightly lower value was measured for $x = 0.05$ compared to other samples, the associated large uncertainty led to conclude that the microhardness of $Nd_{1-2x}Ca_xTh_xPO_4$ ceramics pellets remained unchanged. The obtained value was found to be of the same order of magnitude than the Vicker's hardness determined for other phosphate-based ceramic wasteforms such as fluorapatite (3.7 GPa) [34], β-TPD (4.4 GPa) [35] or NZP (5.9 GPa) [36]. Also, it appeared to be only slightly below the value reported by Popa *et al.* for the $CaTh(PO_4)_2$ cheralite end-member sintered by SPS technique (6.74 ± 0.15 GPa)[20] .

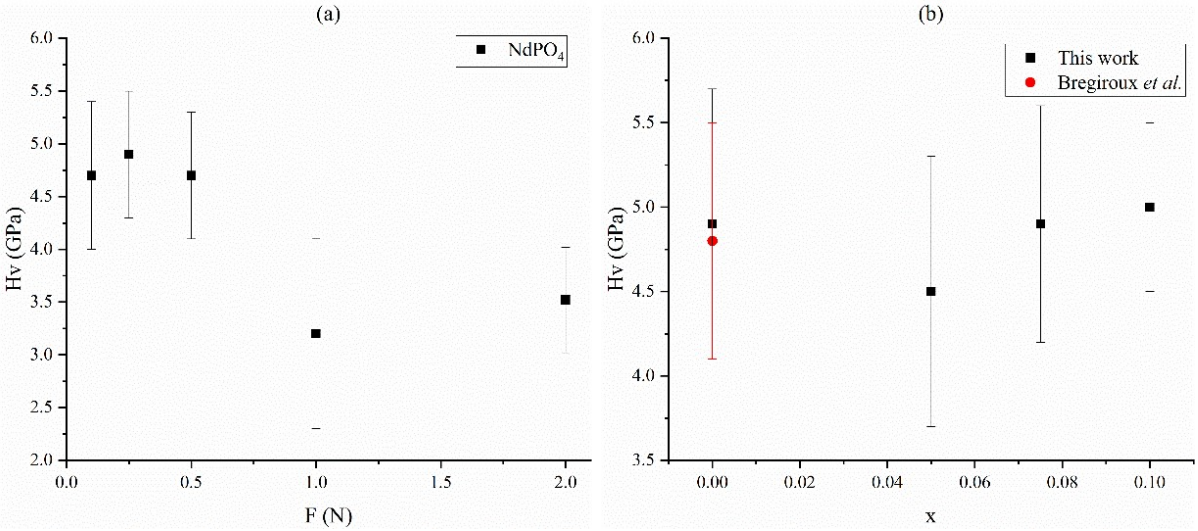

Figure III-16. Evolution of microhardness of $NdPO_4$ *vs* the applied loading force (a) and of the microhardness obtained for $Nd_{1-2x}Ca_xTh_xPO_4$ ceramics *vs* the thorium incorporation rate, *x* (b)

Table III-12. Microhardness obtained for $Nd_{1-2x}Ca_xTh_xPO_4$ ceramics.

x	0	0.05	0.075	0.10
Hv (GPa)	4.9 ± 0.8	4.5 ± 0.8	4.9 ± 0.7	5 ± 0.5

Summary

The results obtained during this study paved the way to an innovative process for the elaboration of highly densified and homogeneous sintered pellets of $Nd_{1-2x}Ca_xTh_xPO_4$ (x = 0 – 0.1). Indeed, the direct sintering of rhabdophane-type precursors let to homogeneous highly densified pellets, at significantly lowered sintering temperature compared to the solid-state routes reported in the literature. Such a dustless process thus avoids the sequence of successive steps of heating or mechanical grinding, which are often associated to potential risks of contamination.

The sintering map of $Nd_{1-2x}Ca_xTh_xPO_4$ solid solutions was further established. No significant grain growth was observed at 1200°C, and the densification appeared to be the predominant behavior. Conversely, the complete densification quickly operated at 1400°C and was followed by an important grain growth. However, the Th-Ca coupled substitution inhibited both densification and grain growth mechanisms, leading the maximum grain size (D_{50}) to decrease by one order of magnitude. Concomitantly, the activation energy associated with the densification ranged from 361 ± 90 to 530 ± 90 $kJ.mol^{-1}$, depending on the chemical composition considered.

Besides, the microhardness of the $Nd_{1-2x}Ca_xTh_xPO_4$ ceramics determined by the Vickers hardness test was found to 4.9 ± 0.8 GPa, which value is consistent with others determined for various phosphate-based radwaste ceramics.

Finally, the process developed from rhabdophane could appear as a promising method to produce highly densified with improved properties such as chemical durability. The study of this essential property to qualify a ceramic for the long-term immobilization of radionuclides will be the aim of the next chapter.

Résumé

Les résultats obtenus au cours de cette étude ouvrent la voie au développement d'un procédé innovant pour élaborer de matrices de confinement de type monazite-chéralite $Nd_{1-2x}Ca_xTh_xPO_4$ (x = 0 - 0,1). En effet, le frittage direct à partir de précurseurs de type rhabdophane étudié au cours de ce travail a conduit à des pastilles homogènes présentant des taux de densification élevés. De plus, la température de densification est significativement inférieure à celles reportées dans la littérature dans le cas de procédés basés sur des réactions par voies sèches. Ainsi, le procédé mis au point au cours de ce travail permet de s'affranchir de la succession éventuelle d'étapes de broyage mécaniques et de calcination, lesquelles sont souvent associées à des risques potentiels de contamination.

La carte de frittage des solutions solides $Nd_{1-2x}Ca_xTh_xPO_4$ a été établie. Aucun grossissement significatif des grains n'a été observé à 1200°C, la densification demeurante prédominante. Inversement, la densification est rapidement achevée à 1400°C. Elle est suivie d'un grossissement très important des grains. Cependant, la substitution couplée Th-Ca semble ralentir à la fois la densification et les mécanismes de grossissement des grains, conduisant à la diminution d'un ordre de grandeur de leur taille maximale (D_{50}). Parallèlement, l'énergie d'activation associée à la densification a été déterminée entre 361 ± 90 et 530 ± 90 $kJ.mol^{-1}$ selon la composition chimique considérée.

De plus, la microdureté des céramiques $Nd_{1-2x}Ca_xTh_xPO_4$ a été évaluée au moyen du test de dureté Vickers. Celle-ci s'établit à 4,9 ± 0,8 GPa, valeur proche de celles relevées pour d'autres céramiques phosphatées étudiées dans le cadre de l'immobilisation spécifique des actinides.

Ainsi, le frittage direct de rhabdophanes en tant que précurseurs des monazites pourrait constituer une méthode prometteuse pour produire des échantillons monolithiques denses d'homogène de monazite-cheralite $Nd_{1-2x}Ca_xTh_xPO_4$ (x = 0 - 0,1). La microstructure obtenue (notamment la diminution de la densité de joints de grains et de pores) pourrait également renforcer la durabilité chimique des matériaux lors des tests de lixiviation. Cette propriété étant essentielle dans le cadre de l'immobilisation à long terme des actinides, elle sera l'objet du prochain chapitre.

Th-rhabdophane

- ✓ Better Homogeneity
- ✓ Larger S_{SA}

Direct Sintering

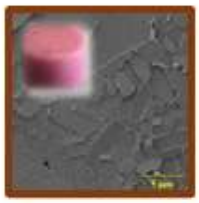

Monazite-Cheralite

- ✓ > 95 % TD
- ✓ Single-phase $Nd_{1-2x}Th_xCa_xPO_4$

Dilatometry

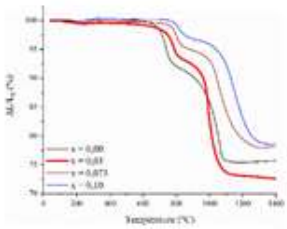

- ➢ Densification takes place at a lower temperature
- ➢ E_A depends on Th-Ca incorporation

Sintering map

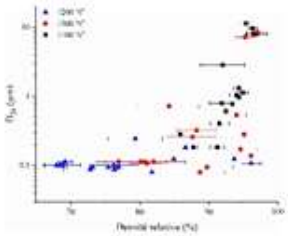

- ➢ Microstructure control
- ➢ Incorporation of thorium slows down densification & grain growth

References

(1) Clavier, N. Elaboration de Phosphate-Diphosphate de Thorium et d'uranium (β-PDTU) et de Matériaux Composites β-PDTU/Monazite à Partir de Précurseurs Cristallisés : Études Du Frittage et de La Durabilité Chimique. PhD Thesis, Université de Paris-Sud, 2004.

(2) Kang, S.-J. L. *Sintering, Densification, Grain Growth & Microstructure*; Elsevier Butterworth-Heinemann: Oxford, 2005.

(3) Bacmann, J. J.; Cizeron, G. Contribution à l'étude Des Mécanismes Du Début de Frittage Du Bioxyde d'uranium. *Journal of Nuclear Materials* **1969**, *33* (3), 271–285. https://doi.org/10.1016/0022-3115(69)90021-X.

(4) Dehaudt, Ph.; Bourgeois, L.; Chevrel, H. Activation Energy of UO_2 and UO_{2+x} Sintering. *Journal of Nuclear Materials* **2001**, *299* (3), 250–259. https://doi.org/10.1016/S0022-3115(01)00661-4.

(5) Bregiroux, D. Synthèse Par Voie Solide et Frittage de Céramiques à Structure Monazite : Application Au Conditionnement Des Actinides Mineurs. PhD Thesis, Université de Limoges, 2005.

(6) Clavier, N.; Podor, R.; Deliere, L.; Ravaux, J.; Dacheux, N. Combining in Situ HT-ESEM Observations and Dilatometry: An Original and Fast Way to the Sintering Map of ThO_2. *Materials Chemistry and Physics* **2013**, *137* (3), 742–749. https://doi.org/10.1016/j.matchemphys.2012.10.003.

(7) Cherkaski, Y.; Clavier, N.; Brissonneau, L.; Podor, R.; Dacheux, N. Densification Behavior and Microstructure Evolution of Yttrium-Doped ThO_2 Ceramics. *Journal of the European Ceramic Society* **2017**, *37* (10), 3381–3391. https://doi.org/10.1016/j.jeurceramsoc.2017.04.015.

(8) Montel, J.-M.; Glorieux, B.; Seydoux-Guillaume, A.-M.; Wirth, R. Synthesis and Sintering of a Monazite–Brabantite Solid Solution Ceramic for Nuclear Waste Storage. *Journal of Physics and Chemistry of Solids* **2006**, *67* (12), 2489–2500. https://doi.org/10.1016/j.jpcs.2006.07.004.

(9) Bregiroux, D.; Lucas, S.; Champion, E.; Audubert, F.; Bernache-Assollant, D. Sintering and Microstructure of Rare Earth Phosphate Ceramics $REPO_4$ with RE=La, Ce or Y. *Journal of the European Ceramic Society* **2006**, *26* (3), 279–287. https://doi.org/10.1016/j.jeurceramsoc.2004.11.004.

(10) Glorieux, B.; Montel, J. M.; Matecki, M. Synthesis and Sintering of a Monazite–Brabantite Solid Solution Ceramics Using Metaphosphate. *Journal of the European Ceramic Society* **2009**, *29* (9), 1679–1686. https://doi.org/10.1016/j.jeurceramsoc.2008.10.004.

(11) Hikichi, Y.; Hukuo, K.; Shiokawa, J. Solid Solutions in the Systems Monazite($CePO_4$)-Huttonite($ThSiO_4$), and Monazite-$Ca_{0.5}Th_{0.5}PO_4$. *NIPPON KAGAKU KAISHI* **1978**, *1978* (12), 1635–1640. https://doi.org/10.1246/nikkashi.1978.1635.

(12) Hikichi, Y.; Nomura, T.; Tanimura, Y.; Suzuki, S.; Miyamoto, M. Sintering and Properties of Monazite-Type $CePO_4$. *Journal of the American Ceramic Society* **1990**, *73* (12), 3594–3596. https://doi.org/10.1111/j.1151-2916.1990.tb04263.x.

(13) Perrière, L.; Bregiroux, D.; Naitali, B.; Audubert, F.; Champion, E.; Smith, D. S.; Bernache-Assollant, D. Microstructural Dependence of the Thermal and Mechanical Properties of Monazite $LnPO_4$ (Ln=La to Gd). *Journal of the European Ceramic Society* **2007**, *27* (10), 3207–3213. https://doi.org/10.1016/j.jeurceramsoc.2006.12.005.

(14) Bregiroux, D.; Audubert, F.; Bernache-Assollant, D. Densification and Grain Growth during Solid State Sintering of $LaPO_4$. *Ceramics International* **2009**, *35* (3), 1115–1120. https://doi.org/10.1016/j.ceramint.2008.05.005.

(15) Babelot, C.; Bukaemskiy, A.; Neumeier, S.; Modolo, G.; Bosbach, D. Crystallization Processes, Compressibility, Sinterability and Mechanical Properties of La-Monazite-Type Ceramics. *Journal of the European Ceramic Society* **2017**, *37* (4), 1681–1688. https://doi.org/10.1016/j.jeurceramsoc.2016.11.047.
(16) Arinicheva, Y.; Bukaemskiy, A.; Neumeier, S.; Modolo, G.; Bosbach, D. Studies on Thermal and Mechanical Properties of Monazite-Type Ceramics for the Conditioning of Minor Actinides. *Progress in Nuclear Energy* **2014**, *72*, 144–148. https://doi.org/10.1016/j.pnucene.2013.09.004.
(17) Arinicheva, Y.; Clavier, N.; Neumeier, S.; Podor, R.; Bukaemskiy, A.; Klinkenberg, M.; Roth, G.; Dacheux, N.; Bosbach, D. Effect of Powder Morphology on Sintering Kinetics, Microstructure and Mechanical Properties of Monazite Ceramics. *Journal of the European Ceramic Society* **2018**, *38* (1), 227–234. https://doi.org/10.1016/j.jeurceramsoc.2017.08.008.
(18) Neumeier, S.; Arinicheva, Y.; Clavier, N.; Podor, R.; Bukaemskiy, A.; Modolo, G.; Dacheux, N.; Bosbach, D. The Effect of the Synthesis Route of Monazite Precursors on the Microstructure of Sintered Pellets. *Progress in Nuclear Energy* **2016**, *92*, 298–305. https://doi.org/10.1016/j.pnucene.2016.07.011.
(19) Meyssamy, H.; Riwotzki, K.; Kornowski, A.; Naused, S.; Haase, M. Wet-Chemical Synthesis of Doped Colloidal Nanomaterials: Particles and Fibers of $LaPO_4$:Eu, $LaPO_4$:Ce, and $LaPO_4$:Ce,Tb. *Advanced Materials* **1999**, *11* (10), 840–844. https://doi.org/10.1002/(SICI)1521-4095(199907)11:10<840::AID-ADMA840>3.0.CO;2-2.
(20) Popa, K.; Cologna, M.; Martel, L.; Staicu, D.; Cambriani, A.; Ernstberger, M.; Raison, P. E.; Somers, J. $CaTh(PO_4)_2$ Cheralite as a Candidate Ceramic Nuclear Waste Form: Spark Plasma Sintering and Physicochemical Characterisation. *Journal of the European Ceramic Society* **2016**, *36* (16), 4115–4121. https://doi.org/10.1016/j.jeurceramsoc.2016.07.016.
(21) Frontera, C.; Rodríguez-Carvajal, J. FullProf as a New Tool for Flipping Ratio Analysis. *Physica B: Condensed Matter* **2003**, *335* (1), 219–222. https://doi.org/10.1016/S0921-4526(03)00241-2.
(22) Raison, P. E.; Heathman, S.; Wallez, G.; Zvoriste, C. E.; Bykov, D.; Ménard, G.; Suard, E.; Popa, K.; Dacheux, N.; Konings, R. J. M.; Caciuffo, R. Structure and Nuclear Density Distribution in the Cheralite—$CaTh(PO_4)_2$: Studies of Its Behaviour under High Pressure (36 GPa). *Physics and Chemistry of Minerals* **2012**, *39* (8), 685–692. https://doi.org/10.1007/s00269-012-0522-z.
(23) Clavier, N.; Podor, R.; Dacheux, N. Crystal Chemistry of the Monazite Structure. *Journal of the European Ceramic Society* **2011**, *31* (6), 941–976. https://doi.org/10.1016/j.jeurceramsoc.2010.12.019.
(24) Johnson, D. L. New Method of Obtaining Volume, Grain-Boundary, and Surface Diffusion Coefficients from Sintering Data. *Journal of Applied Physics* **1969**, *40* (1), 192–200. https://doi.org/10.1063/1.1657030.
(25) Schindelin, J.; Arganda-Carreras, I.; Frise, E.; Kaynig, V.; Longair, M.; Pietzsch, T.; Preibisch, S.; Rueden, C.; Saalfeld, S.; Schmid, B.; Tinevez, J.-Y.; White, D. J.; Hartenstein, V.; Eliceiri, K.; Tomancak, P.; Cardona, A. Fiji: An Open-Source Platform for Biological-Image Analysis. *Nature Methods* **2012**, *9* (7), 676–682. https://doi.org/10.1038/nmeth.2019.
(26) Colomer, M. T. Effect of Sr^{2+} Doping on Sintering Behavior, Microstructural Development and Electrical Properties of $LaPO_4 \cdot nH_2O$ Nanorods Prepared by Dry Mechanical Milling. *International Journal of Hydrogen Energy* **2018**, *43* (29), 13462–13474. https://doi.org/10.1016/j.ijhydene.2018.05.069.

(27) Chen, P.-L.; Chen, I.-W. Grain Growth in CeO_2: Dopant Effects, Defect Mechanism, and Solute Drag. *Journal of the American Ceramic Society* **1996**, *79* (7), 1793–1800. https://doi.org/10.1111/j.1151-2916.1996.tb07997.x.
(28) Caballero, A. C.; Fernández, J. F.; Moure, C.; Durán, P. Effect of Residual Phosphorus Left by Phosphate Ester on $BaTiO_3$ Ceramics. *Materials Research Bulletin* **1997**, *32* (2), 221–229. https://doi.org/10.1016/S0025-5408(96)00179-1.
(29) Naceur, H.; Megriche, A.; El Maaoui, M. Effect of Sintering Temperature on Microstructure and Electrical Properties of $Sr_{1-x}(Na_{0.5}Bi_{0.5})_xBi_2Nb_2O_9$ Solid Solutions. *Journal of Advanced Ceramics* **2014**, *3* (1), 17–30. https://doi.org/10.1007/s40145-014-0089-x.
(30) Cherniak, D. J.; Pyle, J. M. Th Diffusion in Monazite. *Chemical Geology* **2008**, *256* (1), 52–61. https://doi.org/10.1016/j.chemgeo.2008.07.024.
(31) Gardés, E.; Montel, J.-M.; Seydoux-Guillaume, A.-M.; Wirth, R. Pb Diffusion in Monazite: New Constraints from the Experimental Study of $Pb^{2+}⇔Ca^{2+}$ Interdiffusion. *Geochimica et Cosmochimica Acta* **2007**, *71* (16), 4036–4043. https://doi.org/10.1016/j.gca.2007.06.036.
(32) Gardés, E.; Jaoul, O.; Montel, J.-M.; Seydoux-Guillaume, A.-M.; Wirth, R. Pb Diffusion in Monazite: An Experimental Study of $Pb^{2+}+Th^{4+}⇔2Nd^{3+}$ Interdiffusion. *Geochimica et Cosmochimica Acta* **2006**, *70* (9), 2325–2336. https://doi.org/10.1016/j.gca.2006.01.018.
(33) Maître, A.; Beyssen, D.; Podor, R. Modelling of the Grain Growth and the Densification of SnO_2-Based Ceramics. *Ceramics International* **2008**, *34* (1), 27–35. https://doi.org/10.1016/j.ceramint.2006.07.008.
(34) Gao, X.; Huang, Y.; Teng, Y.; Yan, M.; Zhang, H.; Tuo, X.; Peng, S. Fabrication and Chemical Durability of Hot-Pressed Na-Bearing Fluorapatite-Type $Ca_8Sm_1Na_1(PO_4)_6F_2$ Ceramic for Immobilization of Trivalent Minor Actinide. *Journal of Nuclear Materials* **2018**, *507*, 297–305. https://doi.org/10.1016/j.jnucmat.2018.05.017.
(35) Dacheux, N.; Chassigneux, B.; Brandel, V.; Le Coustumer, P.; Genet, M.; Cizeron, G. Reactive Sintering of the Thorium Phosphate-Diphosphate. Study of Physical, Thermal, and Thermomechanical Properties and Chemical Durability during Leaching Tests. *Chem. Mater.* **2002**, *14* (7), 2953–2961. https://doi.org/10.1021/cm011277g.
(36) Orlova, A. I.; Volgutov, V. Yu.; Mikhailov, D. A.; Bykov, D. M.; Skuratov, V. A.; Chuvil'deev, V. N.; Nokhrin, A. V.; Boldin, M. S.; Sakharov, N. V. Phosphate $Ca_{1/4}Sr_{1/4}Zr_2(PO_4)_3$ of the $NaZr_2(PO_4)_3$ Structure Type: Synthesis of a Dense Ceramic Material and Its Radiation Testing. *Journal of Nuclear Materials* **2014**, *446* (1), 232–239. https://doi.org/10.1016/j.jnucmat.2013.11.025.

Chapter IV. Kinetic Study and Saturation Phenomenon of Monazite-Cheralite $Nd_{0.8}Ca_{0.1}Th_{0.1}PO_4$

Results in preparation for publication

Qin, D.; Szenknect, S.; Shelyug, A.; Dacheux, N.; Navrotsky, A.; Clavier, N.; Mesbah, A. Studies on the saturation phenomenon of monazite-cheralite $Nd_{0.8}Ca_{0.1}Th_{0.1}PO_4$

IV-1. Introduction

Deep geological disposal is one of the most promising methods for High-Level radioactive Waste (HLW) management [1,2]. This method deals with storage the HLW in a repository deep underground within a stable geological environment. During the disposal, the waste matrix might be in contact with underground water. The radionuclides, therefore, could be released and then could migrate along with the flow of the groundwater, causing radioactive contamination. The radwaste matrix must exhibit high chemical resistance to weathering conditions. Consequently, the leaching tests were used to evaluate the chemical stability of the prepared matrices.

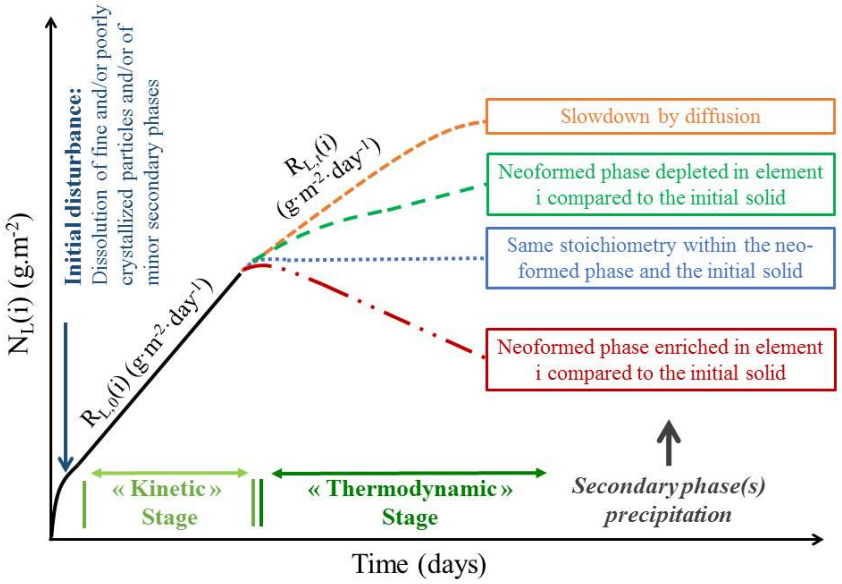

Figure IV-1. Representation of the evolution of the normalized weight loss $N_L(i)$ of an element i during the dissolution of ceramic matrix in a closed system (inspired by Dacheux *et al.* [3]).

The dissolution of a matrix goes through both kinetic and thermodynamic stages. The normalized mass loss $N_L(i,t)$ (g.m^{-2}) is a good indicator to monitor this process, which is written as:

$$N_L(i,t) = \frac{m_i(t)}{f_i \times S} \quad \text{(IV-1)}$$

where $m_i(t)$ (expressed in g) is the mass of element of interest i measured in solution for a given time t; S (m^2) is the reactive surface area of the matrix in contact with the solution, and f_i (g. g^{-1}) is the mass ratio of the element i in the solid matrix. The normalized dissolution rate, $R_L(i)$ (g. m^{-2}. d^{-1}), is then defined as the time-derivative of the $N_L(i,t)$, *i.e.*:

$$R_L(i) = \frac{d\,N_L(i,t)}{dt} = \frac{1}{f_i \times S} \times \frac{d\,m_i(t)}{dt} \quad \text{(IV-2)}$$

It is worth noting that in equation (IV-2), the surface area of the solid and the mass fraction of element i are considered to remain constant. At the beginning of the kinetic stage, the normalized mass loss increases linearly with times after a short period of perturbation (usually called pulse **Figure IV-1**). The initial normalized dissolution rate, $R_{L,0}$, corresponds to the slope obtained from the evolution of the normalized weight loss. Later, neoformed-phases might gradually precipitate onto the surface of the material [4]. The formation of such phases, which could act as a diffusion barrier for the elemental releases, is responsible for the slowing down of the elemental release in solution, leading to a new normalized dissolution rate $R_{L,t}$ [4].

In a closed system, the normalized mass loss thus gradually reaches a plateau, and the dissolution enters the thermodynamic stage (**Figure IV-1**). In the absence of disturbance in the system, the thermodynamic stage controls the long-term behavior of the radwaste matrix, through the establishment of an equilibrium. The solution is then considered to be saturated. If the solubility controlling phases are correctly identified, the solubility products of these solid phases, $K_{s,0}$, can be determined (the index "0" implies that the calculation considered only the non-complexed species). For example, when we consider the following reaction:

$$M_aL_b(s) \rightleftharpoons a\,M^{b+}(aq) + b\,L^{a-}(aq) \quad \text{(IV-3)}$$

$$K_{s,0} = [M^{b+}]^a[L^{a-}]^b \quad \text{(IV-4)}$$

Where $[i]$ (mol.L^{-1}) indicates the molarity of the specie *i* (mol.L^{-1}).

The dissolution tests of ceramic matrices designed for the specific conditioning of actinides are usually conducted in acidic conditions [4–6] because of the very high chemical durability of the materials. In such cases, a protonation equilibrium is involved in the dissolution reaction. Therefore, a new solubility product $^*K_s$ can be defined as follows:

$$M_aL_b(s) + ab\,H^+ + \rightleftharpoons a\,M^{b+}(aq) + b\,H_aL(aq) \quad \text{(IV-5)}$$

$$^*K_s = \frac{[M^{b+}]^a[H_aL]^b}{[H^+]^{ab}} \quad \text{(IV-6)}$$

In order to make possible the extrapolation to standard conditions, the first step is to express the solubility product in terms of molalities, *i.e.* m_i (mol.kg $_{water}$ $^{-1}$), considering the following relation between molality and molarity:

$$m_i = \frac{1000[i]}{1000\rho - [i]M_i} \quad \text{(IV-7)}$$

where ρ ($kg.L^{-1}$) is the density of the solution, and M_i ($g.mol^{-1}$) is the molar mass of species i. Novotny et Söhnel [7] proposed a model to calculate the density of common electrolyte solutions under different temperatures and concentrations.

The solubility constant determined under standard conditions is noted as $K^{\circ}_{s,0}$. According to the International Union of Pure and Applied Chemistry (IUPAC) [8], the standard state pressure, p°, is 1 bar and the reference temperature T is 298.15 K. Therefore, the solubility constant $K^{\circ}_{s,0}$ of reaction IV-3 is,

$$K^{\circ}_{s,0}(25°C) = (M^{b+})_{eqm}{}^{a}(L^{a-})_{eqm}{}^{b} \quad \text{(IV-8)}$$

where (i) represents the activity of species i at 25°C.

It is worth noting that solubility constant is a special case of ions activities product, noted as IAP, which is the product of the activities in an evolving system (*i.e.* not at equilibrium).

$$IAP(t,T,P) = (M^{b+})_{t,T,P}{}^{a}(L^{a-})_{t,T,P}{}^{b} \quad \text{(IV-9)}$$

And the index of solubility, noted as SI, could be determined as the common logarithm of the quote of IAP over $K^{\circ}_{s,0}$,

$$SI = \log_{10}\frac{IAP}{K^{\circ}_{s,0}(25°C)} \quad \text{(IV-10)}$$

The system is at equilibrium when the SI value equals to 0. When SI is positive, the system is over-saturated. Otherwise, it is under-saturated. Besides, the relation between activity (i) and molality m_i is:

$$(i) = \gamma_i m_i \quad \text{(IV-11)}$$

where γ_i is the activity coefficient. In order to estimate γ_i, the Nuclear Energy Agency (NEA) [9] recommended the application of Specific Ion interaction Theory (SIT). The log γ_i is thus evaluated as:

$$\log_{10}\gamma_i = -z_i^2 D + \Sigma_j \varepsilon(i,j) m_j \quad \text{(IV-12)}$$

where, z_i is the charge number of species i, ε(i, j) is the interaction coefficient between ion i and counter-ion j. D is the term of Debye-Hückel, which could be written as,

$$D = \frac{A\sqrt{I_m}}{1+Ba_j\sqrt{I_m}} \quad \text{(IV-13)}$$

$$I_m = \frac{1}{2}\Sigma_j m_j z_j^2 \quad \text{(IV-14)}$$

In this expression I_m is the ionic strength ($mol.kg^{-1}_{water}$). According to NEA[9], A and B are constants, which are temperature and pressure dependent, and a_j is an ion size parameter for

the hydrated ion j. The value of the Debye-Hückel limiting slope, A, is (0.509 ± 0.001) $kg^{½}.mol^{-½}$ at 25 °C and 1 bar [9]. The recommended Ba_j value is equal to 1.5 $kg^{½}.mol^{-½}$ at 25 °C and 1 bar (Scatchard [10] and Ciavatta [11]).

Table IV-1. Debye-Hückel constants reported as a function of temperature for standard pressure (1 bar, *i.e.*) The uncertainties associated to the A and B parameters are estimated to be ± 0.0001 and ± 0.0003 at 25°C, respectively [9]

t(°C)	A ($kg^{½}.mol^{-½}$)	B×10^{-10} ($kg^{½}.mol^{-½}.m^{-1}$)
0	0.491	0.3246
5	0.494	0.3254
15	0.498	0.3261
20	0.501	0.3268
25	0.505	0.3277
30	0.509	0.3284
35	0.513	0.3292
40	0.518	0.3300
50	0.525	0.3312
75	0.534	0.3326

The $\Sigma_j \varepsilon(i,j) m_j$ term could be simplified by considering only the interactions between the ions participating in the reaction and the ions of the electrolyte solution. This approximation can be done because the ions of the electrolyte solution have concentrations much higher than those participating in the reaction. Moreover, the $\varepsilon(i,j)$ value for ions with the same charge sign is equal zero. It is also null for uncharged species. In these conditions, the log $K^{\circ}_{s,0}$ can be expressed as follows:

$$\log_{10} K^{\circ}_{s,0} = \Delta z^2 D + \Delta \varepsilon I_m + \log_{10} K^{m}_{s,0} \qquad \text{(IV-15)}$$

where ΔX stands for $\Sigma_i \nu_i X_i$.

In order to prevent any release of radionuclides in the environment, a well-designed radwaste matrix must exhibit a high chemical durability. It should fulfill two criteria: low normalized dissolution rate of the radionuclides and low solubility associated to the final solubility-controlling neoformed phases.

IV-1.1. Chemical durability of monazites or monazite-cheralite solid solutions in weathering conditions

Monazites are usually mentioned to show very high chemical durability, which also strongly argues for their use as a ceramic waste form for specific long-term conditioning [12,13]. In this field, the normalized dissolution rate reported for monazite is several orders of

magnitude lower than that of borosilicate glass R7T7, which is considered as reference material for radwaste conditioning [14,15]. For a better comparison, the results of several published studies are listed in **Table IV-2.** Most of these studies were performed at 90 °C.

To begin with, Oelkers *et al.* [16] published a multiparameter leaching test on natural Manangotry monazite crystals (with the following composition: $(Ca_{0.04}La_{0.21}Ce_{0.43}Pr_{0.05}$-$Nd_{0.15}Sm_{0.02}Gd_{0.01}Th_{0.13})P_{0.90}Si_{0.09}O_4$) [17]. The reported normalized dissolution rates obtained at 70°C reached 2 – 3.2 × 10^{-5}, 7 × 10^{-6} and 8 × 10^{-7} $g.m^{-2}.d^{-1}$ for pH = 2, 2.6 and 6, respectively [17]. It is important to remind that the dissolution rate of R7T7 glass at 90°C in deionized water was found to be 1 $g.m^{-2}.d^{-1}$ [15]. During his PhD work, Du Fou de Kerdaniel [18] reported the dissolution of $LnPO_4$ ceramic with Ln = La, Ce, Nd, Eu and Gd. At 90°C, the initial dissolution rates $R_{L,0}$ (t < 10 days) equaled 1.0 – 1.8 × 10^{-3} $g.m^{-2}.d^{-1}$ in 0.1 $mol.L^{-1}$ HNO_3. After ten days, the rhabdophane $LnPO_4.nH_2O$ precipitated, leading dissolution rates $R_{L,t}$ (t > 10 days) to drop by about one decade, *i.e.* to 1.2 – 6.8 × 10^{-4} $g.m^{-2}.d^{-1}$. Later, Gausse *et al.* [19,20] performed multiparametric tests on $LnPO_4$ (with Ln = La, Ce, Nd and Gd) in 0.1 $mol.L^{-1}$ HNO_3 to study the impact of the leaching temperature (25 ≤ T ≤ 90°C). The normalized dissolution rate $R_{L,0}$ ranged from 4× 10^{-5} to 3.7 × 10^{-4} $g.m^{-2}.d^{-1}$ at 25°C, which was lower than that obtained at 90°C (0.4 – 4.0 × 10^{-3} $g.m^{-2}.d^{-1}$.)

These dissolution rates were found to be relatively low in comparison to other ceramics designed for the specific conditioning of long-life radionuclides (*e.g.*, zirconolite, Nd-britholite). Indeed, the normalized dissolution rates $R_{L,0}$ of zirconolite was about 10^{-2}·$g.m^{-2}.d^{-1}$ in pure water at 90°C whereas that of Nd-britholite ranged from 10^{-3} to 0.6 $g.m^{-2}.d^{-1}$ between pH = 4 and pH = 7 at 90°C (**Table IV-3**)[5,6]. Moreover, the precipitation of neoformed rhabdophane led to the significant drop of the normalized dissolution rates as a confirmation of the very good chemical durability of monazite based ceramics.

For monazite-type solid solution, several studies investigated the dissolution of $Ce_{1-x}Ln_xPO_4$ (Ln = Pr, Eu and Gd) in distilled water at 90°C [21–26]. The normalized dissolution rates of the synthesized samples were about an order of magnitude higher than that reported for natural Manangotry monazite ($R_{L,0}$ (Ce) = 7.6 × 10^{-6} – 4 × 10^{-5} $g.m^{-2}.d^{-1}$). Moreover, the dissolution process was not stoichiometric, as the $R_{L,0}$ (Ln) values were different from that of $R_{L,0}$ (Ce). This could be linked to the dry chemistry route used to prepare the synthetic samples, which could induce local heterogeneities at the microscopic scale. Such heterogeneities could induce non-stoichiometric dissolution associated with increasing of the Ce release. Nevertheless, these ceramics still revealed a strong resistance to corrosion compared with other

types of ceramics.Finally, Veilly *et al.* [27] recently studied the dissolution kinetics of $Ca_{0.5}Th_{0.5}PO_4$ cheralite. The obtained normalized dissolution rate was $(2.2 \pm 0.2) \times 10^{-5}$ g.m^{-2}.d^{-1}. Later, Du Fou de Kerdaniel [18] investigated the normalized dissolution rate of $Ca_{0.5}Th_{0.4}U_{0.1}PO_4$, $La_{0.4}Eu_{0.1}Ca_{0.25}Th_{0.25}PO_4$ and $La_{0.4}Eu_{0.1}Ca_{0.25}U_{0.25}PO_4$. He reported an initial dissolution rate $R_{L,0}$ (U) of $(2.5 \pm 0.2) \times 10^{-4}$ g.m^{-2}.d^{-1} for $Ca_{0.5}Th_{0.4}U_{0.1}PO_4$ in 0.1 mol.L^{-1} HNO_3 at 90°C. Moreover, the precipitation of uranium was observed after 10 days, leading to the significant decrease of the normalized dissolution rate $R_{L,t}$ (U) down to $(2.5 \pm 0.3) \times 10^{-5}$ g.m^{-2}.d^{-1}. Similarly, this phenomenon has also been observed for $La_{0.4}Eu_{0.1}Ca_{0.25}An_{0.25}PO_4$ (An = Th, U) while the $R_{L,t}$ (An) values were about one order of magnitude lower than $R_{L,0}$ (An). The $R_{L,0}$ (An) and $R_{L,t}$ (An) values associated to these matrices were only $2 – 3 \times 10^{-4}$ g.m^{-2}.d^{-1} and $2 – 3 \times 10^{-5}$ g.m^{-2}.d^{-1}, respectively, despite the high incorporation ratio of actinides (about 25 – 50 wt.%). These results supported once again the very high chemical durability of the monazite-cheralite solid solution.

IV-1.2. Solubility of the neoformed phases during the dissolution

As mentioned above, neoformed phases might precipitate in the back-end of the initial dissolution when the saturation processes occurred in solution (thermodynamic stage). Such a precipitation takes place at the ceramic-solution interface and a thin layer of neoformed phases can gradually cover the surface of the ceramic. This phenomenon prevents the efficient migration of radionuclides. On the one hand, the radionuclides may precipitate as solid phases. On the other hand, such phases may act as a passivating layer, which protects the ceramic against leaching. These saturation phenomena depend on the solubility of the neoformed phases.

Indeed, hydrated lanthanide or actinide phosphates exhibit low solubilities, especially rhabdophane $LnPO_4.nH_2O$ and thorium phosphate hydrogen-phosphate hydrate ($Th_2(PO_4)_2(HPO_4).H_2O$, TPHPH) [28–33]. Therefore, these phases are potential neoformed phases during the leaching of the starting monazite or monazite-cheralite solid solutions (associated thermodynamic data listed in **Table IV-3**). Clavier *et al.* [28,29] reported that the log $K_{s,0}°$ associated to TPHPH reached - 66.4 ± 1.1. More recently, we refined this value to - 71.2 ± 1.3 [30]. When the saturation experiments were performed in 1 mol.L^{-1} HNO_3, the thorium concentration was only $(1.9 \pm 0.1) \times 10^{-3}$ mol.L^{-1}. The solubility of rhabdophane $LnPO_4.nH_2O$ was reported by Jonasson *et al.* [31]. Recently, Gausse *et al.* [19,32] determined the solubility of $LnPO_4.nH_2O$ (Ln = La-Gd) from under-saturation and over-saturation methods. The under-saturation method consisted of reaching the equilibrium by dissolving the rhabdophane in acid

solutions. The over-saturation method consisted of reaching equilibrium by precipitation of rhabdophane. The values of log $K_{s,0}°$ for Ln-rhabdophanes ranged from - 24.1 ± 0.3 to - 25.8 ± 0.3. The obtained lanthanide concentrations when saturation conditions were reached (in 0.1 $mol.L^{-1}$ HNO_3) were found to 1×10^{-3} $mol.L^{-1}$. To conclude, the solubility of TPHPH and rhabdophanes were very low even in strong acid conditions (*i.e.,* for pH = 0 – 1), which explains their precipitation during the leaching of TPD and monazite-cheralite solid solutions [6,34] and reinforces the high chemical durability of the prepared ceramics.

During the dissolution tests mentioned above, the monazite-cheralite-type ceramics were prepared via dry chemistry routes, which could induce some heterogeneities in terms of composition. Therefore, there has been an interest in studying the improvements which could come from the development of wet chemistry methods. As already described, single-phase Th-rhabdophane samples, $Nd_{0.8}Th_{0.1}Ca_{0.1}PO_4.nH_2O$ were prepared in hydrothermal conditions, and thermally converted to monazite-cheralite type ceramics $Nd_{0.8}Th_{0.1}Ca_{0.1}PO_4$ (Chapters I - III). Consequently, a multiparametric study of the dissolution was developed in order to determine the normalized dissolution rates of $Nd_{0.8}Th_{0.1}Ca_{0.1}PO_4$ as well as the thermodynamic data associated with neoformed phases.

Table IV-2. Normalized dissolution rates of monazite samples and monazite-cheralite solid solutions reported in literature [16,18,20–27,35]

		$R_L(i)$ (g. m^{-2}. d^{-1})			
	Temperature (°C)	pH	Ln	Th	U
Natural monazite samples					
Manangotry monazite [16] $(Ca_{0.04}La_{0.21}Ce_{0.43}Pr_{0.05}Nd_{0.15}Sm_{0.02}Gd_{0.01}Th_{0.13})P_{0.90}Si_{0.09}O_4$	70	$R_{L,0}$	2	$2\text{-}3.2 \times 10^{-5}$	
	70	$R_{L,0}$	2.6	7×10^{-6}	
	70	$R_{L,0}$	6	8×10^{-7}	
Synthetic monazite samples					
$LaPO_4$ [18]	90	$R_{L,0}$	1	$(1.4 \pm 0.1) \times 10^{-3}$	
	90	$R_{L,t}$	1	$(1.2 \pm 0.2) \times 10^{-4}$	
$LaPO_4$ [20]	25	$R_{L,0}$	1	$(1.3 \pm 0.2) \times 10^{-4}$	
	40	$R_{L,0}$	1	$(5.89 \pm 0.06) \times 10^{-4}$	
	60	$R_{L,0}$	1	$(8.4 \pm 0.2) \times 10^{-4}$	
	90	$R_{L,0}$	1	$(1.17 \pm 0.04) \times 10^{-3}$	
$CePO_4$ [18]	90	$R_{L,0}$	1	$(1.8 \pm 0.2) \times 10^{-3}$	
	90	$R_{L,t}$	1	$(5.0 \pm 0.5) \times 10^{-4}$	
$CePO_4$ [20]	25	$R_{L,0}$	1	$(4 \pm 2) \times 10^{-5}$	
	40	$R_{L,0}$	1	$(3.04 \pm 0.03) \times 10^{-4}$	
	60	$R_{L,0}$	1	$(2.81 \pm 0.06) \times 10^{-4}$	
	90	$R_{L,0}$	1	$(4.3 \pm 0.1) \times 10^{-4}$	
$NdPO_4$ [18]	90	$R_{L,0}$	1	$(1.0 \pm 0.1) \times 10^{-3}$	
	90	$R_{L,t}$	1	$(1.2 \pm 0.1) \times 10^{-4}$	

		$R_L(i)$ (g. m^{-2}. d^{-1})				
	Temperature (°C)		pH	Ln	Th	U
$NdPO_4$ [20]	25	$R_{L,0}$	1	$(2.6 \pm 0.2) \times 10^{-4}$		
	40	$R_{L,0}$	1	$(7.3 \pm 0.1) \times 10^{-4}$		
	60	$R_{L,0}$	1	$(8.5 \pm 0.1) \times 10^{-4}$		
	90	$R_{L,0}$	1	$(1.01 \pm 0.03) \times 10^{-3}$		
$EuPO_4$ [18]	90	$R_{L,0}$	1	$(1.6 \pm 0.2) \times 10^{-3}$		
	90	$R_{L,t}$	1	$(6.8 \pm 0.7) \times 10^{-4}$		
$GdPO_4$ [18]	90	$R_{L,0}$	1	$(1.0 \pm 0.2) \times 10^{-3}$		
	90	$R_{L,t}$	1	$(4.0 \pm 0.7) \times 10^{-4}$		
$GdPO_4$ [35]	90	$R_{L,0}$	1	$(3.8 \pm 0.8) \times 10^{-4}$		
	90	$R_{L,0}$	4	$(4.8 \pm 1.4) \times 10^{-6}$		
$GdPO_4$ [20]	25	$R_{L,0}$	1	$(3.7 \pm 0.4) \times 10^{-4}$		
	40	$R_{L,0}$	1	$(1.64 \pm 0.04) \times 10^{-3}$		
	60	$R_{L,0}$	1	$(2.58 \pm 0.02) \times 10^{-3}$		
	90	$R_{L,0}$	1	$(4.02 \pm 0.09) \times 10^{-3}$		
$Ce_{0.9}Gd_{0.1}PO_4$ [24]	90	$R_{L,0}$	7	6.0×10^{-6} (Ce) 1.8×10^{-5} (Gd)		
$Ce_{0.5}Eu_{0.5}PO_4$ [23,25]	90	$R_{L,0}$	7	4×10^{-5} (Ce) 2×10^{-4} (Eu)		
$Ce_{0.5}Pr_{0.5}PO_4$ [21,22,26]	90	$R_{L,0}$	7	7.6×10^{-6} (Ce) 3.6×10^{-6} (Pr)		
Monazite-cheralite solid solutions						
$Ca_{0.5}Th_{0.5}PO_4$ [27]	90	$R_{L,0}$	1		$(2.2 \pm 0.2) \times 10^{-5}$	

		$R_L(i)$ (g. m^{-2}. d^{-1})				
	Temperature (°C)		pH	Ln	Th	U
$Ca_{0.5}Th_{0.4}U_{0.1}PO_4$ [18]	90	$R_{L,0}$	1		L.D.	$(2.4 \pm 0.2) \times 10^{-4}$
	90	$R_{L,t}$	1		L.D.	$(2.5 \pm 0.3) \times 10^{-5}$
$La_{0.4}Eu_{0.1}Ca_{0.25}Th_{0.25}PO_4$ [18]	70	$R_{L,0}$	1	$(1.7 \pm 0.2) \times 10^{-6}$ (La) $(4.3 \pm 0.4) \times 10^{-6}$ (Eu)	L.D.	
	70	$R_{L,t}$	1	$(1.9 \pm 0.2) \times 10^{-7}$ (La) $(9.4 \pm 0.9) \times 10^{-6}$ (Eu)	L.D.	
$La_{0.4}Eu_{0.1}Ca_{0.25}U_{0.25}PO_4$ [18]	90	$R_{L,0}$	1	$(1.8 \pm 0.3) \times 10^{-4}$ (La) $(4.5 \pm 0.5) \times 10^{-4}$ (Eu)		$(3.1 \pm 0.3) \times 10^{-4}$
	90	$R_{L,t}$	1	$(7.2 \pm 0.7) \times 10^{-5}$ (La) $(2.5 \pm 0.3) \times 10^{-5}$ (Eu)		$(1.8 \pm 0.2) \times 10^{-5}$

L.D.: Limit of detection

Table IV-3. Normalized dissolution rates of zirconolite, britholite and TPD reported in literature [4–6,15]

	Temperature (°C)		pH	$R_L(i)$ (g. m^{-2}. d^{-1})
R7T7 [15]	90	$R_{L,0}$	Deionized water	1
zirconolite [5]	90	$R_{L,0}$	Deionized water	~ 10^{-2} (Ca)
Nd-britholite [5] $Ca_9Nd(PO_4)_5(SiO_4)F_2$	90	$R_{L,0}$	4 – 7	< 10^{-3} – ~ 0.3 (Ca)
Nd-britholite [6] $Ca_9Nd(PO_4)_5(SiO_4)F_2$	90	$R_{L,0}$	4 – 6	log (R_L) = 4.04 – 1.07 × pH (i.e., $R_L = 4 \times 10^{-3} – 0.6$ g. m^{-2}. d^{-1})
Th-britholite [4] $Ca_9Nd_{0.5}Th_{0.5}(PO_4)_{4.5}(SiO_4)_{1.5}F_2$	25	$R_{L,0}$	1	2.1 ± 0.2 (Ca) 0.7 ± 0.1 (P)
	90	$R_{L,0}$	2	10.3 ± 0.9 (Ca) 3.2 ± 0.3 (P)
	90	$R_{L,0}$	3	8.3 ± 0.8 (Ca) 2.6 ± 0.3 (P)
(Th, U)-britholite [4] $Ca_9Nd_{0.5}Th_{0.25}U_{0.25}(PO_4)_{4.5}(SiO_4)_{1.5}F_2$	90	$R_{L,0}$	1	1.4 ± 0.1 (Th) ; 2.3 ± 0.2 (U) (t < 2h) (2.3 ± 0.1) × 10^{-1} (Th) ; 1.3 ± 0.2 (U) (t > 2h)
	90	$R_{L,0}$	1	1.4 ± 0.1 (Th) 2.3 ± 0.2 (U)
TPD [6] $Th_4(PO_4)_4P_2O_7$	25	$R_{L,0}$	0	1.2 – 2.4 × 10^{-5}

	Temperature (°C)		pH	$R_L(i)$ (g. m^{-2}. d^{-1})
TUPD [6,36] $Th_{4-x}U_xP_6O_{23}$	90	$R_{L,0}$	0	2.8×10^{-4}
TPuPD [6,36] $Th_{4-x}Pu_xP_6O_{23}$	25	$R_{L,0}$	5.5 (distilled water)	$2.4 – 3.6 \times 10^{-7}$
	90	$R_{L,0}$	5.5 (distilled water)	$5.0 – 7.5 \times 10^{-6}$

Table IV-4. Thermodynamic data associated to the neoformed phases formed during the leaching of lanthanide/actinide phosphate-based ceramics [28–33]

	T (°C)	log $K_{s,0}$°(T)	$\Delta_R G$°(T) (kJ.mol^{-1})	$\Delta_R H$° (kJ.mol^{-1})	$\Delta_R S$° (J.mol^{-1}.K^{-1})
$Th_2(PO_4)_2(HPO_4).H_2O$ [28,29]	25	-66.4 ± 1.1		-200	
$Th_2(PO_4)_2(HPO_4).H_2O$ [30]	25	-71.2 ± 1.3	406 ± 7	-50.6 ± 1.7	-1549.5 ± 5.4
$LaPO_4.0.5H_2O$ [31]	25	-24.5 ± 0.32			
$LaPO_4.0.667H_2O$ [32]	25	-24.6/-25.0 ± 0.3	141 ± 3	-26 ± 11	-563 ± 36
$CePO_4.0.667H_2O$ [32]	25	-25.0/-25.5 ± 0.3	144 ± 5	-21 ± 7	-555 ± 19
$PrPO_4.0.5H_2O$ [31]	100	-26.0 ± 0.32			
$PrPO_4.0.667H_2O$ [32]	25	-25.3/-25.8 ± 0.3	146 ± 5	-30 ± 8	-594 ± 23
$NdPO_4.0.5H_2O$ [31]	25	-25.9 ± 0.32			
	100	-25.7 ± 0.32			
$NdPO_4.0.667H_2O$ [32]	25	-25.2/-25.6 ± 0.3	145 ± 3	-22 ± 4	-562 ± 11
$SmPO_4.0.667H_2O$ [32]	25	-24.7/-25.6 ± 0.3	143 ± 7	-22 ± 8	-564 ± 23
$EuPO_4.0.5H_2O$ [31]	25	-24.2 ± 0.32			
	100	-25.5 ± 0.32			
$EuPO_4.0.667H_2O$ [32]	25	-24.3/-25.5 ± 0.3	142 ± 10	-17 ± 7	-546 ± 19
$GdPO_4.0.667H_2O$ [32]	25	-25.0 ± 0.3	143 ± 2	-25 ± 10	-563 ±30
$AmPO_4.nH_2O$ [33]	25	-27.4 ± 0.5			
$CmPO_4.nH_2O$ [33]	25	-29.2 ± 0.4			

For log $K_{s,0}$°(T): “over-saturation values” / “under-saturation values”

IV-2. Materials and methods

For each dissolution test, about 100 mg of powdered $Nd_{0.8}Ca_{0.10}Th_{0.10}PO_4$ was introduced in a 120 mL Savillex jar containing 100 mL of nitric acid. These jars were placed in a VWR incubating mini shaker at fixed temperatures during the entire dissolution process. At regular times, 5 mL of solvent were extracted from the jar and were separated from the suspended solid by centrifugation. The elemental concentrations of Ca, Th, Nd, and P were determined by ICP-OES. Before analysis, the ICP-OES was calibrated. The calibration solutions were diluted from SPEX standard solutions ($C_{initial}$ = 1000 mg.L^{-1}) using 1 % HNO_3. The concentrations of the calibration solutions were fixed to 0, 0.25, 0.5, 0.75, 1, 2.5, 5, 10, and 20 mg.L^{-1} ($C_{Ca} = C_{Th} = C_{Nd} = C_P$). For each element, four recommended wavelengths were considered (**Table A. 1**). In theory, the relation between the counting number of a wavelength and the concentration of solution follows simple linear regression. Therefore, the calibration for a wavelength was considered as valid if the coefficient of determination, R^2 was over 0.999. During the samples analysis, the calibration solutions were measured regularly by ICP-OES. The measurement was considered as reliable if the relative error between the values reported from different wavelengths was lower than 5%. Following this protocol, the detection limits were 2.5 mg.L^{-1} for Ca, 0.25 mg.L^{-1} for Th and Nd, and 1 mg.L^{-1} for P. The evolution of the concentrations was therefore monitored, and the dissolution rates were determined. As the dissolution vessels were considered as closed systems, the elemental concentrations stabilized if a saturation equilibrium was reached. Once three consecutive analyses of the Th, Nd, and P concentrations were not significantly different (relative error ≤ 5%), it was assumed that the thermodynamic equilibrium was reached. As the monazite matrix exhibited a low solubility and as Ca was a minor component in the powder (about only 2 wt.%), its elemental concentration was close to the detection limit of ICP-OES ($C_{Ca} \leq$ 1.5 mg.L^{-1}) leading to large uncertainty on the determined concentration. Therefore, Ca elemental concentration was not used as an indicator of the dissolution reaction. Once the systems reached saturation, the dissolution experiments were stopped. In the case of stoichiometric dissolution, the average values of the concentrations determined in the last measurements were used to calculate the solubility product of monazite-cheralite $Nd_{0.8}Ca_{0.10}Th_{0.10}PO_4$ and of neoformed rhabdophane $Nd_{0.8}Ca_{0.10}Th_{0.10}PO_4.nH_2O$.

The influence of the acidity was firstly considered. Three dissolutions tests were performed in 1 mol.L^{-1}, 0.32 mol.L^{-1}, and 0.1 mol.L^{-1} HNO_3. All these solutions were diluted from 69.5 % HNO_3 (Carlo-Erba). The dissolution temperature also has an impact on both the

dissolution rate of the ceramic matrix and the solubility of the neoformed phases. Consequently, three temperatures were chosen in this multiparametric study, i.e., 25°C, 40°C, and 80°C.

IV-2.1. Preparation of monazite-cheralite $Nd_{0.8}Ca_{0.10}Th_{0.10}PO_4$

The monazite-cheralite $Nd_{0.8}Ca_{0.10}Th_{0.10}PO_4$ powders used for the dissolution experiments were prepared according to the protocol already presented in Chapter I. The Th-rhabdophanes $Nd_{0.8}Ca_{0.10}Th_{0.10}PO_4 \cdot nH_2O$ samples were prepared through optimal hydrothermal conditions, *i.e.* with $(Ca:Th)_{initial}$ = 10:1, at 110°C and during 4 days. The monazite-cheralite $Nd_{0.8}Ca_{0.10}Th_{0.10}PO_4$ powders were converted from the Th-rhabdophane thanks to a heating treatment at 1100°C for 6 hours. The obtained powders were characterized with PXRD. All the XRD patterns confirmed the single-phase nature of the monazite-cheralite samples. The specific surface areas were evaluated by BET method. Finally, the chemical composition of the rhabdophane precursors were determined by ICP-OES after full dissolution of the powders (**Table IV-5**).

Table IV-5. Chemical composition of the rhabdophane samples, $Nd_{0.8}Ca_{0.10}Th_{0.10}PO_4.nH_2O$, determined by ICP-OES and specific surface area measured for the resulting monazite-cheralite solid solutions obtained by thermal conversion.

Batch	$\frac{Ca}{Ca+Th+Ln}$	$\frac{Th}{Ca+Th+Ln}$	$\frac{Ln}{Ca+Th+Ln}$	$\frac{P}{Ca+Th+Ln}$	S_{SA} of monazite-cheralite ($m^2.g^{-1}$)
Disso-RT	0.08 ± 0.02	0.10 ± 0.02	0.82 ± 0.04	0.8 ± 0.2	7.5 ± 0.2
Disso-40°C	0.10 ± 0.02	0.12 ± 0.01	0.79 ± 0.01	1.1 ± .0.1	8.3 ± 0.1
Disso-80C	0.09 ± 0.01	0.11 ± 0.01	0.80 ± 0.05	0.97 ± 0.06	1.2 ± 0.2
Disso-40/80°C	0.09 ± 0.01	0.10 ± 0.01	0.81 ± 0.01	1.07 ± 0.03	6.45 ± 0.04

IV-2.2. Determination of normalized dissolution rates

During the dissolution, the normalized weight loss $N_L(i,t)$ ($g.m^{-2}$) was calculated from the elemental concentration C(i,t), according to Equation (IV-1):

$$N_L(i,t) = \frac{m_i(t)}{f_i \times S} = \frac{C(i,t) \times V}{f_i \times S \times M_i} \quad \text{(IV-16)}$$

where V is the volume of the acid solution in contact with the solid and M_i ($g.mol^{-1}$) is the molecular mass of the element, i, released in solution. Similarly, Eq.IV-2 can be modified as:

$$R_L(i,t) = \frac{d\,N_L(i,t)}{dt} = \frac{V}{f_i \times S \times M_i} \times \frac{d\,C(i,t)}{dt} \quad \text{(IV-17)}$$

It is worth noting that S corresponds to the total surface area of the powdered sample. Due to the low solubility of the potential neoformed phases, such as rhabdophane and TPHPH, during the whole dissolution test, small amounts of the solid would be dissolved (*i.e.* ≤ 5%). Therefore, we considered that:

$$S = S_{SA} \times m_0 \quad \text{(IV-18)}$$

where m_0 (g) is the initial mass of the solid.

According to Lasaga [37], the kinetics of dissolution can be described as:

$$R_L = k_0 \times e^{-\frac{E_a}{RT}} \times \left(H^+\right)^n \times g(I) \times \Pi_j\left(E_j\right)^{n_j} \times f(\Delta G_r) \quad \text{(IV-19)}$$

Where k_0 ($g.m^{-2}.h^{-1}$) is the dissolution rate constant, E_a ($kJ.mol^{-1}$) is the apparent activation energy of the overall reaction, R is the gas constant, and T is the absolute temperature. (E_j) and (H^+) are the activities in the solution of species E_j and H^+, respectively. n and n_j are the partial orders of the dissolution reaction related to the proton and the species E_j activities, respectively. g(I) is a function, which describes the effect of the ionic strength I. $f(\Delta G_r)$ is a function of the Gibbs free energy of the reaction of dissolution, which underlines the thermodynamic contribution when approaching the equilibrium in the solution.

The influence of the ionic strength was not studied in this work. Thus, the influence of g(I), if any, was included in an ionic-strength dependent rate constant. Moreover, according to previous studies [3,19], the $f(\Delta G_r)$ term tended to 1 when the system was far from saturation. So that, for a given temperature, the initial dissolution rate $R_{L,0}$ could be simplified as:

$$R_{L,0} = k'' \times \left(H^+\right)^n \quad \text{(IV-20)}$$

where $R_{L,0}$ is the normalized dissolution rate far from saturation equilibrium, and k" ($g.m^{-2}.d^{-1}$) is the apparent normalized dissolution rate constant at (H^+) = 1. It is worth noting that Eq.IV-20 also becomes:

$$\log\left(R_{L,0}\right) = -n \times pH + \log(k'') \quad \text{(IV-21)}$$

In this case, n and k" can be determined by measuring several $R_{L,0}$ values at various pH.

Similarly, in order to study the impact of temperature, the initial dissolution rate $R_{L,0}$ can be written as:

$$R_{L,0} = k' \times e^{-\frac{E_a}{RT}} \quad \text{(IV-22)}$$

where k' ($g.m^{-2}.d^{-1}$) is a pH-dependent apparent normalized dissolution rate constant. This equation also corresponds to:

$$\ln\left(R_{L,0}\right) = -\frac{E_a}{R} \times \frac{1}{T} + \ln(k') \quad \text{(IV-23)}$$

According to this equation, the apparent activation energy can be determined by measuring several $R_{L,0}$ values at different temperatures.

IV-2.3. Study of saturation phenomena

As described above, the dissolution set-ups can be considered as quasi-closed systems and the saturation equilibrium can be achieved eventually. As the dissolution experiments were performed in 0.1 – 1 mol.L^{-1} HNO_3, thorium, and neodymium might form various complexes. Hence, PHREEQC simulations were performed in order to study the speciation of Ca, Nd, Th and phosphate groups in these acid conditions.

IV-2.3.1. PHREEQC simulations to investigate the speciation at pH 0 – 1.

The speciation was simulated in the solution thanks to the PHREEQC software (version 3.3.8.11728) associated with the ThermoChimie database (version 10a) developed by ANDRA [38]. The complexation constants of the inorganic species in this database were mostly selected from internationally recognized thermodynamic databases. Especially, it included the data of thorium species published by NEA-OECD's Thermochemical Database (TDB) project [9]. However, the data associated to neodymium species were not included in the ThermoChime database. In order to solve this problem, the thermodynamic data of neodymium inorganic complexes were selected from another well-recognized database, the Lawrence Livermore National Laboratory TDB (LLNL-TDB) [39]. Consequently, such values were introduced in the ThermoChimie database with the compatible form. Moreover, since rhabdophane $NdPO_4.0.667\ H_2O$ [32] and $Th_2(PO_4)_2(HPO_4).H_2O$ (TPHPH) [30] are potential neo-formed phases during the dissolution tests, their solubility constant values, evaluated during our previous works, were therefore introduced in the ThermoChimie database as well.

Assuming that rhabdophane and TPHPH were potential solubility-controlling phases, a simulation of the TPHPH-$NdPO_4.0.667\ H_2O/HNO_3$ system was performed by PHREEQC, where the nitric acid concentration varied from 0.05 mol.L^{-1} to 1.26 mol.L^{-1}. According to the ThermoChimie database, all the calcium phosphate based solid phases had much higher solubilities than TPHPH or $NdPO_4.0.667H_2O$. Hence, the calcium speciation was simulated using the brushite/HNO_3, where the brushite ($CaHPO_4.2H_2O$) [40] was introduced at 8.5 mmol per kg solution so that the concentration of total calcium would be equal to the maximum of total thorium concentration in the TPHPH - $NdPO_4.0.667\ H_2O/HNO_3$ simulation.

The dominant species in the solution for these two systems are presented in **Figure IV-2** ($C(HNO_3)$ = 0.05 mol.L^{-1} to 1.26 mol.L^{-1}). In the brushite/HNO_3 system, the solid was completely dissolved in HNO_3, and Ca^{2+} was the predominant species. In the TPHPH - $NdPO_4$.0.667 H_2O/HNO_3 system, the amount of dissolved solid was rapidly reduced with the increase of pH. Th formed various complexes with phosphate, the predominant species for neodymium is the free Nd^{3+} whereas P is mostly present as H_3PO_4. The thermodynamic data associated to the prevailing species are listed in **Table IV-6.**

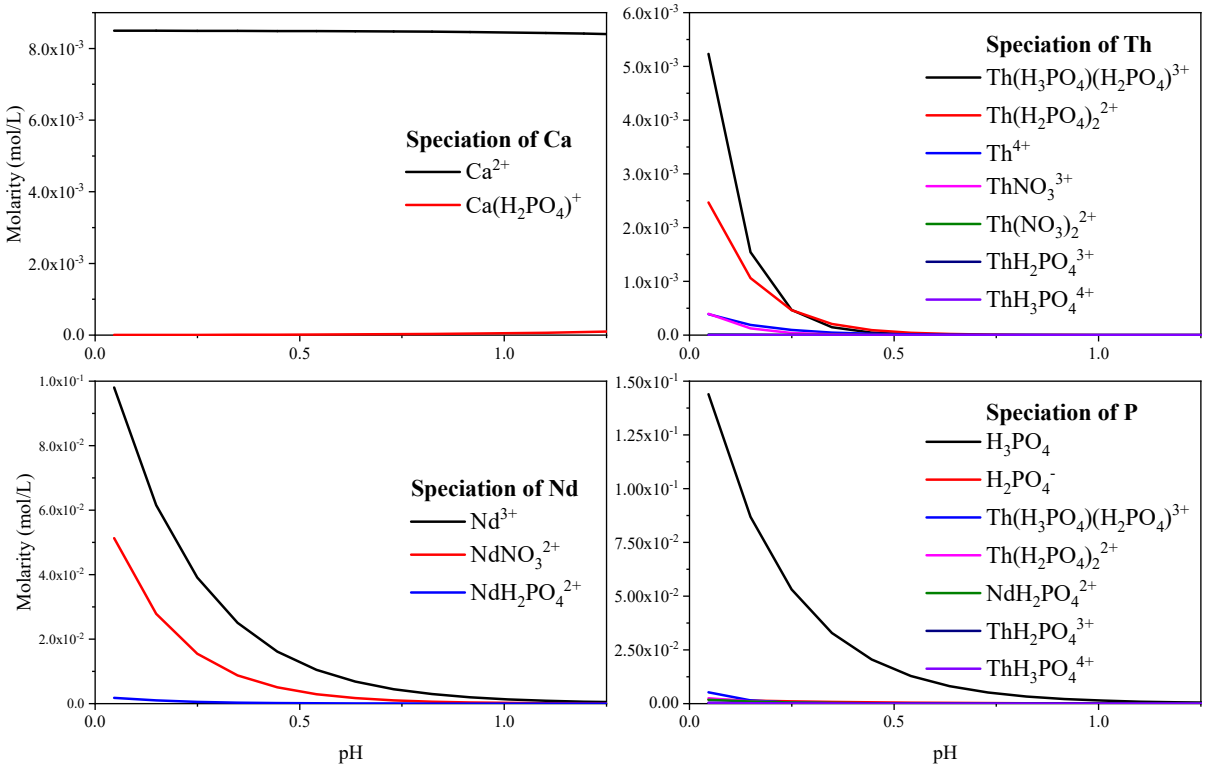

Figure IV-2. Speciation diagrams obtained for the TPHPH / $NdPO_4$.0.667H_2O / HNO_3 and the brushite/HNO_3 systems at 298K ($C(HNO_3)$ = 0.05 mol.L^{-1} to 1.26 mol.L^{-1})

Table IV-6. Thermodynamic data implemented in the Thermochimie database [38], associated with the main reactions involving the species of interest that were taken into account for the speciation calculations [30,32,41] (N.A. means Not Available).

Reaction	$\log_{10} K°$ (298.15 K)	$\Delta_R H°$ (kJ mol^{-1})	$\Delta_R S°$ (J mol^{-1} K^{-1})
$Th^{4+} + H_3PO_4 \rightleftharpoons ThH_2PO_4^{3+}$	3.45 ± 0.32	N.A.	N.A.
$Th^{4+} + 2H_3PO_4 \rightleftharpoons 2\,H^+ + Th(H_2PO_4)_2^{2+}$	6.20 ± 0.32	N.A.	N.A.
$Th^{4+} + 2H_3PO_4 \rightleftharpoons H^+ + Th(H_3PO_4)(H_2PO_4)^{3+}$	5.42 ± 0.32	N.A.	N.A.
$Th^{4+} + H_3PO_4 \rightleftharpoons ThH_3PO_4^{4+}$	1.89 ± 0.31	N.A.	N.A.
$Th^{4+} + 2NO_3^- \rightleftharpoons Th(NO_3)_2^{2+}$	2.3 ± 0.4	N.A.	N.A.
$Th^{4+} + NO_3^- \rightleftharpoons ThNO_3^{3+}$	1.3 ± 0.2	N.A.	N.A.
$Th^{4+} + HPO_4^{2-} \rightleftharpoons Th(HPO_4)^{2+}$	10.6799	N.A.	N.A.
$Th^{4+} + 2HPO_4^{2-} \rightleftharpoons Th(HPO_4)_2$	22.6939	N.A.	N.A.

Reaction	$\log_{10} K°$ (298.15 K)	$\Delta_R H°$ (kJ mol^{-1})	$\Delta_R S°$ (J mol^{-1} K^{-1})
$Th^{4+} + 3HPO_4^{2-} \rightleftharpoons Th(HPO_4)_3^{2-}$	31.1894	N.A.	N.A.
$HPO_4^{2-} + H^+ \rightleftharpoons H_2PO_4^-$	7.212 ± 0.013	-3.6 ± 1.0	126.000 ± 3.363
$HPO_4^{2-} \rightleftharpoons PO_4^{3-} + H^+$	-12.35 ± 0.03	14.6 ± 3.8	-187.470 ± 12.758
$H^+ + H_2PO_4^- \rightleftharpoons H_3PO_4$	2.14 ± 0.03	8.48 ± 0.60	69.412 ± 2.093
$Nd^{3+} + NO_3^- \rightleftharpoons NdNO_3^{2+}$	0.7902	27.8529	N.A.
$Ca^{2+} + H_2PO_4^- \rightleftharpoons CaH_2PO_4^+$	1.410	14.226	N.A.
$Th_2(PO_4)_2(HPO_4).H_2O(s) \rightleftharpoons 2Th^{4+}+2PO_4^{3-}+HPO_4^{2-}+H_2O$	-71.2 ± 1.3	-50.6 ± 1.7	-1549.5 ± 5.4
$NdPO_4.0.667H_2O(s) \rightleftharpoons Nd^{3+} + PO_4^{3-} + 0.667H_2O$	-25.6 ± 0.3	-22 ± 4	-562 ± 11
$CaHPO_4.2H_2O(s) + H^+ \rightleftharpoons Ca^{2+} + H_2PO_4^- + 2H_2O$	0.06		

IV-2.3.2. Determination of the solubility constants of neoformed phases

Several neoformed phases such as rhabdophane, TPHPH, or Th-rhabdophane, $Nd_{0.8}Ca_{0.10}Th_{0.10}PO_4.nH_2O$ could act as solubility-controlling phases and thus control the solubility of Th, Nd, and P in solution. The monazite-cheralite $Nd_{0.8}Ca_{0.10}Th_{0.10}PO_4$ itself could be stable as well and play this role. Indeed, Shelyug *et al.* [42] already reported that the Gibbs free energy of the conversion from rhabdophane $NdPO_4.0.746H_2O$ to monazite $NdPO_4$ at 25°C was - 9.1 ± 9.5 kJ.mol^{-1}. As the Gibbs free energy at 25°C is close to 0 taking into account the uncertainty associated to this value, monazite $NdPO_4$ appears as stable as rhabdophane $NdPO_4.nH_2O$. The Gibbs free energy at 25°C of the conversion from $Nd_{0.8}Ca_{0.10}Th_{0.10}PO_4.nH_2O$ to monazite-cheralite $Nd_{0.8}Ca_{0.10}Th_{0.10}PO_4$ could be also close to zero, which means that both Th-rhabdophane and monazite-cheralite could act as the solubility controlling-phase. Assuming that the Th-rhabdophane is the phase that controls the equilibrium, the dissolution-reprecipitation of $Nd_{0.8}Ca_{0.10}Th_{0.10}PO_4 \cdot nH_2O$ at pH = 0-1 can be written as follows:

$$Nd_{0.8}Ca_{0.1}Th_{0.1}PO_4.nH_2O+3H^+ \rightleftarrows 0.8\ Nd^{3+} + 0.1\ Ca^{2+} + 0.1Th^{4+} + H_3PO_4 + nH_2O \quad \text{(IV-24)}$$

From Equation IV-8, the solubility constant ${}^{*}K_s^{\circ}$ of $Nd_{0.8}Ca_{0.10}Th_{0.10}PO_4.nH_2O$ rhabdophane can be written:

$$ {}^{*}K_s^{\circ}\,(\text{rhabdophane}) = \frac{(Nd^{3+})^{0.8}\times(Ca^{2+})^{0.1}\times(Th^{4+})^{0.1}\times(H_3PO_4)\times(H_2O)^{n}}{(H^{+})^{3}} \quad \text{(IV-25)} $$

If we assume that the monazite-cheralite $Nd_{0.8}Ca_{0.10}Th_{0.10}PO_4$ is the solubility-controlling phase, the solubility constant is written as follows:

$$ {}^{*}K_s^{\circ}\,(\text{monazite}-\text{cheralite}) = \frac{(Nd^{3+})^{0.8}\times(Ca^{2+})^{0.1}\times(Th^{4+})^{0.1}\times(H_3PO_4)}{(H^{+})^{3}} \quad \text{(IV-26)} $$

By the same way, the expression of the solubility product, ${}^{*}K_s^{m}$, expressed as a function of the molalities is given below. Since the m_{H_2O} value is not taken into account for aqueous solution, the solubility product of the Th-rhabdophane becomes the same than that reported for monazite-cheralite, i.e.:

$$ {}^{*}K_s^{m} = \frac{m_{Nd^{3+}}^{0.8}\times m_{Ca^{2+}}^{0.1}\times m_{Th^{4+}}^{0.1}\times m_{H_3PO_4}}{m_{H^{+}}^{3}} \quad \text{(IV-27)} $$

It is worth noting that molalities m_i ($mol.kg_{water}^{-1}$) can be calculated from molarities [i] ($mol.L^{-1}$) thanks to Eq. IV-7. According to Novotny et Söhnel [7], the density of HNO_3, ρ ($kg.L^{-1}$), can be calculated according to the following equation:

$$ \rho_{HNO_3} = \rho_{water} + A\times[HNO_3] + B\times T\times[HNO_3] + C\times T^2\times[HNO_3] + D\times[HNO_3]^{\frac{3}{2}} + E\times T\times[HNO_3]^{\frac{3}{2}} + F\times T^2\times[HNO_3]^{\frac{3}{2}} \quad \text{(IV-28)} $$

$$ \rho_{water} = 0.99965 + 2.0438\times10^{-4}\times T - 6.174\times10^{-5}\times T^{\frac{3}{2}} \quad \text{(IV-29)} $$

where T is the absolute temperature of the solution, $A = 4.063\times10^{-2}$, $B = -1.554\times10^{-4}$, $C = 1.096$, $D = -2.798\times10^{-3}$, $E = 2.478\times10^{-5}$, and $F = -2.761\times10^{-7}$. The densities and the molalities of the nitric acid solutions considered for this study are listed in **Table IV-7**.

Table IV-7. Molarity, density, and molality of HNO_3 solution considered for these experiments.

$[HNO_3]$ ($mol.L^{-1}$)	ρ ($\times10^3$ $kg.m^{-3}$)	m_{HNO_3} ($mol.kg_{water}^{-1}$)
1.00 ± 0.02	1.05 ± 0.01	1.02 ± 0.02
0.32 ± 0.01	1.01 ± 0.01	0.32 ± 0.01
0.100 ± 0.002	1.00 ± 0.01	0.101 ± 0.002

The standard solubility constant $K_{s,0}^{\circ}$ was also calculated by using PO_4^{3-} species so that the result would be consistent with NEA-OECD's convention[9], therefore,

$$K^{\circ}_{s,0}\,(\text{rhabdophane}) = \frac{(Nd^{3+})^{0.8}\times(Ca^{2+})^{0.1}\times(Th^{4+})^{0.1}\times(PO_4^{3-})\times(H_2O)^n}{(H^+)^3} \quad \text{(IV-30)}$$

and:

$$K^{\circ}_{s,0}\,(\text{monazite}-\text{cheralite}) = \frac{(Nd^{3+})^{0.8}\times(Ca^{2+})^{0.1}\times(Th^{4+})^{0.1}\times(PO_4^{3-})}{(H^+)^3} \quad \text{(IV-31)}$$

Similarly, the apparent solubility product $K^m_{s,0}$ could also be expressed in terms of molarities, as follows:

$$K^{m}_{s,0} = \frac{m^{0.8}_{Nd^{3+}} \times m^{0.1}_{Ca^{2+}} \times m^{0.1}_{Th^{4+}} \times m_{PO_4^{3-}}}{m^{3}_{H^+}} \quad \text{(IV-32)}$$

It is worth noting that $K^{\circ}_{s,0}$ and $K^m_{s,0}$ can be deduced from ${}^*K^{\circ}_s$ and ${}^*K^m_s$, as follows:

$$K^{\circ}_{s,0} = {}^*K^{\circ}_s \times K_{a1} \times K_{a2} \times K_{a3} \quad \text{(IV-33)}$$

$$K_{s,0} = {}^*K \times K_{a1} \times K_{a2} \times K_{a3} \quad \text{(IV-34)}$$

where, K_{a1}, K_{a2}, K_{a3} are the phosphoric acidity constants at 298 K related to $H_3PO_4/H_2PO_4^-$ ($pK_{a1} = 2.14$), $H_2PO_4^-/HPO_4^{2-}$ ($pK_{a2} = 7.212$), and HPO_4^{2-}/PO_4^{3-} ($pK_{a3} = 12.35$), respectively[9].

Indeed, the simulation of the TPHPH-$NdPO_4$.0.667 H_2O/HNO_3 system indicated, the H_3PO_4 was the major phosphorus-based. The $K^{\circ}_{s,0}$ and $K^m_{s,0}$ were therefore calculated by equation IV-33 and IV-34, to minimize the uncertainties associated to the simulation.

Table IV-8. Selected thermodynamic data of phosphoric acid

	log(K°)	$\Delta_R G^o$ (kJ.mol^{-1})	$\Delta_R H^o$ (kJ.mol^{-1})
$H_3PO_4 \rightarrow H_2PO_4^-$	-2.140 ± 0.030	12.215 ± 0.171	-8.5 ± 0.6
$H_2PO_4^- \rightarrow HPO_4^{2-}$	-7.212 ± 0.013	41.166 ± 0.074	3.6 ± 1.0
$HPO_4^{2-} \rightarrow PO_4^{3-}$	-12.350 ± 0.030	70.494 ± 0.171	14.6 ± 3.8

Otherwise, the relation between the standard solubility constant and the solubility product (*i.e.* $K^{\circ}_{s,0}$ and $K^m_{s,0}$) is:

$$\log_{10} K^{\circ}_{s,0} = \Delta z^2 \times D + \Delta\varepsilon \times I_m + \log_{10} K^{m}_{s,0}$$

The calculation of D and I_m have been already described in Eq. IV-13 and Eq. IV-14, as follows:

$$D = \frac{A \times \sqrt{I_m}}{1 + Ba_j \times \sqrt{I_m}}$$

$$I_m = \frac{1}{2}\,\Sigma_j\, m_j \times z_j^2$$

The value of A has been listed in **Table IV-1** [9] whereas the Ba_j term equals 1.5 $kg^{½}.mol^{-½}$ at 25 °C and 1 bar [10,11]. Moreover, the values of $\varepsilon_{(i,j)}$ used in the calculations are reported in **Table IV-9** [9].

Table IV-9. Ion interaction coefficient $\varepsilon_{(i,j)}$ values used in this work [9]

	NO_3^-
Th^{4+}	0.7
H^+	0.07
Nd^{3+}	N.A.
Ca^{2+}	0.02

In addition, the difference between both the values of $K_{s,0}°$(rhabdophane) and of $K_{s,0}°$(monazite-cheralite) can be expressed as:

$$\log_{10} K_{s,0}^{\circ}(\text{rhabdophane}) = \log_{10} K_{s,0}^{\circ}(\text{monazite cheralite}) + n \times \log_{10}(H_2O) \quad \text{(IV-35)}$$

According to NEA[9], the activity of water in HNO_3 can be calculated from:

$$\log_{10}(H_2O) = -\frac{2 \times m_{HN\ _3} \times \phi_m}{\ln 10 \times 55.508} \quad \text{(IV-36)}$$

where ϕ_m is the osmotic coefficient of the mixture and 55.508 $mol \cdot kg^{-1}$ is the molality of pure water.

Lewis and Randall [43] have given a general formula to determine the osmotic coefficient for an ionic medium with concentration much larger than those of the reacting ions. Therefore, the osmotic coefficient of the HNO_3 can be calculated as follows:

$$1 - \phi_m = \frac{A \times \ln 10}{I_m \times (Ba_j)^3}\left[1 + Ba_j \times \sqrt{I_m} - 2 \times \ln\left(1 + Ba_j \times \sqrt{I_m}\right) - \frac{1}{1+Ba_j \times \sqrt{I_m}}\right] -$$

$$0.5 \times \ln 10 \times \varepsilon(H^+, NO_3^-) \times m_{HNO_3} \quad \text{(IV-37)}$$

It is worth noting that the dissolution experiments were carried out in strong acid conditions (i.e. pH = 0-1). However, the pH of the buffers used in our laboratory for pH meter calibration is 2-10. The application of pH meter led to significant measurement uncertainty due to such required extrapolation. Meanwhile, few monazite solid was dissolved during the whole dissolution test, *e.g.* less than 7 mg of sample when making the test in 100 mL of 1 $mol.L^{-1}$ HNO_3. This result suggests the concentration of HNO_3 can be considered as unmodified and that the pH value could be deduced from the concentration of HNO_3. W.J. Hamer and Y.C. Wu [44] modified the Debye-Hückel equation by adding more empirical terms:

$$\log_{10} \gamma_{HNO_3} = -\frac{A \times \sqrt{I_m}}{Ba_j \times \sqrt{I_m}} + \beta \times I_m + C \times {I_m}^2 + D \times {I_m}^3 + E \times {I_m}^4 \quad \text{(IV-38)}$$

Where $\beta = 6.2432\times10^{-2}$, $C = 1.3137\times10^{-3}$, $D = -1.2866\times10^{-5}$ and $E = 4.9168\times10^{-7}$. The concentrations of the reacting ions were far lower than that of HNO_3. Therefore, I_m could be approximated by m_{HNO_3}. The pH of the HNO_3 solutions was thus calculated as:

$$pH = -\log_{10}\gamma_{HN\ _3} - \log_{10} m_{HNO_3} \quad \text{(IV-39)}$$

The results of such a calculation are listed in **Table IV-10**

Table IV-10. Calculated pH of nitric acid solutions used for the dissolution tests.

$[HNO_3]$ (mol.L^{-1})	m_{HNO_3} $(mol.kg^{-1}_{water})$	pH
1.00 ± 0.02	1.02 ± 0.02	0.13 ± 0.02
0.32 ± 0.01	0.32 ± 0.01	0.63 ± 0.02
0.100 ± 0.002	0.101 ± 0.002	1.10 ± 0.02

IV-3. Results and Discussions

IV-3.1. Kinetic stage of dissolution tests of monazite-cheralite $Nd_{0.8}Th_{0.1}Ca_{0.1}PO_4$ powder

IV-3.1.1. Investigation on the influence of acidity at 25°C

The evolution of normalized weight losses $N_L(i)$ at the beginning of dissolution tests are gathered in **Figure IV-3**. The fluctuations observed during the first 10 days of leaching tests were attributed to the preferential dissolution of minor phases or impurities because due to the absence of washing stage of the monazite-cheralite samples before the dissolution tests. After this time, the dissolution was stoichiometric for 50 days in 1 mol.L^{-1} HNO_3, as all the normalized dissolution rates $R_{L,0}$ were not significantly different from 3×10^{-5} g.m^{-2}.d^{-1} considering the associated uncertainties, which, once again, demonstrates the high chemical durability of monazite-cheralite solid solution, $Nd_{0.8}Th_{0.1}Ca_{0.1}PO_4$. Gausse[19] reported that the normalized dissolution rate $R_{L,0}$ of $NdPO_4$ monazite was $(1.20 \pm 0.05) \times 10^{-3}$ g.m^{-2}.d^{-1} in the same conditions, which was about two orders of magnitude higher than for $Nd_{0.8}Th_{0.1}Ca_{0.1}PO_4$. This drop of the normalized dissolution rate is probably due to the incorporation of Th. Indeed, Du Fou de Kerdaniel [18], has given the normalized dissolution rates at 90°C in 0.1 mol.L^{-1} HNO_3 for $LaPO_4$ and $EuPO_4$ were $1.6 – 1.8 \times 10^{-3}$ g.m^{-2}.d^{-1} while that of $La_{0.4}Eu_{0.1}Ca_{0.25}Th_{0.25}PO_4$ was $1.7 – 4.3 \times 10^{-6}$ g.m^{-2}.d^{-1}.

In 0.32 mol.L^{-1} HNO_3, however, the saturation was reached after ten days of dissolution. The $R_{L,0}$ values for Th, Nd, and P were almost equal to 0 whereas Ca was released in the solution with a normalized dissolution rate of $R_{L,0}$ (Ca) = $2.1 \pm 0.6 \times 10^{-5}$ g.m^{-2}.d^{-1}. According to the previous PHREEQC simulations in Section IV-2.3.1, calcium has a higher solubility than other elements in such conditions. Therefore, calcium could continue to release from the monazite-cheralite, while other elements has reached the saturation and stayed in the solid phases. In 0.1 mol.L^{-1} HNO_3, the dissolution was found to be non-stoichiometric, with $R_{L,0}$ (P) = $0.39 \pm 0.07 \times 10^{-5}$ g.m^{-2}.d^{-1}, $R_{L,0}$ (Ca) = $1.0 \pm 0.6 \times 10^{-5}$ g.m^{-2}.d^{-1}, $R_{L,0}$ (Th) = $1.0 \pm 0.6 \times 10^{-5}$ g.m^{-2}.d^{-1} and $R_{L,0}$ (Nd) ≈ 0. Such results underline the rapid precipitation of neodymium in these operating conditions, as suggested by the PHREEQC calculation (significant decrease of the neodymium solubility at pH = 1, see section IV-2.3.1). Hence, this non-stoichiometric dissolution may be due to the precipitation of neoformed phases such as rhabdophane $NdPO_4.nH_2O$. For this reason, the determination of normalized dissolution rates must be performed under extreme acid conditions (i.e. $C(H^+) \geq 1$ mol.L^{-1}) in order to avoid any biais in their evaluation.

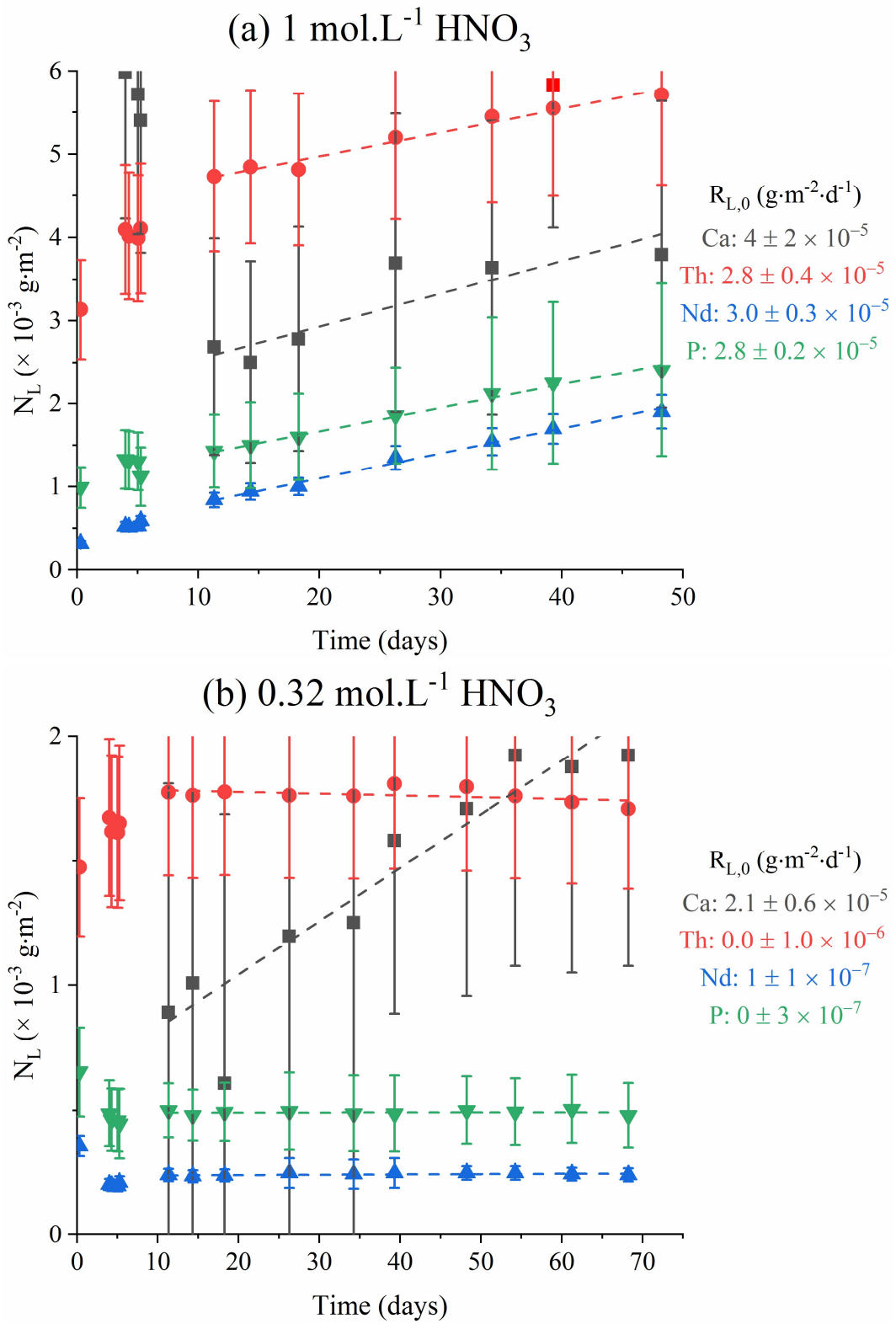
(a) 1 mol.L-1 HNO3
NL (× 10-3 g·m-2)
Time (days)
RL,0 (g·m-2·d-1)
Ca: 4 ± 2 × 10-5
Th: 2.8 ± 0.4 × 10-5
Nd: 3.0 ± 0.3 × 10-5
P: 2.8 ± 0.2 × 10-5
(b) 0.32 mol.L-1 HNO3
NL (× 10-3 g·m-2)
Time (days)
RL,0 (g·m-2·d-1)
Ca: 2.1 ± 0.6 × 10-5
Th: 0.0 ± 1.0 × 10-6
Nd: 1 ± 1 × 10-7
P: 0 ± 3 × 10-7

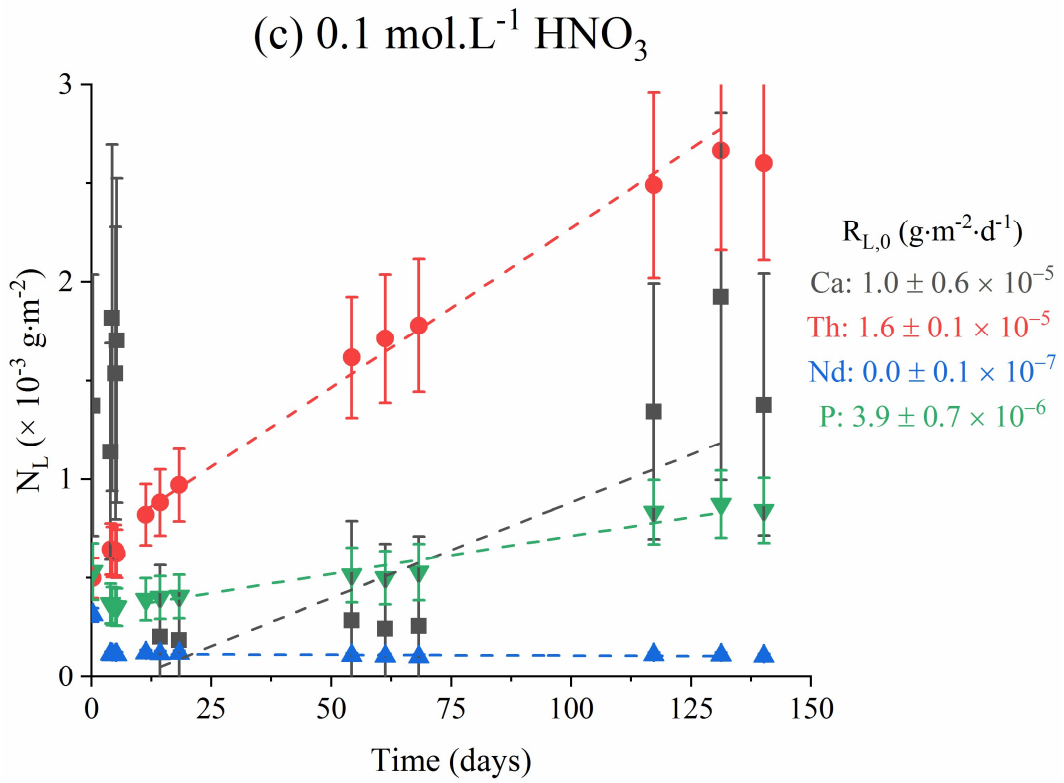

Figure IV-3. Evolution of normalized weight losses $N_L(i)$ obtained during the dissolution of $Nd_{0.8}Th_{0.1}Ca_{0.1}PO_4$ at 25°C in 1 mol.L^{-1} HNO_3 (a), in 0.32 mol.L^{-1} HNO_3 (b) and in 0.1 mol.L^{-1} HNO_3 (c). Evolutions of N_L(Ca) (■), N_L(Th) (●), N_L(Nd) (▲) and N_L(P) (▼)

Table IV-11. Normalized dissolution rates, $R_{L,0}$, obtained during the dissolution of $Nd_{0.8}Th_{0.1}Ca_{0.1}PO_4$ at 25°C in 0.1 – 1 mol.L^{-1} HNO_3.

	$R_{L,0}$ (expressed in 10^{-5} g.m^{-2}.d^{-1})				
	Ca	Th	Nd	P	
25°C, 1 mol.L^{-1}	4 ± 2	2.8 ± 0.4	3.0 ± 0.3	2.8 ± 0.2	Stoichiometric
25°C, 0.32 mol.L^{-1}	2.1 ± 0.6	-0.07 ± 0.08	0.01 ± 0.01	0.00 ± 0.03	Non-stoichiometric
25°C, 0.1 mol.L^{-1}	1.0 ± 0.6	1.6 ± 0.1	-0.08 ± 0.10	0.39 ± 0.07	Non-stoichiometric

IV-3.1.2. Investigation on the influence of temperature in 1 mol.L^{-1} HNO_3

The evolution of normalized weight losses $N_L(i)$ obtained in 1 mol.L^{-1} HNO_3 at 40°C and 80°C is reported in **Figure IV-4**. The dissolution was found to be stoichiometric for both temperatures. The normalized dissolution rates determined at 40°C were close to that determined at 25°C, *i.e.* about (3.0 ± 0.8) × 10^{-5} g.m^{-2}.d^{-1}. However, the $R_{L,0}$ values determined at 80°C were about an order of magnitude higher than for other temperatures (*i.e.* (5.6 ± 0.8) × 10^{-4} g.m^{-2}.d^{-1}, **Table IV-12**)).

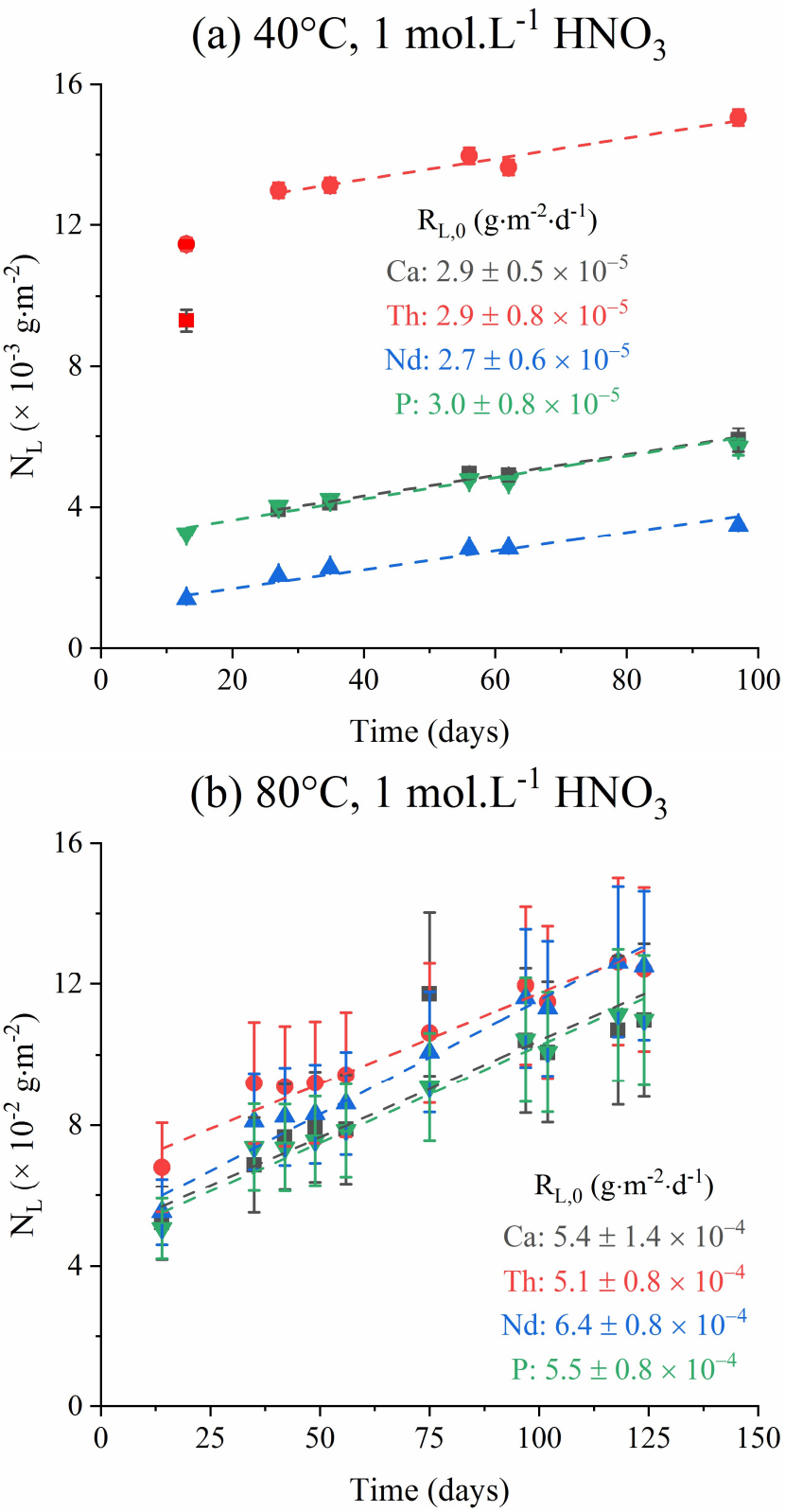

Figure IV-4. Evolution of normalized weight losses $N_L(i)$ obtained during the dissolution of $Nd_{0.8}Th_{0.1}Ca_{0.1}PO_4$ in 1 mol.L^{-1} HNO_3 at 40°C (a) and at 80°C (b). Evolutions of $N_L(Ca)$ (■), $N_L(Th)$ (●), $N_L(Nd)$ (▲) and $N_L(P)$ (▼).

Table IV-12. Normalized dissolution rates, $R_{L,0}(i)$, determined during the dissolution of $Nd_{0.8}Th_{0.1}Ca_{0.1}PO_4$ in 1 mol.L^{-1} HNO_3 for various temperatures.

	$R_{L,0}$ (expressed in 10^{-5} g.m^{-2}.d^{-1})			
	Ca	Th	Nd	P
25°C	4 ± 2	2.8 ± 0.4	3.0 ± 0.3	2.8 ± 0.2
40°C	2.9 ± 0.5	2.9 ± 0.8	2.7 ± 0.6	3.0 ± 0.8
80°C	54 ± 14	51 ± 8	64 ± 8	55 ±8

According to the data reported in the literature, Veilly *et al.* [27] reported that the normalized dissolution rate, $R_{L,0}$, obtained during the dissolution of $Ca_{0.5}Th_{0.5}PO_4$ at 90°C and pH =1 reached (2.2 ± 0.2) × 10^{-5} g.m^{-2}.d^{-1}. More recently, Gausse [19] found that $R_{L,0}$ equaled (1.01 ± 0.03) × 10^{-3} g.m^{-2}.d^{-1} for $NdPO_4$ in the same conditions of dissolution, which confirmed the higher chemical durability of the monazite-cheralite solid solution compared to pure monazite.

Moreover, according to equation IV-8, the apparent activation energies E_a associated to the overall reaction of dissolution can be evaluated when drawing the variation of $\ln(R_{L,0})$ vs. the reciprocal temperature (**Figure IV-1**). The dissolution rate determined at 40°C was close to that of 25°C. According **Figure IV-4-(a)**, the normalized weight loss obtained for thorium was much higher than for the other elements. However, the $R_{L,0}$ (Th) value was compatible with those obtained for Ca, P, and Nd. This might be due to the preferential and quick dissolution of a impurity minor phase containing large thorium content. Moreover, because of the low solubilities of thorium phosphates, a neoformed phase might have precipitated on the pellet surface and could have led to a slowdown of the normalized dissolution rates (R_L). Arinicheva *et al.* [45] already reported the dissolution of La-monazite in 0.01 mol.L^{-1} HNO_3 for temperatures ranging from 50°C to 130°C. They observed two behaviors during dissolution, *i.e.,* surface-controlled phenomena (associated to E_a = 40-140 kJ.mol^{-1}) and transport-controlled phenomena (associated to $E_a \leq 20$ kJ.mol^{-1}). They also suggested that the predominant phenomena below 90°C were surface-controlled ones (E_a = 44 kJ.mol^{-1}). In this study, the activation energy E_a (25 →40°C) was very low, which suggested that the dissolution at 40°C was controlled by transport reactions, which is compatible with the formation of a passivative layer at the surface of the material. However, the E_a value was evaluated to 46 ± 7 kJ. mol^{-1} between 25°C and 80°C (with ln k' was 8 ± 3 g.m^{-2}.d^{-1}, **Table IV-13**), which was characteristic of surface-controlling dissolution and in agreement with the conclusion of Arinicheva *et al.* [45]. Moreover, for $NdPO_4$, Gausse [19] reported the following set of data: E_a =54 ± 4 kJ.mol^{-1} and ln k' = 13.5 ± 1.6 g.m^{-2}.d^{-1}. Additionally, Oelkers and Poitrasson [16] reported E_a = 41.8 ± 12.6 kJ.mol^{-1} between 50 °C and

230°C when dissolving $CePO_4$ and Terra *et al.* [35] obtained E_a = 39 – 45 kJ. mol^{-1} during the dissolution of $GdPO_4$ between 20°C and 90°C. Both sets of data were in good agreement with ours obtained on $Nd_{0.8}Th_{0.1}Ca_{0.1}PO_4$.

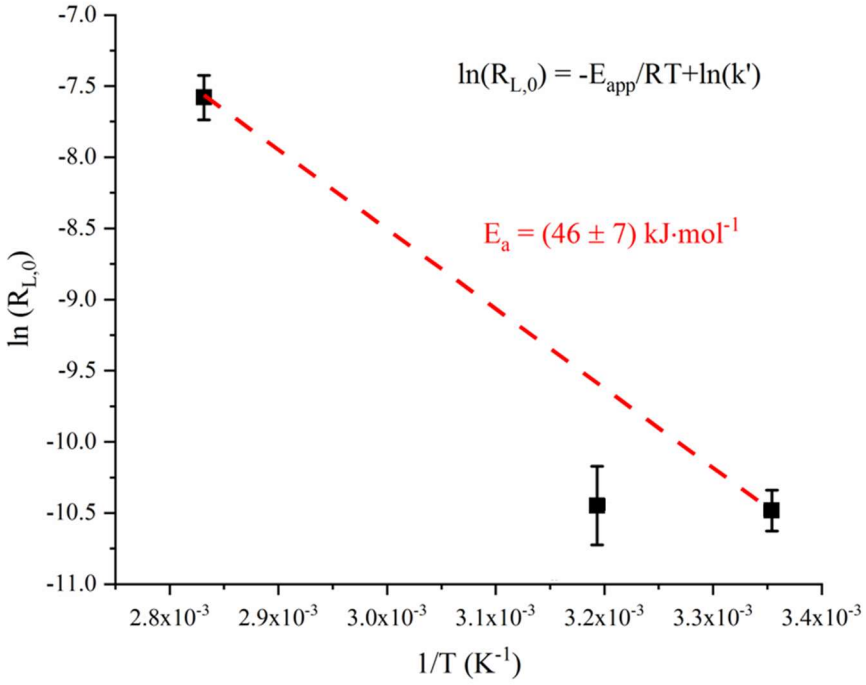

Figure IV-5. Variation of the logarithm of the normalized dissolution rates, $R_{L,0,}$ versus the reciprocal temperature during the dissolution of $Nd_{0.8}Ca_{0.1}Th_{0.1}PO_4$ in 1 $mol.L^{-1}$ HNO_3.

Table IV-13. Apparent activation energy E_a and apparent normalized dissolution rate constant k'.

	This work	Arinicheva *et al.*[45]	Gausse[19]	Oelkers and Poitrasson[16]	Terra *et al.*[35]
E_a ($kJ.mol^{-1}$)	46 ± 7 (25 → 80°C)	44 ± 5 (50 → 90°C)	54 ± 4 (25 → 40°C)	41.84 ± 12.55 (50 → 230°C)	39 – 45 (20 → 90°C)
ln (k') ($g.m^{-2}.d^{-1}$)	8 ± 2 (25 → 80°C)	–	13.5 ± 1.6 (25 → 40°C)	–	–

IV-3.2. Determination of the solubility constants at 298 K, assuming that Th-rhabdophane $Nd_{0.8}Th_{0.1}Ca_{0.1}PO_4.nH_2O$ or monazite-cheralite $Nd_{0.8}Th_{0.1}Ca_{0.1}PO_4$ is the solubility controlling phase.

IV-3.2.1. XRD analysis of the solid residue

Once the system $Nd_{0.8}Th_{0.1}Ca_{0.1}PO_4$ – 1 mol.L^{-1} HNO_3 reached the thermodynamic equilibrium, the solid residue was separated from the solution by centrifugation at 14000 rpm for 10 mins then was finally thoroughly washed twice with deionized water. After drying at 90 °C in an oven overnight, the residue was characterized by PXRD (**Figure IV-6**). The results suggested that the residue was still composed by single-phase monazite-cheralite, without any traces of other secondary phases. Nevertheless, one can not definitively exclude the presence of small amount of $Nd_{0.8}Ca_{0.10}Th_{0.10}PO_4 \cdot n\ H_2O$ (below the detection limit of the PXRD technique). Therefore, at this stage, we were not able to conclude on the nature of the Th-phase controlling the thermodynamic equilibrium.

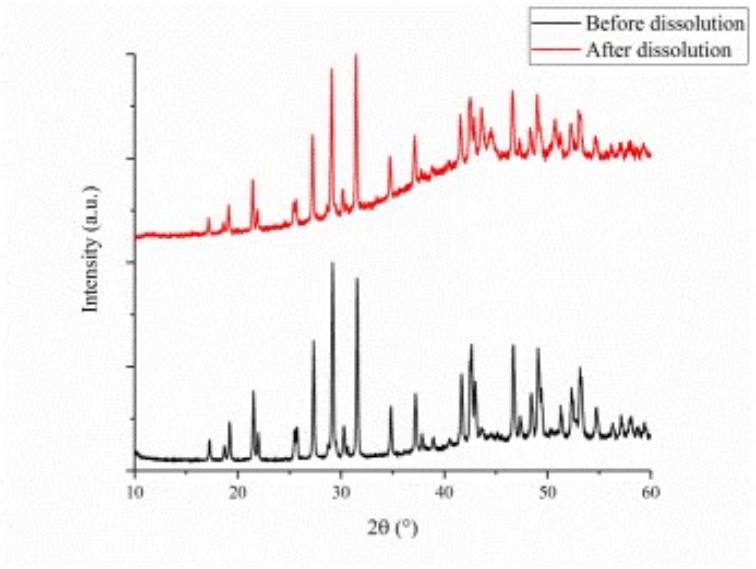

Figure IV-6. XRD patterns recorded for the starting $Nd_{0.8}Ca_{0.1}Th_{0.1}PO_4$ powdered monazite-cheralite sample and for the residue obtained after dissolution in 1 mol·L^{-1} HNO_3 at 298 K.

IV-3.2.2. Study of the saturation phenomenon at 25°C

The evolution of elemental concentrations during the dissolution of monazite-cheralite $Nd_{0.8}Ca_{0.10}Th_{0.10}PO_4$ in 1 mol·L^{-1} HNO_3 is presented in **Figure IV-7**. The elemental concentrations increased gradually then reached a plateau after about 200 days, which suggested that the thermodynamic equilibrium was reached. Simultaneously, the normalized weight losses calculated from Th, Nd, and P releases evolved in the same way; the difference observed between all the elements being within the experimental error. The normalized weight

loss of Ca showed significant fluctuations because the Ca elemental concentration was close to the detection limit of ICP-OES ($C(Ca) \leq 1$ mg.L^{-1}). Thus, the dissolution was considered to be stoichiometric, which means that the ratios between the elements measured in the solution was the same than that was characteristic of the starting monazite-cheralite.

The elemental concentrations obtained when reaching thermodynamic equilibrium are listed in **Table IV-14**. The final thorium concentration was equal to $(2.7 \pm 0.1) \times 10^{-5}$ mol.L^{-1} and the associated relative mass loss reached 6 ± 1 % of the initial Th in monazite-cheralite (**Table IV-15**), which confirmed the very high chemical durability of the prepared monazite-cheralite.

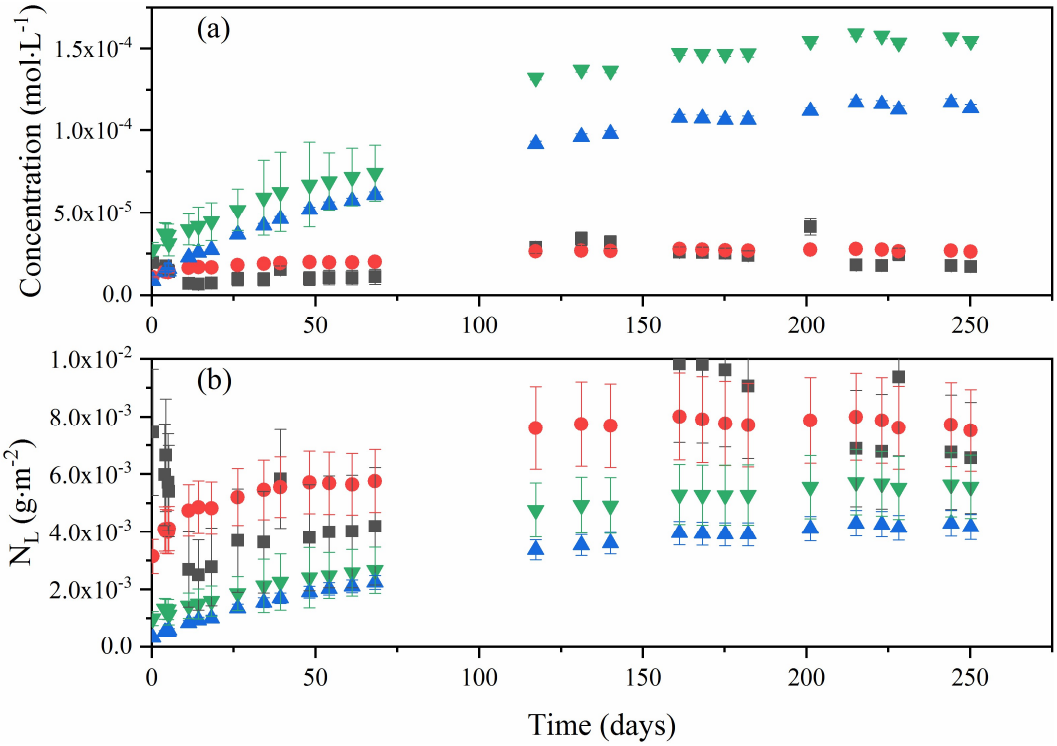

Figure IV-7. Evolution of elemental concentration obtained during the dissolution of $Nd_{0.8}Ca_{0.10}Th_{0.10}PO_4$ in 1 mol.L^{-1} HNO_3 at 298K (a) and evolution of the associated normalized weight losses N_L(Ca) (■), N_L(Th) (●), N_L(Nd) (▲) and N_L(P) (▼) (b)

For the system $Nd_{0.8}Ca_{0.10}Th_{0.10}PO_4$ – 0.32 mol.L^{-1} HNO_3 (**Figure IV-8**), the elemental concentrations of Th, Nd, and P, first increased gradually, to finally reach a maximum after about 100 days. Then the concentrations decreased slowly to reach a plateau after about 350 days. The dissolution was slower than in 1 mol.L^{-1} HNO_3 whereas the concentration at equilibrium was lower by one order of magnitude. The evolution of the normalized weight losses indicated that the dissolution was not stoichiometric between the three cations. However, even if the proportion of Th in the solution was considered to be over-stoichiometric compared to the initial powder, about 1% of Th was released in the solution only (see **Table IV-15**).

Consequently, the dissolved solid could be affected by the preferential dissolution of minor Th enriched phases (*e.g.* ThO_2).

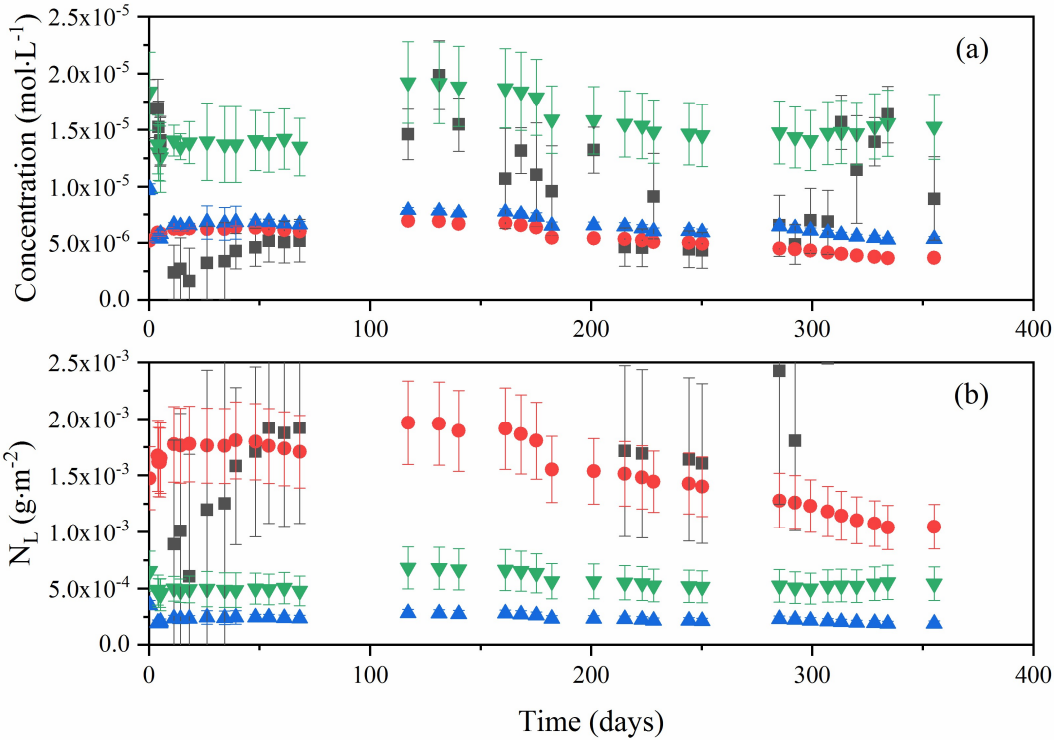

Figure IV-8. Evolution of elemental concentration obtained during the dissolution of $Nd_{0.8}Ca_{0.10}Th_{0.10}PO_4$ in 0.32 mol.L^{-1} HNO_3 at 298K (a) and evolution of the associated normalized weight losses N_L(Ca) (■), N_L(Th) (●), N_L(Nd) (▲) and N_L(P) (▼) (b)

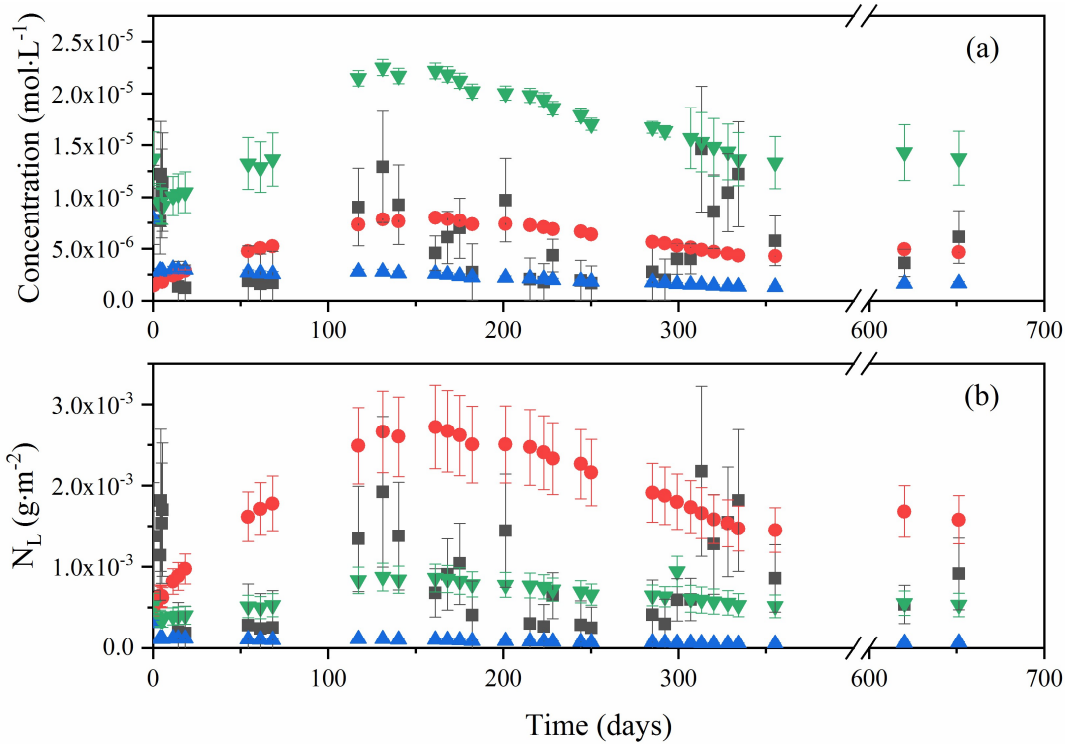

Figure IV-9. Evolution of elemental concentration obtained during the dissolution of $Nd_{0.8}Ca_{0.10}Th_{0.10}PO_4$ in 0.1 mol.L^{-1} HNO_3 at 298K (a) and evolution of the associated normalized weight losses N_L(Ca) (■), N_L(Th) (●), N_L(Nd) (▲) and N_L(P) (▼) (b).

Likewise, for the system $Nd_{0.8}Ca_{0.10}Th_{0.10}PO_4$ – 0.1 mol·L^{-1} HNO_3, the evolution of elemental concentrations is reported in **Figure IV-9**. The dissolution was even slower than that reported in 0.32 mol·L^{-1} HNO_3. The maximum of the concentrations took place at about 150 days whereas the equilibrium was reached for 600 days. The relative mass loss of thorium equaled about 1 % of the initial thorium content in the solid when reaching the equilibrium.

IV-3.2.3. Calculation of solubility constants and solubility products at 298 K

The elemental concentrations obtained at thermodynamic equilibrium are listed in **Table IV-14** whereas the mass losses of thorium are listed in **Table IV-15**. According to the thorium loss, the amount of dissolved monazite-cheralite reached about 3×10^{-5} mol in 1 mol.L^{-1} HNO_3, and 4×10^{-6} mol in 0.32 and 0.1 mol.L^{-1} HNO_3. Based on Eq. IV-24, the associated consumption of H^+ was about 8×10^{-4} mol in 1 mol.L^{-1} HNO_3 and 1×10^{-4} mol in 0.32 and 0.1 mol.L^{-1} HNO_3. Therefore, the proportion of H^+ consumed consequently to the dissolution of monazite-cheralite reached 0.8%, 0.4% and 1.3% in 1 mol.L^{-1}, 0.32 mol.L^{-1}, and 0.1 mol.L^{-1}, respectively. All these results validated the hypothesis made concerning the invariant proton concentration during the dissolution tests. Consequently, the pH of the leaching solutions were considered to remain constant and were calculated thanks to Eq. IV-39 (**Table IV-10**). The obtained values were equal to 0.13 ± 0.02, 0.63 ± 0.02 and 1.10 ± 0.02 for 1 mol.L^{-1} HNO_3, 0.32 mol.L^{-1} HNO_3 and 0.1 mol.L^{-1} HNO_3, respectively.

Table IV-14. Elemental concentrations obtained at thermodynamic equilibrium during dissolution tests of $Nd_{0.8}Ca_{0.10}Th_{0.10}PO_4$ at 298 K.

C_{HNO_3} [mol.L^{-1}]	C_{Ca} [mol.L^{-1}]	C_{Th} [mol.L^{-1}]	C_{Nd} [mol.L^{-1}]	C_P [mol.L^{-1}]
1.00 ± 0.02	$(1.9 \pm 0.6) \times 10^{-5}$	$(2.7 \pm 0.1) \times 10^{-5}$	$(1.15 \pm 0.04) \times 10^{-4}$	$(1.56 \pm 0.05) \times 10^{-4}$
0.32 ± 0.01	$(1.0 \pm 0.9) \times 10^{-5}$	$(5 \pm 2) \times 10^{-6}$	$(6 \pm 2) \times 10^{-6}$	$(1.6 \pm 0.4) \times 10^{-5}$
0.100 ± 0.002	$(8 \pm 8) \times 10^{-6}$	$(4.7 \pm 0.6) \times 10^{-6}$	$(1.5 \pm 0.3) \times 10^{-6}$	$(1.4 \pm 0.3) \times 10^{-5}$

Table IV-15. Relative mass loss of thorium obtained at equilibrium during dissolution tests of $Nd_{0.8}Ca_{0.10}Th_{0.10}PO_4$ at 298 K.

C_{HNO_3} [mol.L^{-1}]	$\frac{m_{Th}(dissolved)}{m_{Th}(solid)} \times 100\%$
1.00 ± 0.02	6 ± 1 %
0.32 ± 0.01	1 ± 1 %
0.100 ± 0.002	1.0 ± 0.2 %

The speciation in solution was calculated by PHREEQC considering the elemental concentrations (**Table IV-14**) and pH values (**Table IV-10**) measured at equilibrium. The

molalities and the activities of the species of interest (*i.e.*, Ca^{2+}, Th^{4+}, Nd^{3+}, H_3PO_4) were evaluated (see **Table IV-16** and **Table IV-17**).

Table IV-16. pH values and calculated molalities of the species of interest obtained at thermodynamic equilibrium during dissolution tests of $Nd_{0.8}Ca_{0.10}Th_{0.10}PO_4$ at 298 K

pH	$m_{Ca^{2+}}$ [mol.kg^{-1}]	$m_{Th^{4+}}$ [mol.kg^{-1}]	$m_{Nd^{3+}}$ [mol.kg^{-1}]	$m_{H_3PO_4}$ [mol.kg^{-1}]
0.13 ± 0.02	$(1.9 \pm 0.6) \times 10^{-5}$	$(4.9 \pm 0.2) \times 10^{-7}$	$(7.6 \pm 0.3) \times 10^{-5}$	$(1.49 \pm 0.06) \times 10^{-4}$
0.63 ± 0.02	$(1.0 \pm 0.9) \times 10^{-5}$	$(3 \pm 1) \times 10^{-6}$	$(5 \pm 1) \times 10^{-6}$	$(1.5 \pm 0.3) \times 10^{-5}$
1.10 ± 0.02	$(8 \pm 8) \times 10^{-6}$	$(3.2 \pm 0.4) \times 10^{-6}$	$(1.3 \pm 0.2) \times 10^{-6}$	$(1.3 \pm 0.2) \times 10^{-5}$

Table IV-17. pH values and calculated activities of the species of interest obtained at thermodynamic equilibrium during dissolution tests of $Nd_{0.8}Ca_{0.10}Th_{0.10}PO_4$ at 298 K

pH	(Ca^{2+}) [mol kg^{-1}]	(Th^{4+}) [mol kg^{-1}]	(Nd^{3+}) [mol kg^{-1}]	(H_3PO_4) [mol kg^{-1}]
0.13 ± 0.02	$(3 \pm 1) \times 10^{-5}$	$(1.3 \pm 0.1) \times 10^{-9}$	$(1.11 \pm 0.04) \times 10^{-6}$	$(1.49 \pm 0.04) \times 10^{-4}$
0.63 ± 0.02	$(2 \pm 2) \times 10^{-6}$	$(1.7 \pm 0.7) \times 10^{-8}$	$(2.0 \pm 0.5) \times 10^{-7}$	$(1.5 \pm 0.3) \times 10^{-5}$
1.10 ± 0.02	$(3 \pm 3) \times 10^{-6}$	$(7 \pm 1) \times 10^{-8}$	$(1.3 \pm 0.2) \times 10^{-7}$	$(1.3 \pm 0.2) \times 10^{-5}$

According to Eq. IV-27, the values of $\log_{10}\ {}^{*}K_s^m$ were evaluated to -7.8 ± 0.1, -8.2± 0.3, and -7.4 ± 0.2 in 1 mol.L^{-1} HNO_3, 0.32 mol.L^{-1} HNO_3, and 0.1 mol.L^{-1} HNO_3, respectively.

Making the assumption that the monazite-cheralite was the solubility-controlling phase, the $\log_{10}\ {}^{*}K_s^o$(monazite-cheralite) value was calculated from Eq. IV-26, *i.e.* The calculated $\log_{10}\ {}^{*}K_s^o$ were found to -9.6 ± 0.1, -9.6 ± 0.3 and – 8.4 ± 0.2 for 1 mol.L^{-1} HNO_3, 0.32 mol.L^{-1} HNO_3 and 0.1 mol.L^{-1} HNO_3, respectively. According to Eq. IV-33, the associated values of standard solubility constant $\log_{10}(K_{s,0}^o)$ reached -31.1 ± 0.1, -31.3 ± 0.4, and -30.1 ± 0.3, respectively.

On the contrary, if we considered that Th-rhabdophane was the solubility controlling phase, the solubility constants could be calculated thanks to Eq. IV-35. According to TG analyses, performed by A. Shelyug and A. Navrotsky (UC-Davis, California) [42], the number of water molecule n was 0.968. Based on Eq. IV-36 and IV-37, the values of $n \times \log_{10}(H_2O)$ reached -0.015, -0.005 and -0.001 in 1 mol.L^{-1} HNO_3, 0.32 mol.L^{-1} HNO_3 and 0.1 mol.L^{-1} HNO_3, respectively. These values were an order of magnitude smaller than the uncertainty associated to $\log_{10} K_{s,0}^{\circ}$(monazite-cheralite) (*i.e.* 0.1-0.4). Therefore, we could assume that $\log_{10} K_{s,0}^{\circ}(\text{Th-rhabdophane}) \approx \log_{10} K_{s,0}^{\circ}(\text{monazite-cheralite})$. All the values obtained in the three dissolution media considered are reported in the **Table IV-18**.

All the $\log_{10}(K^{o}_{s.0})$ values determined at pH = 0.13 and 0.63 were consistent taking into account the associated uncertainties. This observation underlined that the same phase controlled the saturation equilibrium in both media. Meanwhile, the $\log_{10} K^{\circ}_{s,0}$ value determined at pH = 1.10 was significantly higher than the values determined at other pH. Therefore it was not considered in the estimation of the final $\log_{10} K^{\circ}_{s,0}$ (Th-rhabdophane or Th-monazite-cheralite) value at 298 K.

Table IV-18. Solubility products and standard solubility constants calculated obtained at thermodynamic equilibrium during dissolution tests of $Nd_{0.8}Ca_{0.10}Th_{0.10}PO_4$ at 298 K in several nitric acid media.

pH	$\log_{10}\left({}^{*}K_s^{m}\right)$	$\log_{10}\left({}^{*}K_s^{o}\right)$	$\log_{10}(K^{o}_{s.0})$
0.13 ± 0.01	-7.8 ± 0.1	-9.6 ± 0.1	-31.3 ± 0.1
0.63 ± 0.01	-8.2 ± 0.3	-9.6 ± 0.3	-31.3 ± 0.4
1.10 ± 0.01	-7.4 ± 0.2	-8.4 ± 0.2	-30.1 ± 0.3

IV-3.2.4. Justification of Th-rhabdophane or Th-monazite-cheralite as a solubility-controlling phase by PHREEQC simulations.

Once the $\log(K^{o}_{s.0})$ was determined, this thermodynamic constant was introduced into the ThermoChimie database and PHREEQC simulation of the $Nd_{0.8}Th_{0.1}Ca_{0.1}PO_4$ / HNO_3 system. The evolution of the elemental concentrations at thermodynamic equilibrium as the function of pH is presented in **Figure IV-10**. The results of the PHREEQC simulation of the $Nd_{0.8}Th_{0.1}Ca_{0.1}PO_4$ / HNO_3 system were consistent with the experimental data reported in **Table IV-14**. However, they suggested that the Nd and P elemental concentrations should be about three orders of magnitude higher than the experimental data if controlled by the TPHPH / $NdPO_4.0.667\ H_2O$ / HNO_3 system. Meanwhile, if controlled by the TPHPH / $NdPO_4.0.667\ H_2O$ / HNO_3 system, the simulated Th concentration should be two orders of magnitude higher than that obtained at at pH =0.1. However, at pH = 1.1, the simulated Th concentration was lower than the experimental data. It might suggest that the solubility-controlling phase was always Th-rhabdophane $Nd_{0.8}Th_{0.1}Ca_{0.1}PO_4.nH_2O$ or monazite-cheralite $Nd_{0.8}Th_{0.1}Ca_{0.1}PO_4$ when the concentration of HNO_3 was comprised between 0.32 $mol.L^{-1}$ and 1 $mol.L^{-1}$. However, for acid concentration equal or lower than 0.1 $mol.L^{-1}$, THPTH could have been formed in a mixture containing Th-rhabdophane slightly depleted in thorium. The system was still moving towards equilibrium after more than 600 days of leaching. This might be another reason for incongruence between the elemental concentrations observed during the dissolution experiment performed in 0.1 $mol.L^{-1}$ HNO_3. It could also explain why the $\log_{10} K^{\circ}_{s,0}$ determined at pH = 1.1 was not consistent with the values obtained at pH 0.13 and 0.63 (**Table IV-18**).

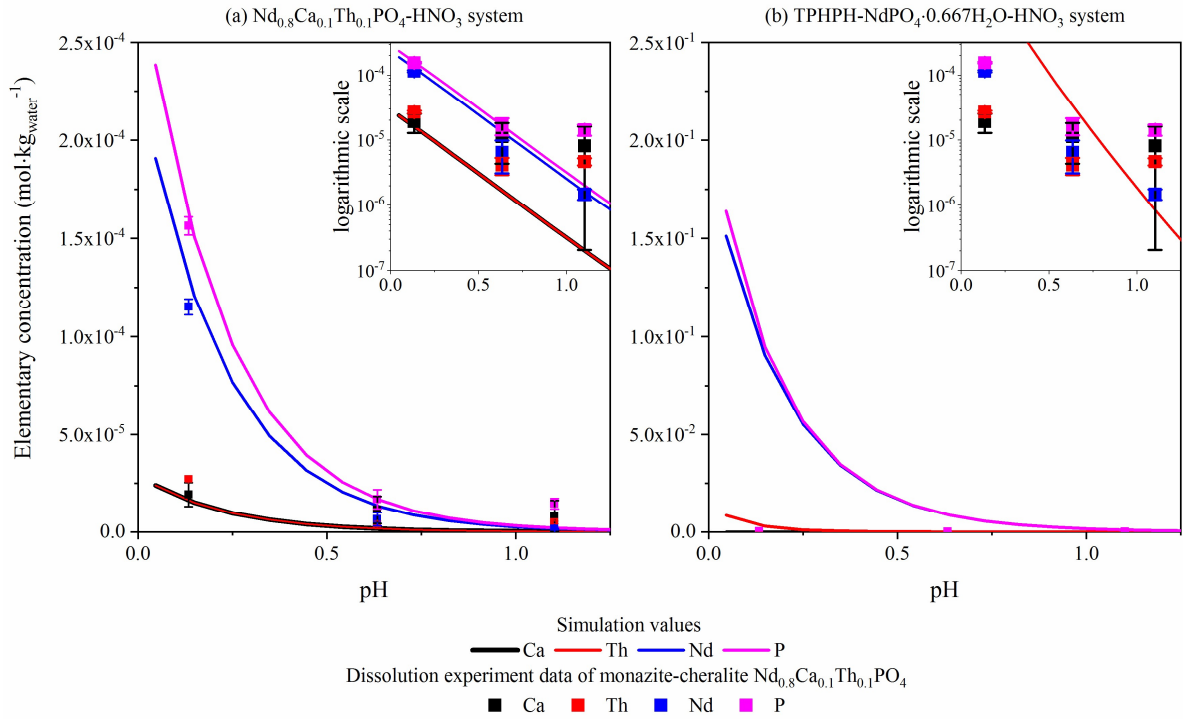

Figure IV-10. Evolution of elemental concentrations at thermodynamic equilibrium vs. the pH value and comparison of the experimental data obtained at equilibrium with the results of the simulations.

Finally, as the aqueous conditions in the repository site is neutral or lightly alkaline [1], a complementary simulation by PHREEQC was from 0 to 8.5 in order to determine the elemental concentrations obtained when reaching saturation conditions for both TPHPH / ThO_2 / $NdPO_4.0.667H_2O$ / HNO_3-NaOH and $Nd_{0.8}Th_{0.1}Ca_{0.1}PO_4$ / HNO_3-NaOH systems. It is worth noting that in order to better simulate the contribution of other phosphate minerals to the aqueous phosphate species, the elemental concentration of P was set to above 10^{-6} mol.L^{-1} during the whole simulation. For the first system, the thorium molality dropped below 10^{-12} mol. kg_{water}^{-1} when the pH is above 6. The solubility-controlling phases for thorium was ThO_2. For the second system, m_{Th} was even less than 10^{-1} mol. kg_{water}^{-1} [7] for pH ≥ 6, which was even lower than the case that ThO_2 is the solubility-controlling phase. Consequently, by applying the $\log(K_{s,0}^{o})$ value determined in this study, these results of simulation suggest that $Nd_{0.8}Th_{0.1}Ca_{0.1}PO_4$ has exceptional chemical stability in near neutral conditions.

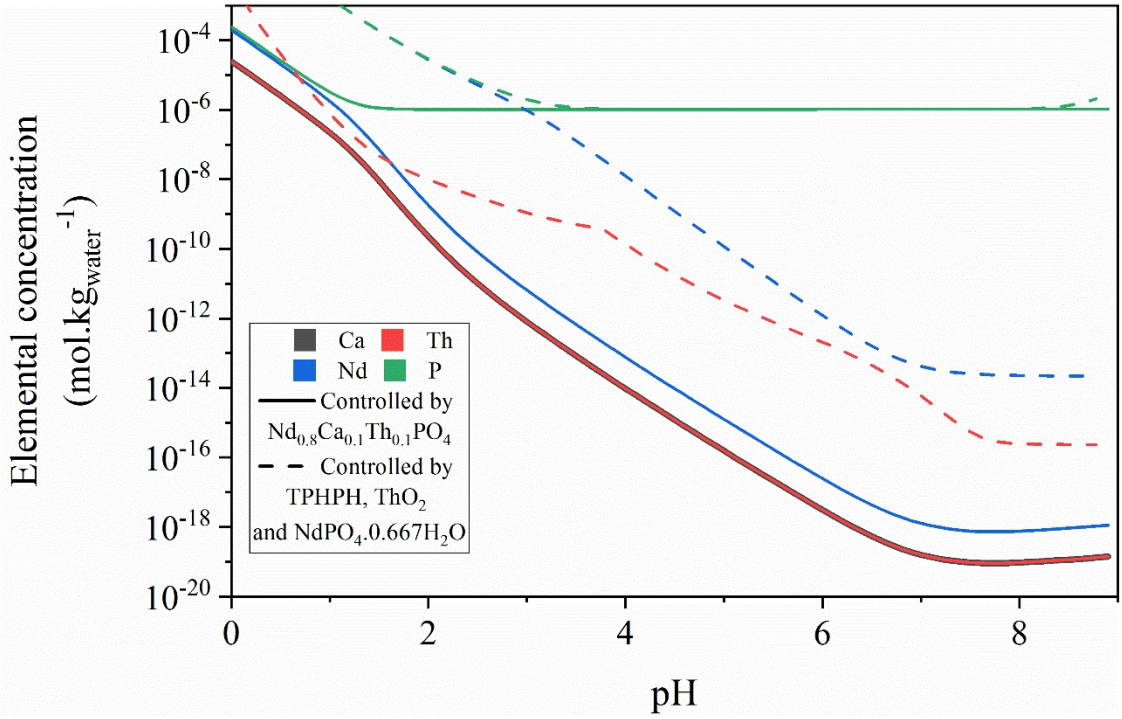

Figure IV-11. Elemental concentrations obtained at thermodynamic equilibrium in near neutral conditions when considering the TPHPH / ThO_2 / $NdPO_4.0.667H_2O$ / HNO_3-NaOH system and the $Nd_{0.8}Th_{0.1}Ca_{0.1}PO_4$ / HNO_3-NaOH system with C $(P)_{min} = 10^{-6}$ mol.L^{-1}.

IV-3.2.5. Determination of the associated thermodynamic data

The $\log_{10}(K^{o}_{s,0})$ value associated to the reaction:

$$Nd_{0.8}Ca_{0.1}Th_{0.1}PO_4.nH_2O \rightleftarrows 0.8\ Nd^{3+} + 0.1\ Ca^{2+} + 0.1Th^{4+} + PO_4^{3-} + nH_2O$$

was evaluated from dissolution experiments. This value allowed the evaluation of the corresponding variation of Gibb's free energy, $\Delta_rG°$ (kJ.mol^{-1}) at 298K, according to:

$$\Delta_rG^{\circ} = -R\times T\times \ln\left(K^{\circ}_{s,0}\ (\text{monazite, or rhabdophane,T})\right) \qquad \text{(IV-40)}$$

where R is the gas constant and T the absolute temperature.

As $\log_{10}K^{o}_{s,0}$(Th-rhabdophane) $\simeq$ $\log_{10}K^{o}_{s,0}$(monazite-cheralite), the values of $\Delta_rG°$ (Th-rhabdophane) and $\Delta_rG°$ (monazite-cheralite) were found to be the same: $\Delta_rG^{\circ} = 179 \pm 2$ kJ.mol^{-1}.

Moreover, the variation of the standard Gibbs energy associated to the formation of $Nd_{0.8}Ca_{0.10}Th_{0.10}PO_4$ and $Nd_{0.8}Ca_{0.10}Th_{0.10}PO_4.nH_2O$ from its constitutive elements, Δ_fG°(298K), were determined by applying the Hess's law, according to:

$$\Delta_f G^\circ(\text{Th-rhabdophane}) = 0.8 \times \Delta_f G^\circ\left(Nd^{3+}\right) + 0.1 \times \Delta_f G^\circ(Ca^{2+}) + 0.1 \times \Delta_f G^\circ\left(Th^{4+}\right) + \Delta_f G^\circ\left(PO_4^{3-}\right) + 0.968 \times \Delta_f G^\circ(H_2O) - \Delta_r G^\circ \quad \text{(IV-41)}$$

and

$$\Delta_f G^\circ(\text{monazite-cheralite}) = 0.8 \times \Delta_f G^\circ\left(Nd^{3+}\right) + 0.1 \times \Delta_f G^\circ(Ca^{2+}) + 0.1 \times \Delta_f G^\circ\left(Th^{4+}\right) + \Delta_f G^\circ\left(PO_4^{3-}\right) - \Delta_r G^\circ \quad \text{(IV-42)}$$

Thus, the standard free energy of formation of the two phases differs by: $0.968 \times \Delta_f G^\circ(H_2O) = -229.55 \pm 0.04$ kJ.mol^{-1}. The thermodynamic data used in this calculation are listed in **Table IV-19**. Based on these data, the $\Delta_f G^\circ$(Th-rhabdophane) equals -2097 ± 9 kJ.mol^{-1}. If we considered that the monazite-cheralite was the solubility controlling phase, the $\Delta_f G^\circ$(monazite-cheralite) reaches - 1868 ± 9 kJ.mol^{-1}.

Table IV-19. Selected data of the standard free energies and enthalpies of formation from elements as well as entropies (T = 298.15 K) [9,46–48]

	$\Delta_f G^\circ$ (kJ.mol^{-1})	$\Delta_f H^\circ$ (kJ.mol^{-1})	S_m° (J.K^{-1}.mol^{-1})	Ref.
H_2O	-237.14 ± 0.04	-285.83 ± 0.04	69.950 ± 0.030	NEA
Nd_2O_3	-1719.8 ± 6.6	-1806.9 ± 3.0	158.7 ± 1.0	Navrotsky *et al* Konings
ThO_2	– 1168.988 ± 3.504	-1226.4 ± 3.5	65.230 ± 0.200	NEA
CaO	– 603.296 ± 0.916	-643.92 ± 0.9	38.100 ± 0.400	NEA
P_2O_5	-1361.6 ± 0.5	-1504.9 ± 0.5	114.4 ± 0.4	Robie *et al.*
Nd^{3+}	-672*	-696.6 ± 1.7	-207*	Morss *et al.*
Th^{4+}	– 704.783 ± 5.298	-768.7 ± 2.3	423.100 ± 16.000	NEA
Ca^{2+}	– 552.806 ± 1.050	543.000 ± 1.000	– 56.200 ± 1.000	NEA
PO_4^{3-}	– 1025.491 ± 1.576	– 1284.400 ± 4.085	– 220.970 ± 12.846	NEA

* no available uncertainty data

As mentioned above, through a collaboration between the University of California Davis and ICSM, we determined with A. Shelyug and A. Navrotsky the enthalpy of formation of the Th-monazite ($Nd_{0.8}Ca_{0.10}Th_{0.10}PO_4$) and Th-rhabdophane ($Nd_{0.8}Ca_{0.10}Th_{0.10}PO_4.0.968\ H_2O$) samples by high-temperature oxide melt solution calorimetry. About 5 mg powder samples were pressed into pellets and dropped into lead borate melt ($2PbO.B_2O_3$) in a Pt crucible in the calorimeter at 800 °C. The setup was flushed (40ml.min^{-1}) with oxygen and the solvent was bubbled (4.5ml.min^{-1}) to promote dissolution and remove the water vapor from the cell. The phosphate samples would be completely dissolved, leading to the formation of Nd_2O_3, ThO_2, CaO, P_2O_5, and H_2O. The obtained values of enthalpies of formation were found to $\Delta_f H_{ox}$ = -266 ± 8 kJ.mol^{-1} and $\Delta_f H_{ox}$ = -317 ± 9 kJ.mol^{-1}, for Th-rhabdophane and Th-monazite-cheralite,

respectively. For these values, the index "ox" suggests that these enthalpies were calculated from oxides. According to Hess's law, the enthalpy of formation from elements was calculated as follows:

$$\Delta_f H^\circ = \Delta_f H_{ox}{}^\circ(\text{rhabdophane/monazite-cheralite}) + \Sigma\Delta_f H^\circ(\text{oxides}) \quad \text{(IV-43)}$$

In the case of this study,

$$\Delta_f H^\circ = 0.4 \times \Delta_f H^\circ(Nd_2O_3) + 0.1 \times \Delta_f H^\circ(CaO) + 0.1 \times \Delta_f H^\circ(ThO_2) + 0.5 \times \Delta_f H^\circ(P_2O_5) + n \times \Delta_f H^\circ(H_2O) + \Delta_f H_{ox}{}^\circ(\text{rhabdophane/monazite-cheralite}) \quad \text{(IV-44)}$$

Therefore, $\Delta_f H^\circ$ reaches - 2205 ± 8 kJ.mol^{-1} for Th-Rhabdophane and - 1980 ± 9 kJ.mol^{-1} for Th-monazite-cheralite. From these data, the standard molar entropy of formation $\Delta_f S^\circ$ were deduced from the following equation:

$$\Delta_f S^\circ = \frac{\Delta_f H^\circ - \Delta_f G^\circ}{T} \quad \text{(IV-45)}$$

Consequently, the standard molar entropy of formation $\Delta_f S^\circ$ at 298K was found to - 360 ± 58 J.mol^{-1}.K^{-1} for Th-Rhabdophane and to - 376 ± 58 J.mol^{-1}.K^{-1} for Th-monazite-cheralite. Finally, the standard molar entropy, S_m° , can be expressed as follows:

$$S_m^\circ(\text{Th-rhabdophane}) = \Delta_f S^\circ(\text{Th-rhabdophane}) + 0.8 \times S_m^\circ(Nd, cr) + 0.1 \times S_m^\circ(Th,cr) + 0.1 \times S_m^\circ(Ca,cr) + S_m^\circ(P,cr) + 2 \times S_m^\circ(O_2,g) + 0.96 \times \left[\frac{1}{2} \times S_m^\circ(O_2,g) + S_m^\circ(H_2,g)\right] \quad \text{(IV-46)}$$

and

$$S_m^\circ(\text{monazite-cheralite}) = \Delta_f S^\circ(\text{monazite-cheralite}) + 0.8 \times S_m^\circ(Nd, cr) + 0.1 \times S_m^\circ(Th,cr) + 0.1 \times S_m^\circ(Ca,cr) + S_m^\circ(P,cr) + 2 \times S_m^\circ(O_2,g) \quad \text{(IV-47)}$$

These thermodynamic data of formation from elements are listed in **Table IV-20**.

Table IV-20. Thermodynamic data determined for the formation of $Nd_{0.8}Ca_{0.10}Th_{0.10}PO_4$ and $Nd_{0.8}Ca_{0.10}Th_{0.10}PO_4.0.968\ H_2O$ from elements (T =298.15 K).

	$\Delta_f G^\circ$ (kJ.mol^{-1})	$\Delta_f H^\circ$ (kJ.mol^{-1})	$\Delta_f S^\circ$ (J.mol^{-1}.K^{-1})	S_m° (J.mol^{-1}.K^{-1})
Th-rhabdophane	- 2097 ± 9	- 2205 ± 8	- 360 ± 58	383 ± 58
Th-monazite-cheralite	- 1868 ± 9	- 1980 ± 9	- 376 ± 58	142 ± 59

Table IV-21. Selected standard molar entropies used for the determination of the thermodynamic data associated to the formation of $Nd_{0.8}Ca_{0.10}Th_{0.10}PO_4$ and $Nd_{0.8}Ca_{0.10}Th_{0.10}PO_4.0.968\ H_2O$ [9,49]

	S_m° (J.K^{-1}.mol^{-1})	Ref.
H_2 (g)	130.680 ± 0.003	NEA
O_2 (g)	205.152 ± 0.005	NEA

	$S_m°$ (J.K^{-1}.mol^{-1})	Ref.
Nd (cr)	71.09 ± 4.18	Robie *et al.*
Th (cr)	52.640 ± 0.500	NEA
Ca (cr)	41.590 ± 0.400	NEA
P (cr)	41.090 ± 0.250	NEA

Finally, A. Shelyug and A. Navrotsky determined the enthalpy of conversion of Th-rhabdophane into monazite-cheralite plus 0.968 H_2O. They found that Δ_rH(conversion, 298K) = -52 ± 1 kJ.mol^{-1}. Since the reaction is exothermic, the conversion of Th-rhabdophane into monazite-cheralite is unfavored by an increase of temperature.

Summary

In this chapter, multiparametric dissolution tests of $Nd_{0.8}Ca_{0.1}Th_{0.1}PO_4$ were performed in order to evaluate the chemical durability of the synthesized monazite-cheralite samples. From a kinetic point of view, the normalized dissolution rate $R_{L,0}$ was about 3×10^{-5} $g.m^{-2}.d^{-1}$ at 25°C, which is in good agreement with the values reported for other kinds of monazite-cheralite ceramics. Such normalized dissolution rates are lower than that reported for other ceramics matrices, such as, britholite and zirconolite. The apparent activation energy associated with the dissolution reaction, E_a, equals 46 ± 7 $kJ.mol^{-1,}$ and the logarithm of associated apparent normalized dissolution rate constant, k' equals $(3.5 \pm 1.0) \times 10^3$ $g.m^{-2}.d^{-1}$. The dissolution of monazite-cheralite solid solution appeared to be stoichiometric in strongly acidic conditions, *i.e.* for $C(H^+) \geq 1$ $mol.L^{-1}$. The rapid precipitation of neoformed phases took place even at 0.32 $mol.L^{-1}$ HNO_3, which argue for the high chemical stability of this matrix.

When saturation conditions were reached in the solution, Th-rhabdophane $Nd_{0.8}Ca_{0.1}Th_{0.1}PO_4.nH_2O$ or monazite-cheralite $Nd_{0.8}Ca_{0.1}Th_{0.1}PO_4$ were suspected to act as the solubility-controlling phase. The associated solubility product was found to $K_{s,0}° = 10^{-31.3 \pm 0.1}$. The solubility of this solubility-controlling phase was lower than that calculated for the rhabdophane $NdPO_4.nH_2O$ + TPHPH combination. Later, the thermodynamic data associated to the formation of both phases from elements were determined. The Δ_fG°, Δ_fH° and Δ_fS° values (Th-rhabdophane / monazite-cheralite) were - 2097 ± 9 and - 1868 ± 9 $kJ.mol^{-1}$, - 2205 ± 8 and - 1980 ± 9 $kJ.mol^{-1}$, - 360 ± 58 and - 376 ± 58 $J.mol^{-1}.K^{-1}$ for Th-rhabdophane and Th-monazite-cheralite, respectively.

In conclusion, all the obtained data (either kinetics and thermodynamics) argue for the very high chemical durability of the monazite-cheralite solid solutions in field of its use as a specific conditioning matrix for the long-term immobilization of actinides.

Dans ce chapitre, une étude multiparamétrique relative à la dissolution des échantillons de monazite-chéralite $Nd_{0,8}Ca_{0,1}Th_{0,1}PO_4$ a été menée afin d'évaluer sa durabilité chimique. D'un point de vue cinétique, la vitesse de dissolution normalisée, $R_{L,0}$, déterminée à 25 ° C s'établit à environ 3×10^{-5} $g.m^{-2}.j^{-1}$, ce qui apparait en bon accord avec les vitesses relevées dans le cadre d'autres études portant sur des échantillon synthétiques ou naturels de monazite-cheralite et significativement plus faible que celles déterminées pour d'autres matrices céramiques, telles que les britholites ou la zirconolite. L'énergie d'activation apparente associée à la réaction de dissolution, E_a, est égale à 46 ± 7 $kJ.mol^{-1}$ tandis que le logarithme de la constante apparente de la vitesse de dissolution normalisée associée, k', est de $(3,5 \pm 1,0) \times 10^3$ $g.m^{-2}.j^{-1}$. Sur la base des tests de dissolution mis en place, la dissolution apparaît stœchiométrique dans des milieux de forte acidité, c'est-à-dire pour C $(H^+) \geq 1$ M. En milieu moins acide (tel que HNO_3 0,3 $mol.L^{-1}$), une reprécipitation rapide de phases néoformées est pressentie , ce qui renforce la durabilité de la céramique initiale.

Lorsque les conditions de saturation sont atteintes en solution, deux phases, la rhabdophane $Nd_{0,8}Ca_{0,1}Th_{0,1}PO_4,nH_2O$ et la monazite-chéralite $Nd_{0,8}Ca_{0,1}Th_{0,1}PO_4$ sont susceptibles de contrôler les concentrations en solution. Le produit de solubilité associé a été évalué à $K_{s,0}° = 10^{-31,3 \pm 0,1}$. Sur la base des calculs de spéciation, la solubilité de ces deux phases apparaît inférieure à celle de l'association rhabdophane $NdPO_4,nH_2O$ + PHPTH. Les données thermodynamiques associées à la formation de ces deux phases à partir des éléments ont été évaluées. Les valeurs de $\Delta_f G^\circ$, $\Delta_f H^\circ$ et $\Delta_f S^\circ$ atteignent respectivement pour la rhabdophane et pour la monazite-cheralite : - 2097 ± 9 et -1868 ± 9 $kJ.mol^{-1}$, - 2205 ± 8 et -1980 ± 9 $kJ.mol^{-1}$ et enfin - 360 ± 58 et - 376 ± 58 $J.mol^{-1}.K^{-1}$.

En conclusion, sur les bases de l'ensemble de ces résultats (aspects cinétique et thermodynamique), la solution solide de monazite-cheralite est caractérisée par une excellente durabilité chimique, laquelle est associée à de très faibles vitesses de dissolution normalisées et à des phases néoformées de très faibles solubilités. Ainsi, cette matrice céramique apparaît comme une matrice très efficace pour assurer le conditionnement spécifique des actinides, à long terme.

Multiparametric Dissolution Tests

$Nd_{0.8}Th_{0.1}Ca_{0.1}PO_4$
Monazite-cheralite
powder

Potential ceramic for specific conditioning of actinides

Kinetic Stage

$R_L = (3.0 \pm 0.8) \times 10^{-5}$ g·m^{-2}·d^{-1}

Good Chemical durability

Thermodynamic Stage

Precipitation of Th-rhabdophane

$\log_{10}(K^o_{s,0}) = -31.3 \pm 0.1$

Low solubility of neoformed phases

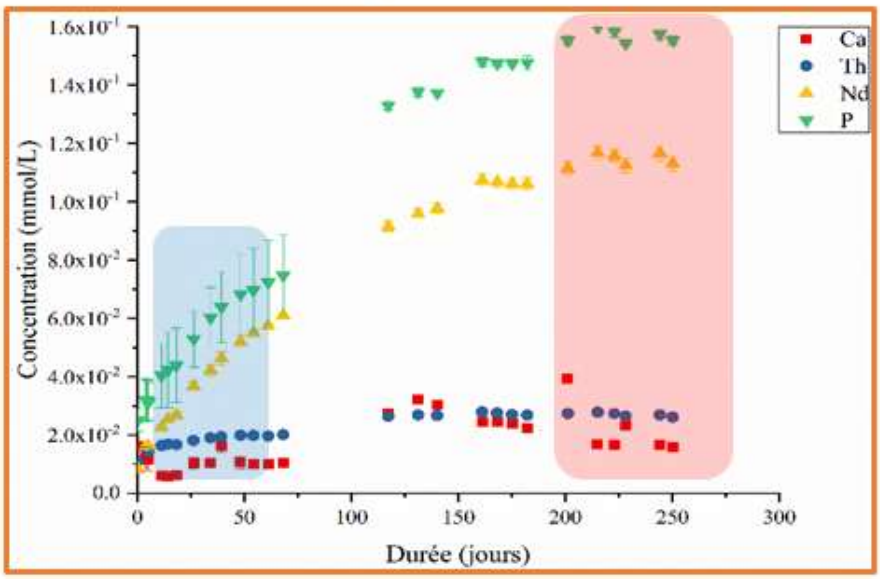

References:

(1) OECD; Agency, N. E. *Geological Disposal of Radioactive Waste*; 1999. https://doi.org/10.1787/9789246180547-en.

(2) Kim, J.-S.; Kwon, S.-K.; Sanchez, M.; Cho, G.-C. Geological Storage of High Level Nuclear Waste. *KSCE Journal of Civil Engineering* **2011**, *15* (4), 721–737. https://doi.org/10.1007/s12205-011-0012-8.

(3) Dacheux, N.; Clavier, N.; Ritt, J. Behavior of Thorium–Uranium (IV) Phosphate–Diphosphate Sintered Samples during Leaching Tests. Part I – Kinetic Study. *Journal of Nuclear Materials* **2006**, *349* (3), 291–303. https://doi.org/10.1016/j.jnucmat.2005.11.009.

(4) Dacheux, N.; Du Fou de Kerdaniel, E.; Clavier, N.; Podor, R.; Aupiais, J.; Szenknect, S. Kinetics of Dissolution of Thorium and Uranium Doped Britholite Ceramics. *Journal of Nuclear Materials* **2010**, *404* (1), 33–43. https://doi.org/10.1016/j.jnucmat.2010.06.023.

(5) Guy, C.; Audubert, F.; Lartigue, J.-E.; Latrille, C.; Advocat, T.; Fillet, C. New Conditionings for Separated Long-Lived Radionuclides. *Comptes Rendus Physique* **2002**, *3* (7), 827–837. https://doi.org/10.1016/S1631-0705(02)01377-4.

(6) Dacheux, N.; Clavier, N.; Robisson, A.-C.; Terra, O.; Audubert, F.; Lartigue, J.-É.; Guy, C. Immobilisation of Actinides in Phosphate Matrices. *Comptes Rendus Chimie* **2004**, *7* (12), 1141–1152. https://doi.org/10.1016/j.crci.2004.02.019.

(7) Novotny, P.; Sohnel, O. Densities of Binary Aqueous Solutions of 306 Inorganic Substances. *J. Chem. Eng. Data* **1988**, *33* (1), 49–55. https://doi.org/10.1021/je00051a018.

(8) A Report of IUPAC Commission 1.2 on Thermodynamics Notation for States and Processes, Significance of the Word "Standard" in Chemical Thermodynamics, and Remarks on Commonly Tabulated Forms of Thermodynamic Functions. *The Journal of Chemical Thermodynamics* **1982**, *14* (9), 805–815. https://doi.org/10.1016/0021-9614(82)90154-9.

(9) OECD; Agency, N. E. *Chemical Thermodynamics of Thorium*; 2008. https://doi.org/10.1787/9789264056688-en.

(10) Scatchard, G. *Equilibrium in Solutions and Surface and Colloid Chemistry*; Harvard University Press: Cambridge (MA), 2013.

(11) Ciavatta, L. The Specific Interaction Theory in the Evaluating Ionic Equilibria. *Annali di Chimica (Rome)* **1980**, *70*, 551–562.

(12) Lumpkin, G. R.; Geisler-Wierwille, T. 5.22 - Minerals and Natural Analogues. In *Comprehensive Nuclear Materials*; Konings, R. J. M., Ed.; Elsevier: Oxford, 2012; pp 563–600. https://doi.org/10.1016/B978-0-08-056033-5.00111-7.

(13) Boatner, L. A.; Sales, B. C. Monazite. In *Radioactive waste forms for the future*; Lutze, W., Ewing, R. C., Eds.; Elsevier: Amsterdam, 1988; pp 495–564.

(14) Dacheux, N.; Clavier, N.; Podor, R. Versatile Monazite: Resolving Geological Records and Solving Challenges in Materials Science: Monazite as a Promising Long-Term Radioactive Waste Matrix: Benefits of High-Structural Flexibility and Chemical Durability†. *American Mineralogist* **2013**, *98* (5–6), 833–847. https://doi.org/10.2138/am.2013.4307.

(15) Delage, F.; Dussossoy, J. L. R7T7 Glass Initial Dissolution Rate Measurements Using a High-Temperature Soxhlet Device. *MRS Proceedings* **1990**, *212*, 41. https://doi.org/10.1557/PROC-212-41.

(16) Oelkers, E. H.; Poitrasson, F. An Experimental Study of the Dissolution Stoichiometry and Rates of a Natural Monazite as a Function of Temperature from 50 to 230 °C and PH from 1.5 to 10. *Chemical Geology* **2002**, *191* (1), 73–87. https://doi.org/10.1016/S0009-2541(02)00149-3.

(17) Paquette, J.-L.; Nédélec, A.; Moine, B.; Rakotondrazafy, M. U-Pb, Single Zircon Pb-Evaporation, and Sm-Nd Isotopic Study of a Granulite Domain in SE Madagascar. *The Journal of Geology* **1994**, *102* (5), 523–538.
(18) Du Fou de Kerdaniel, E. Etude de La Dissolution de Britholites et de Solutions Solides Monazite / Brabantite Dopées Avec Des Actinides. PhD Thesis, Université de Paris XI Orsay, 2007.
(19) Gausse, C. Synthèse et Dissolution de Matrices Phosphatées de Structure Monazitique. PhD Thesis, Université de Montpellier, 2016.
(20) Gausse, C.; Szenknect, S.; Mesbah, A.; Clavier, N.; Neumeier, S.; Dacheux, N. Dissolution Kinetics of Monazite $LnPO_4$ (Ln = La to Gd): A Multiparametric Study. *Applied Geochemistry* **2018**, *93*, 81–93. https://doi.org/10.1016/j.apgeochem.2018.04.005.
(21) Ma, J.; Teng, Y.; Wu, L.; Zhang, K.; Huang, Y.; Zhao, X.; Wang, G. Effect of Sintering Technique on Mechanical Property and Chemical Durability of $Ce_{0.5}Pr_{0.5}PO_4$ Ceramics. *Ceramics International* **2015**, *41* (10, Part B), 14597–14603. https://doi.org/10.1016/j.ceramint.2015.07.178.
(22) Ma, J.; Teng, Y.; Huang, Y.; Wu, L.; Zhang, K.; Zhao, X. Effects of Sintering Process, PH and Temperature on Chemical Durability of $Ce_{0.5}Pr_{0.5}PO_4$ Ceramics. *Journal of Nuclear Materials* **2015**, *465*, 550–555. https://doi.org/10.1016/j.jnucmat.2015.06.046.
(23) Zhao, X.; Teng, Y.; Wu, L.; Huang, Y.; Ma, J.; Wang, G. Chemical Durability and Leaching Mechanism of $Ce_{0.5}Eu_{0.5}PO_4$ Ceramics: Effects of Temperature and PH Values. *Journal of Nuclear Materials* **2015**, *466*, 187–193. https://doi.org/10.1016/j.jnucmat.2015.08.012.
(24) Zhao, X.; Teng, Y.; Yang, H.; Huang, Y.; Ma, J. Comparison of Microstructure and Chemical Durability of Ce<0.9>Gd<0.1>PO<4> Ceramics Prepared by Hot-Press and Pressureless Sintering. *Ceramics International* **2015**, *41* (9, Part A), 11062–11068. https://doi.org/10.1016/j.ceramint.2015.05.051.
(25) Teng, Y.; Wang, X.; Huang, Y.; Wu, L.; Zeng, P. Hot-Pressure Sintering, Microstructure and Chemical Durability of $Ce_{0.5}Eu_{0.5}PO_4$ Monazite Ceramics. *Ceramics International* **2015**, *41* (8), 10057–10062. https://doi.org/10.1016/j.ceramint.2015.04.095.
(26) Teng, Y.; Zeng, P.; Huang, Y.; Wu, L.; Wang, X. Hot-Pressing of Monazite $Ce_{0.5}Pr_{0.5}PO_4$ Ceramic and Its Chemical Durability. *Journal of Nuclear Materials* **2015**, *465*, 482–487. https://doi.org/10.1016/j.jnucmat.2015.06.044.
(27) Veilly, E.; du Fou de Kerdaniel, E.; Roques, J.; Dacheux, N.; Clavier, N. Comparative Behavior of Britholites and Monazite/Brabantite Solid Solutions during Leaching Tests: A Combined Experimental and DFT Approach. *Inorg. Chem.* **2008**, *47* (23), 10971–10979. https://doi.org/10.1021/ic801169d.
(28) Clavier, N. Elaboration de Phosphate-Diphosphate de Thorium et d'uranium (β-PDTU) et de Matériaux Composites β-PDTU/Monazite à Partir de Précurseurs Cristallisés : Études Du Frittage et de La Durabilité Chimique. PhD Thesis, Université de Paris-Sud, 2004.
(29) Clavier, N.; Dacheux, N.; Wallez, G.; Quarton, M. Hydrothermal Methods as a New Way of Actinide Phosphate Preparation. *MRS Proceedings* **2006**, *985*, 0985-NN04-08. https://doi.org/10.1557/PROC-985-0985-NN04-08.
(30) Qin, D.; Gausse, C.; Szenknect, S.; Mesbah, A.; Clavier, N.; Dacheux, N. Solubility Product of the Thorium Phosphate Hydrogen-Phosphate Hydrate ($Th_2(PO_4)_2(HPO_4)\cdot H_2O$, TPHPH). *The Journal of Chemical Thermodynamics* **2017**, *114*, 151–164. https://doi.org/10.1016/j.jct.2017.01.003.
(31) Jonasson, R. G.; Bancroft, G. M.; Nesbitt, H. W. Solubilities of Some Hydrous REE Phosphates with Implications for Diagenesis and Sea Water Concentrations. *Geochimica et Cosmochimica Acta* **1985**, *49* (10), 2133–2139. https://doi.org/10.1016/0016-7037(85)90071-7.

(32) Gausse, C.; Szenknect, S.; Qin, D. W.; Mesbah, A.; Clavier, N.; Neumeier, S.; Bosbach, D.; Dacheux, N. Determination of the Solubility of Rhabdophanes $LnPO_4 \cdot 0.667H_2O$ (Ln = La to Dy). *European Journal of Inorganic Chemistry* **2016**, *2016* (28), 4615–4630. https://doi.org/10.1002/ejic.201600517.
(33) Robisson, A. C.; Dacheux, N.; Aupiais, J. Influence of the PH on the Dissolution of TPD and Associated Solid Solutions. *Journal of Nuclear Materials* **2002**, *306* (2), 134–146. https://doi.org/10.1016/S0022-3115(02)01246-1.
(34) Du Fou de Kerdaniel, E.; Clavier, N.; Dacheux, N.; Terra, O.; Podor, R. Actinide Solubility-Controlling Phases during the Dissolution of Phosphate Ceramics. *Journal of Nuclear Materials* **2007**, *362* (2), 451–458. https://doi.org/10.1016/j.jnucmat.2007.01.132.
(35) Terra, O.; Clavier, N.; Dacheux, N.; Podor, R. Preparation and Characterization of Lanthanum–Gadolinium Monazites as Ceramics for Radioactive Waste Storage. *New J. Chem.* **2003**, *27* (6), 957–967. https://doi.org/10.1039/B212805P.
(36) Thomas, A.-C. Étude de La Dissolution Du Phosphate-Diphophate de Thorium: - Aspect Cinétique - Aspect Thermodynamique : Analyse Des Phases Néoformée. PhD Thesis, Université de Paris XI Orsay, 2000.
(37) Lasaga, A. C. Fundamental Approaches in Describing Mineral Dissolution and Precipitation Rates. *Reviews in Mineralogy and Geochemistry* **1995**, *31* (1), 23–86.
(38) Giffaut, E.; Grivé, M.; Blanc, Ph.; Vieillard, Ph.; Colàs, E.; Gailhanou, H.; Gaboreau, S.; Marty, N.; Madé, B.; Duro, L. Andra Thermodynamic Database for Performance Assessment: ThermoChimie. *Applied Geochemistry* **2014**, *49*, 225–236. https://doi.org/10.1016/j.apgeochem.2014.05.007.
(39) Wolery, T. J. *EQ3/6, a Software Package for Geochemical Modeling of Aqueous Systems: Package Overview and Installation Guide (Version 70)*; United States, 1992; p 70.
(40) Nancollas, G. H. The Nucleation and Growth of Phosphate Minerals. In *Phosphate Minerals*; Nriagu, J. O., Moore, P. B., Eds.; Springer Berlin Heidelberg: Berlin, Heidelberg, 1984; pp 137–154. https://doi.org/10.1007/978-3-642-61736-2_2.
(41) Van der Lee, J.; de Windt, L. *CHESS Tutorial and Cookbook*; Rapport technique LHM/RD/99/05; École des Mines de Paris, Fontainebleau, 1999.
(42) Shelyug, A.; Mesbah, A.; Szenknect, S.; Clavier, N.; Dacheux, N.; Navrotsky, A. Thermodynamics and Stability of Rhabdophanes, Hydrated Rare Earth Phosphates $REPO_4 \cdot nH_2O$. *Front Chem* **2018**, *6*, 604. https://doi.org/10.3389/fchem.2018.00604.
(43) Lewis, G. N.; Randall, M. *Thermodynamics*, 2nd edition.; New York McGraw-Hill, 1961.
(44) Hamer, W. J.; Wu, Y. Osmotic Coefficients and Mean Activity Coefficients of Uni-univalent Electrolytes in Water at 25°C. *Journal of Physical and Chemical Reference Data* **1972**, *1* (4), 1047–1100. https://doi.org/10.1063/1.3253108.
(45) Arinicheva, Y.; Gausse, C.; Neumeier, S.; Brandt, F.; Rozov, K.; Szenknect, S.; Dacheux, N.; Bosbach, D.; Deissmann, G. Influence of Temperature on the Dissolution Kinetics of Synthetic $LaPO_4$-Monazite in Acidic Media between 50 and 130 °C. *Journal of Nuclear Materials* **2018**, *509*, 488–495. https://doi.org/10.1016/j.jnucmat.2018.07.009.
(46) Konings, R. J. M.; Beneš, O.; Kovács, A.; Manara, D.; Sedmidubský, D.; Gorokhov, L.; Iorish, V. S.; Yungman, V.; Shenyavskaya, E.; Osina, E. The Thermodynamic Properties of the F-Elements and Their Compounds. Part 2. The Lanthanide and Actinide Oxides. *Journal of Physical and Chemical Reference Data* **2014**, *43* (1), 013101. https://doi.org/10.1063/1.4825256.
(47) Robie, R. A.; Hemingway, B. S. *Thermodynamic Properties of Minerals and Related Substances at 298.15 K and 1 Bar (10^5 Pascals) Pressure and at Higher Temperatures*; Bulletin; Report 2131; 1995. https://doi.org/10.3133/b2131.

(48) Navrotsky, A.; Lee, W.; Mielewczyk-Gryn, A.; Ushakov, S. V.; Anderko, A.; Wu, H.; Riman, R. E. Thermodynamics of Solid Phases Containing Rare Earth Oxides. *The Journal of Chemical Thermodynamics* **2015**, *88*, 126–141. https://doi.org/10.1016/j.jct.2015.04.008.

(49) Robie, R. A.; Hemingway, B. S.; Fisher, J. R. *Thermodynamic Properties of Minerals and Related Substances at 298.15 K and 1 Bar (10^5 Pascals) Pressure and at Higher Temperatures*; Bulletin; Report 1452; 1978. https://doi.org/10.3133/b1452.

Chapter V. Incorporation of Uranium into Monazite-type Ceramics $Nd_{1-2x}Ca_xU^{IV}_xPO_4$

V-1. Introduction

In the previous chapters, Th-rhabdophane $Ln_{1-2x}Ca_xTh_xPO_4.nH_2O$ compounds have been synthesized via hydrothermal conditions and the associated single-phase monazite-cheralite solid solutions $Ln_{1-2x}Ca_xTh_xPO_4$ have been obtained by thermal conversion. Later, the direct sintering from Th-rhabdophane was achieved and the sintering map of $Nd_{1-2x}Ca_xTh_xPO_4$ was built. Finally, a multi-parametric study of the dissolution suggested that monazite-cheralite $Nd_{0.8}Ca_{0.1}Th_{0.1}PO_4$ presented an excellent chemical durability with respect to its low normalized dissolution rates and the low solubility of the solubility-controlling phase (*i.e.*, Th-rhabdophane or monazite-cheralite). All these results argue for the use of monazite-cheralite ceramics as a specific matrix for actinides immobilization. However, thorium has only one stable oxidation state, *i.e.*, +IV, while U, Np or Pu present multiple stabilized oxidation states ranging as instance from +III to +VI for plutonium. The associated redox chemistry then might lead to the formation of new phases and therefore alter the thermostability and/or chemical durability of the host matrices. In the PhD work of N. Dacheux [1], the synthesis of the uranium phosphates was investigated. The thermal behavior of $UClPO_4.4H_2O$ in air was different to that obtained in argon atmosphere, leading to different high temperature stabilized phases, *i.e.*, $U(UO_2)(PO_4)_2$ and $U_2O(PO_4)_2$, respectively. Moreover, though several precursors could result in the formation of $U(UO_2)(PO_4)_2$, the conversion temperature was equal to 1170°C starting from $UClPO_4.4H_2O$ or to 900°C when starting from $(UO_2)HPO_4.4H_2O$ and $NH_4(UO_2)(PO_4).3H_2O$. In terms of chemical stability, uranium(VI) is more mobile than thorium. N. Clavier [2] investigated the leaching of β-TUPD $(Th_{4-x}U^{IV}_x(PO_4)_4)P_2O_7$ in HNO_3 solutions. For pH values ranging from 2 to 5, the ratio of normalized dissolution rate $R_L(U)/R_L(Th)$ was over 10 and sometimes reached a factor of 1000. On the contrary, U(+IV) might have a much lower solubility than U(+VI). Therefore, U(+IV) might be more suitable for uranium conditioning compared with U(+VI). For Neptunium, even though Np(+IV) is the predominant oxidation state in the spent nuclear fuel, Np(+V) is more stable in weathering conditions [3]. Moreover, Np(+V) is much more soluble than Np(+IV), leading to high mobility under oxidizing conditions [3]. Consequently, in terms of actinides conditioning, the host matrices should stabilize uranium and neptunium in tetravalent oxidation state.

Several studies have been dedicated to $Ln_{1-2x}Ca_xAn^{IV}_xPO_4$ solid solutions (with An = U, Np, and Pu). McCarthy *et al.* [4] reported the synthesis of $Ln_{1-2x}Ca_xTh_{x-y}U_yPO_4$ (Ln acting as a mixture of La, Ce, Pr, Nd, Sm, Gd, and Y). Nitric solutions of Ln, Ca, Th, and UO_2^{2+} were mixed in stoichiometric conditions with $NH_4H_2PO_4$. The mixture was boiled down to a paste

and then calcined at 600°C for 2 hours. The residue was ground into powder, pressed into pellets, and then finally fired at 1200°C for 48 hours. According to XRD patterns, the dominant phase was monazite-cheralite, while secondary phases $U_3(PO_4)_4/U_2P_2O_{10}$ and U_3O_8 were presented in the final product. According to the PhD work of Dacheux [1], the existence of $U_3(PO_4)_4$ might be questionable and these secondary phases should be $U(UO_2)(PO_4)_2$ and U_3O_8. In the PhD work of R. Podor [5], well crystallized and single phase $La_{1-2x}Ca_xU^{IV}_xPO_4$ ($0 \le x \le 0.5$) solid solutions were prepared under hydrothermal conditions (T = 780°C, P = 200 MPa). The variation of the unit cell parameters followed the Vegard's law (which means the unit cell parameters of the solid solutions could be expressed as a combination of those of end-members $LaPO_4$ and $Ca_{0.5}U_{0.5}PO_4$). Terra [6] also synthesized these end-members as well as solid solutions $La_{1-2x}Ca_xTh_{x-y}U^{IV}_yPO_4$ (with $0.1 \le x \le 0.4$ and $y = x/5$) by dry chemistry routes. AnO_2 was previously calcined at 1200°C for 10 hours under Ar atmosphere then milled at 30Hz for 15 minutes. After mixing with La_2O_3 and $(NH_4)(H_2PO_4)$, several cycles of milling/calcination (30Hz – 15 minutes / 1200°C – 10 hours) were applied. In order to guarantee the homogeneity of the final samples, at least two milling/calcination cycles were required. Bregiroux *et al.* [7] investigated the formation of $Ca_{0.5}An^{IV}_{0.5}PO_4$, (An = U, Ce) through DTA/TGA experiments. The temperature associated to the formation of single-phase $Ca_{0.5}U^{IV}_{0.5}PO_4$ under inert atmosphere (Ar) equaled 1200°C. The choice of the synthesis temperature was difficult. Indeed, below this temperature, α-UP_2O_7 would exist as secondary phase in the sample while decomposition would take place for T > 1300°C. Otherwise, single-phase $Ca_{0.5}Ce^{IV}_{0.5}PO_4$ was not obtained, as Ce(IV) was always partly reduced into Ce(III) even under air, resulting in mixtures of $Ce^{III}_{1-2x}Ca_xCe^{IV}_xPO_4$ and α–$Ca_2P_2O_7$. A similar behavior was described when incorporating plutonium in $Pu^{III}_{1-2x}Ca_xPu^{IV}_xPO_4$ (x = 0, 0.3 and 0.5) [8] solid solutions. The stabilization of Pu(IV) probably depended on the oxygen partial pressure (P_{O_2}) during the synthesis: no Pu(IV) was evidenced in the final powder under Ar atmosphere while 40% of the Pu remained tetravalent in air. Finally, $Ca_{0.5}Np^{IV}_{0.5}PO_4$ was prepared by Raison *et al.*[9] by applying solid state reaction at 1250 °C for 100 hours in N_2 atmosphere.

Our study of uranium samples focused on the synthesis of U-rhabdophane, $Nd_{1-2x}Ca_xU^{IV}_xPO_4.nH_2O$, and on the stabilization of associated monazite-cheralite $Nd_{1-2x}Ca_xU^{IV}_xPO_4$. Even though Np is important contributors to the radiotoxicity of spent fuel [10], $Nd_{1-2x}Ca_xU^{IV}_xPO_4$ could be considered a potential surrogate of $Nd_{1-2x}Ca_xNp^{IV}_xPO_4$ phases. As R Podor [5,11] reported two criteria required to stabilize the monazite-cheralite solid solution, *i.e.*,

$$1.107\text{Å} \le \overline{^{IX}r\left(M^{II+III+IV}\right)} \le 1.216\text{Å} \qquad \text{(V-1)}$$

and

$$1 \leq \overline{^{IX}r\left(M^{II+III}\right)} / \overline{^{IX}r\left(M^{III+IV}\right)} \leq 1.238 \quad \text{(V-2)}$$

one can note that uranium ionic radius is close to those of Np, *i.e.*, in 8-fold coordination (i.e. $r_{U^{4+}} = 1.00$ Å, $r_{Np^{4+}} = 0.98$ Å). Another advantage of using uranium as a surrogate element is that it could bring information on the impact of redox reactions on the properties of the material. Finally, uranium is far less radioactive than neptunium and is more easily accessible in terms of radiation safety. Consequently, the hydrothermal synthesis of (Th, U)-rhabdophane, $Nd_{1-2x}Ca_xTh_{x-y}U^{IV}_yPO_4.nH_2O$, was developed thanks to the protocol optimized for Th-rhabdophanes. Then, the conversion from U-rhabdophane into monazite-cheralite, $Nd_{1-2x}Ca_xTh_{x-y}U^{IV}_yPO_4$, was investigated through TGA and dilatometry experiments.

V-2. Experiments and results

V-2.1. Preparation of $Nd_{1-2x}Ca_xTh_{x-y}U^{IV}_yPO_4.nH_2O$ rhabdophane and associated monazite-cheralite $Nd_{1-2x}Ca_xTh_{x-y}U^{IV}_yPO_4$ solid solutions

The hydrothermal synthesis of $Nd_{1-2x}Ca_xTh_{x-y}U^{IV}_yPO_4.nH_2O$ (x = 0, 0.05, 0.075, 0.1, 0.15, and 0.2) was adapted from the protocol reported in **Chapter I**. Uranium source consisted in concentrated solution of U(IV) prepared in hydrochloric medium with C(U) ≈ 0.5 mol.L^{-1}. Following the protocol proposed by Dacheux *et al.* [12], these solutions were prepared from uranium metal chips, which were stored in the organic alkane solution in order to avoid any oxidation of uranium. These metal chips were firstly washed with acetone then with ethanol and water to remove the traces of oil (necessary for the storage of the uranium metal chips). Later, they were washed with 1 mol.L^{-1} HCl solution in order to eliminate the traces of uranium oxides potentially present onto the surface of the chips. Finally, uranium metal was dissolved in 6 mol.L^{-1} HCl cooled with the help of an ice bath to limit the effects of such an exothermic dissolution. Uranium concentration in the solution was determined by ICP-OES analysis. It usually reached 0.5 to 0.7 mol.L^{-1}. Similar to the synthesis of Th-rhabdophane, the initial Ca:An molar ratio was fixed to 10:1. The hydrothermal synthesis lasted four days at 110°C under air atmosphere.

The chemical composition of the obtained U-rhabdophane was determined after total dissolution of the prepared powders (listed in **Table V-1**). For $x \leq 0.1$, the Ca/U and P/(Ca + U + Nd) ratios were close to 1 considering the uncertainty of measurement. The cation contents, *i.e.* x_{Ca}, x_{Th} and x_{Nd}, reached the expected values as well. There is a slight fluctuation of these ratios between different batches of synthesis, which might result from differences of the starting cationic solutions. In fact, the solutions were prepared for each batch resulting in a variation of the initial cation concentrations. Despite this small shift of the cationic ratios between various batches, the final compositions of all the obtained rhabdophane samples ($x \leq 0.1$) were consistent with the expected values, especially in terms of Ca/U and P/(Ca + U + Nd) mole ratios.

However, for $x > 0.1$, the Ca/U ratios were found below unit while the P/(Ca + U + Nd) mole ratio significantly exceeded this value. One of the possibilities is that the coupled substitution $Ca^{2+} + An^{4+} \leftrightarrow 2\ Nd^{3+}$ occurred simultaneously to the formation of the cation vacancies $3\ An^{4+} \leftrightarrow 4\ Nd^{3+} + \square$. The formation of cations vacancies led to the incorporation of excess uranium and phosphate groups within the rhabdophane structure. Another explanation

could come from the presence of small amount of gelatinous phase, which could not be detected by PXRD. Consequently, similarly to that was mentioned for the preparation of Th-rhabdophane, $Nd_{1-2x}Ca_xTh_xPO_4.nH_2O$, the maximum uranium mole loading could be limited to about 10 mol.% of uranium.

Table V-1. Chemical composition of the samples of $Nd_{1-2x}Ca_xTh_{x-y}U_yPO_4.nH_2O$ determined after total powder dissolution

x	Ca	Th	U	Nd	P/∑Cations
			Batch 1		
0.10	0.09 ± 0.02	-	0.08 ± 0.02	0.83 ± 0.02	0.98 ± 0.02
0.05 U + 0.05 Th	0.09 ± 0.02	0.05 ± 0.02	0.04 ± 0.02	0.82 ± 0.02	0.99 ± 0.02
			Batch 2		
0.05	0.06 ± 0.02	–	0.07 ± 0.02	0.87 ± 0.02	1.00 ± 0.03
0.075	0.08 ± 0.02	–	0.09 ± 0.02	0.83 ± 0.02	1.00 ± 0.06
0.10	0.10 ± 0.02	–	0.12 ± 0.02	0.78 ± 0.02	1.01 ± 0.06
			Batch 3		
0.05	0.04 ± 0.02	–	0.04 ± 0.02	0.92 ± 0.02	1.04 ± 0.04
0.075	0.07 ± 0.02	–	0.06 ± 0.02	0.87 ± 0.02	1.03 ± 0.04
0.10	0.08 ± 0.02	–	0.08 ± 0.02	0.84 ± 0.02	1.04 ± 0.04
0.15	0.11 ± 0.02	–	0.14 ± 0.02	0.75 ± 0.02	1.07 ± 0.04
0.20	0.11 ± 0.01	–	0.20 ± 0.01	0.69 ± 0.01	1.10 ± 0.04

The associated monazite-cheralite solid solutions were obtained from U-rhabdophanes by thermal conversion at 1100°C for 6 hours under argon atmosphere. These powders and the initial U-rhabdophanes were characterized with PXRD analyses (**Figure V-1**.). For $x \leq 0.1$, the PXRD patterns suggested that the final powders were single-phase, with the absence of crystallized secondary phases. Nevertheless, the existence of an amorphous secondary phase could not be completely excluded. Moreover, small amounts of α-UP_2O_7 [13] and $U(UO_2)(PO_4)_2$ [14] were evidenced for $x > 0.1$. It is worth noting that according to the PhD work of Dacheux [1], the oxidation of U(IV) is not likely to happen under inert atmosphere, and thus $U(UO_2)(PO_4)_2$ should be probably converted into $U_2O(PO_4)_2$. Such amounts of $U(UO_2)(PO_4)_2$ might be due to the potential presence of dioxygen during the heating treatment. Back to the evidence of

secondary phases, such a behavior was also observed during the conversion of Th-rhabdophane with the formation of α-ThP_2O_7 for x > 0.1 (**Chapter I**). If the hypothesis of the formation of cation vacancies in the rhabdophane is validated, as Podor *et al.* [11] pointed out the low tolerance of the monazite structure for vacancies, the excess of An and phosphate group would have been segregated from the monazite-cheralite when heating. Otherwise, these secondary phases might have been converted form the potential amorphous phases which could have contained the excessed uranium and phosphate groups. Finally, the stability domain of $Nd_{1-2x}Ca_xAn_xPO_4$ with An = Th or U seems to limited to $0 \leq x \leq 0.1$. It is worth noting that the maximum mass percentage of actinides in $Nd_{0.8}Ca_{0.1}An_{0.1}PO_4$ is about 10 wt.%, which is considered to be the higher incorporation rate admitted in a specific conditioning matrix for actinide conditioning, due to the associated radiation damages [15].

Additionally, the unit cell volume of monazite-cheralite was calculated by the Rietvled method. The obtained values as well as the selected volume data for end-members, *i.e.*, $NdPO_4$ (V = 292.18 Å³) and $Ca_{0.5}U_{0.5}PO_4$ (V = 283.35 Å³) [16] are presented in **Figure V-2**. For $0 \leq x \leq 0.1$, the unit cell volumes were consistent between the different batches prepared. Moreover, the variation of the volume followed the Vegard's law, which meant that the distribution of Ca^{2+}, Nd^{3+} and U^{4+} was homogenous and that the cation positions in the crystal structure were randomly occupied by these cations. In this case, the unit cell volume of $Nd_{1-2x}Ca_xU_xPO_4$ could be considered as the weighted average of those of $NdPO_4$ and $Ca_{0.5}U_{0.5}PO_4$. Hence, the unit cell volume of the as-prepared monazite-cheralite, $Nd_{1-2x}Ca_xU_xPO_4$, could be expressed as $V(Å^3) = -17.66\,x + 292.18$.

For $x > 0.1$, one can note a linear correlation between the unit cell volume and the x_{Ca} value (**Figure V-2 a**). However, if the unit cell volume was presented as a function of x_U (**Figure V-2 b**), the unit cell volumes would have been found to be higher than the weighted averages of the end-members for $x = 0.15$ and 0.20. As mentioned above, for $x > 0.1$, secondary phases α-$U_2P_2O_7$ and $U(UO_2)(PO_4)_2$ presented in the obtained solid-solutions. Therefore, the x_U values determined after full dissolution were higher than the actual uranium contents in the monazite-cheralite structure. Moreover, the linear trend between the unit cell volume and x_{Ca} suggested that the actual uranium contents might be the same as that of calcium, *i.e.* x_U(incorporated) = x_{Ca}. Indeed, for both the samples, the x_{Ca} values determined after total dissolution were close to 0.1, which corresponds to the maximum incorporation ratio and agrees well with the stability domain already suggested for monazite-cheralite. Consequently, for $x >$

0.1, the obtained monazite-cheralite solid solutions might be the mixture of $Nd_{1-2x_{Ca}}Ca_{x_{Ca}}Th_{x_{Ca}}PO_4$ ($x_{Ca} \approx 0.1$), α-$U_2P_2O_7$ and $U(UO_2)(PO_4)_2$.

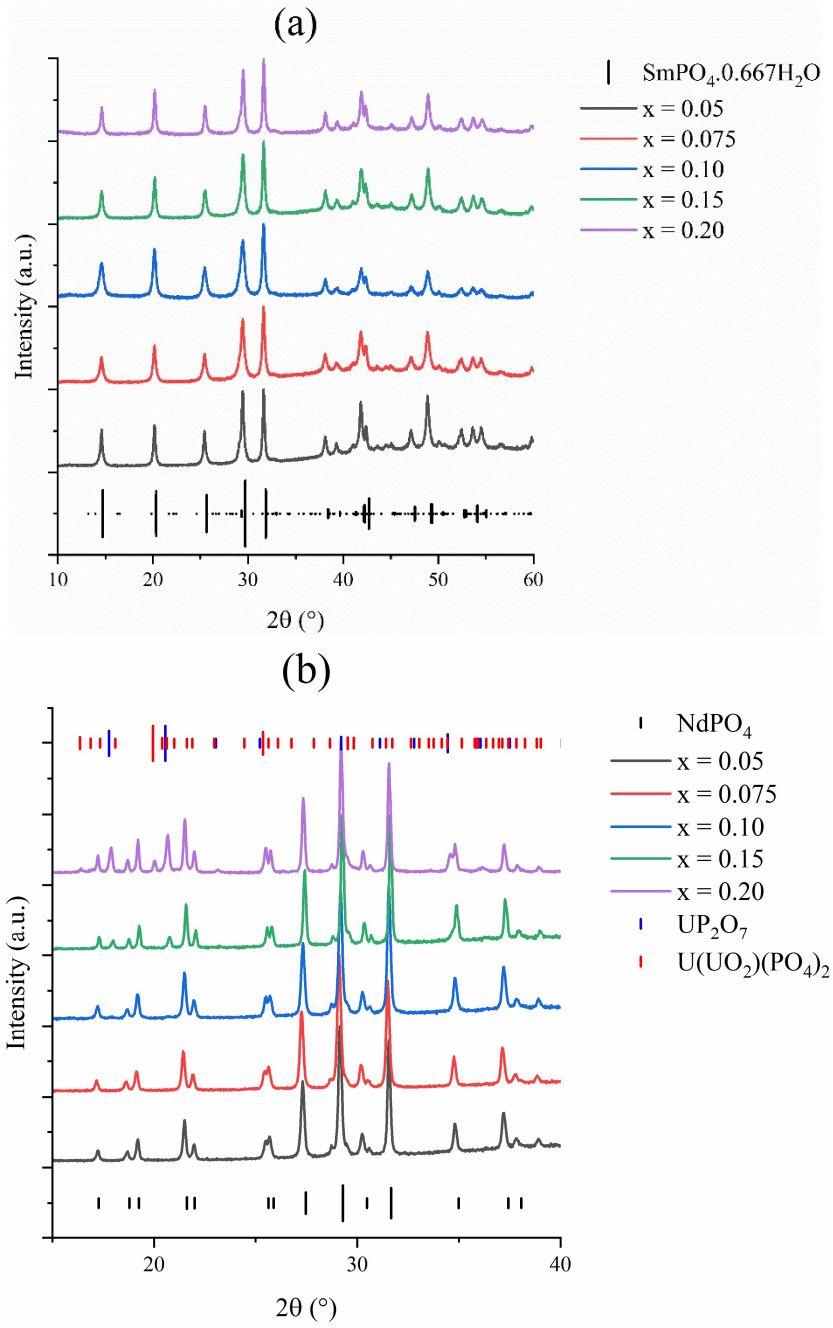

Figure V-1. PXRD patterns of synthesized U-rhabdophane (a) and of associated monazite-cheralite solid solutions (b). The standard pattern of rhabdophane is $SmPO_4.0.667\ H_2O$ [17], and that of monazite is $NdPO_4$ [18]. The impurities phases are UP_2O_7 [13]and $U(UO_2)(PO_4)_2$ [14]

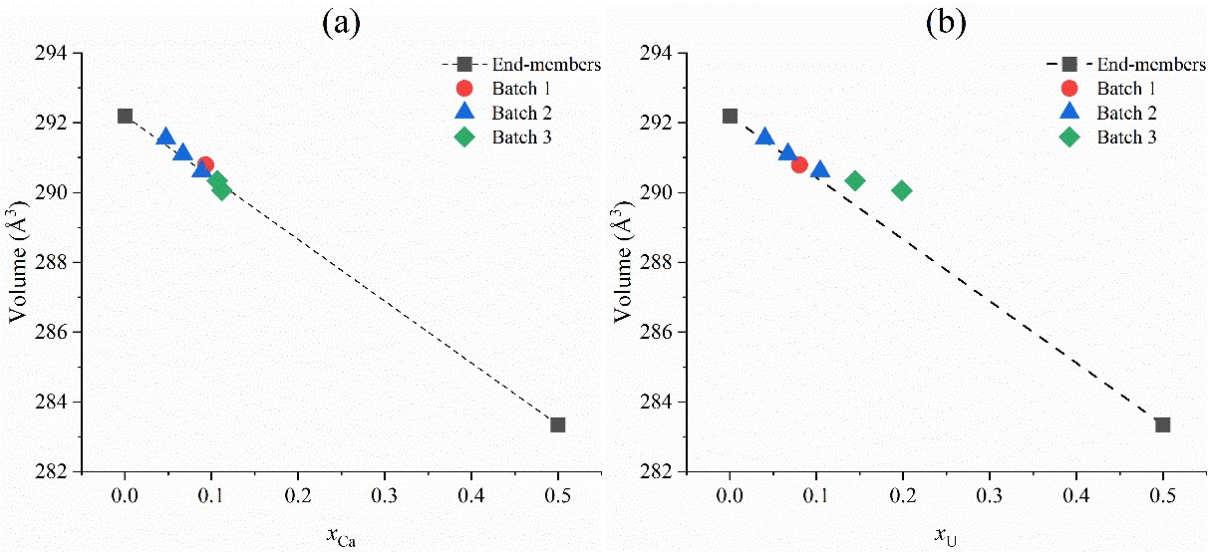

Figure V-2. Variation of the unit cell volume of $Nd_{1-2x}Ca_xU_xPO_4$ monazite-cheralite as a function of x_{Ca} (a) and x_U (b) The value for $Ca_{0.5}U_{0.5}PO_4$ end-member was taken from O. Terra *et al.* [16].

As mentioned above, (Th, U)-rhabdophane sample, $Nd_{0.8}Ca_{0.1}Th_{0.05}U_{0.05}PO_4.nH_2O$, was also synthesized and characterized. The chemical composition of the sample was in agreement with the expected value (**Table V-1**). Similarly, the associated monazite-cheralite was prepared by heating at 1100°C for 6 hours under argon atmosphere. The PXRD patterns (**Figure V-3**) showed that both rhabdophane, and monazite-cheralite were single-phase. Applying the Rietveld method, the unit cell volume was evaluated as well. **Figure V-4** suggested a linear correlation between the unit cell volume of monazite-cheralite $Nd_{0.8}Ca_{0.1}Th_{0.05}U_{0.05}PO_4$ and the proportion of uranium, y in the sample. The increase of the uranium content is associated to the decrease of the average ionic radii and of the unit cell volume of the $Nd_{0.8}Ca_{0.1}Th_{0.1-y}U_yPO_4$, which is in good agreement with the values reported by Shannon (^{IX}r (U) = 1.05 Å, the other ionic radii were listed in **Table II-4**) [19].

As mentioned above, the conversion of U-rhabdophane into monazite-cheralite was performed under argon atmosphere in order to prevent the oxidation of U(IV) into U(VI). Nevertheless, an additional test of $Nd_{0.8}Ca_{0.1}U_{0.1}PO_4.nH_2O$ was also performed in air in order to study the impact of the firing conditions on the nature of the prepared samples . The PXRD pattern of the obtained powder is presented in **Figure V-5**. It did not evidence any difference in comparison to the powder prepared under Ar-atmosphere. Notably, no secondary phase containing U(VI) was observed. The unit cell volumes calculated for these two samples were identical considering the associated uncertainty, *i.e.* (290.79 ± 0.02) Å^3 and (290.77 ± 0.01) Å^3 when heating under inert atmosphere and in air, respectively. Therefore, it seemed that the

oxidation of U(IV) into U(VI) did not occur. A possible explanation arose from the potential protection of U(IV) to oxidize due to the presence of phosphate in the material.

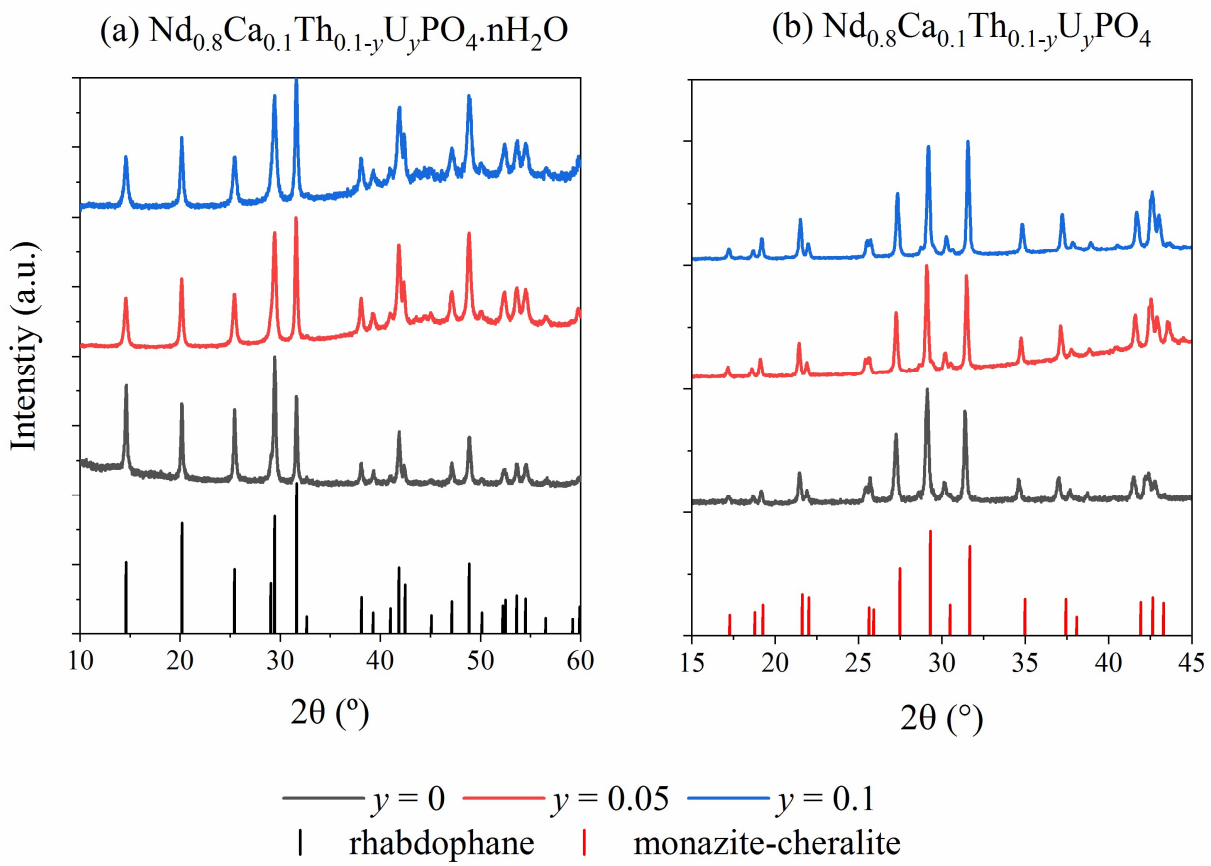

Figure V-3. PXRD patterns of synthesized (Th,U)-rhabdophane, $Nd_{0.8}Ca_{0.1}Th_{0.1-y}U_yPO_4.nH_2O$ (a) and of associated monazite-cheralite solutions, $Nd_{0.8}Ca_{0.1}Th_{0.1-y}U_yPO_4$ (b).

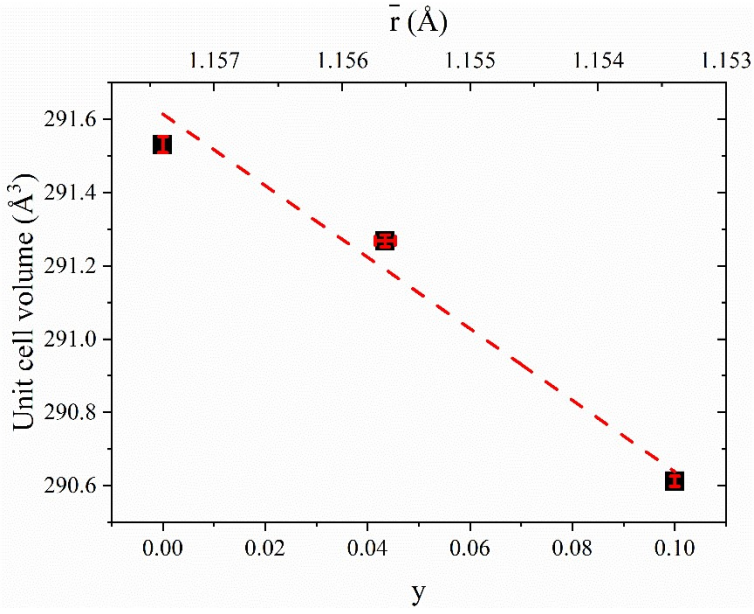

Figure V-4. Unit cell volume of monazite-cheralite $Nd_{0.8}Ca_{0.1}Th_{0.1-y}U_yPO_4$.

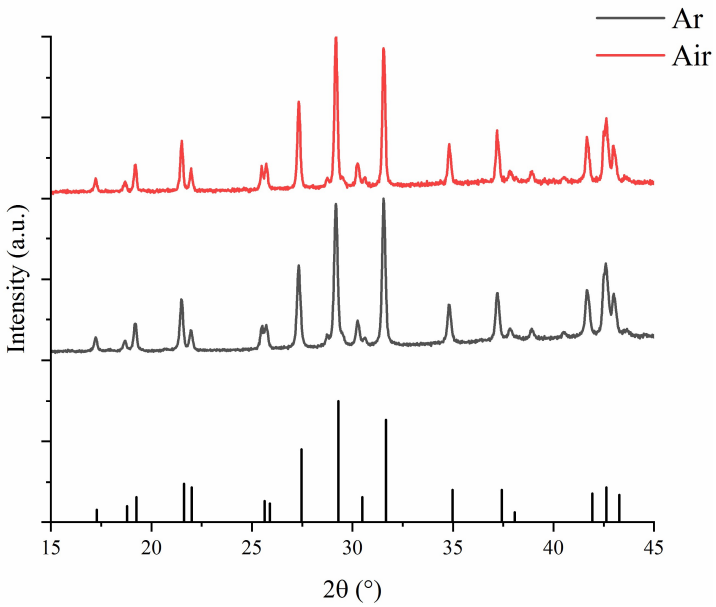

Figure V-5. PXRD patterns of monazite-cheralite $Nd_{0.8}Ca_{0.1}U_{0.1}PO_4$ prepared by heating treatment under various atmospheres.

V-2.2. Thermal behavior of U-rhabdophanes $Nd_{1-2x}Ca_xU_xPO_4.nH_2O$

V-2.2.1. TGA study

In order to investigate the thermal behavior of the prepared samples of $Nd_{1-2x}Ca_xU^{IV}_xPO_4.nH_2O$ ($0 \leq x \leq 0.1$), TGA experiments were performed from room temperature to 1000°C with a heating rate of 5°C.min^{-1}. In order to study the influence of the atmosphere, the experiments were performed under both air and argon atmospheres. Under argon, two vacuum/refill cycles were performed before the TGA experiment in order to ensure the absence of dioxygen in the furnace (**Figure V-6**). No weight loss was observed above 300°C. According to the study reported by Mesbah *et al.* [20] on the thermal behaviors of $LnPO_4.0.667H_2O$ and the results reported in **Chapter II**, the weight loss observed below 300 °C was probably due to the dehydration process. The TGA curves obtained under Ar atmosphere showed only one step at about 200°C while those performed in air suggested a two-step dehydration, with successive weight losses at about 100°C and 200°C. The weight loss at about 100°C was associated to the elimination of 0.3 H_2O per formula unit. As the experiment in air did not go through the vacuum/refill cycles, this dehydration could be due to the elimination of absorbed water. Unlike the crystallization water, absorbed water could be easily removed in vacuum, which might explain why only one weight loss step was observed when working under argon.

Table V-2. Temperature associated to the peak observed on the derivative of the TG curves and associated water contents.

		$\Delta n(H_2O)$		
x	Peak (°C)	First step	Second step	Total
		Ar		
0	218 ± 3	–	- 0.48± 0.03	- 0.48± 0.03
0.05	218 ± 3	–	- 0.51± 0.03	- 0.51± 0.03
0.075	223 ± 3	–	- 0.51± 0.03	- 0.51± 0.03
0.1	223 ± 3	–	- 0.49± 0.03	- 0.49± 0.03
		Air		
0	219 ± 3	- 0.3± 0.1	- 0.5± 0.1	- 0.8± 0.1
0.05	219 ± 3	- 0.3± 0.1	- 0.5± 0.1	- 0.8± 0.1
0.075	221 ± 3	- 0.3± 0.1	- 0.5± 0.1	- 0.8± 0.1
0.1	220 ± 3	- 0.3± 0.1	- 0.5± 0.1	- 0.8± 0.1

Later, according to the derivative of the TG curves, the temperature associated with the maximum weight loss rate ranged between 218°C and 223°C. The conversion temperatures were highly identical for both atmospheres. Moreover, the weight loss at this temperature corresponded to 0.5 H_2O per formula unit whatever the considered atmosphere. Therefore, the dehydration scheme was probably similar for the two conditions studied and corresponded to the conversion of the hemihydrated rhabdophane into the anhydrous form. Consequently, the atmosphere did not seem to influence the thermal behavior of U-rhabdophane.

The TG curves were quite similar for the samples prepared with various chemical compositions, showing small impact of the uranium incorporation rate. Moreover, the temperatures associated to the conversion from hemihydrated to anhydrous rhabdophane were identical taking into account the associated uncertainties.

Additionally, the comparison between the TG curves of U-rhabdophane ($Nd_{0.8}Ca_{0.1}U_{0.1}PO_4.nH_2O$, prepared in air) and of Th-rhabdophane ($Nd_{0.8}Ca_{0.1}Th_{0.1}PO_4.nH_2O$) is given in **Figure V-7**. Once again, the evolution of the TG curves was identical. The conversion temperature of the hemihydrated Th-rhabdophane was equal to 220°C. Above 300°C, no evident gain in mass was underlined for both samples, which suggest the absence of oxidation of U(IV) into U(VI) during the heating treatment in air.

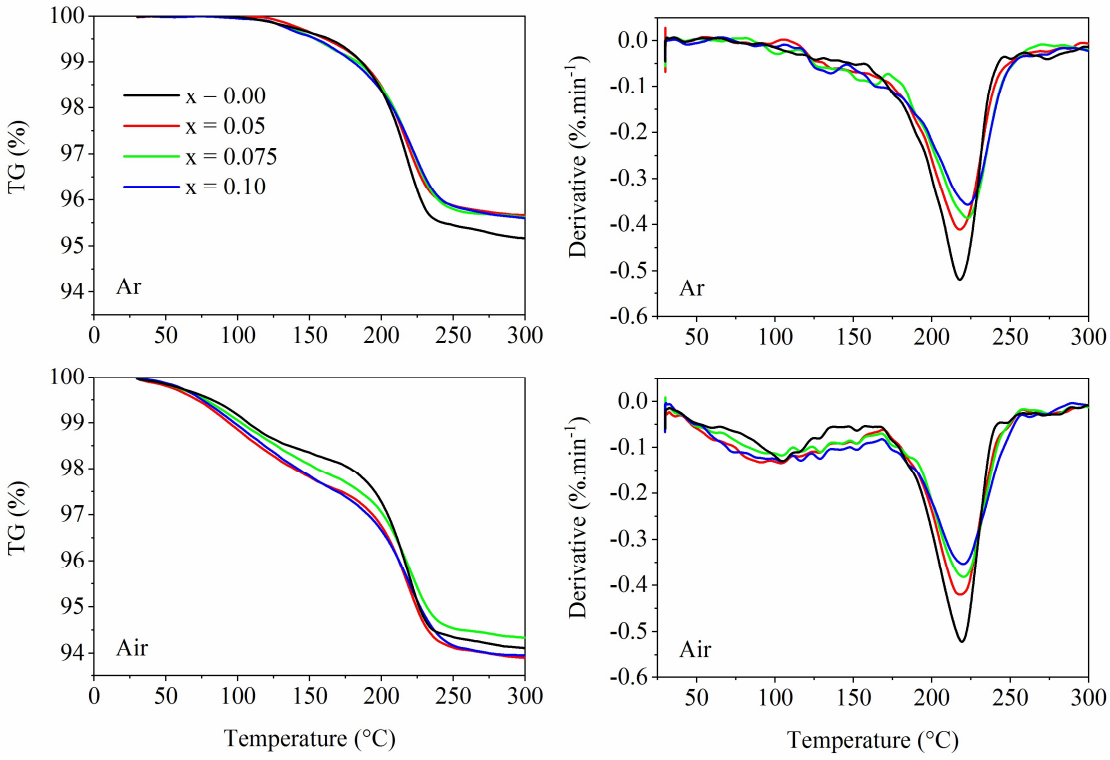

Figure V-6. TG curves and associated derivatives recorded for $Nd_{1-2x}Ca_xU_xPO_4.nH_2O$ ($T \leq 300°C$).

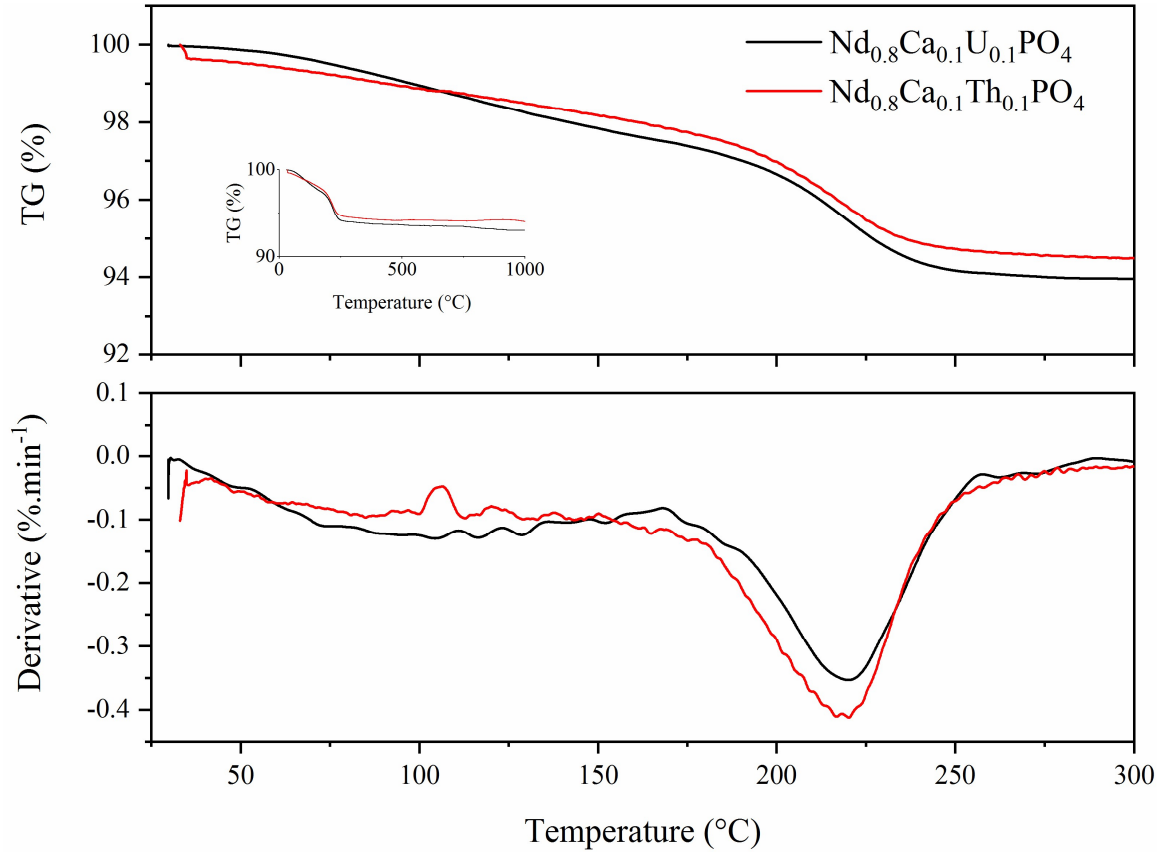

Figure V-7. TG curves and associated derivatives recorded in air for U-rhabdophane ($Nd_{0.8}Ca_{0.1}U_{0.1}PO_4.nH_2O$) and for Th-rhabdophane ($Nd_{0.8}Ca_{0.1}Th_{0.1}PO_4.nH_2O$ ($T \leq 300°C$).

The direct comparison of the data obtained for both U- and Th-rhabdophanes underlined that the two dehydration processes were similar. The initial hydrated form lose absorbed water under vacuum or at T ≈ 100°C, leading to the formation of the hemihydrate form. It was followed by the complete dehydration, which took place at about 220°C. Because of the complexation with the phosphate groups, uranium(IV) was prevented from oxidation during when heating (T ≤ 1000°C) for $0 \leq x \leq 0.1$, not only in argon atmosphere, but also in air.

V-2.2.2. Dilatometry study

For each dilatometry experiment, about 250 mg of sample was shaped into a cylindrical pellet (Ø = 8 mm and a thickness of about 1.8 mm) by uniaxial pressing at 500 MPa. The samples were heated up to 1400 °C with a rate of 5°C.min^{-1}, then cooled down to room temperature with a rate of 30°C.min^{-1}. In order to avoid any oxidation, two cycles of vacuum/Ar-refill were performed before the heat treatment. During the whole experiment, the reaction chamber was flushed by an argon flux of 20 mL.min^{-1}. The relative shrinkage related to the thickness and the associated derivative are presented in **Figure V-8**.

Four main variations of the pellets thickness were observed during the dilatometry tests. The first one took place at about 200°C, and accounted for a 0.5% thickness reduction. This variation was assigned to the dehydration process described in the previous section. Later, a shrinkage of about 7.5% took place between 670°C and 850°C. It was assigned to the conversion of anhydrous rhabdophane into monazite-cheralite. From 850°C to 1300°C, an additional linear shrinkage of about 20% occurred, which underlined the densification of the sample. Finally, an additional dilatation step was observed above 1300 °C, which might be due to decomposition reaction according the paper published by Bregiroux *et al.* [7] Indeed, these authors reported the decomposition of $Ca_{0.5}U^{IV}_{0.5}PO_4$ to form CaO, UO_2, and P_4O_{10} (gas) for T ≥ 1300°C [7]. Consequently, the sintering of $Nd_{1-2x}Ca_xU_xPO_4$ should be performed at temperatures below 1300 °C.

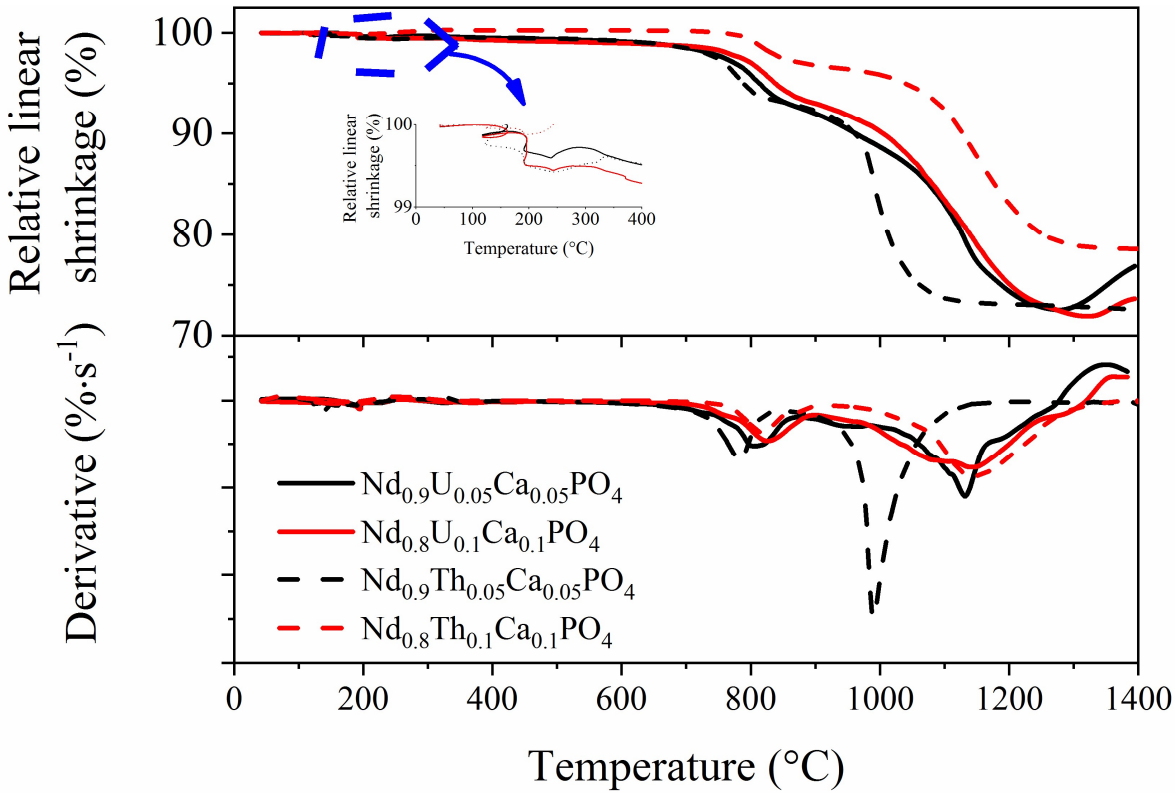

Figure V-8. Relative linear shrinkage and associate derivative obtained for An-rhabdophane $Nd_{1-2x}Ca_xAn_xPO_4.nH_2O$ (with An = Th, U) and for x = 0.05 and 0.1.

Table V-3. Temperatures associated to the thermal conversion of U- and Th-Rhabdophanes into monazite-cheralite solid solutions as well as to the densification and decomposition of resulting monazite-cheralite solid solutions.

	Temperatures (°C)			
x	Dehydration	Conversion	Densification	Decomposition
		U-rhabdophane		
0.05	195 ± 20	803 ± 58	1131 ± 54	1277 ± 26
0.1	195 ± 20	827 ± 61	1144 ± 91	1319 ± 30
		Th-rhabdophane		
0.05	187 ± 20	780 ± 45	990 ± 40	–
0.1	190 ± 20	817± 54	1150 ± 103	–

According to the derivative curves obtained for U-rhabdophanes, the temperatures associated to dehydration, conversion, densification and decomposition (associated to positive variation) are gathered in **Table V-3**.

The temperature of dehydration was identical for x = 0.05 and for x = 0.1 while the conversion, densification and decomposition steps occurred at slightly higher temperature for x = 0.05. A similar trend was already mentioned for Th-rhabdophane (**Chapter II and III**).

The conversion temperatures of U-rhabdophane were compared with those obtained for Th-rhabdophanes and those reported by Jonasson and Vance [21] and by Kijkowska *et al.* [22] for lanthanide end-members (**Figure V-9**). The conversion temperatures from rhabdophane to monazite-cheralite varied linearly as a function of the ionic radius. It seems that the decrease of the ionic radius strengthened the stability of the rhabdophane structure. Besides, the conversion temperatures determined in this work were close to those of Kijkowska *et al.* However, it is difficult to determine precisely such conversion temperatures. Several factors could affect the final results, such as, the thermocouple, the heating rate, the density of the green pellet, etc. In fact, the conversion temperatures of the Th-rhabdophanes (**Chapter II**) were about 30°C lower than those determined for U-rhabdophanes. It was surely due to the difference of the beating rates considered (1°C.min^{-1} and 5°C.min^{-1} for Th- and U-rhabdophane, respectively). With a lower heating rate, the progress of the conversion reaction of U-rhabdophane could have been increased, leading to peaks located at lower temperatures on the derivative curves.

Regarding to the sample densification, the dilatometry studies of Th-rhabdophane showed that the incorporation of 5 mol.% Th significantly accelerated the densification. In this way, the densification temperature of $Nd_{0.9}Ca_{0.05}Th_{0.05}PO_4$ was about 160°C lower than that of $Nd_{0.8}Ca_{0.1}Th_{0.1}PO_4$ (*i.e.* (990 ± 40) °C compared to (1150 ± 103) °C). This phenomenon was not observed for the U-rhabdophanes. Indeed, for these later compounds, the densification temperatures reached (1131 ± 54) °C and (1144 ± 91) °C for $x = 0.05$ and $x = 0.10$, respectively. The abnormal rapid densification observed for $Nd_{0.9}Ca_{0.05}Th_{0.05}PO_4$ then might be due to the slight excess of Ca of the starting rhabdophane (x_{Ca}/x_{An} = 1.4 ± 0.5). However, this ratio was found to 1.0 ± 0.25 for $Nd_{0.9}Ca_{0.05}U_{0.05}PO_4$, so that the densification was similar to those of $Nd_{0.8}Ca_{0.1}Th_{0.1}PO_4$ and $Nd_{0.8}Ca_{0.1}U_{0.1}PO_4$. Nevertheless, higher incorporation of uranium seemed to slightly slow down the densification, as the densification temperature, raised from about 13°C (and the FWMH of peak increased from 54°C to 91°C).

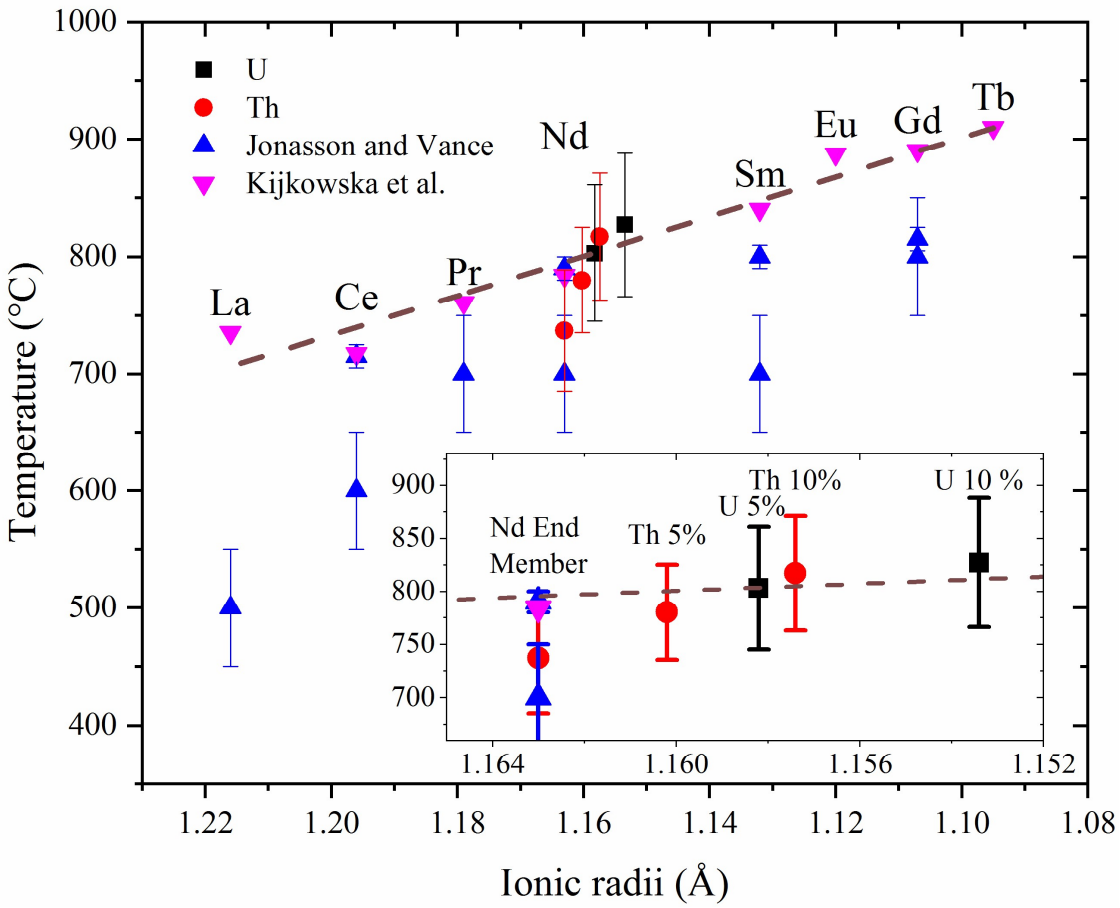

Figure V-9. Variation of the temperature of conversion of rhabdophane into monazite-cheralite solid solution as a function of the ionic radius. The data of the monazite end-members was extracted from Jonasson and Vance [21] and Kijkowska *et al.* [22]

Summary

In this last chapter, (Th,U)-rhabdophane $Nd_{1-2x}Ca_xTh_{x-y}U_yPO_4.nH_2O$ ($0 \leq x \leq 0.1$, $0 \leq y \leq 0.1$) was successfully prepared by applying the hydrothermal treatment described for Th-rhabdophane. The associated monazite-cheralite solid solutions were obtained by heating at 1100°C for 6 hours under argon atmosphere. The as-prepared rhabdophane and monazite-cheralite were single phase and fulfilled the target chemical compositions. This protocol provided a new wet chemistry route to incorporate tetravalent actinides into the monazite matrix, which could reduce the risk of contamination, avoid long and repetitive grinding/heating steps and improve the homogeneity of the final samples compared to the conventional solid-state routes.

The thermal behavior of the U-rhabdophane was also investigated. The thermogravimetric study suggested that the dehydration was composed by two-steps, in agreement with that observed for Ln- and Th-rhabdophanes. The hemihydrate was obtained through either an evaporation in vacuum or heating for $T \geq 100$°C. The complete dehydration took place above 220 °C. Moreover, it is worth noting that phosphates seemed to prevent U(IV) from oxidation. The dilatometry study suggested that the conversion of U-rhabdophane into monazite-cheralite took place between 670°C and 850°C. It also showed the linear trend between the conversion temperature and the ionic radius. The densification process happened between 850°C and 1300°C and the decomposition took place above 1300°C. Therefore, the sintering of the $Nd_{1-2x}Ca_xU_xPO_4$ should be performed below this temperature.

Résumé

Dans ce dernier chapitre, des échantillons de rhabdophanes-(Th,U), de formule $Nd_{1-2x}Ca_xTh_{x-y}U_yPO_4,nH_2O$ ($0 \leq x \leq 0,1$; $0 \leq y \leq 0,1$), ont été préparés avec succès en appliquant le protocole développé pour les échantillons contenant du thorium. Les monazite-chéralite associées ont été préparées par calcination à 1100°C pendant 6 heures sous atmosphère inerte. Les rhabdophanes et les monazites-chéralites telles que préparées se sont avérées monophasées et de compositions attendues. Ce protocole apparaît donc comme une nouvelle méthode d'incorporation par voie humide des actinides tétravalents au sein de solutions solides de monazite/chéralite. Ainsi, il permet de réduire les risques de contamination, élimine des cycles longs et répétitifs de broyage et de calcination et améliore de manière significative l'homogénéité du produit final par rapport aux méthodes habituelles de réactions en phase solide.

Le comportement thermique des rhabdophanes contenant de l'uranium a été étudié. L'étude thermogravimétrique a montré que la déshydratation intervenait en deux étapes, comme cela a déjà été reporté dans le cas des éléments lanthanide et du thorium. La forme hémihydratée peut être obtenue soit par évaporation sous vide, soit par traitement thermique au-delà de 100°C. La déshydratation complète intervient au-delà de 220°C. De plus, les groupements phosphate apparaissent comme protecteurs de l'uranium (IV) vis-à-vis de l'oxydation. L'étude dilatométrique suggère que la conversion de le rhabdophane-U en monazite-chéralite intervient entre 670°C et 850°C. Une relation linéaire entre la température de conversion et le rayon ionique moyen a été établi. Le processus de densification intervient entre 850°C et 1300°C tandis que la décomposition débute au-delà de 1300°C. Sur la base des résultats obtenus, le frittage de $Nd_{1-2x}Ca_xU_xPO_4$ devrait être réalisé en deçà de cette température.

Incorporation of U(IV) into monazite

Ca:An = 10, T = 110°C, t = 4 days

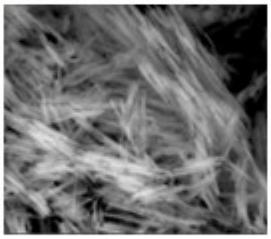

Hydrothermal synthesis

rhabdophane $Nd_{1-2x}Ca_xTh_{x-y}U^{IV}_yPO_4.nH_2O$

TGA

Hemihydrated form
(Vacuum / T ≥ 100°C)
↓
Anhydrous form
(T ≥ 220°C)

Monazite-cheralite
$Nd_{1-2x}Ca_xTh_{x-y}U^{IV}_yPO_4$

Dilatometry

Conversion
(670 °C ≤ T ≤ 850°C)
↓
Densification
(850 °C ≤ T ≤ 1300°C)
↓
Decomposition
(T ≥ 1300°C)

References

(1) Dacheux, N. Matrices a Base de Phosphate d'uranium et de Thorium : Syntheses, Caracterisations et Lixiviation. PhD Thesis, Université de Paris XI Orsay, 1995.

(2) Clavier, N. Elaboration de Phosphate-Diphosphate de Thorium et d'uranium (β-PDTU) et de Matériaux Composites β-PDTU/Monazite à Partir de Précurseurs Cristallisés : Études Du Frittage et de La Durabilité Chimique. PhD Thesis, Université de Paris-Sud, 2004.

(3) Burns, P. C.; Klingensmith, A. L. Uranium Mineralogy and Neptunium Mobility. *Elements* **2006**, *2* (6), 351–356. https://doi.org/10.2113/gselements.2.6.351.

(4) McCarthy, G. J.; White, W. B.; Pfoertsch, D. E. Synthesis of Nuclear Waste Monazites, Ideal Actinide Hosts for Geologic Disposal. *Materials Research Bulletin* **1978**, *13* (11), 1239–1245. https://doi.org/10.1016/0025-5408(78)90215-5.

(5) Podor, R. Synthèse et Caractérisation Des Monazites Uranifères et Thorifères. PhD Thesis, Université de Lorraine, 1994.

(6) Terra, O. Incorporation d'actinides Tétravalents Dans Trois Matrices Phosphatées : Britholite, Monazite/Brabantite et Phosphate-Diphosphate de Thorium (β-PDT). PhD Thesis, Université de Paris XI Orsay, 2005.

(7) Bregiroux, D.; Terra, O.; Audubert, F.; Dacheux, N.; Serin, V.; Podor, R.; Bernache-Assollant, D. Solid-State Synthesis of Monazite-Type Compounds Containing Tetravalent Elements. *Inorg. Chem.* **2007**, *46* (24), 10372–10382. https://doi.org/10.1021/ic7012123.

(8) Bregiroux, D.; Belin, R.; Valenza, P.; Audubert, F.; Bernache-Assollant, D. Plutonium and Americium Monazite Materials: Solid State Synthesis and X-Ray Diffraction Study. *Journal of Nuclear Materials* **2007**, *366* (1), 52–57. https://doi.org/10.1016/j.jnucmat.2006.12.042.

(9) Raison, P. E.; Jardin, R.; Bouëxière, D.; Konings, R. J. M.; Geisler, T.; Pavel, C. C.; Rebizant, J.; Popa, K. Structural Investigation of the Synthetic $CaAn(PO_4)_2$ (An = Th and Np) Cheralite-like Phosphates. *Physics and Chemistry of Minerals* **2008**, *35* (10), 603–609. https://doi.org/10.1007/s00269-008-0252-4.

(10) OECD. Physics and Safety of Transmutation Systems. **2006**. https://doi.org/10.1787/oecd_papers-v6-art13-en.

(11) Podor, R.; Cuney, M.; Nguyen, T. C. Experimental Study of the Solid Solution between Monazite-(La) and $(Ca_{0.5}U_{0.5})PO_4$ at 780 °C and 200 MPa. *American Mineralogist* **1995**, *80* (11–12), 1261–1268. https://doi.org/10.2138/am-1995-11-1215.

(12) Dacheux, N.; Brandel, V.; Genet, M.; Bak, K.; Berthier, C. Solid Solutions of Uranium and Thorium Phosphates: Synthesis, Characterization and X-Ray Photoelectron Spectroscopy. *New Journal of Chemistry* **1996**, *20* (3), 301–310.

(13) Wallez, G.; Raison, P. E.; Dacheux, N.; Clavier, N.; Bykov, D.; Delevoye, L.; Popa, K.; Bregiroux, D.; Fitch, A. N.; Konings, R. J. M. Triclinic–Cubic Phase Transition and Negative Expansion in the Actinide IV (Th, U, Np, Pu) Diphosphates. *Inorg. Chem.* **2012**, *51* (7), 4314–4322. https://doi.org/10.1021/ic300036y.

(14) Benard, P.; Louer, D.; Dacheux, N.; Brandel, V.; Genet, M. U(UO2)(PO4)2, a New Mixed-Valence Uranium Orthophosphate: Ab Initio Structure Determination from Powder Diffraction Data and Optical and X-Ray Photoelectron Spectra. *Chem. Mater.* **1994**, *6* (7), 1049–1058. https://doi.org/10.1021/cm00043a029.

(15) Dacheux, N.; Clavier, N.; Podor, R. Versatile Monazite: Resolving Geological Records and Solving Challenges in Materials Science: Monazite as a Promising Long-Term Radioactive Waste Matrix: Benefits of High-Structural Flexibility and Chemical Durability†. *American Mineralogist* **2013**, *98* (5–6), 833–847. https://doi.org/10.2138/am.2013.4307.

(16) Terra, O.; Dacheux, N.; Clavier, N.; Podor, R.; Audubert, F. Preparation of Optimized Uranium and Thorium Bearing Brabantite or Monazite/Brabantite Solid Solutions. *Journal of the American Ceramic Society* **2008**, *91* (11), 3673–3682. https://doi.org/10.1111/j.1551-2916.2008.02678.x.
(17) Mesbah, A.; Clavier, N.; Elkaim, E.; Gausse, C.; Kacem, I. B.; Szenknect, S.; Dacheux, N. Monoclinic Form of the Rhabdophane Compounds: $REEPO_4 \cdot 0.667H_2O$. *Crystal Growth & Design* **2014**, *14* (10), 5090–5098. https://doi.org/10.1021/cg500707b.
(18) Swanson, H. E. *Standard X-Ray Diffraction Powder Patterns. Section 11, Data for 70 Substances*; Washington, D.C. : U.S. Dept. of Commerce, National Bureau of Standards : For sale by the Supt. of Docs, U.S. G.P.O., 1974., 1974.
(19) Shannon, R. D. Revised Effective Ionic Radii and Systematic Studies of Interatomic Distances in Halides and Chalcogenides. *Acta Crystallographica Section A* **1976**, *32* (5), 751–767. https://doi.org/10.1107/S0567739476001551.
(20) Mesbah, A.; Clavier, N.; Elkaim, E.; Szenknect, S.; Dacheux, N. In Pursuit of the Rhabdophane Crystal Structure: From the Hydrated Monoclinic $LnPO_4.0.667H_2O$ to the Hexagonal $LnPO_4$ (Ln = Nd, Sm, Gd, Eu and Dy). *Journal of Solid State Chemistry* **2017**, *249*, 221–227. https://doi.org/10.1016/j.jssc.2017.03.004.
(21) Jonasson, R. G.; Vance, E. R. DTA Study of the Rhabdophane to Monazite Transformation in Rare Earth (La-Dy) Phosphates. *Thermochimica Acta* **1986**, *108*, 65–72. https://doi.org/10.1016/0040-6031(86)85078-X.
(22) Kijkowska, R. Thermal Decomposition of Lanthanide Orthophosphates Synthesized through Crystallisation from Phosphoric Acid Solution. *Thermochimica Acta* **2003**, *404* (1), 81–88. https://doi.org/10.1016/S0040-6031(03)00085-6.

Conclusions and Perspectives

This PhD work was dedicated to the incorporation of tetravalent actinides (An^{IV} = Th, U) into the monazite structure type, leading to monazite-cheralite solid solutions of general formula $Ln_{1-2x}Ca_xAn_xPO_4$ (Ln^{III} = Pr, Nd) by thermal conversion. An original hydrothermal synthesis protocol was first developed in order to prepare rhabdophane-type precursors $Ln_{1-2x}Ca_xTh_xPO_4.nH_2O$ (Ln = Pr, Nd). Heat treatment of these precursors at 1100 °C resulted in single-phase monazite-cheralite, $Ln_{1-2x}Ca_xTh_xPO_4$. Three operating parameters were optimized to reach this result: initial molar ratio Ca:Th equal to 10:1, optimal temperature of 110 °C, and duration longer than 4 days. Under these conditions, the stability domain of $Pr_{1-2x}Ca_xTh_xPO_4.nH_2O$ and $Nd_{1-2x}Ca_xTh_xPO_4.nH_2O$ ranged from $x = 0$ to $x = 0.15$ and from $x = 0$ to $x = 0.10$, respectively. This new wet chemistry route led to single-phase thorium-bearing monazite-cheralite solid solutions, avoiding the use of long and repetitive grinding/heating steps. In addition, it allowed improving significantly the cationic homogeneity and the specific surface area of thorium-bearing monazite-cheralite solid solutions compared to previously reported dry chemistry routes.

The thermal behavior of the as-prepared rhabdophanes $Nd_{1-2x}Ca_xTh_xPO_4.nH_2O$ ($x \leq 0.10$) was then studied by combining *in situ* HT-PXRD, TGA, and dilatometry. The dehydration occurred in two steps: the hemihydrate formed at 100°C whereas the complete dehydration took place between 200 and 220°C. The conversion of the rhabdophane into the monazite-cheralite solid solution was observed between 600 and 850°C. The Ca-Th coupled incorporation rate resulted in the increase of the conversion temperature. The contraction of the average cation radius seemed to enhance the structure stability.

The third chapter of this manuscript was further dedicated to the elaboration of monazite-cheralite ceramics, $Nd_{1-2x}Ca_xTh_xPO_4$ ($x = 0 – 0.1$), through the direct sintering of rhabdophane-type precursors. This innovative process led to homogeneous and highly densified pellets at about 1200°C, which appears to be significantly lower than those reported in the literature for solid-state routes (1450°C). The sintering map of $Nd_{1-2x}Ca_xTh_xPO_4$ solid solutions was also established. The densification remained predominant at 1200°C. However, the complete densification quickly operated at 1400°C and was followed by an important grain growth step. These maps also suggested that the Th-Ca coupled substitution slowed down both densification and grain growth processes, leading the maximum grain size (D_{50}) to decrease by an order of magnitude compared with $NdPO_4$. Concomitantly, the activation energy associated with the densification ranged from 361 ± 90 to 530 ± 90 $kJ.mol^{-1}$. Additionally, the microhardness of the $Nd_{1-2x}Ca_xTh_xPO_4$ ($x = 0 – 0.1$) ceramics determined by the Vickers hardness test was found

to 4.9 ± 0.8 GPa, which was compatible with the values reported for monazite type ceramics (~5 GPa) [1–6].

A multiparametric dissolution study of $Nd_{0.8}Ca_{0.1}Th_{0.1}PO_4$ was then performed in order to evaluate the chemical durability of the prepared samples of monazite-cheralite. The normalized dissolution rate $R_{L,0}$ (25°C, 1 mol.L^{-1} HNO_3) determined during the kinetic stage reached 3 × 10^{-5} g.m^{-2}.d^{-1}, which is significantly lower than the normalized dissolution rates reported in the literature for other ceramic wasteforms, such as britholite and zirconolite. The apparent activation energy associated with the dissolution reaction, E_A (25°C → 80°C, 1 mol.L^{-1} HNO_3) equaled 46 ± 7 kJ.mol^{-1}. This value is close to those determined for $LnPO_4$ end members (44 – 54 kJ.mol^{-1}) [7–10]

When reaching saturation conditions in the solution, either Th-rhabdophane $Nd_{0.8}Ca_{0.1}Th_{0.1}PO_4.nH_2O$ or monazite-cheralite $Nd_{0.8}Ca_{0.1}Th_{0.1}PO_4$ were identified as the solubility-controlling phase. The standard solubility constant at 298 K, $K_{s,0}°$ was found to $10^{-31.3 \pm 0.4}$. The thorium and neodymium concentrations obtained at thermodynamic equilibrium with this solubility-controlling phase were even lower than that would be constrained by a mixture of $NdPO_4.nH_2O$ and TPHPH ($Th_2(PO_4)_2(HPO_4).H_2O$). Consequently, during the whole dissolution test (*i.e.* kinetic and thermodynamic stages), the as-prepared monazite-cheralite ceramic showed an excellent chemical durability, which appears in favor of its use as radwaste matrix for the specific conditioning of actinides.

Besides, complete sets of standard thermodynamic data were determined for Th-rhabdophane, $Nd_{0.8}Ca_{0.1}Th_{0.1}PO_4.nH_2O$ and monazite-cheralite, $Nd_{0.8}Ca_{0.1}Th_{0.1}PO_4$. The Δ_fG°, Δ_fH°, and Δ_fS° (298.15 K, Th-rhabdophane / monazite-cheralite) were found to - 2097 ± 9 kJ.mol^{-1} and - 1868 ± 9 kJ.mol^{-1}, to - 2205 ± 8 and - 1980 ± 9 kJ.mol^{-1}, and to - 360 ± 58 and - 376 ± 58 J.mol^{-1}.K^{-1}, respectively.

Finally, the incorporation of tetravalent uranium in the monazite/cheralite structure was investigated. The hydrothermal synthesis protocol developed for thorium was successfully applied for the preparation of U-rhabdophane, $Nd_{1-2x}Ca_xU^{IV}_xPO_4.nH_2O$ ($0 \leq x \leq 0.1$), leading to associated single-phase monazite-cheralite $Nd_{1-2x}Ca_xU^{IV}_xPO_4$. The thermal conversion of rhabdophane into monazite/cheralite took place at 1100°C in air or in argon atmosphere, which suggested that phosphate groups might protect U^{IV} from oxidation.

The thermal behavior of the U-rhabdophane was also investigated. Its dehydration and thermal conversion were similar to those obtained for Th- and Ln-rhabdophanes. Moreover, a linear correlation between the conversion temperature and the ionic radius was also observed

for U-rhabdophanes. The temperature of the densification process ranged between 1000°C and 1300°C. Above 1300°C, the decomposition of $Nd_{1-2x}Ca_xU^{IV}_xPO_4$ took place. All these results provide the first valuable insights into the sintering of $Nd_{1-2x}Ca_xU^{IV}_xPO_4$.

In view of these results, many interesting topics are worth investigating in the field of actinide (IV)-bearing monazite-cheralite. Regarding the hydrothermal synthesis, a study dedicated to the effect of pH on the properties of the rhabdophane precursors would provide new insights, especially in terms of morphological properties. Indeed, several publications have reported the synthesis of Ln-rhabdophane end-members in basic conditions [5,11]. According to these studies, such conditions could influence the morphology and the crystallinity of the final rhabdophane, and thus change its sintering ability, even though the hydroxides might present as secondary phases [1,12]. Besides, neptunium also presents in the spent fuel and it is considered as a major source of radiotoxicity [13]. Contrary to its most common oxidation state, *i.e.*, Np (V) in natural systems [13], tetravalent neptunium is much less mobilized in the neutral media (C(Np) = 10^{-8} mol.kg^{-1}_{water} *vs.* ~ 10^{-4} mol.kg^{-1}_{water}) [14]. Consequently, there is an interest in the preparation of $Ln_{1-2x}Ca_xNp^{IV}_xPO_4$ with the application of our hydrothermal synthesis protocol.

Regarding the densification process, the sintering properties of $Nd_{1-2x}Ca_xU^{IV}_xPO_4.nH_2O$ have not been fully investigated. In the following study, a more thorough dilatometric study would be performed under various atmospheres (Air or Ar/H_2) and the dilatation phenomenon observed above 1300 °C should be investigated in details. Additionally, the sintering maps might be established. Besides, it is worth exploring the sintering properties of the mixed An^{IV}-rhabdophane and Np^{IV}-rhabdophane to have a better simulation of the final monazite-type ceramics used in actinide conditioning.

In this study, powdered $Nd_{0.8}Ca_{0.1}Th_{0.1}PO_4$ showed an excellent chemical durability. However, saturation phenomena occurred for the less acidic media, *i.e.*, $C(H^+) \leq 0.3$ mol.L^{-1}. In future studies, leaching tests could be performed in flow-through reactor, in which the leaching solution could be continuously renewed. As such, the system could remain far from saturation equilibrium even at more elevated pH, thus allowing the evaluation of accurate leaching rates in less acidic media.

Besides, the kinetic dissolution of the uranium bearing monazite-cheralite $Nd_{0.8}Ca_{0.1}U^{IV}_{0.1}PO_4$ could be studied in different media (*e.g.* HNO_3, HCl, distilled water, etc.) so that the impact of the redox behaviors of uranium ($U^{IV} \leftrightarrow U^{VI}$) could be underlined.

When reaching the saturation conditions, the residue of the dissolution tests would go through a more detailed characterization to precise the nature of the solubility-controlling

phases. Additionally, in order to confirm the very high chemical durability of the prepared materials under weathering conditions, saturation phenomena obtained during dissolution of sintered monazite-cheralite ceramic pellets should be investigated in conditions close to that associated to the repository site. The leaching solution could be a synthetic media characteristic of the groundwater composition. Moreover, temperature could reach 80-90°C. During such long-term experiments, the evolution of the microstructure at the liquid-solid interface could be monitored by Environmental Scanning Electron Microscope (ESEM) in order to follow the formation of secondary phases.

From a general point of view, this study confirmed the possibility to prepared dense monazite-cheralite type ceramics with an important incorporation ratio of tetravalent actinides (~10 mol.%) through wet chemistry routes. Moreover, some thermodynamic data related to dissolution of monazite-cheralite $Nd_{0.8}Ca_{0.1}Th_{0.1}PO_4$ were determined. These observations deepened our understanding of the monazite-cheralite type ceramic matrix and provided useful information in the future study on the long-term behavior of monazite-cheralite type ceramic under environmental conditions.

Ce travail de thèse a été consacré à l'incorporation d'actinides tétravalents (An^{IV} = Th, U) au sein de la structure type monazite, conduisant ainsi à des solutions solides de monazite-chéralite $Ln_{1-2x}Ca_xAn_xPO_4$ (Ln^{III} = Pr, Nd). Un protocole de synthèse original reposant sur l'utilisation de conditions hydrothermales a, tout d'abord, été développé pour préparer des précurseurs de structure rhabdophane, $Ln_{1-2x}Ca_xTh_xPO_4,nH_2O$ (Ln = Pr, Nd). Leur conversion thermique (T= 1100°C) a alors conduit à la formation de solutions solides monophasées de monazite-chéralite, $Ln_{1-2x}Ca_xTh_xPO_4$. Dans cet objectif, trois paramètres principaux ont été optimisés au cours de la synthèse : le rapport molaire initial (Ca : Th = 10 : 1), la température (optimum obtenu pour 110 °C), et la durée de traitement hydrothermal ($t_{synthèse} \geq 4$ jours). En appliquant ce protocole, le domaine de stabilité des rhabdophanes $Pr_{1-2x}Ca_xTh_xPO_4,nH_2O$ et $Nd_{1-2x}Ca_xTh_xPO_4,nH_2O$ a atteint respectivement $x \leq 0,15$ et $x \leq 0,10$. Cette nouvelle méthode de synthèse par voie humide a conduit à la préparation de solutions solides monophasées de monazite-cheralite tout en évitant d'avoir recours à des étapes de broyage-calcination longues et répétitives. De plus, cette méthode a contribué à améliorer l'homogénéité cationique et à augmenter la surface spécifique des précurseurs de type rhabdophane, par rapport aux valeurs reportées précédemment par voies sèches.

Par la suite, le comportement thermique des rhabdophanes $Nd_{1-2x}Ca_xTh_xPO_4,nH_2O$ ($x \leq 0,10$) a été étudié en combinant des analyses DRX *in situ* à haute température ainsi que des suivis par ATG et par dilatométrie. Le processus de déshydratation intervient en deux étapes : la formation de la forme hémi-hydratée a été observée vers 100°C, puis la déshydratation complète entre 200 et 220°C. La température associée à la conversion des rhabdophanes en solutions solides de monazite-chéralite varie entre 600 et 850°C. Il apparaît que la substitution couplée du néodyme par le calcium et le thorium tend à augmenter la température de conversion. La diminution du rayon cationique moyen semble donc renforcer la stabilité de la structure.

Des céramiques de type monazite-chéralite $Nd_{1-2x}Ca_xTh_xPO_4$ (x = 0 - 0,1) ont ensuite été obtenues en frittant directement les précurseurs rhabdophanes. Cette méthode a conduit à des pastilles homogènes présentant des taux de densification élevés. De plus, la température de densification est significativement plus basse que celle reportée dans la littérature dans le cas de l'utilisation de voies sèches (1200°C *vs.*1450°C). Une carte de frittage a été établie pour les solutions solides $Nd_{1-2x}Ca_xTh_xPO_4$. La densification demeure prédominante à 1200°C. Cependant, la densification est rapidement achevée à 1400°C. Elle est suivie d'un grossissement des grains très important. Ces données montrent également que la substitution couplée Th-Ca semble ralentir à la fois la densification et les mécanismes de grossissement des grains,

conduisant à la diminution d'un ordre de grandeur de leur taille maximale (D_{50}) par rapport au pôle pur $NdPO_4$. Parallèlement, l'énergie d'activation associée à la densification a été déterminée. Elle varie entre 361 ± 90 et 530 ± 90 kJ.mol^{-1}. D'autre part, la microdureté des céramiques $Nd_{1-2x}Ca_xTh_xPO_4$ (x = 0 – 0,1) a été évaluée au moyen de tests de dureté Vickers (4,9 ± 0,8 GPa), ce qui est compatible avec les valeurs publiées pour les céramiques de type monazite (~ 5 GPa) [1–6].

Une étude multiparamétrique de la dissolution de monazite-chéralite $Nd_{0,8}Ca_{0,1}Th_{0,1}PO_4$ a ensuite été réalisée afin d'évaluer la durabilité chimique des échantillons préparés. En régime cinétique, la vitesse de dissolution normalisée, $R_{L,0}$ (25 °C, 1 mol.L^{-1} HNO_3) atteint environ 3 × 10^{-5} g.m^{-2}.j^{-1}, ce qui apparaît en bon accord avec les données de la littérature, et significativement plus faible que d'autres matrices céramiques telles que la britholite et la zirconolite. L'énergie d'activation apparente associée à la dissolution, E_A (25°C → 80°C, 1 mol.L^{-1} HNO_3) atteint 46 ± 7 kJ.mol^{-1}. Ce résultat est en accord avec les données relevées dans la littérature pour les pôles purs $LnPO_4$ (44 – 54 kJ.mol^{-1}) [7–10].

En conditions de saturation, la Th-rhabdophane $Nd_{0,8}Ca_{0,1}Th_{0,1}PO_4.nH_2O$ ou la monazite-chéralite $Nd_{0,8}Ca_{0,1}Th_{0,1}PO_4$ peuvent contrôler les concentrations en thorium et en néodyme. Le produit de solubilité de ces phases a été déterminé en conditions standard. Il atteint $K_{s,0}° = 10^{-31,3 \pm 0,1}$ à 298 K. Les concentrations en néodyme et en thorium, relevée à l'équilibre sont plus faibles que celles qui pourraient être imposées par un mélange constitué de rhabdophane, $NdPO_4.nH_2O$ et de PHPTH ($Th_2(PO_4)_2(HPO_4),H_2O$). En résumé, durant tout le processus de dissolution, c'est-à-dire au cours des stades cinétique et thermodynamique, la monazite-chéralite a montré une excellente durabilité chimique ce qui justifie son statut de matrice prometteuse pour le conditionnement des actinides (IV).

De plus, un ensemble complet de données thermodynamiques standard a été déterminé pour la Th-rhabdophane et la solution solide monazite-chéralite. Les valeurs obtenues pour Δ_fG°, Δ_fH°, et Δ_fS° (Th-rhabdophane / monazite-chéralite) sont respectivement de - 2097 ± 9 et - 1868 ± 9 kJ.mol^{-1}, de - 2205 ± 8 et - 1980 ± 9 kJ.mol^{-1} et de - 360 ± 58 et - 376 ± 58 J.mol^{-1}.K^{-1}.

Enfin, l'incorporation de l'uranium(IV) au sein de la structure monazite a été finalement étudiée. Le protocole de synthèse hydrothermale mis au point pour le thorium a été appliqué avec succès pour la préparation des U-rhabdophanes $Nd_{1-2x}Ca_xU^{IV}_xPO_4$ ($0 \leq x \leq 0,1$). Les monazite-chéralites associées ont été obtenues après conversion des rhabdophanes à 1100°C,

sous argon et sous air. La présence de phosphates semble donc inhiber l'oxydation de l'uranium (IV) au cours du traitement thermique (1100°C, sous air).

Le comportement thermique des U-rhabdophanes a également été étudié. Il est apparu que les précurseurs suivaient le même schéma de déshydratation puis de conversion que les pôles purs Ln-rhabdophanes et Th-rhabdophanes. De plus, une relation linéaire entre les températures de conversion et le rayon ionique a pu être établie. Le processus de densification a lieu entre 1000°C et 1300°C tandis que la décomposition intervient au-dessus de 1300°C. Le frittage de $Nd_{1-2x}Ca_x\ U^{IV}_xPO_4$ doit donc être réalisé en dessous de cette température. Ainsi, ces résultats fournissent les premières informations disponibles sur le frittage de $Nd_{1-2x}Ca_xU^{IV}_xPO_4$.

De nombreux sujets restent néanmoins à traiter concernant les monazites-chéralites incorporant des actinides tétravalents. Concernant la synthèse hydrothermale, une étude consacrée à l'effet du pH sur les propriétés des précurseurs de type rhabdophane apporterait de nouvelles connaissances, notamment en termes de la morphologie. En effet, plusieurs publications ont rapporté la synthèse des pôles purs Ln-rhabdophanes dans des conditions basiques [5,11]. Selon ces études, le pH pourrait influencer la morphologie et la cristallinité des poudres obtenues et ainsi modifier leur aptitude au frittage. Enfin, le neptunium existe dans les combustibles usés et il est considéré comme une des sources principales de la radiotoxicité. Contrairement à son degré d'oxydation le plus courant, *i.e.*, Np (V) dans les systèmes naturels [13], tétravalent neptunium est beaucoup moins mobile dans les milieux aqueux neutres (C(Np) = 10^{-8} mol.kg^{-1}_{eau} *vs.* ~ 10^{-4} mol.kg^{-1}_{eau}) [14]. Par conséquent, il existe un intérêt pour la préparation de $Ln_{1-2x}Ca_xNp^{IV}_xPO_4$ via le protocole de synthèse hydrothermale développé dans cette thèse.

En outre, l'étude sur le frittage du $Nd_{1-2x}Ca_xU^{IV}_xPO_4.nH_2O$ menée lors de ce travail pourrait être complétée. Une étude dilatométrique plus détaillée pourrait par exemple être effectuée pour étudier les impacts des atmosphères différentes (Air ou Ar/H_2) et pour les phénomènes de dilatation observés pour T ≥ 1300°C. Parallèlement, des cartes de frittage supplémentaires pourraient être établies. En outre, explorer le frittage de composés mixtes An^{IV}- et Np^{IV}-rhabdophane permettrait d'avoir un meilleur analogue des céramiques finales de type monazite utilisées pour le conditionnement des actinides.

Pendant les tests de dissolution, les poudres de $Nd_{0,8}Ca_{0,1}Th_{0,1}PO_4$ ont montré une excellente durabilité chimique. La précipitation rapide de phases néoformées a été observée dans le milieu le moins acide étudié, c'est-à-dire C (H^+) ≤ 0,3 mol.L^{-1}. Des tests de lixiviation pourraient être menés dans des réacteurs à circulation, afin d'assurer le renouvellement continu

de la solution lixiviante, et ainsi déterminer précisément les vitesses de lixiviation en l'absence de tout phénomène de saturation.

En outre, la dissolution cinétique des solutions solides de type monazite-chéralite $Nd_{0,8}Ca_{0,1}U^{IV}_{0,1}PO_4$ devra être explorée dans les milieux de différentes natures (*e.g.* HNO_3, HCl, eau distillé, etc.) afin d'avoir une meilleure compréhension de l'impact de la chimie redox de l'uranium lors des phénomènes d'altération.

Concernant les phénomènes de saturation, le résidu de dissolution devra être caractérisé de manière plus détaillée pour préciser la nature de la phase contrôlant la solubilité. De plus, les phénomènes de saturation devront être étudiés lors de la lixiviation de pastilles frittées de monazite-cheralite dans des conditions similaires à celles d'un site de stockage (solution synthétique représentant celle d'un site de stockage, température pouvant atteindre 80 à 90°C). Parallèlement, l'évolution de l'interface solide/liquide sera suivie par Microscopie Électronique à Balayage Environnemental (MEBE) afin de mettre en évidence la formation des phases secondaires puis de les caractériser.

D'un point de vue général, cette étude a confirmé la possibilité de préparer, par voie humide, des matériaux céramiques de haute densité avec un taux d'incorporation important en actinides tétravalents (~ 10 mol.%). De plus, certaines données thermodynamiques associées à la dissolution de monazite-cheralite $Nd_{0,8}Ca_{0,1}Th_{0,1}PO_4$ ont été évaluées. Elles ont fourni des informations importantes dans le cadre de l'étude du comportement à long terme de telles céramiques monazite-cheralite en conditions environnementales.

References

(1) Hikichi, Y.; Nomura, T.; Tanimura, Y.; Suzuki, S.; Miyamoto, M. Sintering and Properties of Monazite-Type $CePO_4$. *Journal of the American Ceramic Society* **1990**, *73* (12), 3594–3596. https://doi.org/10.1111/j.1151-2916.1990.tb04263.x.

(2) Perrière, L.; Bregiroux, D.; Naitali, B.; Audubert, F.; Champion, E.; Smith, D. S.; Bernache-Assollant, D. Microstructural Dependence of the Thermal and Mechanical Properties of Monazite $LnPO_4$ (Ln=La to Gd). *Journal of the European Ceramic Society* **2007**, *27* (10), 3207–3213. https://doi.org/10.1016/j.jeurceramsoc.2006.12.005.

(3) Bregiroux, D. Synthèse Par Voie Solide et Frittage de Céramiques à Structure Monazite : Application Au Conditionnement Des Actinides Mineurs. PhD Thesis, Université de Limoges, 2005.

(4) Babelot, C.; Bukaemskiy, A.; Neumeier, S.; Modolo, G.; Bosbach, D. Crystallization Processes, Compressibility, Sinterability and Mechanical Properties of La-Monazite-Type Ceramics. *Journal of the European Ceramic Society* **2017**, *37* (4), 1681–1688. https://doi.org/10.1016/j.jeurceramsoc.2016.11.047.

(5) Arinicheva, Y.; Clavier, N.; Neumeier, S.; Podor, R.; Bukaemskiy, A.; Klinkenberg, M.; Roth, G.; Dacheux, N.; Bosbach, D. Effect of Powder Morphology on Sintering Kinetics, Microstructure and Mechanical Properties of Monazite Ceramics. *Journal of the European Ceramic Society* **2018**, *38* (1), 227–234. https://doi.org/10.1016/j.jeurceramsoc.2017.08.008.

(6) Popa, K.; Cologna, M.; Martel, L.; Staicu, D.; Cambriani, A.; Ernstberger, M.; Raison, P. E.; Somers, J. $CaTh(PO_4)_2$ Cheralite as a Candidate Ceramic Nuclear Waste Form: Spark Plasma Sintering and Physicochemical Characterisation. *Journal of the European Ceramic Society* **2016**, *36* (16), 4115–4121. https://doi.org/10.1016/j.jeurceramsoc.2016.07.016.

(7) Arinicheva, Y.; Gausse, C.; Neumeier, S.; Brandt, F.; Rozov, K.; Szenknect, S.; Dacheux, N.; Bosbach, D.; Deissmann, G. Influence of Temperature on the Dissolution Kinetics of Synthetic $LaPO_4$-Monazite in Acidic Media between 50 and 130 °C. *Journal of Nuclear Materials* **2018**, *509*, 488–495. https://doi.org/10.1016/j.jnucmat.2018.07.009.

(8) Gausse, C. Synthèse et Dissolution de Matrices Phosphatées de Structure Monazitique. PhD Thesis, Université de Montpellier, 2016.

(9) Oelkers, E. H.; Poitrasson, F. An Experimental Study of the Dissolution Stoichiometry and Rates of a Natural Monazite as a Function of Temperature from 50 to 230 °C and PH from 1.5 to 10. *Chemical Geology* **2002**, *191* (1), 73–87. https://doi.org/10.1016/S0009-2541(02)00149-3.

(10) Terra, O.; Clavier, N.; Dacheux, N.; Podor, R. Preparation and Characterization of Lanthanum–Gadolinium Monazites as Ceramics for Radioactive Waste Storage. *New J. Chem.* **2003**, *27* (6), 957–967. https://doi.org/10.1039/B212805P.

(11) Neumeier, S.; Arinicheva, Y.; Clavier, N.; Podor, R.; Bukaemskiy, A.; Modolo, G.; Dacheux, N.; Bosbach, D. The Effect of the Synthesis Route of Monazite Precursors on the Microstructure of Sintered Pellets. *Progress in Nuclear Energy* **2016**, *92*, 298–305. https://doi.org/10.1016/j.pnucene.2016.07.011.

(12) Hikichi, Y.; Hukuo, K.; Shiokawa, J. Solid Solutions in the Systems Monazite($CePO_4$)-Huttonite($ThSiO_4$), and Monazite-$Ca_{0.5}Th_{0.5}PO_4$. *NIPPON KAGAKU KAISHI* **1978**, *1978* (12), 1635–1640. https://doi.org/10.1246/nikkashi.1978.1635.

(13) Czerwinski, K.; Reed, D. *Chemical Speciation of Neptunium in Spent Fuel*; Annual Report DE-FG03-99SF21903; Actinide Research Group in the Nuclear Engineering Department at the Massachusetts Institute of Technology, 2000.

(14) Runde, W. The Chemical Interactions of Actinides in the Environment. *Los Alamos Science* **2000**, *26*, 392–411.

Appendices

A.1 Selected wavelengths for the determination of the elemental concentrations by ICP-OES

Table A. 1 Selected wavelengths for the determination of the elemental concentrations by ICP-OES

Elements	Wavelength positions (nm)
Ca	183.801
	315.887
	317.933
	422.673
P	177.495
	178.287
	213.618
	214.914
Nd	401.225
	406.109
	417.731
	430.358
Th	274.716
	283.231
	283.730
	401.913
U	279.394
	367.997
	385.958
	409.014

A.2 Support information for Rietveld refinement

Applying a least squares approach, the Rietveld method [1] refined a theoretical line profile until it matches the measured profile. The different statistical criteria [2,3] met for refinements are reported below:

Profile R-factor,

$$R_p = \frac{\Sigma|y_{i_{obs}} - y_{i_{calc}}|}{\Sigma y_{i_{obs}}} \quad \text{(A-1)}$$

Weighted profile R-factor,

$$R_{wp} = \left[\frac{\Sigma w_i (y_{i_{obs}} - y_{i_{calc}})^2}{\Sigma w_i y_{i_{obs}}^2}\right]^{\frac{1}{2}} \quad \text{(A-2)}$$

Expected R-factor,

$$R_{\exp} = \left[\frac{N-P}{w_i y_{i_{obs}}^2)}\right]^{\frac{1}{2}} \quad \text{(A-3)}$$

Goodness of fit,

$$\chi^2 = \left[\frac{R_{wp}}{R_{\exp}}\right]^2 \quad \text{(A-4)}$$

where, $y_{i_{obs}}$ and $y_{i_{calc}}$ are the measured intensity and the calculated intensity for each point i. w_i is the weight of point i. N is the number of observation and P is the number of estimated least-squares parameters. It is worth noting that, in Fullprof suite, the $y_{i_{calc}}$ is normally a sum of weighted pseudo-Voigt functions [2,4].

The aim of the Rietveld refinement is to reduce the goodness of fit χ^2 to the least possible [5]. The expected R-factor R_{exp} is considered as the "best possible R_{wp}" [5] and therefore is a constant. However, the value of R_{wp} could be modified by adjusting unit cell parameters, atom positions, crystallinity, etc.

A.3 Determination of temperatures (T_1 and T_2) and velocity of densification (v_{1f} and v_{2i}) for the calculation of activation energy E_A (Dorn's method).

As mentioned in **Section III-2.5**, the energy activation associated with the densification could be determined by Dorn's method, which is dilatometric experiments consist of a serious of incremental isothermal heat treatments. **Figure A. 1** presents one of the temperature rises, where the temperature of the first stage (T_1) rapidly raise to that of the second stage (T_2) within the time Δt. The velocity of densification at the end of the 1st stage (v_{1f}) could be determined easily. However, the determination of the velocity of densification at the beginning of 2nd stage, (v_{2i}) is delicate. In the transition state (within Δt), the temperature was firstly raised above T_2 with a gap of ΔT, then dropped back to T_2, as the system would reach a new equilibrium. The v_{2i} was determined by applying a linear extrapolation at the moment t_{2i} from the velocities of densification at T_2 (equilibrium state), when t_{2i} is the moment that the temperature reached T_2 in the first time during the transition state Δt. Therefore, the activation energy calculated associated with the densification could be calculated according to Eq.**III-13**,

$$E_A = \frac{RT_1T_2}{T_1 - T_2} \ln\left(\frac{v_{1f}T_1}{v_{2i}T_2}\right)$$

Finally, the determined parameters for the E_A calculation were presented in **Table A. 2**.

Table A. 2 Determined parameters and activation energy associated with densification E_A

x	T_1 (K)	T_2 (K)	v_{1f} ($\times 10^{-3}$ %.s^{-1})	v_{2i} ($\times 10^{-3}$ %.s^{-1})	E_A (kJ.mol^{-1})	$\overline{E_A}$ (kJ.mol^{-1})
0.00	1273	1323	-2.3 ± 0.1	-15 ± 2	530 ± 90	530 ± 90
0.05	1273	1323	-1.2 ± 0.1	-4.3 ± 0.6	358 ± 90	360 ± 90
	1323	1373	-0.3 ± 0.01	-0.9 ± 0.1	363 ± 90	
0.075	1423	1473	-0.41 ± 0.02	-1.3 ± 0.2	403 ± 90	440 ± 120
	1473	1523	-0.45 ± 0.02	-1.5 ± 0.2	457 ± 90	
0.10	1273	1323	-0.43 ± 0.02	-2.7 ± 0.4	525 ± 90	480 ± 130
	1323	1373	-1.03 ± 0.04	-5.4 ± 0.7	512 ± 90	
	1373	1423	-1.05 ± 0.05	-4.0 ± 0.5	444 ± 90	
	1423	1473	-0.78 ± 0.03	-2.9 ± 0.4	470 ± 90	
	1473	1523	-0.58 ± 0.03	-1.9 ± 0.3	453 ± 90	

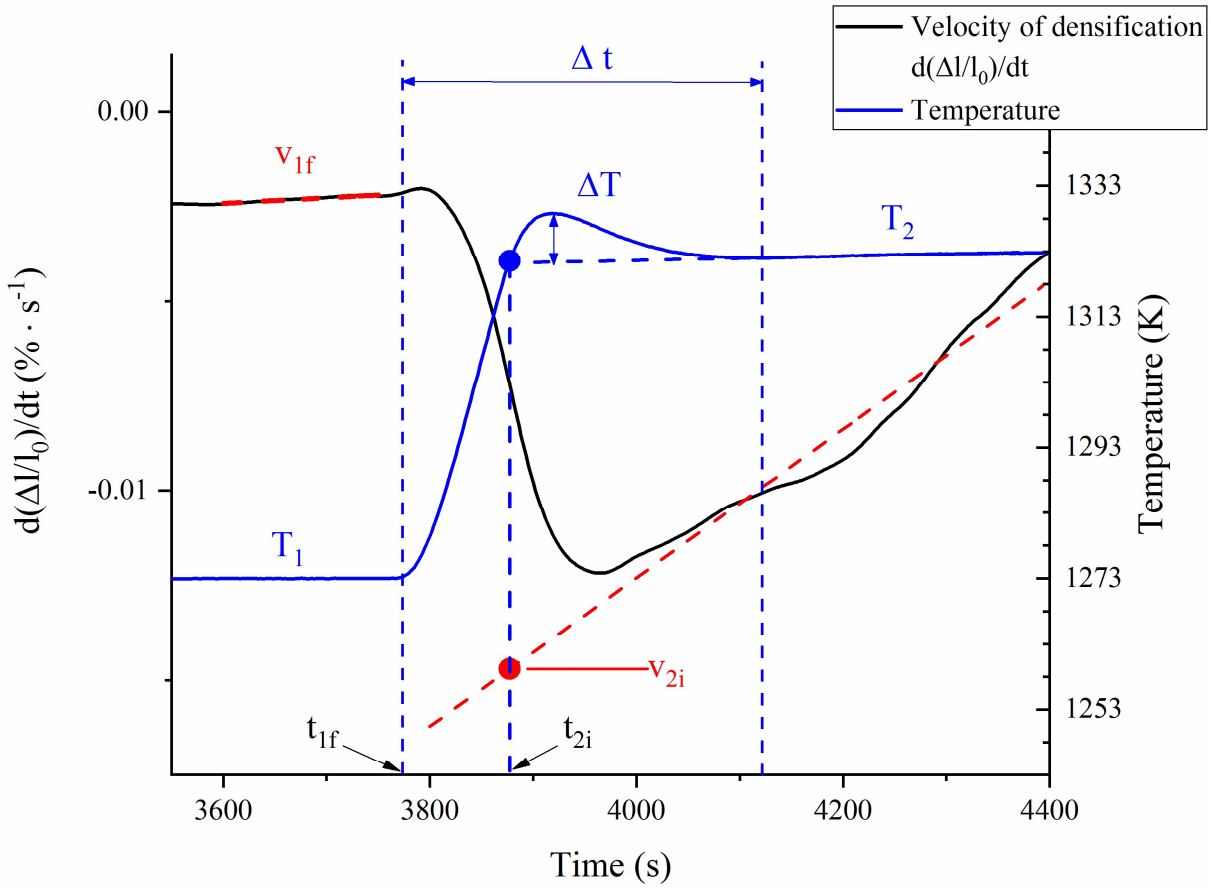

Figure A. 1 Determination of the velocity of densification at the beginning of 2nd stage, v_{2i} (inspired by Bregiroux [6])

References

(1) Rietveld, H. M. A Profile Refinement Method for Nuclear and Magnetic Structures. *Journal of Applied Crystallography* **1969**, *2* (2), 65–71. https://doi.org/10.1107/S0021889869006558.

(2) Mesbah, A. I) Cristallochimie Des Carboxylates Métalliques Inhibiteurs de La Corrosion de Métaux et II) Structure et Magnétisme de Dicarboxylates (Téréphtalate et Thiophène) de Métaux de Transition. PhD Thesis, Université Henri Poincaré, Nancy I, 2008.

(3) Rafiuddin, M. R.; Grosvenor, A. P. A Structural Investigation of Hydrous and Anhydrous Rare-Earth Phosphates. *Inorg. Chem.* **2016**, *55* (19), 9685–9695. https://doi.org/10.1021/acs.inorgchem.6b01471.

(4) Frontera, C.; Rodríguez-Carvajal, J. FullProf as a New Tool for Flipping Ratio Analysis. *Physica B: Condensed Matter* **2003**, *335* (1), 219–222. https://doi.org/10.1016/S0921-4526(03)00241-2.

(5) Toby, B. H. R Factors in Rietveld Analysis: How Good Is Good Enough? *Powder Diffraction* **2006**, *21* (1), 67–70. https://doi.org/10.1154/1.2179804.

(6) Bregiroux, D. Synthèse Par Voie Solide et Frittage de Céramiques à Structure Monazite : Application Au Conditionnement Des Actinides Mineurs. PhD Thesis, Université de Limoges, 2005.

Abstract

The management and disposal of HLW radwaste is one of the main challenges for the nuclear industry. In this field, the specific conditioning of actinides appears of strong interest, as they act as the main contributors to the long-term radiotoxicity during the storage in an underground geological repository. Monazite-type ceramics have been often considered as promising ceramic wasteform due to their ability to incorporate large amounts of tri- and tetravalent actinides, their excellent chemical durability and their exceptional high resistance to self-irradiation. Nevertheless, the incorporation of tetravalent actinides in the monazite structure *via* wet chemistry routes has been rarely reported. Consequently, this study was firstly aimed to synthesize single-phase thorium-bearing rhabdophane type precursors by multiparametric hydrothermal process. Their thermal conversion into monazite-cheralite ceramics was investigated and followed by a complete sintering study. As instance, sintering maps were further established in order to obtain highly densified and single phase ceramics showing controlled microstructure. Later, multiparametric dissolution tests were performed on $Nd_{0.8}Ca_{0.1}Th_{0.1}PO_4$ monazite-cheralite in acid media. They confirmed the very high chemical durability of the prepared materials as well as the very low solubility of the neoformed phases. Finally, uranium-bearing rhabdophanes were also prepared *via* the same wet chemistry route and then converted to single-phase monazite-cheralite solid solutions by heating. This study then provided new insights in the preparation of monazite-cheralite type wasteforms by wet chemistry route and contributed to the better understanding of the long-term behavior of such kind of ceramics in the field of the storage of radioactive waste in an underground repository site.

Résumé

L'un des défis majeurs de l'industrie électronucléaire réside dans la gestion et le stockage des déchets radioactifs. Le stockage spécifique des actinides présente un intérêt particulier, ces derniers étant les principaux contributeurs à la radiotoxicité à long terme des colis de déchets de haute activité et de longue période. Dans ce cadre, les céramiques de type monazite sont souvent considérées comme des matrices prometteuses pour un stockage à long terme de tels déchets en raison de leur capacité à incorporer des quantités importantes d'actinides tri- et tétravalents, de leur excellente durabilité chimique et de leur exceptionnelle résistance à l'auto-irradiation. Néanmoins, l'incorporation, par voie humide, d'actinides tétravalents au sein de la structure monazitique n'a été que très rarement reportée. En conséquence, cette étude a d'abord été consacrée à l'incorporation de thorium, par synthèse hydrothermale, au sein de composés de structure rhabdophane dans le but de préparer des précurseurs monophasés. Par la suite, leur conversion thermique en céramiques de type monazite-chéralite monophasées a été examinée puis des études de frittage de ces matériaux ont été conduites. Ainsi, les cartes de frittage de plusieurs monazite-chéralites ont été établies afin d'optimiser les conditions de préparation de céramiques denses et de microstructure contrôlée. Des tests multiparamétriques de dissolution, menés sur $Nd_{0,8}Ca_{0,1}Th_{0,1}PO_4$ en milieu acide, ont démontré sa très bonne résistance à l'altération ainsi que la très faible solubilité des phases néoformées. Enfin, des échantillons de rhabdophanes dopés avec de l'uranium ont également été synthétisées avec succès par voie humide, puis ont été convertis en solutions solides de monazite-chéralites par calcination. Cette étude a donc permis la mise au point d'une nouvelle méthode de préparation de monazite-chéralites dopées avec des actinides et l'amélioration des connaissances relatives à leur comportement à long terme.